

UC Berkeley

UC Berkeley Electronic Theses and Dissertations

Title

Nonlinear 3d frame element with multi-axial coupling under consideration of local effects

Permalink

<https://escholarship.org/uc/item/0sw164c3>

Author

Le Corvec, Veronique

Publication Date

2012

Peer reviewed|Thesis/dissertation

**Nonlinear 3d frame element with multi-axial coupling
under consideration of local effects**

by

Véronique Le Corvec

A dissertation submitted in partial satisfaction of the
requirements for the degree of
Doctor of Philosophy

in

Engineering - Civil and Environmental Engineering

in the

Graduate Division

of the

University of California, Berkeley

Committee in charge:

Professor Filip C. Filippou, Chair
Professor Robert L. Taylor
Professor Panayiotis Papadopoulos

Spring 2012

**Nonlinear 3d frame element with multi-axial coupling
under consideration of local effects**

Copyright 2012
by
Véronique Le Corvec

Abstract

Nonlinear 3d frame element with multi-axial coupling
under consideration of local effects

by

Véronique Le Corvec

Doctor of Philosophy in Engineering - Civil and Environmental Engineering

University of California, Berkeley

Professor Filip C. Filippou, Chair

This study concerns the formulation and validation of a 3d frame element that accounts for the inelastic response under the interaction of axial, flexural, shear and torsional effects. The proposed finite element addresses the need for a general beam element capable of accurately simulating the global as well as the local response of slender structural elements.

The new element accounts for the warping of arbitrary cross sections due to shear and torsion by introducing warping degrees of freedom at each section in order to accommodate higher order strain kinematics. The warping profile at a section uses the necessary number of Lagrange interpolation functions for the desired accuracy of local response. The warping distribution along the element axis is described by either Lagrange polynomials or spline interpolation functions. The number of interpolation parameters can be adjusted to control the accuracy of the local and global response.

The 3d beam element formulation is derived from a mixed Hu-Washizu variational potential, with the inclusion of the warping displacements as independent variables. In the proposed formulation the section response is coupled through the interpolation of the stress resultants and the warping displacements along the element axis. Because the stress resultants satisfy the element equilibrium exactly with the use of suitable force interpolation functions, the element is free of shear-locking. Non-uniform warping is accommodated by the warping displacement distributions, so that the proposed element can represent the stresses arising from local warping constraints. The element is incorporated in a general purpose finite element analysis program with the consistent linearization of the governing equations for warping force equilibrium and for element compatibility resulting in a robust algorithm for the element state determination.

The element is validated with several examples of linear and nonlinear material response of steel members. The linear elastic response is validated with analytical results, finite element models and some available experimental measurements. The inelastic response under monotonic and cyclic load conditions involves shear link specimens with wide flange and

box section under high shear. The accuracy and computational efficiency of the proposed element is demonstrated by comparing the numerical results with available experimental measurements from eccentrically braced steel frames and with local response results from solid and shell finite element models.

The study concludes with the investigation of the axial, flexural and torsion interaction under large displacements. The corotational formulation is derived from a general hypothesis that establishes the accuracy and scope of application of this method. Several numerical examples are used for the illustration of key nonlinear geometry aspects of slender elements under the interaction of axial, flexural and torsional effects.

Contents

List of Figures	iii
List of Tables	v
1 Introduction	1
1.1 General	1
1.2 Literature review	2
1.2.1 Beam theories	2
1.2.2 Shear response	3
1.2.3 Torsional response	5
1.2.4 Shear-lag modeling	6
1.2.5 Nonlinear geometric response	6
1.3 Objectives and scope	8
2 Element formulation and implementation	11
2.1 Overview	11
2.2 Element kinematics	13
2.3 Section kinematics	14
2.4 Variational formulation	16
2.4.1 Governing equations	16
2.4.2 Partial discretization of governing equations	22
2.4.3 Linearization	24
2.4.4 Complete discretization of governing equations	29
2.5 Warping displacement interpolation	33
2.5.1 Warping profile	34
2.5.2 Warping distribution	38
2.6 Numerical implementation	38
2.6.1 General	38
2.6.2 Element state determination	39
2.6.3 Implementation of inelastic material model	42

3	Evaluation for linear material response	45
3.1	Reference models	45
3.1.1	Shear beam model	45
3.1.2	Beam model with single warping mode	46
3.1.3	Shell model	47
3.2	Examples	48
3.2.1	Shear stress profile	48
3.2.2	Shear-lag effect	53
3.2.3	Torsional response	62
4	Evaluation for inelastic material response	70
4.1	Shear link with tubular box section	70
4.2	Shear link with I-section	83
5	Corotational formulation	95
5.1	Kinematics of continuous rod	95
5.2	Finite rotation parametrization	97
5.3	Corotational framework	100
5.3.1	Definition of element frame	101
5.3.2	Element kinematics	102
5.3.3	Definition of strain in element frame	107
5.3.4	Consistent stiffness matrix	110
5.3.5	Transformations due to rotation parametrization	111
5.3.6	On the non-symmetry of the tangent stiffness	115
5.3.7	Conclusions	115
5.4	Element with nonlinear axial-torsion interaction	116
5.5	Examples	118
5.5.1	L-shape cantilever beam	119
5.5.2	Hockling of a cable	121
5.5.3	Axial-torsional buckling	122
5.5.4	Inelastic torsion of girder	123
5.5.5	Six-story steel frame	125
6	Summary and conclusions	128
6.1	Summary	128
6.2	Conclusions	129
6.3	Recommendations for further research	131
	Bibliography	132
A	Warping displacements as global degrees of freedom	140

List of Figures

2.1	Kinematic variables of beam element without rigid body modes	13
3.1	Shell model for wide flange beam	47
3.2	Beam geometry for examples	48
3.3	Cross-sections for examples	48
3.4	Cantilever beam with loading	48
3.5	Geometry and mechanical properties for rectangular section	49
3.6	Number and location of warping degrees of freedom for rectangular section .	49
3.7	Warping displacement and shear stress distribution for rectangular section .	50
3.8	Geometry and mechanical properties for wide flange section	50
3.9	Number and location of warping degrees of freedom for wide flange section .	51
3.10	Warping profile of wide flange section with $n_w = 12$ degrees of freedom . . .	51
3.11	Warping displacement distribution for wide flange section	52
3.12	Shear stress distribution for wide flange section	52
3.13	Normal and shear stress profile for rectangular section at support of cantilever	54
3.14	Normal stress σ_{xx}^w due to warping at support of cantilever beam	54
3.15	Axial stress profile at support of cantilever beam with wide flange section . .	56
3.16	Shear-lag coefficient along x -axis of cantilever beam with wide flange section	56
3.17	Simply supported box girder of span L under concentrated and uniform load	57
3.18	Geometry and material properties of box girder section	57
3.19	Shear-lag coefficient of box girder under concentrated and uniform load . . .	59
3.20	Axial stress profile at midspan section of box girder under concentrated load	59
3.21	Three span continuous box girder bridge	61
3.22	Box girder section geometry	61
3.23	Shear-lag coefficient and moment distribution over half of continuous girder .	62
3.24	Cantilever beam of span $L = 5$ with concentrated torque T	63
3.25	Cross section geometries	63
3.26	Warping profile at free end of cantilever beam	66
3.27	Twist angle distribution for cantilever with I-section under warping constraint	67
3.28	Stress profile in lower flange of fixed cantilever end under warping constraint	68
3.29	Shear stress profile in lower flange of free cantilever end	68

4.1	Eccentrically braced frame specimen by Berman and Bruneau [12]	71
4.2	Shear link section dimensions and simulation model	71
4.3	Shear link with tubular box section at failure from [13]	72
4.4	Shear force vs. deformation γ of shear link with tubular box section	74
4.5	Shear force vs. deformation γ of shear link before first reversal	75
4.6	Stress profiles of shear link with tubular box section at LP A	79
4.7	Stress profiles of shear link with tubular box section at LP B	80
4.8	Stress profiles of shear link with tubular box section at LP C	81
4.9	Stress profiles of shear link with tubular box section at LP D	82
4.10	Geometry of I-section for shear link of Hjelmstad and Popov [42]	83
4.11	Shear force-displacement of shear-link with I-section	84
4.12	Stress profiles of shear link with I-section under displacement of 0.12 in	85
4.13	Stress profiles of shear link section at 0.175L under displacement of 0.12 in	87
4.14	Schemes for interpolation grid of warping profile for I-section	88
4.15	Response of shear link with I-section under eccentric shear force	89
4.16	Twist angle distribution for half of shear link with I-section	90
4.17	Warping displacement profile at midspan section of shear link with I-section	91
4.18	Stress profiles at fixed end of shear link under eccentric shear of 96 kips	92
4.19	Stress profiles at quarter span of shear link under eccentric shear of 96 kips	93
5.1	Kinematics of material point of beam element	96
5.2	Original and deformed configuration of 3d beam element with node triads	101
5.3	Definition of element frame with arbitrary origin	102
5.4	Kinematics in element frame	103
5.5	Geometry and properties of L-shape cantilever beam	119
5.6	Load-displacement relation for L-shape cantilever beam	120
5.7	Deformed shapes of L-shape cantilever beam with five-fold magnification	120
5.8	Geometry and properties of propped cantilever with torque at the tip	121
5.9	Torque versus twist angle at the tip of the hocking cable	121
5.10	Deformed shape history of twisting cable with magnification factor of 1	122
5.11	Axial buckling	123
5.12	Geometry and section dimensions of I-Beam with torque at midspan	124
5.13	Relation of applied torque with midspan twist angle for different models	124
5.14	Geometry and member sizes of six-story steel frame	125
5.15	Roof drift in x and y -direction under gravity and wind loading	126
5.16	Deformed shape of six-story frame with tenfold magnification	126

List of Tables

2.1	Interpolation grid for warping profile with n_w degrees of freedom for typical cross-section geometries	35
3.1	Tip displacement of cantilever beam with rectangular section	50
3.2	Tip displacement of cantilever beam with wide flange section	51
3.3	Midspan deflection of box girder under concentrated and uniform load	58
3.4	End twist angle θ for cantilever beam under end torque T	64
4.1	Number of elements and degrees of freedom for different models of shear link	73
4.2	Shear force of models at specific load points (LP) of shear link response . . .	75
4.3	Transverse displacement and twist angle under eccentric shear force of 96 kips	90
5.1	Transformation sequence for corotational formulation	114

Acknowledgments

First and foremost, I would like to thank my advisor, Professor Filippou, who has accepted me as one of his PhD students. I am grateful for his trust and his advices during the course of this work. I would like furthermore to express my gratitude for the opportunity he gave me to assist him in teaching several of his classes.

I would like to also thank all the professors of the Civil Engineering Department and the Mechanical Department who I met during my studies. I thank in particular the members of my dissertation committee, Professor Taylor and Professor Papadopoulos, for their valuable time and attention. I am also grateful to the other professors who accepted to serve in my qualification committee: Professor Chopra, Professor Wilkening and Professor Lee.

My five years in Berkeley have been a rich experience for me in learning and discovering new fields. I was particularly fortunate to enjoy the classes of Professor Armero, Professor Papadopoulos and Professor Chopra.

Part of this work was supported by the french company Setec TPI. I am grateful for their support and the fruitful exchange we had during the last two years of my PhD. I hope the collaboration which started with Dr. Kahan and Mr. Cespedes will be pursued.

A word of thanks goes also to the department administration and especially Shelley Okimoto who is always available and ensures that our academic stay goes well.

Finally I am most in debt with my family and friends. This thesis may not reflect completely the amount of work and the efforts behind. My friends and family were the best witnesses of my efforts and struggles and they have been my best support. I thank them for their infinite patience with me.

Chapter 1

Introduction

1.1 General

In today's professional practice structural engineers are often called to design and analyze large scale structures with irregular geometry and advanced materials under severe loading conditions. Performance based design guidelines require the evaluation of damage limit states and the determination of the ultimate capacity of structures in zones of moderate or high seismic risk for a large portfolio of loading scenarios including ensembles of three dimensional earthquake excitations. These challenging problems require the use of nonlinear analysis with general or special purpose finite element software. With the increased expectations from the results of finite element analyses of complex structures under extreme loading conditions the development of accurate, robust and computationally efficient elements is of great interest.

The type of finite elements that may be suitable for the analysis of structures in professional engineering practice ranges from one-dimensional beam elements to three-dimensional solid elements. Beam elements have one privileged direction and can model slender structures and components, such as bridge columns or moment resisting frame members. They are widely used in professional engineering practice for the low computational cost and the ease of post-processing and evaluation of the analysis results. For structural elements with small span to depth ratio, such as deep beams, shear walls, diaphragms and coupling beams, two-dimensional plate or shell elements are often used. Finally, solid elements can be employed for the study of local effects in critical structural members, and for the study of connections and of special detailing problems.

Among all available finite element models beam elements strike a good balance between accuracy and computational efficiency for most problems concerned with the global and local response of structures composed of slender elements. Several finite elements have been proposed to date in this category capable of handling inelastic material response and nonlinear geometry conditions. There are numerous beam elements that describe the interaction of axial force and flexure under linear or nonlinear geometry. The kinematic assumptions for

these elements permits the use of uniaxial material models and simplify considerably the formulation. There are few beam elements that account for the effect of shear and these are often limited to two dimensions. The extension to three dimensions necessitates the inclusion of torsion complicating the formulation considerably. This complexity increases further with the coupling of internal forces under nonlinear geometry conditions.

To address the need for a general 3d beam element that is suitable for the large scale simulation of structures undergoing inelastic material response and large displacements under monotonic and cyclic excitations, this study presents a 3d inelastic beam with nonlinear geometry under consideration of the multi-axial coupling of axial force, shear, flexure and torsion. Relevant studies for this topic are reviewed in the following section.

1.2 Literature review

The following review of relevant literature is divided into five parts: first, the review of models based on classical beam theories is presented followed by extensions of these to include shear and then torsion under inelastic material behavior. The fourth part reviews models capable of describing the shear lag effect, and the review concludes with past contributions to the corotational formulation for the description of nonlinear 3d beam kinematics.

1.2.1 Beam theories

From the mechanical standpoint beam elements are defined as a series of cross-sections which are orthogonal to an axis. Classical beam theories under linear elastic material behavior are based on the assumption that plane sections remain plane under deformation. In the Euler-Bernoulli beam theory, cross-sections also remain orthogonal to the axis, and shear deformations are neglected. In the Timoshenko beam theory [96], a first order correction for shear flexibility is included by relaxing the requirement that the cross-section remain orthogonal to the beam axis. These two theories constitute the basis for the development of several linear and nonlinear beam finite elements.

Beam finite elements that account for nonlinear material behavior can be subdivided in two categories: concentrated plasticity models and distributed plasticity models.

In the concentrated plasticity models the inelastic behavior is concentrated at plastic hinges typically located at the element ends, while the rest of the beam element remains elastic. The better known models in this category are the two-component model [18] and the one component model [35], whose formulation is described by Filippou and Fenves [29]. The plastic hinge response is defined in terms of axial force-axial deformation, moment-rotation or torque-twist angle relations based on concepts of plasticity theory [72]. Concentrated plasticity models have limitations in reproducing complex material response under cyclic loading. Moreover, it is challenging to describe the coupling between axial force, bending moments, shears, and torque in a 3d inelastic element and to calibrate the plastic hinge

parameters, which not only depend on the material parameters but also on the element geometry and the boundary conditions.

In the distributed inelasticity models, the element response is determined by numerical integration of the nonlinear response at several monitoring sections along the element. The relation between section and element response is based either on kinematics with the use of displacement interpolation functions, or on statics with force interpolation functions. The former approach gives a displacement formulation, while the latter approach results in a force or mixed formulation. Taylor et al. [92] and Lee [50] present the theoretical framework of the mixed formulation of a 3d beam element and compare its results with those of the displacement formulation. Several examples in these studies highlight the advantages of the mixed formulation.

The section response can either be described by a constitutive relation between section force resultants and corresponding deformations or obtained by numerical integration of the nonlinear material response over the cross section. The former approach is based on plasticity theory for section resultants [45], while the latter approach is known as 'fiber section model'. In the fiber section model the plane section assumption of classical beam theories is used to relate the material strains to section deformations. This approach is very efficient and accurate for the description of the coupling between axial force and biaxial bending moment [89], [90].

The inclusion of shear and torsion deformations under inelastic material response is more challenging, requiring refinement of section kinematics. Section models proposed to date are described in the next two sections. It is noteworthy that the adopted mixed formulation for the beam element overcomes the shear locking of displacement-based elements [92].

1.2.2 Shear response

Shear plays an important role in the structural element behavior either of short metallic members used for energy dissipation in structural applications like eccentrically braced frames, or of shear critical RC beams, deep beams and shear walls. In the latter case the amount of longitudinal and transverse reinforcement has a significant effect on the response.

Ceresa et al. [14] and Bairan and Mari [32] offer an extensive review of existing fiber beam models that account for shear. These reviews focus on reinforced concrete beams where the challenge lies in the section kinematics for including shear, and in the constitutive relation of the material as well as the interaction of concrete and reinforcing steel. In the following these two aspects are reviewed separately for the sake of clarity.

Shear models can be divided in four categories: (a) the shear force-deformation behavior is described as a uniaxial relation, (b) the effect of shear results from a fiber model with specified shear strain or stress distribution, (c) the effect of shear results from a fiber model with the shear strain distribution derived from equilibrium considerations, and (d) layer theories are used to describe the shear effect.

Typical of the models in the first category is the one proposed by Marini and Spacone

[60] for a uniaxial shear force-deformation law in conjunction with a fiber model for the description of the axial force and bending moment. The coupling between shear on the one hand and axial force and bending moment on the other is not accounted for and the model is limited to 2d section response.

Models in the second and third category include the effect of shear in the fiber section response by the assumption of section kinematics and an appropriate biaxial or triaxial material law. The models in the second group are based on the section kinematics of Timoshenko beam theory. Most models in the group assume that the shear strains or shear stresses are constant over the section. Examples include the reinforced concrete beam models of Rahal and Collins [75], Mazars et al. [61], Ceresa et al. [15], Mullapudi and Ayoub [63]. The distinguishing characteristic is the constitutive relation for concrete. Rahal and Collins [75] and Ceresa et al. [15] use the modified compression field theory for the purpose and are limited to monotonic loading. Mullapudi and Ayoub [63] use a biaxial law for the concrete constitutive model that is suitable for cyclic loading conditions. Finally, Mazars et al. [61] make use of a 3d damage constitutive law for concrete under cyclic load conditions. In these models the contribution of the longitudinal and transverse reinforcement is included by satisfying transverse force equilibrium between steel and concrete based on the method of Petrangeli et al. [69], [70].

The model of Petrangeli et al. [69], [70] is the first to use a parabolic shear strain distribution over a rectangular RC cross-section instead of a constant stress. The idea of using higher order strain or stress profiles was subsequently pursued by several authors. The shear strain profile was derived for rectangular, I-beam, and box sections from the linear elasticity solution and then used unaltered for inelastic material response. In this group of models belong those of Saritas [82], Navarro Gregori [37], and Papachristidis et al. [68]. Saritas [82] proposed a variationally consistent 2d shear beam model for steel and RC beams with rectangular or I-sections. Navarro Gregori et al. [37] extended the idea to 3d RC beams with application to rectangular and tubular box sections. Finally, Papachristidis et al. [68] proposed an enhancement of the shear strain profile to better account for the flow of shear stress between the web and flanges of steel wide flange and tubular box sections.

The advantage of this group of models is their relative simplicity and consequent computational efficiency. Their limitation stems from the point-wise violation of longitudinal and transverse equilibrium and the consequent inability to represent accurately localization and failure. The third group of shear models attempts to address this limitation by allowing for a variable shear strain profile that explicitly satisfies longitudinal and transverse equilibrium.

The first model with inter-fiber equilibrium was proposed by Vecchio and Collins [98] in the form of a dual section analysis, in which the shear strain profile is determined from the equilibrium of two adjacent sections. Bentz [11] derives the shear stress profile by the rate of change of flexural stresses, while Navarro Gregori [38] uses a similar idea for the variable strain profile of his model. The most advanced formulation in this group is due to Bairan [3] who included warping degrees of freedom as parameters of the transverse shear strain and of the axial strain distribution and used it for the study of 3d RC beams under

general monotonic loading. Mohr addressed the computational complexity of the model by simplifying the formulation for the analysis of 2d RC beams [62].

In the last group of models belong the layer beam models for laminate composite structures, which are extensively reviewed by Ghugal and Shimpi [34] starting with the seminal work of Reddy [77] who was the first to propose a higher-order theory for laminated plates with shear deformation. These models are suitable for the shear analysis of inhomogeneous, linear elastic beams and plates, but their suitability for inelastic material response is unclear, and they are, therefore, not pursued further in this study.

1.2.3 Torsional response

The linear elastic torsional response of beams cannot be represented correctly with the plane section hypothesis of classical beam theories. St Venant introduced warping functions for the representation of uniform torsion with the warping amplitude proportional to the constant twist rate [95]. This theory is, however, not able to describe the normal stresses caused by warping constraints. Higher order beam theories, such as the beam theory of Vlasov [36], remove the limiting assumption of uniform torsion, but keep the assumption that the warping amplitude is proportional to the twist rate. Finally, Bencoster [10], [83] developed a more general torsional theory that includes shear deformations by introducing an extra degree of freedom per node.

The preceding classical torsion theories are successful in the description of the linear elastic response of beams. Several studies focused on the derivation of suitable warping functions for use in finite element analysis. Prokic [73] proposed a general method for the derivation of warping functions of thin-walled sections that was used in several applications [74], [80]. The general beam element by El Fatmi, [23], [24] extends this idea to the shear deformation profile with application to thin-walled and compact sections under shear and torsion. More recent models by El Fatmi and Ghazouani [25] [33], Saade et al. [81], and Jang and Kim [44] describe the complete section warping including the in-plane distortion with additional degrees of freedom. These beam models, which are limited to linear elastic material response, account for different warping constraints at the boundaries and can reproduce local effects as accurately as shell finite element models [24], [44]. The model of Saade is also suitable for the study of instability problems [80].

The beam elements for inelastic torsional response can be divided into two categories: simple concentrated plasticity models or distributed plasticity models based on fixed warping profiles. In the first group of models the inelastic torsional response is either uncoupled from the flexural response or coupled with it on the basis of resultant plasticity theory, as proposed by Powell and Chen [72]. In the second group of models belong fiber beam models with fixed warping profiles for the section kinematics based on linear elastic beam theories. With this approach variational beam formulations were proposed by Pi and Trahair [71], Gruttman et al. [39] and Nukala and White [66] for the inelastic response of beams with wide flange cross-section. For compact sections Mazars et al. [61] proposed a fixed warping profile based

on St Venant beam theory. Klinkel and Govindjee [47] derived the warping profile for a beam with anisotropic material response using a solid finite element model.

1.2.4 Shear-lag modeling

Shear lag refers to the non-uniform axial stress distribution in the flanges of a cross section under shear loading. The problem is of interest for beams with wide flange cross-sections and, in particular, for bridge box girder sections. The shear-lag effect gives rise to higher axial stresses than predicted by classical beam theory in portions of the cross-section near the supports and near load application points. The phenomenon is similar to the additional normal stresses caused by warping constraints. In the case of shear-lag the stress concentration is related to the shear deformation profile.

The non-uniform axial stress distribution in the flanges of the cross section can be described either with stress amplification factors or with the concept of effective flange width, as is the case in design recommendations, such as those of the Eurocode [30].

Models for the shear-lag effect are limited to linear elastic response and can be divided into two categories: (a) finite element models with plate and solid elements, or (b) beam formulations. Tenchev [94], Lee Sung et al. [52], and Lertsima et al. [53] used linear finite element simulations to derive empirical formulas for the shear-lag coefficients.

For the numerical solution of the response of beam elements with shear-lag Reissner used the principle of minimum potential energy [78] and Song used harmonic stress analysis [88], while Koo presented a mixed formulation for the problem [48]. These models are based on the assumption of either a parabolic or a cubic axial stress distribution in the section flange and introduce additional degrees of freedom for the beam element.

Further improvements of these models aim at the inclusion of prestressing effects [17] [16], and the interaction between flexure and shear-lag [100]. Finally, the model of Luo et al. [56], [57], [59] applies to beams of variable depth and accounts for shear deformations. Noteworthy experimental results on the shear-lag effect of box girder sections are reported by Luo and his research team [58].

1.2.5 Nonlinear geometric response

Structures subjected to extreme loads, such as high earthquake accelerations, may undergo large displacements. Consequently, an inelastic beam model needs to account for nonlinear geometry effects to be suitable for the simulation of structures under extreme load conditions. The Lagrangian formulation is most commonly used for the inclusion of nonlinear geometry effects, expressing the deformed element configuration with respect to a reference configuration [101]. Three variants of the formulation are known: the total Lagrangian formulation, the updated Lagrangian formulation, and the corotational formulation [26].

The total Lagrangian formulation uses as fixed reference configuration the undeformed structure. The updated Lagrangian formulation uses the last deformed configuration as

reference configuration for the current time step. Finally, the corotational formulation defines a new undeformed reference configuration at every time step whose position is based on the end node coordinates of the deformed element.

The following brief review refers to the corotational formulation, because this approach is followed for the 3d beam element formulation in this study. According to the historic review by Felippa and Haugen [26] the term corotational or co-rotated was introduced in the sixties in the context of field theory and continuum mechanics.

The key idea of the corotational formulation is the definition of a rigid *element frame*, that follows the element as it deforms. It allows for the decomposition of the total node displacements into the rigid body motion of the element reference frame and the deformational displacements. The element reference frame is defined by the geometric properties of the element and its privileged directions (chord, normal, etc.), while the deformational displacements correspond to the local motion relative to the element frame.

Assuming that the deformations in the element frame are small in the context of small strains permits the element response to be established under the assumption of first order geometry. The great promise of the method for practical applications is that, although the total displacements at the structural level are large, the local deformations relative to the reference frame can be made as small as necessary for the assumption of linear geometry by mesh subdivision of the structural member. The kinematic assumption of small deformations is, however, independent of the corotational formulation, since it is used only for the determination of the element response in the reference frame.

Among the seminal contributions for the development of the corotational approach is the work of Brogan, Rankin and Nour-Omid, and Crisfield. This work culminates in the concept of the *element independent* formulation with the use of projector operators. Crisfield also proposed a consistent element independent formulation [20] without resorting to projectors.

The formulation of Nour-Omid and Rankin forms the basis of several recent element formulations due to its compact derivation with the use of projection matrices [5], [7], [8], [9], [26], [31]. With this approach the corotational framework can be used with a large library of elements, since the necessary geometric transformations for large displacements are *element-independent*. Examples include the two-node beam elements [8], [26], the three node triangular element [5], [26], and the 4-node membrane element [7].

Research in the nonlinear geometry under large displacements with the corotational formulation seeks to address two issues: the definition of the element frame, and the representation of large rotations in three dimensions.

The element frame is not unique for a 3d beam and a surface element. For a two node beam element, the chord joining the two nodes is the direction of axial deformation and axial force and constitutes the first direction of the reference frame. Two orthonormal directions in the plane normal to the chord then complete the selection. There are several choices for these directions. Since the goal of selecting a reference frame is the extraction of the rigid body modes in a way that keeps the local displacements as small as possible, the reference frame selection considers the node rotations, as well as the node positions. Methods for averaging

the two end node rotations were proposed by Nour-Omid and Rankin [76], Crisfield [20], [21] and Levy and Spillers [54]. The problem becomes more involved for membrane and plate elements with three or more nodes ([9], [26], [40]).

There exist several ways of treating finite rotations in 3d finite element analysis: the rotation tensor, the rotation vector, and the method of quaternions. The rotation tensor belongs to a non-commutative group, which distinguishes it from translations which belong to a vector space. This fact gives rise to implementation difficulties in terms of the choice of parametrization and of the method for rotation updating in a iterative nonlinear solution algorithm. The proposal by Rankin and Nour-Omid [65] that was also followed by Felippa and Haugen [26] uses the rotation tensor for the parametrization of the global rotation, and the rotation vector for the rotations in the element frame, thus requiring a multiplicative rotation update. This drawback was overcome by Battini and Pacoste [8] through a transformation of the update to a rotation vector, leading to an additive update of rotations. For a more elegant and computationally efficient formulation with additive rotation update Battini [5] later proposed the use of quaternions and compared the different methods in [6].

In spite of the successful use of the corotational formulation for the solution of several challenging problems of nonlinear geometry, such as elastic and plastic instability, post-buckling behavior, and snap-through, a few questions still remain regarding the symmetry of the stiffness matrix, and the invariance and independence of the element frame.

The corotational formulation breaks down when the nonlinear strains cannot be approximated by large node displacements through mesh refinement. This is the case for beam elements under large twist rotations requiring the assumption of nonlinear strains in the element frame [8]. Pi and Trahair [71], [97] and Nukala and White [66] proposed beam elements for large twist rotations and the associated Wagner effect using a total lagrangian formulation.

1.3 Objectives and scope

This study deals with the nonlinear material and geometric response of three-dimensional beam elements under consideration of the multi-axial coupling of axial force, shear, flexure and torsion. Its main objectives are as follows:

- The development of a general 3d beam element able to describe the multi-axial inelastic response of structural elements with particular consideration of the effect of 3d shear and torsion. To accomplish this task the section kinematics use additional degrees of freedom for the description of warping deformations. The assumptions of the model are kept general so that it can be used with any type of cross section and material.
- The inclusion of boundary effects and non-uniform warping in the element formulation. As a consequence, there is coupling of section response along the element with the warping deformations affecting the axial and shear strains at several sections. The

element is thus capable of studying the effect of boundary stress concentrations due to warping constraints.

- The derivation of the enhanced beam element from a consistent potential based on the Hu-Washizu variational principle, so as to avoid the shear-locking problems common in displacement-based formulations.
- The element formulation should be such that it can be used in conjunction with simpler elements in the modeling of structures, thus avoiding excessive computational cost in regions of the structural model where the effects of shear and torsion are not significant. To accomplish this objective various alternatives of the enhanced beam element are explored with different degree of accuracy.
- The assessment of the element benefits by comparison with the results of standard beam elements that do not account for the interaction of shear and torsion or include the effect of 2d shear only. Three features of the response of 3d beams are used for the purpose: the distribution of shear strains and stresses over the cross section, the shear-lag effect, and the torsional response for linear elastic material. The local response is also compared with shell and solid finite element models.
- The evaluation of the element for the representation of the shear-lag effect in continuous box girder bridges.
- The evaluation of the element response for inelastic materials by comparison with experimental results of shear-link beams. This investigation also tests the robustness and computational efficiency of the formulation for response simulations of large scale structures under earthquake excitations.
- The derivation of a general and consistent corotational framework for 3d beams under multi-axial coupling of axial force, shear, flexure and torsion. The framework renders the nonlinear geometry effects of the 3d beam response independent of the material response. The advantages and some limitations of the formulation are illustrated with 3d beam examples from the literature involving the coupling of axial force, moment and torque.

The thesis is organized in six chapters. Chapter 2 presents the derivation of the new beam element with warping degrees of freedom. The chapter starts with the review of the assumptions of the formulation in the context of existing models. It is followed by the derivation of the element response from a variational potential, and concludes with some details of the numerical implementation of the element. Chapter 3 evaluates the response of the proposed beam element by comparison with existing beam, shell and solid finite element models under linear elastic material response. Chapter 4 presents the use of the proposed beam element for the simulation of the inelastic steel shear link response, and

for the simulation of the shear lag effect in a three span box girder bridge under linear elastic material response. Chapter 5 describes the incorporation of large displacements in the proposed beam formulation in the context of the corotational framework of nonlinear geometry. Several examples from the literature are used to showcase the element response under large displacements. Finally, Chapter 6 summarizes the study and offers conclusions and directions for further study.

Chapter 2

Element formulation and implementation

This chapter presents the derivation of a fiber-beam element that accounts for section warping deformations and their variation along the element and is capable of describing constrained warping and the shear-lag effect. The frame element describes the elastic and inelastic response of prismatic 3d beams under the combination of axial force, flexure, shear and torsion.

The following presentation starts with the main assumptions of the model and the definition of element and section kinematics followed by the derivation of the mixed variational formulation. The finite element discretization results in the consistent resisting force vector and stiffness matrix of the element. This is followed by the description of the different basis functions for the interpolation of the warping displacements over the section and along the element. It concludes with the element state determination process and the incorporation of inelastic material response in the element formulation.

2.1 Overview

The element kinematics are based on the assumption of small displacements, thus permitting the element formulation to be based on first-order displacements only. Without loss of generality the element formulation is described in a local reference system that excludes rigid body modes.

The beam element is described by a series of cross-sections on the assumption that the section kinematics are described locally. According to the review in chapter 1, there are two approaches for arriving at the section strain distribution: in the first the axial strain profile is linear and the shear strain profile is assumed independently based on the section geometry; in the second approach the axial strain profile is no longer linear with the strain profile parameters derived from the satisfaction of transverse and longitudinal force equilibrium at the section. Once the section kinematics are postulated, the section response is obtained by numerical integration of the local material response with an integration method for the

section integrals (fiber approach). With this approach the element is able to simulate both elastic and inelastic material response through the use of appropriate multi-axial material constitutive laws.

In spite of its simplicity the assumption of a fixed shear strain profile for the beam section suffers from several shortcomings: its strong dependence on section geometry, the violation of shear stress flow and local equilibrium, and its dependence on the assumption of a homogeneous, linear elastic section, free to warp. To overcome these model inconsistencies a shear correction factor is necessary for matching the analytical solution of the linear elastic response. Its role under inelastic material response is, however, unclear.

Models with a variable shear strain profile for the beam section seek to overcome the shortcomings of the fixed strain profile models at the expense of complexity and calculation cost. The model in this study draws inspiration from the earlier models of Bairan [3] and Gregori Navarro [38]. Its distinction with respect to the model of Gregori Navarro is the use of warping displacements as additional section degrees of freedom for the derivation of shear strains instead of deriving directly the shear strain profile of the cross section. With this approach the coupling of the torsional and shear response can be described consistently and accurately. With respect to the model of Bairan the current model neglects the in-plane section deformations for a significant increase in computational efficiency without loss of accuracy for the applications of interest.

The proposed 3d beam element is derived in the framework of force-based elements from a variational potential, referred to as the Hu-Washizu potential. The warping displacements are assumed as an independent field in the derivation of the element response, thus leading to a mixed formulation with the independent interpolation of basic element forces and warping displacements over the element. This approach overcomes the shear-locking problem of elements that are based only on interpolation of the displacements.

With the introduction of warping displacements as an independent field it is possible to describe the shear and torsional response of 3d beams. Moreover, with the interpolation of the warping displacements over the element length it is possible to describe the local response of 3d beams caused by warping constraints and shear lag. The additional warping degrees of freedom for the element can be treated as global degrees of freedom of the structural model or local degrees of freedom that are condensed out before assembly of the element resisting force vector and stiffness matrix. The former case is possible only when all elements of the structural model are of the same type, as is the case in multi-span box girder bridges with warping constraints affecting the response over the entire length of the structure. The latter case becomes necessary when the structural model consists of beam elements with warping displacement degrees of freedom and standard beam elements without such degrees of freedom, as dictated by requirements of computational efficiency for the study of the local effect of warping constraints in multi-span box girder bridges. Because of their practical importance both formulations are pursued in this study, as discussed in the following sections which present the element formulation and its implementation in a general purpose finite element analysis program.

2.2 Element kinematics

The proposed frame element is represented by a collection of cross-sections along its axis x . The axis is a straight line in the reference configuration delimited by end nodes I and J, as shown in figure (2.1). The element formulation takes place in a local reference frame, called the basic system, that results from the removal of the rigid body displacements from the total displacements. Figure (2.1) shows the boundary conditions of the choice of basic system in this study: all translations and the rotation about the x -axis are restrained at node I, while the translations in the y and z -direction are restrained at node J.

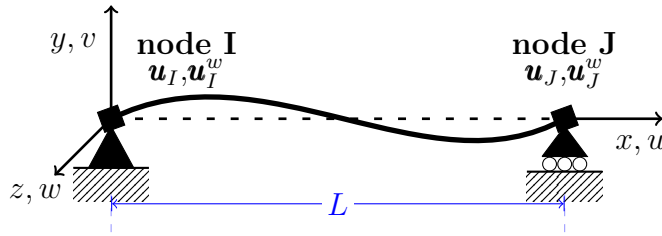


Figure 2.1: Kinematic variables of beam element without rigid body modes

The displacements of a standard 3d beam element consist of three translations u , v , and w in x , y , and z , respectively, and three rotations ϕ , θ_y , and θ_z about axes x , y and z , respectively. These are functions of position x along the element axis and are collected in displacement vector $\mathbf{u}(x)$

$$\mathbf{u}(x) = [u(x) \quad v(x) \quad w(x) \quad \phi(x) \quad \theta_y(x) \quad \theta_z(x)]^T \quad (2.1)$$

The 3d beam element in the present study is enhanced with warping displacements $\mathbf{u}^w(x, y, z)$ which are kept separate from the displacements $\mathbf{u}(x)$ of the standard 3d beam element.

The element degrees of freedom of a standard 3d beam in the local reference system are also kept separate from the additional warping degrees of freedom of the enhanced beam element in this study. The former are denoted with \mathbf{u}_{IJ} and the latter with \mathbf{u}_{IJ}^w , the subscript indicating that the displacements at nodes I and J are collected into a single vector.

$$\mathbf{u}_{IJ} = \begin{pmatrix} \mathbf{u}_I \\ \mathbf{u}_J \end{pmatrix} \quad \text{and} \quad \mathbf{u}_{IJ}^w = \begin{pmatrix} \mathbf{u}_I^w \\ \mathbf{u}_J^w \end{pmatrix} \quad (2.2)$$

In accordance with equation (2.1) there are six standard degrees of freedom per node. As discussed in section 2.5, there are n_w warping degrees of freedom per section, so that \mathbf{u}_{IJ}^w has as many as $2n_w$ terms if the warping displacements are unknown at the end nodes of the element.

The element deformations \mathbf{v} are the relative translation u in the x -direction at node J, the rotations θ_y and θ_z at node I about the y and z -axis, respectively, the relative rotation

or angle of twist ϕ about the x -axis at node J, and the rotations θ_y and θ_z at node J about the y and z -axis, respectively.

$$\mathbf{v} = [u \ \theta_{zI} \ \theta_{zJ} \ \phi \ \theta_{yI} \ \theta_{yJ}]^T \quad (2.3)$$

The element deformations \mathbf{v} can be uniquely determined from the displacements \mathbf{u}_{IJ} in the local reference system. Under linear geometry, the relation between element deformations \mathbf{v} and displacements \mathbf{u}_{IJ} is given by the compatibility matrix \mathbf{a}_g with constant coefficients

$$\mathbf{v} = \mathbf{a}_g \mathbf{u}_{IJ} \quad (2.4)$$

where

$$\mathbf{a}_g = \begin{bmatrix} -1 & 0 & 0 & 0 & 0 & 0 & 1 & 0 & 0 & 0 & 0 & 0 \\ 0 & 1/L & 0 & 0 & 0 & 1 & 0 & -1/L & 0 & 0 & 0 & 0 \\ 0 & 1/L & 0 & 0 & 0 & 0 & 0 & -1/L & 0 & 0 & 0 & 1 \\ 0 & 0 & 0 & -1 & 0 & 0 & 0 & 0 & 0 & 1 & 0 & 0 \\ 0 & 0 & -1/L & 0 & 1 & 0 & 0 & 0 & 1/L & 0 & 0 & 0 \\ 0 & 0 & -1/L & 0 & 0 & 0 & 0 & 0 & 1/L & 0 & 1 & 0 \end{bmatrix} \quad (2.5)$$

L is the undeformed element length.

2.3 Section kinematics

Under the assumption that the section does not deform in its plane, the displacements $\mathbf{u}^m(x, y, z)$ of a material point m with coordinates (y, z) at a section with distance x from the origin of the reference frame are decomposed into displacements $\mathbf{u}^r(x, y, z)$ describing the rigid body motion of the section plane and warping displacements $\mathbf{u}^w(x, y, z)$

$$\mathbf{u}^m(x, y, z) = \mathbf{u}^r(x, y, z) + \mathbf{u}^w(x, y, z) \quad (2.6)$$

This displacement assumption is sufficiently accurate for the description of phenomena that are of interest in this study such as shear stress distribution under shear and torsion, and normal stress distribution under warping constraints. The displacements \mathbf{u}^r are those of an Euler-Bernoulli 3d beam element.

After expressing the displacements \mathbf{u}^r in terms of the cross-section generalized displacements $\mathbf{u}(x)$ in equation (2.1) gives the following equation

$$u_x^m(x, y, z) = u(x) - y\theta_z(x) + z\theta_y(x) + u_x^w(x, y, z) \quad (2.7a)$$

$$u_y^m(x, y, z) = v(x) - z\phi(x) + u_y^w(x, y, z) \quad (2.7b)$$

$$u_z^m(x, y, z) = \underbrace{w(x) + y\phi(x)}_{\mathbf{u}^r} + u_z^w(x, y, z) \quad (2.7c)$$

with the assumption that the warping displacement components u_x^w , u_y^w and u_z^w are non-zero. For a unique description of section deformations the warping displacements \mathbf{u}^w must be free of rigid body modes and the procedure for accomplishing this is described in section 2.5.1.

The strain displacement relations are

$$\epsilon_{xx} = \frac{\partial u_x^m}{\partial x} = \frac{\partial u}{\partial x} - y \frac{\partial \theta_z}{\partial x} + z \frac{\partial \theta_y}{\partial x} + \frac{\partial u_x^w}{\partial x} \quad (2.8a)$$

$$\epsilon_{yy} = \frac{\partial u_y^m}{\partial y} = \frac{\partial u_y^w}{\partial y} \quad (2.8b)$$

$$\epsilon_{zz} = \frac{\partial u_z^m}{\partial z} = \frac{\partial u_z^w}{\partial z} \quad (2.8c)$$

$$2\epsilon_{xy} = \frac{\partial u_x^m}{\partial y} + \frac{\partial u_y^m}{\partial x} = -\theta_z + \frac{\partial u_x^w}{\partial y} + \frac{\partial v}{\partial x} - z \frac{\partial \phi}{\partial x} + \frac{\partial u_y^w}{\partial x} \quad (2.8d)$$

$$2\epsilon_{xz} = \frac{\partial u_x^m}{\partial z} + \frac{\partial u_z^m}{\partial x} = \theta_y + \frac{\partial u_x^w}{\partial z} + \frac{\partial w}{\partial x} + y \frac{\partial \phi}{\partial x} + \frac{\partial u_z^w}{\partial x} \quad (2.8e)$$

Because the section is assumed not to deform in its plane, the strains ϵ_{yy} and ϵ_{zz} are zero

$$\epsilon_{yy} = 0 \quad \epsilon_{zz} = 0 \quad (2.9)$$

requiring, after the removal of rigid body modes from \mathbf{u}^w , that the warping displacement components u_y^w and u_z^w be zero. Consequently, the warping displacements simplify to $\mathbf{u}^w(x, y, z) = [u_x^w(x, y, z), 0, 0] = [u^w(x, y, z), 0, 0]$. After introducing these simplifications in equation (2.8) followed by the separation of the effect of the displacements \mathbf{u}^r from the warping displacements u^w the strain-displacement relations become

$$\boldsymbol{\epsilon}(x, y, z) = \begin{pmatrix} \epsilon_{xx} \\ 2\epsilon_{xy} \\ 2\epsilon_{xz} \end{pmatrix} = \boldsymbol{\epsilon}^r(\mathbf{u}^r) + \boldsymbol{\epsilon}^w(u^w) \quad (2.10)$$

where

$$\boldsymbol{\epsilon}^r(x, y, z) = \mathbf{a}_s(y, z) \mathbf{e}[\mathbf{u}(x)] \quad (2.11)$$

with the section compatibility matrix $\mathbf{a}_s(y, z)$

$$\mathbf{a}_s(y, z) = \begin{bmatrix} 1 & -y & 0 & 0 & z & 0 \\ 0 & 0 & 1 & -z & 0 & 0 \\ 0 & 0 & 0 & y & 0 & 1 \end{bmatrix} \quad (2.12)$$

and the section deformation vector $\mathbf{e}(x)$ with terms consisting of displacement components of the generalized displacement vector $\mathbf{u}(x)$ of the beam in equation (2.1) and their derivatives

$$\mathbf{e}(x) = [u' \quad \theta'_z \quad (v' - \theta_z) \quad \phi' \quad \theta'_y \quad (w' + \theta_y)]^T \quad (2.13)$$

where the symbol $()'$ denotes the derivative of the corresponding term with respect to coordinate x . The components of the generalized section deformation vector $\mathbf{e}(x)$ are the axial strain ϵ_0 at the reference x -axis, the derivative of the twist angle κ_x , the curvatures about the z - and y -axis, κ_z and κ_y , respectively, and the shear deformations in the y - and z -direction, γ_y and γ_z , respectively.

$$\mathbf{e}(x) = [\epsilon_0 \quad \kappa_z \quad \gamma_y \quad \kappa_x \quad \kappa_y \quad \gamma_z]^T \quad (2.14)$$

where

$$\begin{aligned} \epsilon_0 &= u' \\ \kappa_z &= \theta'_z \\ \gamma_y &= v' - \theta_z \\ \kappa_x &= \phi' \\ \kappa_y &= \theta'_y \\ \gamma_z &= w' + \theta_y \end{aligned}$$

With equation (2.8) the warping strains in equation (2.10) can be written in the form

$$\boldsymbol{\epsilon}^w(x, y, z) = \begin{pmatrix} \epsilon_{xx}^w \\ 2\epsilon_{xy}^w \\ 2\epsilon_{xz}^w \end{pmatrix} = \begin{pmatrix} \frac{\partial u^w(x, y, z)}{\partial x} \\ \frac{\partial u^w(x, y, z)}{\partial y} \\ \frac{\partial u^w(x, y, z)}{\partial z} \end{pmatrix} \quad (2.15)$$

As can be seen from equation (2.15), the warping displacements u^w contribute to the axial strain ϵ_{xx} as well as to the shear strains ϵ_{xy} and ϵ_{xz} . The additional strains $\boldsymbol{\epsilon}^w$ due to the warping displacements play a critical role in the description of the effect of warping constraints on the additional stresses of a 3d beam section.

2.4 Variational formulation

2.4.1 Governing equations

The governing equations of element response are derived with the Hu-Washizu mixed variational principle [50] using potential minimization for establishing the weak form of the element equilibrium and compatibility equations and for deriving the element stiffness matrix.

The independent fields of the Hu-Washizu potential Π are assumed to be the generalized displacements \mathbf{u} of the Euler-Bernoulli 3d beam, the warping displacements u^w , the section

deformations \mathbf{e} , and the stresses $\boldsymbol{\sigma}$. The latter are work-conjugate to the strains $\boldsymbol{\epsilon}$ in equation (2.15) so that

$$\boldsymbol{\sigma} = \begin{pmatrix} \sigma_{xx} \\ \sigma_{xy} \\ \sigma_{xz} \end{pmatrix} \quad (2.16)$$

The definition of the Hu-Washizu potential Π over the element volume V starts with the strains $\boldsymbol{\epsilon}$ and stresses $\boldsymbol{\sigma}$ with the former decomposed into $\boldsymbol{\epsilon}^r$ and $\boldsymbol{\epsilon}^w$

$$\begin{aligned} \Pi(\mathbf{u}, u^w, \boldsymbol{\epsilon}^r, \boldsymbol{\epsilon}^w, \boldsymbol{\sigma}) &= \int_V \boldsymbol{\sigma}^T [\boldsymbol{\epsilon}^r(\mathbf{u}) + \boldsymbol{\epsilon}(u^w) - (\boldsymbol{\epsilon}^r + \boldsymbol{\epsilon}^w)] dV \\ &+ \int_V W(\boldsymbol{\epsilon}^r, \boldsymbol{\epsilon}^w) dV + \Pi_{ext}(\mathbf{u}, \mathbf{u}_{IJ}, \mathbf{u}_{IJ}^w) \end{aligned} \quad (2.17)$$

where W is the internal potential energy and Π_{ext} is the external potential.

Expressing the strains $\boldsymbol{\epsilon}^r$ in terms of the section deformations \mathbf{e} according to equation (2.11) modifies the Hu-Washizu potential Π to the form

$$\begin{aligned} \Pi(\mathbf{u}, u^w, \mathbf{e}, \boldsymbol{\epsilon}^w, \boldsymbol{\sigma}) &= \int_V \boldsymbol{\sigma}^T \mathbf{a}_s [\mathbf{e}(\mathbf{u}) - \mathbf{e}] dV + \int_V \boldsymbol{\sigma}^T [\boldsymbol{\epsilon}^w(u^w) - \boldsymbol{\epsilon}^w] dV \\ &+ \int_V W(\mathbf{e}, \boldsymbol{\epsilon}^w) dV + \Pi_{ext}(\mathbf{u}, \mathbf{u}_{IJ}, \mathbf{u}_{IJ}^w) \end{aligned} \quad (2.18)$$

with the dependence of the potential on the section deformations \mathbf{e} replacing the dependence on the strains $\boldsymbol{\epsilon}^r$. The assumption that the strain field $\boldsymbol{\epsilon}^w$ is derived from the warping displacements u^w according to equation (2.15) removes the dependence of the Hu-Washizu potential Π from $\boldsymbol{\epsilon}^w$. The second volume integral in equation (2.18) is then identically equal to zero, and the Hu-Washizu potential Π simplifies to

$$\Pi(\mathbf{u}, u^w, \mathbf{e}, \boldsymbol{\sigma}) = \int_V \boldsymbol{\sigma}^T \mathbf{a}_s [\mathbf{e}(\mathbf{u}) - \mathbf{e}] dV + \int_V W(\mathbf{e}, u^w) dV + \Pi_{ext}(\mathbf{u}, \mathbf{u}_{IJ}, \mathbf{u}_{IJ}^w) \quad (2.19)$$

The expression in square brackets under the first volume integral indicates that the displacements $\mathbf{u}(x)$ and the section deformations $\mathbf{e}(x)$ are retained as independent fields of the Hu-Washizu potential Π , with the consequence that this kinematic relation is satisfied only in the weak sense.

Noting that \mathbf{a}_s is a function of y and z according to equation (2.12), and \mathbf{e} a function of x according to equation (2.13), the first volume integral in equation (2.19) can be decomposed into the product of an integral over the cross section area A and of an integral over the element length L . With the definition of the generalized section resultants $\mathbf{s}(x)$ in the form

$$\mathbf{s}(x) = \int_A \mathbf{a}_s^T(y, z) \boldsymbol{\sigma}(x, y, z) dA \quad (2.20)$$

the Hu-Washizu potential Π simplifies further to

$$\Pi(\mathbf{u}, u^w, \mathbf{e}, \boldsymbol{\sigma}) = \int_0^L \mathbf{s}^T [\mathbf{e}(\mathbf{u}) - \mathbf{e}] dx + \int_V W(\mathbf{e}, u^w) dV + \Pi_{ext}(\mathbf{u}, \mathbf{u}_{IJ}, \mathbf{u}_{IJ}^w) \quad (2.21)$$

The six components of the section force vector $\mathbf{s}(x)$ in equation (2.20) are the section resultants or internal forces at a distance x from the origin of the reference system. The section resultants $\mathbf{s}(x)$ consist of the normal force $N(x)$, the bending moments $M_y(x)$ and $M_z(x)$, about the y - and z -axis, respectively, the shear forces $V_y(x)$ and $V_z(x)$, in the y - and z -axis, respectively, and the torsional moment $T(x)$ so that

$$\mathbf{s}(x) = [N(x) \quad M_z(x) \quad V_y(x) \quad T(x) \quad M_y(x) \quad V_z(x)]^T \quad (2.22)$$

The external potential Π_{ext} in equation (2.21) involves contributions of applied nodal forces $\bar{\mathbf{p}}_{IJ}$, uniform element loading $\bar{\mathbf{p}}^u(x)$, and applied nodal forces $\bar{\mathbf{p}}_{IJ}^w$ associated with warping, and takes the form

$$\Pi_{ext} = -\mathbf{u}_{IJ}^T \bar{\mathbf{p}}_{IJ} - \int_0^L \mathbf{u}^T \bar{\mathbf{p}}^u(x) dx - \mathbf{u}_{IJ}^{wT} \bar{\mathbf{p}}_{IJ}^w \quad (2.23)$$

The applied nodal forces $\bar{\mathbf{p}}_{IJ}$ and $\bar{\mathbf{p}}_{IJ}^w$ act at the end nodes of the element and are work conjugate with the ordinary degrees of freedom \mathbf{u}_{IJ} and the warping degrees of freedom \mathbf{u}_{IJ}^w , respectively. If both end sections are free to warp, then the applied warping forces are zero $\bar{\mathbf{p}}_{IJ}^w = \mathbf{0}$. Otherwise, warping displacements \mathbf{u}^w are imposed at node I or node J and the corresponding forces need to be determined. The uniform element loading $\bar{\mathbf{p}}^u(x)$ consists of four components: the axial load \bar{p}_x^u in x , the transverse load in directions y and z , \bar{p}_y^u and \bar{p}_z^u , respectively, and the torque \bar{p}_ϕ^u .

$$\bar{\mathbf{p}}^u(x) = [\bar{p}_x^u(x) \quad \bar{p}_y^u(x) \quad \bar{p}_z^u(x) \quad \bar{p}_\phi^u(x) \quad 0 \quad 0]^T \quad (2.24)$$

The determination of the element response requires the minimization of the potential Π . It is accomplished by setting equal to zero the variation of Π with respect to the independent fields $\mathbf{u}(x)$, $u^w(x, y, z)$, $\mathbf{e}(x)$, and $\boldsymbol{\sigma}(x, y, z)$ using either equation (2.19) or equation (2.21).

- The variation of the potential Π in equation (2.21) with respect to the displacement field $\mathbf{u}(x)$ of the standard 3d beam element gives

$$\delta_{\mathbf{u}} \Pi = \int_0^L \delta \mathbf{e}(\mathbf{u})^T \mathbf{s} dx - \delta \mathbf{u}_{IJ}^T \bar{\mathbf{p}}_{IJ} - \int_0^L \delta \mathbf{u}^T \bar{\mathbf{p}}^u dx \quad (2.25)$$

With the definition of the section deformations $\mathbf{e}(\mathbf{u})$ from equation (2.13) and integration by parts, the potential variation $\delta_{\mathbf{u}} \Pi$ in equation (2.25) can be rewritten in the

form

$$\delta_{\mathbf{u}}\Pi = (\delta u N + \delta\theta_z M_z + \delta v V_y + \delta\phi T + \delta\theta_y M_y + \delta w V_z)|_0^L - \delta\mathbf{u}_{IJ}^T \bar{\mathbf{p}}_{IJ}$$

$$- \int_0^L [\delta u \quad \delta\theta_z \quad \delta v \quad \delta\phi \quad \delta\theta_y \quad \delta w] \begin{pmatrix} \frac{dN}{dx} \\ \frac{dM_z}{dx} + V_y \\ \frac{dV_y}{dx} \\ \frac{dT}{dx} \\ \frac{dM_y}{dx} - V_z \\ \frac{dV_z}{dx} \end{pmatrix} dx - \int_0^L \delta\mathbf{u}^T \bar{\mathbf{p}}^u dx$$

After reordering the terms in the column vector of the first integral to match the order of the generalized displacements $\mathbf{u}(x)$ in equation (2.1) gives

$$\delta_{\mathbf{u}}\Pi = [\delta u N + \delta\theta_z M_z + \delta v V_y + \delta\phi T + \delta\theta_y M_y + \delta w V_z]|_0^L - \delta\mathbf{u}_{IJ}^T \bar{\mathbf{p}}_{IJ}$$

$$- \int_0^L \delta\mathbf{u}^T \left[\begin{pmatrix} \frac{dN}{dx} \\ \frac{dV_y}{dx} \\ \frac{dV_z}{dx} \\ \frac{dT}{dx} \\ \frac{dM_z}{dx} + V_y \\ \frac{dM_y}{dx} - V_z \end{pmatrix} + \bar{\mathbf{p}}^u \right] dx \quad (2.26)$$

The distribution of the section forces $\mathbf{s}(x)$ over the element is selected so as to satisfy *exactly* the following differential equations which appear inside the parenthesis under the integral

$$\begin{pmatrix} \frac{dN}{dx} \\ \frac{dV_y}{dx} \\ \frac{dV_z}{dx} \\ \frac{dT}{dx} \\ \frac{dM_z}{dx} + V_y \\ \frac{dM_y}{dx} - V_z \end{pmatrix} + \bar{\mathbf{p}}^u = \begin{pmatrix} 0 \\ 0 \\ 0 \\ 0 \\ 0 \\ 0 \end{pmatrix} \quad (2.27)$$

The general solution of these equations can be written in the form

$$\mathbf{s}(x) = \mathbf{b}(x) \mathbf{q} + \mathbf{s}^u(x) \quad (2.28)$$

where $\mathbf{b}(x)$ are the internal force interpolation functions for the homogeneous solution

of the differential equations

$$\mathbf{b}(x) = \begin{bmatrix} 1 & 0 & 0 & 0 & 0 & 0 \\ 0 & x/L - 1 & x/L & 0 & 0 & 0 \\ 0 & -1/L & -1/L & 0 & 0 & 0 \\ 0 & 0 & 0 & 1 & 0 & 0 \\ 0 & 0 & 0 & 0 & x/L - 1 & x/L \\ 0 & 0 & 0 & 0 & 1/L & 1/L \end{bmatrix} \quad (2.29)$$

$\mathbf{s}^u(x)$ are the internal force interpolation functions for the particular solution of the differential equations

$$\mathbf{s}^u(x) = \begin{bmatrix} L - x & 0 & 0 & 0 & 0 & 0 \\ 0 & x(x - L)/2 & 0 & 0 & 0 & 0 \\ 0 & L/2 - x & 0 & 0 & 0 & 0 \\ 0 & 0 & 0 & L - x & 0 & 0 \\ 0 & 0 & x(L - x)/2 & 0 & 0 & 0 \\ 0 & 0 & L/2 - x & 0 & 0 & 0 \end{bmatrix} \bar{\mathbf{p}}^u \quad (2.30)$$

and \mathbf{q} are the basic element forces which are defined such that the boundary terms of the homogeneous solution of the differential equilibrium equations in (2.27) can be written in the form

$$\delta \mathbf{u}_{IJ}^T \mathbf{p}_{IJ} = \delta \mathbf{v}^T \mathbf{a}_g^T \mathbf{p}_{IJ} = \delta \mathbf{v}^T \mathbf{q}$$

\mathbf{p}_{IJ} are the nodal forces that are work conjugate with the node displacements \mathbf{u}_{IJ} , and the basic element forces \mathbf{q} are work-conjugate with the element deformations \mathbf{v} in equation (2.3). With reference to the basic element in Figure (2.1) the basic forces are the axial force N_J at node J, the bending moment M_z about the z -axis at nodes I and J, M_{zI} M_{zJ} , respectively, the torsional moment T , and the bending moment M_y about y -axis at nodes I and J, M_{yI} M_{yJ} , respectively

$$\mathbf{q} = [N \quad M_{zI} \quad M_{zJ} \quad T \quad M_{yI} \quad M_{yJ}]^T \quad (2.31)$$

Since the section force resultants $\mathbf{s}(x)$ satisfy the differential equilibrium equations in (2.27), the integral in equation (2.26) vanishes and the variation $\delta_{\mathbf{u}}\Pi$ of the Hu-Washizu potential simplifies to

$$\delta_{\mathbf{u}}\Pi = \delta \mathbf{u}_{IJ}^T (\mathbf{a}_g^T \mathbf{q} - \bar{\mathbf{p}}_{IJ}^u) - \delta \mathbf{u}_{IJ}^T \bar{\mathbf{p}}_{IJ}^u \quad (2.32)$$

where $\bar{\mathbf{p}}_{IJ}^u$ are the equivalent nodal forces under the element loading $\bar{\mathbf{p}}^u$

$$\bar{\mathbf{p}}_{IJ}^u = [\bar{p}^u L \quad \bar{p}_y^u L/2 \quad -\bar{p}_z^u L/2 \quad \bar{p}_\phi^u L \quad 0 \quad 0 \quad 0 \quad \bar{p}_y^u L/2 \quad -\bar{p}_z^u L/2 \quad 0 \quad 0 \quad 0]^T \quad (2.33)$$

- The variation of the potential Π in the form of equation (2.19) with respect to the section deformation field $\mathbf{e}(x)$ gives

$$\begin{aligned}\delta_{\mathbf{e}}\Pi &= \int_V \delta \mathbf{e}^T \left(-\mathbf{a}_s^T \boldsymbol{\sigma} + \frac{\partial W}{\partial \boldsymbol{\epsilon}} \frac{\partial \boldsymbol{\epsilon}}{\partial \mathbf{e}} \right) dV \\ &= \int_0^L \delta \mathbf{e}^T \left(\int_A \mathbf{a}_s^T (-\boldsymbol{\sigma} + \frac{\partial W}{\partial \boldsymbol{\epsilon}}) dA \right) dx\end{aligned}\quad (2.34)$$

With the requirement that $\delta \Pi_{\mathbf{e}} = \mathbf{0}$ for a minimum of Π , the expression under the integral gives

$$\boldsymbol{\sigma} = \frac{\partial W}{\partial \boldsymbol{\epsilon}} \quad (2.35)$$

which can be generalized to any constitutive relation of the form

$$\boldsymbol{\sigma} = \hat{\boldsymbol{\sigma}}(\boldsymbol{\epsilon}) \quad (2.36)$$

where $\hat{\boldsymbol{\sigma}}$ refers to the constitutive equation in the form of a function of total strains $\boldsymbol{\epsilon}$ and of internal variables for inelastic material response. The case of classical J2 plasticity will be discussed in section 2.6.3.

- The variation of the potential Π in equation (2.19) with respect to the stress field $\boldsymbol{\sigma}(x, y, z)$ gives

$$\begin{aligned}\delta_{\boldsymbol{\sigma}}\Pi &= \int_V \delta \boldsymbol{\sigma}^T \mathbf{a}_s [\mathbf{e}(\mathbf{u}) - \mathbf{e}(x)] dV \\ &= \int_0^L \left[\int_A (\mathbf{a}_s^T \delta \boldsymbol{\sigma})^T dA \right] [\mathbf{e}(\mathbf{u}) - \mathbf{e}(x)] dx \\ &= \int_0^L \delta \mathbf{s}^T(x) [\mathbf{e}(\mathbf{u}) - \mathbf{e}(x)] dx \\ &= \delta \mathbf{q}^T \left[\mathbf{v} - \int_0^L \mathbf{b}^T(x) \mathbf{e}(x) dx \right]\end{aligned}\quad (2.37)$$

where equations (2.20) and (2.28) were used in the transformations to arrive at the last equation.

- The variation of the potential Π in equation (2.19) with respect to the warping displacement field u^w gives

$$\begin{aligned}\delta_{u^w}\Pi &= \int_V \delta \boldsymbol{\epsilon}(u^w)^T \frac{\partial W}{\partial \boldsymbol{\epsilon}} dV - \delta \mathbf{u}_{IJ}^{wT} \bar{\mathbf{p}}_{IJ}^w \\ &= \int_V (\delta \boldsymbol{\epsilon}^w)^T \boldsymbol{\sigma} dV - \delta \mathbf{u}_{IJ}^{wT} \bar{\mathbf{p}}_{IJ}^w\end{aligned}\quad (2.38)$$

with the additional strain $\boldsymbol{\epsilon}^w$ due to warping from equation (2.15) and the use of the constitutive equation (2.35) in the last step. Setting $\delta_{\mathbf{u}^w}\Pi = 0$ in equation (2.38) corresponds to satisfying the stress equilibrium of the continuum $div(\boldsymbol{\sigma}) = 0$ in the weak sense form of

$$\int_V \delta u^w div(\boldsymbol{\sigma}) dV = 0 \quad (2.39)$$

Noting that $u^w = u_x^w$ in accordance with the kinematic assumptions of section 2.3, so that $\delta u_y^w = \delta u_z^w = 0$ simplifies the variation of the Hu-Washizu potential in equation (2.38) to

$$\delta_{\mathbf{u}^w}\Pi = \int_V (\delta\epsilon_{xx}^w \sigma_{xx} + 2\delta\epsilon_{xy}^w \sigma_{xy} + 2\delta\epsilon_{xz}^w \sigma_{xz}) dV - \delta \mathbf{u}_{IJ}^{wT} \bar{\mathbf{p}}_{IJ}^w \quad (2.40)$$

Further processing of equation (2.40) is not possible without discretization of the strain variation $\delta\boldsymbol{\epsilon}$, which requires discretization of the warping displacements $u^w(x, y, z)$, as discussed in the following section.

2.4.2 Partial discretization of governing equations

The warping displacement function $u^w(x, y, z)$ is assumed to be the product of two independent sets of interpolation functions, one set of functions $\chi(x)$ for the warping distribution over the element axis, and another set $\psi(y, z)$ for the warping displacement profile over the cross-section. The choice of interpolations functions for $\chi(x)$ and $\psi(y, z)$ is discussed in section 2.5.

The interpolation of $\chi(x)$ uses a grid with index i in the reference axis direction x , and the interpolation of $\psi(y, z)$ uses a grid with indices j, k in the reference axis directions y and z , respectively. The warping displacement values at (x_i, y_j, z_k) serve as independent warping degrees of freedom.

The warping displacement profile at a section $x = x_i$ is described by the expression

$$u^w(x_i, y, z) = \sum_j \sum_k \psi_{jk}(y, z) u_{ijk}^w \quad (2.41)$$

where $u_{ijk}^w = u^w(x_i, y_j, z_k)$ are the warping displacement values at point (x_i, y_j, z_k) . This can be written in a form that dispenses with the double summation by collecting the warping displacement values at a section i in vector \mathbf{u}_i^w

$$\mathbf{u}_i^w = [u^w(x_i, y_1, z_1) \quad \dots \quad u^w(x_i, y_j, z_1) \quad \dots \quad u^w(x_i, y_1, z_k) \quad \dots \quad u^w(x_i, y_j, z_k)]^T \quad (2.42)$$

and the corresponding interpolation functions $\psi_{jk}(y, z)$ in a row vector $\boldsymbol{\psi}(y, z)$

$$\boldsymbol{\psi}(y, z) = [\psi_{11}(y, z) \quad \dots \quad \psi_{j1}(y, z) \quad \dots \quad \psi_{1k}(y, z) \quad \dots \quad \psi_{jk}(y, z)] \quad (2.43)$$

With these definitions the warping displacement profile at section $x = x_i$ becomes

$$u^w(x_i, y, z) = \boldsymbol{\psi}(y, z) \mathbf{u}_i^w \quad (2.44)$$

Equation (2.45) reflects clearly the fact that the interpolation functions $\boldsymbol{\psi}(y, z)$ for the warping profile are the same at each section i , while the warping profile changes from section to section on account of the different warping displacement values \mathbf{u}_i^w . The general form of the warping displacement function $u^w(x, y, z)$ is

$$u^w(x, y, z) = \sum_i \chi_i(x) [\boldsymbol{\psi}(y, z) \mathbf{u}_i^w] \quad (2.45)$$

The variation of the Hu-Washizu potential Π in equation (2.38) requires the variation of the strains $\boldsymbol{\epsilon}^w$ due to warping, which after substitution of equation (2.45) in equation (2.15), gives

$$\delta \epsilon_{xx}^w(x, y, z) = \sum_i \frac{\partial \chi_i(x)}{\partial x} [\boldsymbol{\psi}(y, z) \delta \mathbf{u}_i^w] \quad (2.46a)$$

$$2\delta \epsilon_{xy}^w(x, y, z) = \sum_i \chi_i(x) \left[\frac{\partial \boldsymbol{\psi}(y, z)}{\partial y} \delta \mathbf{u}_i^w \right] \quad (2.46b)$$

$$2\delta \epsilon_{xz}^w(x, y, z) = \sum_i \chi_i(x) \left[\frac{\partial \boldsymbol{\psi}(y, z)}{\partial z} \delta \mathbf{u}_i^w \right] \quad (2.46c)$$

With the strain variation in the form of equation (2.46) the Hu-Washizu potential variation $\delta \Pi$ in equation (2.40) converts to the following discrete form

$$\delta_{u^w} \Pi = \int_V \sum_i (\delta \mathbf{u}_i^w)^T \left(\boldsymbol{\psi}^T \frac{\partial \chi_i}{\partial x} \sigma_{xx} + \frac{\partial \boldsymbol{\psi}^T}{\partial y} \chi_i \sigma_{xy} + \frac{\partial \boldsymbol{\psi}^T}{\partial z} \chi_i \sigma_{xz} \right) dV - \delta \mathbf{u}_{IJ}^{wT} \bar{\mathbf{p}}_{IJ}^w \quad (2.47)$$

which becomes after the switch of summation and integral sign and after decoupling the latter into an integral over the element length L and an integral over the section area A

$$\begin{aligned} \delta_{u^w} \Pi = \sum_i (\delta \mathbf{u}_i^w)^T & \left[\int_0^L \frac{\partial \chi_i}{\partial x} \int_A \boldsymbol{\psi}^T \sigma_{xx} dA dx \right. \\ & \left. + \int_0^L \chi_i \int_A \left(\frac{\partial \boldsymbol{\psi}^T}{\partial y} \sigma_{xy} + \frac{\partial \boldsymbol{\psi}^T}{\partial z} \sigma_{xz} \right) dA dx \right] - \delta \mathbf{u}_{IJ}^{wT} \bar{\mathbf{p}}_{IJ}^w \end{aligned} \quad (2.48)$$

With the following definition for the warping forces $\mathbf{s}^w(x)$

$$\mathbf{s}_x^w(x) = \int_A \boldsymbol{\psi}^T(y, z) \sigma_{xx}(x, y, z) dA \quad (2.49a)$$

$$\mathbf{s}_{yz}^w(x) = \int_A \left[\frac{\partial \boldsymbol{\psi}^T(y, z)}{\partial y} \sigma_{xy}(x, y, z) + \frac{\partial \boldsymbol{\psi}^T(y, z)}{\partial z} \sigma_{xz}(x, y, z) \right] dA \quad (2.49b)$$

the discrete form of the Hu-Washizu potential variation in equation (2.48) becomes

$$\delta_{u^w} \Pi = \sum_i (\delta \mathbf{u}_i^w)^T \left[\int_0^L \frac{\partial \chi_i(x)}{\partial x} \mathbf{s}_x^w(x) dx + \int_0^L \chi_i(x) \mathbf{s}_{yz}^w(x) dx \right] - \delta \mathbf{u}_{IJ}^{wT} \bar{\mathbf{p}}_{IJ}^w \quad (2.50)$$

The warping force vectors \mathbf{s}_x^w and \mathbf{s}_{yz}^w have n_w terms each. With the following definition for the warping force vector \mathbf{p}_i^w at section i

$$\mathbf{p}_i^w = \int_0^L \frac{\partial \chi_i(x)}{\partial x} \mathbf{s}_x^w(x) dx + \int_0^L \chi_i(x) \mathbf{s}_{yz}^w(x) dx \quad (2.51)$$

the discrete form of the Hu-Washizu potential variation in equation (2.50) finally becomes

$$\delta_{u^w} \Pi = \sum_i (\delta \mathbf{u}_i^w)^T \mathbf{p}_i^w - \delta \mathbf{u}_{IJ}^{wT} \bar{\mathbf{p}}_{IJ}^w \quad (2.52)$$

The warping force vector \mathbf{p}_i^w has n_w terms. Each term is the integral of the corresponding term of the section warping force vectors \mathbf{s}_x^w and \mathbf{s}_{yz}^w according to equation (2.51).

The requirement that $\delta_{u^w} \Pi = 0$ results in the following equation

$$\bar{\mathbf{p}}_i^w = \mathbf{p}_i^w \quad (2.53)$$

for all sections with a warping displacement profile, where \mathbf{p}_i^w is the resisting warping force in equation (2.51) and $\bar{\mathbf{p}}_i^w$ is the applied warping force at section i . In practice, all interior sections of the beam are free to warp so that $\bar{\mathbf{p}}_i^w = \mathbf{0}$. Section warping forces $\bar{\mathbf{p}}_{IJ}^w$ can only be imposed at the beam element boundary corresponding to nodes I and J.

The minimization of potential Π requires that $\delta \Pi = \mathbf{0}$. This leads to the following combination of equations (2.32), (2.36), (2.37), and (2.52)

$$\bar{\mathbf{p}}_{IJ} + \bar{\mathbf{p}}_{IJ}^u = \mathbf{a}_g^T \mathbf{q} \quad (2.54a)$$

$$\mathbf{v} = \int_0^L \mathbf{b}^T(x) \mathbf{e}(x) dx \quad (2.54b)$$

$$\boldsymbol{\sigma} = \hat{\boldsymbol{\sigma}}(\boldsymbol{\epsilon}) \quad (2.54c)$$

$$\bar{\mathbf{p}}_i^w = \mathbf{p}_i^w = \int_0^L \frac{\partial \chi_i(x)}{\partial x} \mathbf{s}_x^w(x) dx + \int_0^L \chi_i(x) \mathbf{s}_{yz}^w(x) dx \quad (2.54d)$$

noting that equation (2.54a) is based on the section forces \mathbf{s} satisfying equation (2.28). The first three equations with equation (2.28) correspond to the mixed variational formulation of the regular beam: the equilibrium equations (2.54a) and (2.28), the compatibility equation (2.54b), and the constitutive law (2.54c). The fifth equation (2.54d) states the equilibrium of warping section forces \mathbf{s}_x^w and \mathbf{s}_{yz}^w at section i .

2.4.3 Linearization

During the element state determination process, the section deformations $\mathbf{e}(x)$ and warping displacement parameters \mathbf{u}_i^w serve as unknowns of an internal iterative process to satisfy the

equilibrium equations (2.28) and (2.54d) and the compatibility equation (2.54b) for given element deformations \mathbf{v} . On account of the nonlinear nature of the constitutive equation (2.54c) the governing equations are nonlinear functions of the section deformations $\mathbf{e}(x)$ and of the warping displacement parameters \mathbf{u}_i^w . For the solution of the governing equations their linearization with respect to the unknowns is, therefore, required. Noting that the section deformations $\mathbf{e}(x)$ are continuous functions of x , whereas the warping displacement parameters \mathbf{u}_i^w are discrete variables, the linearization is presented in the form of the linear variation of the governing equation instead of differentiation.

The linear variation of the governing equations in (2.54) and (2.28) gives

$$\delta \mathbf{p}_{IJ} = \mathbf{a}_g^T \delta \mathbf{q} \quad (2.55a)$$

$$\delta \mathbf{v} = \int_0^L \mathbf{b}^T(x) \delta \mathbf{e}(x) dx \quad (2.55b)$$

$$\delta \mathbf{s}(x) = \mathbf{b}(x) \delta \mathbf{q} \quad (2.55c)$$

$$\delta \boldsymbol{\sigma} = \frac{\partial \hat{\boldsymbol{\sigma}}}{\partial \boldsymbol{\epsilon}} \delta \boldsymbol{\epsilon} \quad (2.55d)$$

$$\delta \mathbf{p}_i^w = \int_0^L \frac{\partial \chi_i(x)}{\partial x} \delta \mathbf{s}_x^w(x) dx + \int_0^L \chi_i(x) \delta \mathbf{s}_{yz}^w(x) dx \quad (2.55e)$$

The derivative of the constitutive law with respect to the total strain $\boldsymbol{\epsilon}$ defines the material stiffness \mathbf{k}_m

$$\mathbf{k}_m = \frac{\partial \hat{\boldsymbol{\sigma}}}{\partial \boldsymbol{\epsilon}} \quad (2.56)$$

With the auxiliary matrices $\mathbf{a}_x^w(y, z)$ and $\mathbf{a}_{yz}^w(y, z)$

$$\mathbf{a}_x^w(y, z) = \begin{bmatrix} \boldsymbol{\psi} \\ \mathbf{0} \\ \mathbf{0} \end{bmatrix} \quad \text{and} \quad \mathbf{a}_{yz}^w(y, z) = \begin{bmatrix} \mathbf{0} \\ \frac{\partial \boldsymbol{\psi}}{\partial y} \\ \frac{\partial \boldsymbol{\psi}}{\partial z} \end{bmatrix} \quad (2.57)$$

where $\mathbf{0}$ is a row vector with n_w terms and $\boldsymbol{\psi}$ are the interpolation polynomials for the warping profile, the warping strain $\boldsymbol{\epsilon}^w$ in equation (2.15) can be written in compact form in terms of the warping displacement parameters \mathbf{u}_i^w

$$\boldsymbol{\epsilon}^w(x, y, z) = \sum_i \left[\frac{\partial \chi_i(x)}{\partial x} \mathbf{a}_x^w(y, z) + \chi_i(x) \mathbf{a}_{yz}^w(y, z) \right] \mathbf{u}_i^w \quad (2.58)$$

The variation of the total strain $\boldsymbol{\epsilon}$ then becomes

$$\delta \boldsymbol{\epsilon}(x, y, z) = \mathbf{a}_s(y, z) \delta \mathbf{e}(x) + \sum_i \left[\frac{\partial \chi_i(x)}{\partial x} \mathbf{a}_x^w(y, z) + \chi_i(x) \mathbf{a}_{yz}^w(y, z) \right] \delta \mathbf{u}_i^w \quad (2.59)$$

The warping forces $\mathbf{s}^w(x)$ in equation (2.49) can be written in compact form with the aid of the definitions in equation (2.57)

$$\mathbf{s}_x^w(x) = \int_A (\mathbf{a}_x^w)^T \boldsymbol{\sigma}(x, y, z) dA \quad (2.60a)$$

$$\mathbf{s}_{yz}^w(x) = \int_A (\mathbf{a}_{yz}^w)^T \boldsymbol{\sigma}(x, y, z) dA \quad (2.60b)$$

The variation of the section forces \mathbf{s} , \mathbf{s}_x^w and \mathbf{s}_{yz}^w in equations (2.20) and (2.49) gives

$$\begin{aligned} \delta \mathbf{s}(x) &= \int_A \mathbf{a}_s^T \mathbf{k}_m \delta \boldsymbol{\epsilon}(x, y, z) dA \\ \delta \mathbf{s}_x^w(x) &= \int_A (\mathbf{a}_x^w)^T \mathbf{k}_m \delta \boldsymbol{\epsilon}(x, y, z) dA \\ \delta \mathbf{s}_{yz}^w(x) &= \int_A (\mathbf{a}_{yz}^w)^T \mathbf{k}_m \delta \boldsymbol{\epsilon}(x, y, z) dA \end{aligned}$$

where $\mathbf{k}_m = \mathbf{k}_m(x, y, z)$. After substituting the strain variation $\delta \boldsymbol{\epsilon}$ from equation (2.59) the variation of the section forces becomes

$$\begin{aligned} \delta \mathbf{s}(x) &= \left(\int_A \mathbf{a}_s^T \mathbf{k}_m \mathbf{a}_s dA \right) \delta \mathbf{e} + \int_A \mathbf{a}_s^T \mathbf{k}_m \sum_i \left(\frac{\partial \chi_i}{\partial x} \mathbf{a}_x^w + \chi_i \mathbf{a}_{yz}^w \right) \delta \mathbf{u}_i^w dA \\ \delta \mathbf{s}_x^w(x) &= \left(\int_A (\mathbf{a}_x^w)^T \mathbf{k}_m \mathbf{a}_s dA \right) \delta \mathbf{e} + \int_A (\mathbf{a}_x^w)^T \mathbf{k}_m \sum_i \left(\frac{\partial \chi_i}{\partial x} \mathbf{a}_x^w + \chi_i \mathbf{a}_{yz}^w \right) \delta \mathbf{u}_i^w dA \\ \delta \mathbf{s}_{yz}^w(x) &= \left(\int_A (\mathbf{a}_{yz}^w)^T \mathbf{k}_m \mathbf{a}_s dA \right) \delta \mathbf{e} + \int_A (\mathbf{a}_{yz}^w)^T \mathbf{k}_m \sum_i \left(\frac{\partial \chi_i}{\partial x} \mathbf{a}_x^w + \chi_i \mathbf{a}_{yz}^w \right) \delta \mathbf{u}_i^w dA \end{aligned}$$

Switching the order of the integral over the section area A and the summation over all sections i in the second term of the above equations gives

$$\begin{aligned} &\sum_i \left(\frac{\partial \chi_i}{\partial x} \int_A \mathbf{a}_s^T \mathbf{k}_m \mathbf{a}_x^w dA + \chi_i \int_A \mathbf{a}_s^T \mathbf{k}_m \mathbf{a}_{yz}^w dA \right) \delta \mathbf{u}_i^w \\ &\sum_i \left(\frac{\partial \chi_i}{\partial x} \int_A (\mathbf{a}_x^w)^T \mathbf{k}_m \mathbf{a}_x^w dA + \chi_i \int_A (\mathbf{a}_x^w)^T \mathbf{k}_m \mathbf{a}_{yz}^w dA \right) \delta \mathbf{u}_i^w \\ &\sum_i \left(\frac{\partial \chi_i}{\partial x} \int_A (\mathbf{a}_{yz}^w)^T \mathbf{k}_m \mathbf{a}_x^w dA + \chi_i \int_A (\mathbf{a}_{yz}^w)^T \mathbf{k}_m \mathbf{a}_{yz}^w dA \right) \delta \mathbf{u}_i^w \end{aligned}$$

With the following section stiffness definitions

$$\mathbf{k}_{ss}(x) = \int_A \mathbf{a}_s^T \mathbf{k}_m \mathbf{a}_s dA$$

$$\begin{aligned}
\mathbf{k}_{sw}^x(x) &= \int_A \mathbf{a}_s^T \mathbf{k}_m \mathbf{a}_x^w dA \\
\mathbf{k}_{sw}^{yz}(x) &= \int_A \mathbf{a}_s^T \mathbf{k}_m \mathbf{a}_{yz}^w dA \\
\mathbf{k}_{ws}^x(x) &= \int_A (\mathbf{a}_x^w)^T \mathbf{k}_m \mathbf{a}_s dA = (\mathbf{k}_{sw}^x)^T \\
\mathbf{k}_{ws}^{yz}(x) &= \int_A (\mathbf{a}_{yz}^w)^T \mathbf{k}_m \mathbf{a}_s dA = (\mathbf{k}_{sw}^{yz})^T \\
\mathbf{k}_{ww}^x(x) &= \int_A (\mathbf{a}_x^w)^T \mathbf{k}_m \mathbf{a}_x^w dA \\
\mathbf{k}_{ww}^{yz}(x) &= \int_A (\mathbf{a}_{yz}^w)^T \mathbf{k}_m \mathbf{a}_{yz}^w dA \\
\mathbf{k}_{ww}^{xy}(x) &= \int_A (\mathbf{a}_x^w)^T \mathbf{k}_m \mathbf{a}_{yz}^w dA \\
\mathbf{k}_{ww}^{yx}(x) &= \int_A (\mathbf{a}_{yz}^w)^T \mathbf{k}_m \mathbf{a}_x^w dA = (\mathbf{k}_{ww}^{xy})^T
\end{aligned} \tag{2.61}$$

the variation of the section forces finally becomes

$$\delta \mathbf{s}(x) = \mathbf{k}_{ss}(x) \delta \mathbf{e}(x) + \sum_i \left[\frac{\partial \chi_i}{\partial x} \mathbf{k}_{sw}^x(x) + \chi_i \mathbf{k}_{sw}^{yz}(x) \right] \delta \mathbf{u}_i^w \tag{2.62a}$$

$$\delta \mathbf{s}_x^w(x) = \mathbf{k}_{ws}^x(x) \delta \mathbf{e}(x) + \sum_i \left[\frac{\partial \chi_i}{\partial x} \mathbf{k}_{ww}^x(x) + \chi_i \mathbf{k}_{ww}^{xy}(x) \right] \delta \mathbf{u}_i^w \tag{2.62b}$$

$$\delta \mathbf{s}_{yz}^w(x) = \mathbf{k}_{ws}^{yz}(x) \delta \mathbf{e}(x) + \sum_i \left[\frac{\partial \chi_i}{\partial x} \mathbf{k}_{ww}^{yx}(x) + \chi_i \mathbf{k}_{ww}^{yz}(x) \right] \delta \mathbf{u}_i^w \tag{2.62c}$$

The variation of the warping forces \mathbf{p}_i^w from equation (2.54d) becomes

$$\delta \mathbf{p}_i^w = \int_0^L \frac{\partial \chi_i}{\partial x} \delta \mathbf{s}_x^w(x) dx + \int_0^L \chi_i \delta \mathbf{s}_{yz}^w(x) dx \tag{2.63}$$

Finally, substituting the variation of the warping forces \mathbf{s}_x^w and \mathbf{s}_{yz}^w from (2.62) gives

$$\begin{aligned}
\delta \mathbf{p}_i^w &= \int_0^L \frac{\partial \chi_i}{\partial x} \left\{ \mathbf{k}_{ws}^x(x) \delta \mathbf{e}(x) + \sum_n \left[\frac{\partial \chi_n}{\partial x} \mathbf{k}_{wn}^x(x) + \chi_n \mathbf{k}_{wn}^{xy}(x) \right] \delta \mathbf{u}_n^w \right\} dx \\
&+ \int_0^L \chi_i \left\{ \mathbf{k}_{ws}^{yz}(x) \delta \mathbf{e}(x) + \sum_n \left[\frac{\partial \chi_n}{\partial x} \mathbf{k}_{wn}^{yx}(x) + \chi_n \mathbf{k}_{wn}^{yz}(x) \right] \delta \mathbf{u}_n^w \right\} dx
\end{aligned} \tag{2.64}$$

After switching the order of the integral and the summation over the sections i the final

expression for the variation of the warping forces \mathbf{p}_i^w results

$$\begin{aligned} \delta \mathbf{p}_i^w &= \int_0^L \left[\frac{\partial \chi_i}{\partial x} \mathbf{k}_{ws}^x(x) + \chi_i \mathbf{k}_{ws}^{yz}(x) \right] \delta \mathbf{e}(x) dx \\ &+ \sum_n \int_0^L \left(\frac{\partial \chi_i}{\partial x} \frac{\partial \chi_n}{\partial x} \mathbf{k}_{ww}^x(x) + \frac{\partial \chi_i}{\partial x} \chi_n \mathbf{k}_{wy}^{xy}(x) + \chi_i \frac{\partial \chi_n}{\partial x} \mathbf{k}_{wy}^{yx}(x) + \chi_i \chi_n \mathbf{k}_{ww}^{yz}(x) \right) dx \delta \mathbf{u}_n^w \end{aligned} \quad (2.65)$$

In summary, the state determination is based on satisfying the governing equations of the element response in (2.54). The linearization of these equations results in the following system of equations after the substitution of intermediate terms

$$\begin{aligned} \delta \mathbf{v} &= \int_0^L \mathbf{b}^T(x) \delta \mathbf{e}(x) dx \\ \delta \mathbf{s}(x) &= \mathbf{b}(x) \delta \mathbf{q} = \mathbf{k}_{ss}(x) \delta \mathbf{e}(x) + \sum_n \left(\frac{\partial \chi_n}{\partial x} \mathbf{k}_{sw}^x(x) + \chi_n \mathbf{k}_{sw}^{yz}(x) \right) \delta \mathbf{u}_n^w \\ \delta \mathbf{p}_i^w &= \int_0^L \left[\frac{\partial \chi_i}{\partial x} \mathbf{k}_{ws}^x(x) + \chi_i \mathbf{k}_{ws}^{yz}(x) \right] \delta \mathbf{e}(x) dx \\ &+ \sum_n \int_0^L \left[\frac{\partial \chi_i}{\partial x} \frac{\partial \chi_n}{\partial x} \mathbf{k}_{ww}^x(x) + \frac{\partial \chi_i}{\partial x} \chi_n \mathbf{k}_{ww}^{xy}(x) + \chi_i \frac{\partial \chi_n}{\partial x} \mathbf{k}_{ww}^{yx}(x) + \chi_i \chi_n \mathbf{k}_{ww}^{yz}(x) \right] dx \delta \mathbf{u}_n^w \\ \delta \mathbf{p}_{IJ} &= \mathbf{a}_g^T \delta \mathbf{q} \end{aligned}$$

In the preceding equations the first equation represents the element compatibility, and the other three the element equilibrium. The last equation among the equilibrium equations is used to establish the tangent stiffness \mathbf{k} of the element without rigid body modes

$$\delta \mathbf{p}_{IJ} = \mathbf{a}_g^T \frac{\partial \mathbf{q}}{\partial \mathbf{v}} \delta \mathbf{v} = \mathbf{a}_g^T \mathbf{k} \mathbf{a}_g \delta \mathbf{u}_{IJ} \quad (2.66)$$

where use was made of the linear variation of the element deformations \mathbf{v} in equation (2.3). The element resisting forces \mathbf{p}_{IJ} follow from equation (2.54a).

The problem of the element state determination is, therefore, the determination of the basic forces \mathbf{q} and tangent element stiffness \mathbf{k} for given element deformations \mathbf{v} and applied warping forces $\bar{\mathbf{p}}_i^w$. The iterative process is based on the solution of the following linear equations

$$\delta \mathbf{v} = \int_0^L \mathbf{b}^T(x) \delta \mathbf{e}(x) dx \quad (2.67a)$$

$$\delta \mathbf{s}(x) = \mathbf{b}(x) \mathbf{k} \delta \mathbf{v} = \mathbf{k}_{ss}(x) \delta \mathbf{e}(x) + \sum_n \left[\frac{\partial \chi_n}{\partial x} \mathbf{k}_{sw}^x(x) + \chi_n \mathbf{k}_{sw}^{yz}(x) \right] \delta \mathbf{u}_n^w \quad (2.67b)$$

$$\begin{aligned} \delta \mathbf{p}_i^w &= \int_0^L \left[\frac{\partial \chi_i}{\partial x} \mathbf{k}_{ws}^x(x) + \chi_i \mathbf{k}_{ws}^{yz}(x) \right] \delta \mathbf{e}(x) dx \\ &+ \sum_n \int_0^L \left[\frac{\partial \chi_i}{\partial x} \frac{\partial \chi_n}{\partial x} \mathbf{k}_{ww}^x(x) + \frac{\partial \chi_i}{\partial x} \chi_n \mathbf{k}_{ww}^{xy}(x) + \chi_i \frac{\partial \chi_n}{\partial x} \mathbf{k}_{ww}^{yx}(x) + \chi_i \chi_n \mathbf{k}_{ww}^{yz}(x) \right] dx \delta \mathbf{u}_n^w \end{aligned} \quad (2.67c)$$

with the section deformations $\mathbf{e}(x)$ and the warping displacement parameters \mathbf{u}_n^w at each section n of the beam as unknowns. So far, the section deformations $\mathbf{e}(x)$ and the warping displacement distribution $\chi(x)$ over the element length were treated as continuous fields. As a consequence, the linear equations (2.67) involve integrals of x . At the same time the different section stiffness contributions in equation (2.61) involve integrals over the cross section area A . The complete discretization of these equations, therefore, depends on the numerical evaluation of these integrals, as discussed in the next section.

2.4.4 Complete discretization of governing equations

The numerical evaluation of the section integrals in equation (2.61) is performed with an integration rule such as the midpoint integration rule. This type of integration gives rise to the name fiber section model. Each rectangular part of the cross section is subdivided into fibers of equal size with the centroid of each fiber serving as integration point and the fiber area serving as integration weight. It is important to point out that the section subdivision into fibers is independent of the interpolation grid for the warping profile, which uses n_w interpolation grid points, as mentioned earlier and discussed in more detail in the next section. With the midpoint integration rule the integrals over the section area convert into a sum over the number of fibers n_f . The resulting expression for the section stiffness \mathbf{k}_{ss} suffices to illustrate the concept

$$\mathbf{k}_{ss} = \int_A \mathbf{a}_s^T \mathbf{k}_m \mathbf{a}_s dA \approx \sum_{n=1}^{n_f} w_n (\mathbf{a}_{s,n}^T \mathbf{k}_{m,n} \mathbf{a}_{s,n}) \quad (2.68)$$

where w_n is the integration weight and

$$\mathbf{a}_{s,n} = \begin{bmatrix} 1 & -y_n & 0 & 0 & z_n & 0 \\ 0 & 0 & 1 & -z_n & 0 & 0 \\ 0 & 0 & 0 & y_n & 0 & 1 \end{bmatrix}$$

Analogous expressions can be obtained for the other section stiffness matrices in equation (2.61).

For the integration over the element length in equations (2.67a) and (2.67a) the Gauss-Lobatto integration rule is used, because it places an integration point at the end points of the integration interval where significant inelastic deformations take place. The number of integration points over the element length is n_{ip} . The warping displacement parameters \mathbf{u}_n^w

for the warping profile are defined at n_l of the n_{ip} sections with $n_l \leq n_{ip}$. This selection is made for computational economy for cases for which the warping effects are concentrated near one or both element ends. The integration point locations and weights of the Gauss-Lobatto integration rule can be found in standard reference texts on numerical integration [1].

With the numerical integration over the element length as summation over the index $l = 1 \dots n_{ip}$ with integration weights w_l the equations (2.67) become

$$\delta \mathbf{v} = \sum_{l=1}^{n_{ip}} w_l \mathbf{b}_l^T \delta \mathbf{e}_l \quad (2.69a)$$

$$\delta \mathbf{s}_l = \mathbf{b}_l (\mathbf{k} \delta \mathbf{v}) = \mathbf{k}_{ss,l} \delta \mathbf{e}_l + \sum_{n=1}^{nl} \left(\frac{\partial \chi_{n,l}}{\partial x} \mathbf{k}_{sw,l}^x + \chi_{n,l} \mathbf{k}_{sw,l}^{yz} \right) \delta \mathbf{u}_n^w \quad (2.69b)$$

$$\begin{aligned} \delta \mathbf{p}_i^w &= \sum_{l=1}^{n_{ip}} w_l \left(\frac{\partial \chi_{i,l}}{\partial x} \mathbf{k}_{ws,l}^x + \chi_{i,l} \mathbf{k}_{ws,l}^{yz} \right) \delta \mathbf{e}_l \quad (2.69c) \\ &+ \sum_{n=1}^{nl} \sum_{l=1}^{n_{ip}} w_l \left(\frac{\partial \chi_{i,l}}{\partial x} \frac{\partial \chi_{n,l}}{\partial x} \mathbf{k}_{ww,l}^x + \frac{\partial \chi_{i,l}}{\partial x} \chi_{n,l} \mathbf{k}_{ww,l}^{xy} + \chi_{i,l} \frac{\partial \chi_{n,l}}{\partial x} \mathbf{k}_{ww,l}^{yx} + \chi_{i,l} \chi_{n,l} \mathbf{k}_{ww,l}^{yz} \right) \delta \mathbf{u}_n^w \end{aligned}$$

where $\mathbf{e}_l = \mathbf{e}(x_l)$, $\mathbf{b}_l = \mathbf{b}(x_l)$, $\chi_{i,l} = \chi_i(x_l)$, $\mathbf{k}_{sw,l} = \mathbf{k}_{sw}(x_l)$ and $\mathbf{k}_{ww,l} = \mathbf{k}_{ww}(x_l)$ for superscripts x , xy , yx and yz . With the introduction of the following stiffness matrices

$$[\mathbf{k}_{sw}]_{ln} = \frac{\partial \chi_{n,l}}{\partial x} \mathbf{k}_{sw,l}^x + \chi_{n,l} \mathbf{k}_{sw,l}^{yz} \quad (2.70)$$

$$[\bar{\mathbf{k}}_{ww}]_{in} = \sum_{l=1}^{n_{ip}} w_l \left(\frac{\partial \chi_{i,l}}{\partial x} \frac{\partial \chi_{n,l}}{\partial x} \mathbf{k}_{ww,l}^x + \frac{\partial \chi_{i,l}}{\partial x} \chi_{n,l} \mathbf{k}_{ww,l}^{xy} + \chi_{i,l} \frac{\partial \chi_{n,l}}{\partial x} \mathbf{k}_{ww,l}^{yx} + \chi_{i,l} \chi_{n,l} \mathbf{k}_{ww,l}^{yz} \right) \quad (2.71)$$

the governing equations in (2.69) can be written in compact form

$$\begin{aligned} \delta \mathbf{v} &= \sum_{l=1}^{n_{ip}} w_l \mathbf{b}_l^T \delta \mathbf{e}_l \\ \delta \mathbf{s}_l &= \mathbf{b}_l (\mathbf{k} \delta \mathbf{v}) = \mathbf{k}_{ss,l} \delta \mathbf{e}_l + \sum_{n=1}^{nl} [\mathbf{k}_{sw}]_{ln} \delta \mathbf{u}_n^w \\ \delta \mathbf{p}_i^w &= \sum_{l=1}^{n_{ip}} w_l [\mathbf{k}_{sw}]_{li}^T \delta \mathbf{e}_l + \sum_{n=1}^{nl} [\bar{\mathbf{k}}_{ww}]_{in} \delta \mathbf{u}_n^w \end{aligned}$$

where use was made of $\mathbf{k}_{ws} = \mathbf{k}_{sw}^T$. Solving for $\delta \mathbf{e}_l$ from the second equation

$$\delta \mathbf{e}_l = [\mathbf{k}_{ss,l}]^{-1} \left(\delta \mathbf{s}_l - \sum_{n=1}^{nl} [\mathbf{k}_{sw}]_{ln} \delta \mathbf{u}_n^w \right) \quad (2.73)$$

and substituting into the third gives

$$\begin{aligned}
\delta \mathbf{p}_i^w &= \sum_{l=1}^{n_{ip}} w_l [\mathbf{k}_{sw}]_{li}^T [\mathbf{k}_{ss,l}]^{-1} \left(\delta \mathbf{s}_l - \sum_{n=1}^{nl} [\mathbf{k}_{sw}]_{ln} \delta \mathbf{u}_n^w \right) + \sum_{n=1}^{nl} [\bar{\mathbf{k}}_{ww}]_{in} \delta \mathbf{u}_n^w \\
&= \sum_{l=1}^{n_{ip}} w_l [\mathbf{k}_{sw}]_{li}^T [\mathbf{k}_{ss,l}]^{-1} \delta \mathbf{s}_l - \sum_{l=1}^{n_{ip}} w_l [\mathbf{k}_{sw}]_{li}^T [\mathbf{k}_{ss,l}]^{-1} \sum_{n=1}^{nl} [\mathbf{k}_{sw}]_{ln} \delta \mathbf{u}_n^w + \sum_{n=1}^{nl} [\bar{\mathbf{k}}_{ww}]_{in} \delta \mathbf{u}_n^w \\
&= \sum_{l=1}^{n_{ip}} w_l [\mathbf{k}_{sw}]_{li}^T [\mathbf{k}_{ss,l}]^{-1} \mathbf{b}_l (\mathbf{k} \delta \mathbf{v}) + \sum_{n=1}^{nl} \left([\bar{\mathbf{k}}_{ww}]_{in} - \sum_{l=1}^{n_{ip}} w_l [\mathbf{k}_{sw}]_{li}^T [\mathbf{k}_{ss,l}]^{-1} [\mathbf{k}_{sw}]_{ln} \right) \delta \mathbf{u}_n^w
\end{aligned}$$

Writing the last equation for all sections $i = 1 \dots n_l$ with warping displacement parameters $\delta \mathbf{u}_i^w$ gives a system of as many linear equations as unknown warping displacement parameters for n_l sections of the beam element. To write this equation system in compact form the warping forces $\delta \mathbf{p}_i^w$ of each section i are stacked below the preceding section to form a single vector $\delta \mathbf{P}^w$ and the same is done for the warping displacement parameters $\delta \mathbf{u}_i^w$ to form a single vector $\delta \mathbf{U}^w$. Furthermore, the stiffness matrix \mathbf{K}_{ww} that relates the warping forces with the warping displacement parameters is the collection of $n_w \times n_w$ submatrices $[\mathbf{K}_{ww}]_{in}$ which are defined as follows

$$[\mathbf{K}_{ww}]_{in} = [\bar{\mathbf{k}}_{ww}]_{in} - \sum_{l=1}^{n_{ip}} w_l [\mathbf{k}_{sw}]_{li}^T [\mathbf{k}_{ss,l}]^{-1} [\mathbf{k}_{sw}]_{ln} \quad (2.74)$$

so that

$$\mathbf{K}_{ww} = \begin{bmatrix} [\mathbf{K}_{ww}]_{11} & \cdots & [\mathbf{K}_{ww}]_{1n_l} \\ \vdots & \ddots & \vdots \\ [\mathbf{K}_{ww}]_{n_l 1} & \cdots & [\mathbf{K}_{ww}]_{n_l n_l} \end{bmatrix}$$

\mathbf{K}_{ww} is a square matrix of size $n_l \cdot n_w$ and is symmetric. Finally, the force influence matrix \mathbf{B}_{wq} that relates the basic element forces $\delta \mathbf{q}$ to the warping forces $\delta \mathbf{P}^w$ is the collection of $n_w \times 6$ submatrices $[\mathbf{B}_{wq}]_i$ which are defined as follows

$$[\mathbf{B}_{wq}]_i = \sum_{l=1}^{n_{ip}} w_l [\mathbf{k}_{sw}]_{li}^T [\mathbf{k}_{ss,l}]^{-1} \mathbf{b}_l \quad (2.75)$$

so that

$$\mathbf{B}_{wq} = \begin{bmatrix} [\mathbf{B}_{wq}]_{11} \\ \vdots \\ [\mathbf{B}_{wq}]_{n_l 1} \end{bmatrix}$$

Finally, the equilibrium equations at the warping degrees of freedom become

$$\delta \mathbf{P}^w = \mathbf{B}_{wq} \delta \mathbf{q} + \mathbf{K}_{ww} \delta \mathbf{U}^w \quad \text{with} \quad \delta \mathbf{q} = \mathbf{k} \delta \mathbf{v} \quad (2.76)$$

For the element state determination the element deformations \mathbf{v} are given and the matrices \mathbf{k} , \mathbf{K}_{ww} and \mathbf{B}_{wq} for the current state can be determined. Thus, given the warping forces \mathbf{P}^w equation (2.76) can be solved for the warping displacement parameters $\delta\mathbf{U}^w$ as long as these are local degrees of freedom of the element. If the displacement parameters $\mathbf{u}_{l,j}^w$ at the end sections of the element are treated as global degrees of freedom, equation (2.76) needs to account for the split between local and global warping displacement degrees of freedom. The derivation of the corresponding expressions for determining the internal warping degrees of freedom is presented in Appendix A.

The warping forces \mathbf{p}_i^w are zero at all sections i in the element interior, since these are free to warp. At the end sections of the beam element we distinguish two cases: (a) the section warping is free and the corresponding forces are consequently zero, and (b) the section warping is restrained, so that the corresponding warping displacements are zero. Either way, the solution of equation (2.76) with $\delta\mathbf{P}^w = \mathbf{0}$ gives the values at the free warping displacement degrees of freedom

$$\delta\mathbf{U}^w = -[\mathbf{K}_{ww}]^{-1} \mathbf{B}_{wq} \delta\mathbf{q} \quad (2.77)$$

Substituting the values for the warping displacement parameters $\delta\mathbf{U}^w$ from equation (2.77) into equation (2.73) gives

$$\delta\mathbf{e}_l = [\mathbf{k}_{ss,l}]^{-1} (\mathbf{b}_l + \mathbf{K}_{sw,l} [\mathbf{K}_{ww}]^{-1} \mathbf{B}_{wq}) \delta\mathbf{q} \quad (2.78)$$

with

$$\mathbf{K}_{sw,l} = [[\mathbf{k}_{sw}]_{l1} \quad \dots \quad [\mathbf{k}_{sw}]_{ln_l}] \quad (2.79)$$

Substituting $\delta\mathbf{e}_l$ from equation (2.73) into equation (2.73) gives

$$\delta\mathbf{v} = \sum_{l=1}^{n_{ip}} w_l \mathbf{b}_l^T [\mathbf{k}_{ss,l}]^{-1} (\mathbf{b}_l + \mathbf{K}_{sw,l} [\mathbf{K}_{ww}]^{-1} \mathbf{B}_{wq}) \delta\mathbf{q} = \mathbf{f} \delta\mathbf{q} \quad (2.80)$$

where the element flexibility matrix \mathbf{f} is given by

$$\mathbf{f} = \sum_{l=1}^{n_{ip}} w_l \mathbf{b}_l^T [\mathbf{k}_{ss,l}]^{-1} (\mathbf{b}_l + \mathbf{K}_{sw,l} [\mathbf{K}_{ww}]^{-1} \mathbf{B}_{wq}) \quad (2.81)$$

The element flexibility matrix \mathbf{f} is made up of two contributions $\mathbf{f} = \mathbf{f}_b + \mathbf{f}_w$ where

$$\mathbf{f}_b = \sum_{l=1}^{n_{ip}} w_l \mathbf{b}_l^T [\mathbf{k}_{ss,l}]^{-1} \mathbf{b}_l \quad (2.82a)$$

$$\mathbf{f}_w = \sum_{l=1}^{n_{ip}} w_l \mathbf{b}_l^T [\mathbf{k}_{ss,l}]^{-1} \mathbf{K}_{sw,l} [\mathbf{K}_{ww}]^{-1} \mathbf{B}_{wq} \quad (2.82b)$$

The matrix \mathbf{f}_b corresponds to the flexibility matrix of the standard beam without warping displacements and is obviously symmetric. The matrix \mathbf{f}_w represents the contribution of the warping displacements \mathbf{U}^w to the flexibility matrix of the 3d beam and is also symmetric on account of the symmetry of \mathbf{K}_{ww} and of equations (2.75) and (2.79) which give

$$\begin{aligned} \sum_{l=1}^{n_{ip}} w_l \mathbf{b}_l^T [\mathbf{k}_{ss,l}]^{-1} \mathbf{K}_{sw,l} &= \sum_{l=1}^{n_{ip}} w_l \mathbf{b}_l^T [\mathbf{k}_{ss,l}]^{-1} [[\mathbf{k}_{sw}]_{l1} \quad \dots \quad [\mathbf{k}_{sw}]_{ln_l}] \\ &= [[\mathbf{B}_{wq}]_1 \quad \dots \quad [\mathbf{B}_{wq}]_i \quad \dots \quad [\mathbf{B}_{wq}]_{n_l}] = \mathbf{B}_{wq}^T \end{aligned}$$

Thus,

$$\mathbf{f}_w = \mathbf{B}_{wq}^T [\mathbf{K}_{ww}]^{-1} \mathbf{B}_{wq} \quad (2.83)$$

The stiffness matrix \mathbf{k} of the element without rigid body modes is then equal to the inverse of the flexibility matrix \mathbf{f}

$$\mathbf{k} = \mathbf{f}^{-1} \quad (2.84)$$

The element stiffness matrix \mathbf{k}_{IJ} is then given by equation (2.66)

$$\mathbf{k}_{IJ} = \mathbf{a}_g^T \mathbf{k} \mathbf{a}_g \quad (2.85)$$

and the element end forces by the equation

$$\mathbf{p}_{IJ} = \mathbf{a}_g^T \mathbf{q} \quad (2.86)$$

The element stiffness matrix \mathbf{k}_{IJ} and the end forces \mathbf{p}_{IJ} are assembled into the structure stiffness matrix and force vector with standard procedures of structural analysis. This completes the derivation of the necessary equations for the element state determination. The step-by-step iterative process is discussed in the implementation section 2.6.

2.5 Warping displacement interpolation

The proposed beam element assumes that the warping displacement profile over the cross section is interpolated independently from the warping displacement distribution over the element length. With this approach the warping displacements $u^w(x, y, z)$ can be expressed as the product of a function in (y, z) with a function in x , as equation (2.45) shows.

The following sections discuss the selection of suitable interpolation functions for the warping displacement profile $\psi(y, z)$ over the cross section, and for the warping displacement distribution $\chi(x)$ over the element length.

2.5.1 Warping profile

According to equation (2.45) the warping displacement profile at section i is described by interpolation functions $\psi(y, z)$ with parameters $\mathbf{u}^w(x_i)$ serving as independent degrees of freedom of the beam element. The interpolation functions for the warping displacement profile are defined over a fixed grid (y_j, z_k) over the section.

The warping displacement differentials in the description of the warping strain ϵ^w in equation (2.15) require that the interpolation functions be continuously differentiable, thus excluding piece-wise linear polynomials between grid points. For this reason Lagrange polynomials are selected in this study. The grid points of the interpolation functions are distributed uniformly over the cross section under consideration of its geometry. Figure (2.1) shows typical interpolation grids for common cross-section geometries where n_w is the total number of interpolation grid points.

An alternative approach to the use of Lagrange polynomials utilizes warping profile interpolations functions $\psi(y, z)$ that satisfy the governing equilibrium equations and the boundary conditions of the linear elastic problem for the particular section geometry. The governing equilibrium equations of the problem result in a Laplacian, which can be solved with the membrane analogy for typical cross section geometries. Examples of warping functions for classical torsion problems can be found in [36]. Recently, Ferrari [27] proposed a numerical method for establishing the warping functions for any thin-walled section geometry under linear elastic shear and torsion. Because it is not clear what advantage these interpolation functions offer over the more general Lagrange polynomials for inelastic material response, it was decided not to pursue this approach in this study.

The choice of Lagrange polynomials for the warping displacement profile has the following advantages:

1. It is applicable to any section geometry and material response without modifications. Specifically, Lagrange polynomials prove suitable for thin-walled as well as for solid cross sections, in contrast to the warping functions in the literature, which are typically limited to thin-walled sections.
2. It furnishes a continuous function of y, z , which can be evaluated at any point of the cross section. This is significant for the numerical evaluation of section area integrals, for which the integration point location is independent of the warping profile interpolation grid.
3. It furnishes a continuous derivative function of y, z , which can be evaluated at any point of the cross section, as required for the numerical evaluation of the warping force integrals in equation (2.49).

On the other hand the choice of Lagrange polynomials requires more interpolation parameters or warping degrees of freedom n_w than the selection of special functions that take advantage of section geometry and boundary conditions, and is, therefore, more costly. Furthermore,

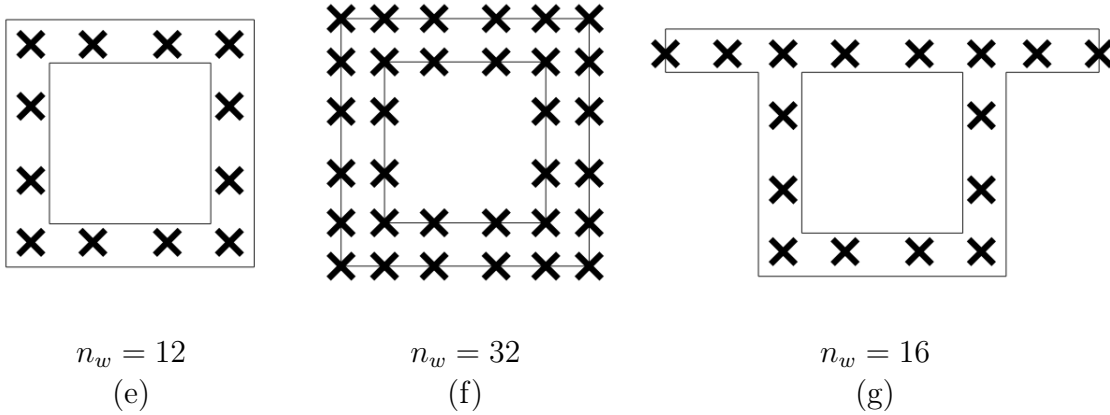
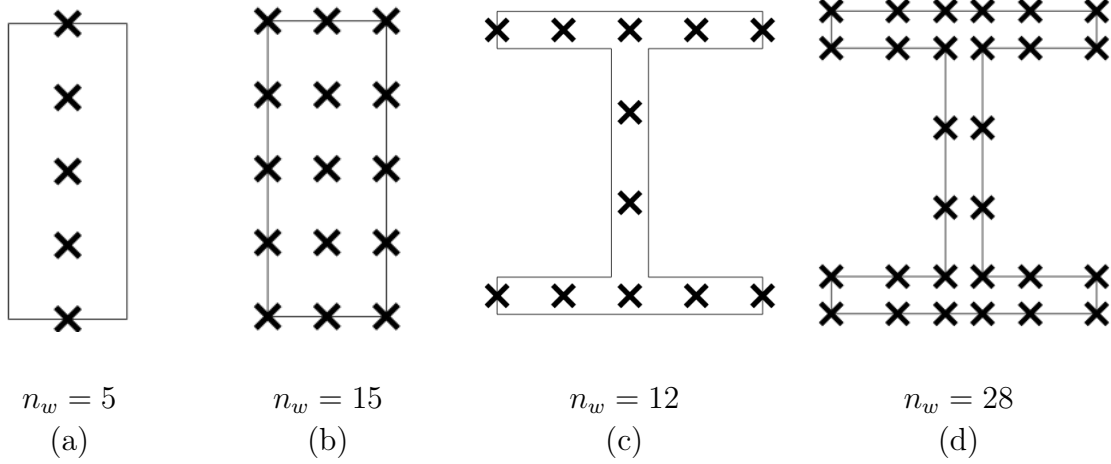


Table 2.1: Interpolation grid for warping profile with n_w degrees of freedom for typical cross-section geometries

the Lagrange polynomials are not free of rigid body modes, as required by the decomposition of the beam displacements in equation (2.6), and a special procedure to remove these is required, as described next.

For the warping displacements $u^w(x, y, z)$ to be free of rigid body modes, these need to be orthogonal to the displacements \mathbf{u}^r that describe the rigid body motion of the section plane. Consequently, the interpolation functions for the warping profile $\boldsymbol{\psi}(y, z)$ must belong to a space of polynomials W such that

$$W = \left\{ \boldsymbol{\psi}(y, z) / \int_A \begin{pmatrix} 1 \\ y \\ z \end{pmatrix} \psi_{jk}(y, z) dA = \begin{pmatrix} 0 \\ 0 \\ 0 \end{pmatrix} \right\} \quad (2.87)$$

A projection matrix \mathbf{P}_r is used to enforce the orthogonality of the interpolation functions $\boldsymbol{\psi}(y, z)$ for the warping profile to the displacements \mathbf{u}^r that describe the rigid body motion of the section plane. It is constructed from two matrices \mathbf{R} and \mathbf{V} as follows. The matrix \mathbf{R} consists of three vectors, one for each rigid body mode of the section plane. The terms of each vector represent the effect of the corresponding rigid body mode on the points (y_j, z_k) of the interpolation grid. Each vector, therefore, has n_w terms. Denoting the vector for the effect of the uniform translation in x with \mathbf{u}_1^r , of the rotation about the y -axis with \mathbf{u}_2^r , and of the rotation about the z -axis with \mathbf{u}_3^r leads to the following expression for matrix \mathbf{R}

$$\mathbf{R} = [\alpha_1 \mathbf{u}_1^r \quad \alpha_2 \mathbf{u}_2^r \quad \alpha_3 \mathbf{u}_3^r] \quad (2.88)$$

with the rigid body modes scaled by constants α_1 , α_2 and α_3 to be determined. The rigid body mode vectors at each section grid point (y_j, z_k) take the following form

$$\mathbf{u}_1^r = [1 \quad \dots \quad 1 \dots \quad 1]^T \quad (2.89a)$$

$$\mathbf{u}_2^r = [y_1 \quad \dots \quad y_{jk} \dots \quad y_{n_w}]^T \quad (2.89b)$$

$$\mathbf{u}_3^r = [z_1 \quad \dots \quad z_{jk} \dots \quad z_{n_w}]^T \quad (2.89c)$$

where jk is an index from 1 to n_w , the number of interpolation grid points in the section. The matrix \mathbf{V} is defined as the product of the rigid body displacements \mathbf{u}^r of the section plane with the interpolation functions $\boldsymbol{\psi}(y, z)$ for the warping profile

$$\mathbf{V} = \int_A \begin{pmatrix} 1 \\ y \\ z \end{pmatrix} \boldsymbol{\psi} dA \quad (2.90)$$

and is, therefore, of size $3 \times n_w$. It contains the polynomial coefficients of $\boldsymbol{\psi}(y, z)$ that result in interpolation functions in the space \mathbf{R} . The constants α_1 , α_2 and α_3 are then determined so that matrices \mathbf{R} and \mathbf{V} satisfy the relation

$$\mathbf{V}\mathbf{R} = \mathbf{I}_3 \quad (2.91)$$

where \mathbf{I}_3 is the identity matrix of dimension 3. The projection matrix \mathbf{P}_r is then formed so as to remove the components of $\boldsymbol{\psi}(y, z)$ in the space of \mathbf{R} by the standard form

$$\mathbf{P}_r = \mathbf{I}_{n_w} - \mathbf{R}\mathbf{V} \quad (2.92)$$

where \mathbf{I}_{n_w} is the identity matrix of dimension n_w . Under consideration of equation (2.91) it is easy to show that the projection matrix \mathbf{P}_r satisfies the relation $\mathbf{P}_r \mathbf{P}_r = \mathbf{P}_r$. The multiplication of the interpolation functions $\boldsymbol{\psi}(y, z)$ for the warping displacement profile by the matrix \mathbf{P}_r of scalar coefficients strips the interpolation functions of the components in

the space of \mathbf{R} so that they satisfy the relation in (2.87). Denoting these polynomials with $\tilde{\boldsymbol{\psi}}$ it holds that

$$\tilde{\boldsymbol{\psi}}(y, z) = \mathbf{P}_r \boldsymbol{\psi}(y, z) \quad (2.93)$$

The corresponding warping section forces $\mathbf{s}_x^w(x)$ and $\mathbf{s}_{yz}^w(x)$ in equation (2.60) become

$$\tilde{\mathbf{s}}_x^w(x) = \mathbf{P}_r^T \mathbf{s}_x^w(x) \quad (2.94a)$$

$$\tilde{\mathbf{s}}_{yz}^w(x) = \mathbf{P}_r^T \mathbf{s}_{yz}^w(x) \quad (2.94b)$$

With the same consideration the corresponding section stiffness matrices in equation (2.60) become

$$\tilde{\mathbf{k}}_{sw}^x = \mathbf{k}_{sw}^x \mathbf{P}_r \quad (2.95a)$$

$$\tilde{\mathbf{k}}_{sw}^{yz} = \mathbf{k}_{sw}^{yz} \mathbf{P}_r \quad (2.95b)$$

$$\tilde{\mathbf{k}}_{ww}^x = \mathbf{P}_r^T \mathbf{k}_{ww}^x \mathbf{P}_r \quad (2.95c)$$

$$\tilde{\mathbf{k}}_{ww}^{xy} = \mathbf{P}_r^T \mathbf{k}_{ww}^{xy} \mathbf{P}_r \quad (2.95d)$$

$$\tilde{\mathbf{k}}_{ww}^{yz} = \mathbf{P}_r^T \mathbf{k}_{ww}^{yz} \mathbf{P}_r \quad (2.95e)$$

The transformation of the section stiffness matrices in equation (2.60) with the projection matrix \mathbf{P}_r adds the rigid body modes in the section plane $\mathbf{u}_1^r, \mathbf{u}_2^r$ and \mathbf{u}_3^r to the null space of the section stiffness matrices $\mathbf{k}_{ww}^x, \mathbf{k}_{ww}^{xy}$ and \mathbf{k}_{ww}^{yz} . The presence of singular values in the section stiffness matrices $\tilde{\mathbf{k}}_{ww}^x, \tilde{\mathbf{k}}_{ww}^{xy}$ and $\tilde{\mathbf{k}}_{ww}^{yz}$ renders the stiffness matrix \mathbf{K}_{ww} in equation (2.76) singular and makes the numerical solution for $\delta \mathbf{U}^w$ impossible. To overcome this problem a rank three matrix \mathbf{k}_β is added to the singular section stiffness matrices $\tilde{\mathbf{k}}_{ww}^x, \tilde{\mathbf{k}}_{ww}^{xy}$ and $\tilde{\mathbf{k}}_{ww}^{yz}$. Matrix \mathbf{k}_β is defined by

$$\mathbf{k}_\beta = \beta \mathbf{V} \mathbf{V}^T \quad (2.96)$$

with \mathbf{V} from equation (2.90) and β an arbitrary constant that is selected so as to reduce the condition number of the modified section stiffness matrix. The modified section stiffness matrices thus become

$$\tilde{\tilde{\mathbf{k}}}_{ww}^x = \tilde{\mathbf{k}}_{ww}^x + \mathbf{k}_\beta \quad (2.97a)$$

$$\tilde{\tilde{\mathbf{k}}}_{ww}^{xy} = \tilde{\mathbf{k}}_{ww}^{xy} + \mathbf{k}_\beta \quad (2.97b)$$

$$\tilde{\tilde{\mathbf{k}}}_{ww}^{yz} = \tilde{\mathbf{k}}_{ww}^{yz} + \mathbf{k}_\beta \quad (2.97c)$$

where $\tilde{\tilde{\mathbf{k}}}$ denotes the non-singular section stiffness matrix. The addition of matrix \mathbf{k}_β to the section stiffness matrices $\mathbf{k}_{ww}^x, \mathbf{k}_{ww}^{xy}$ and \mathbf{k}_{ww}^{yz} has no effect on the solution of the system of equations for the warping displacement parameters in equation (2.76).

Before concluding the discussion on the interpolation functions for the warping profile, it is worth noting that the beam element formulation in section 2.4 is general and independent of the choice of the interpolation functions $\boldsymbol{\psi}$ for it. The examples of the following chapter demonstrate the benefits of the choice of Lagrange polynomials for the problems of interest in this study.

2.5.2 Warping distribution

The distribution of the warping displacements over the beam element length is described with interpolation functions $\chi(x)$. The response accuracy for problems of constrained warping is very sensitive to the selection of these interpolation functions. The linear elastic solution for a homogeneous, prismatic beam results in an exponential distribution of warping displacements along the element. Consequently, possible choices for warping distribution functions χ are exponential functions, Lagrange polynomials, and quadratic spline functions.

Exponential functions are commonly used for linear elastic finite element solutions, because they correspond to the exact analytical solution of a linear elastic, homogeneous, prismatic beam [100], [27]. For the more general case of variable cross section with inelastic material response, the advantage of using these functions disappears. For this reason they are not pursued further in this study, which instead focuses on Lagrange polynomials and quadratic spline functions. These functions are smooth and continuously differentiable as required for the warping strain definition in equation (2.13). The Lagrange polynomials for the examples of the following two chapters are limited to degree 1 to 4 in order to avoid the pronounced oscillations for polynomials of higher degree. If a more accurate interpolation of the warping displacements is desirable, quadratic spline functions should be used. In such case, the beam element is subdivided into n_{sg} segments with a quadratic interpolation function $\chi(x)$ over each segment. The continuity of the function $\chi(x)$ and its derivative $\frac{d\chi}{dx}$ is enforced at the segment ends. An additional condition is required for a unique interpolation of the $n_{sg} + 1$ warping displacement values at the segment ends. The assumption of free warping $\frac{d\chi}{dx} = 0$ at one beam end is selected for the purpose, because it is assumed that the beam extends a sufficient distance beyond the zone of constrained warping for the condition to be approximately satisfied.

2.6 Numerical implementation

2.6.1 General

The proposed 3d beam element that accounts for the interaction of shear and torsion with flexure and axial force under inelastic material response is implemented in the Matlab®-based general purpose finite element program FEDEASLab [28]. The program has a standard interface for finite elements and uses standard assembly procedures for the structure stiffness matrix and resisting force vector. Consequently, any other general purpose finite element analysis program could have been used for the purpose. The following discussion, therefore, addresses only the element state determination process.

2.6.2 Element state determination

The response of the proposed beam element is determined by assembly of the section responses. The key equation of the proposed mixed formulation is the compatibility equation (2.54b) to be satisfied by the section deformations $\mathbf{e}(x)$. Accordingly, the element corresponds to a series spring model of the monitoring sections. Furthermore, the section responses are coupled through the equilibrium equation (2.54d) for the warping forces that the warping displacements \mathbf{u}_i^w at each section i need to satisfy. This section coupling is not present in the standard mixed formulation for the 2d beam element [82]. The linearization of the discrete governing equations leads to equations (2.69) with the section deformations \mathbf{e}_l and the warping displacements \mathbf{u}_i^w as independent variables. The numerical solution of the governing equations within the element state determination process gives rise to an iterative or non-iterative element state determination algorithm [82], [51]. In the former case the nonlinear governing equations (2.54b) and (2.54d) are satisfied iteratively to within an acceptable convergence tolerance every time the element state determination is invoked. In the latter case, only the consistent linear solution of the equations (2.69) is determined with the residual of these equations stored and accounted for in the next element state determination during the next iteration of the solution algorithm for the global equilibrium equations. The numerical implementation of the 3d beam element in this study follows the iterative approach.

The state determination process requires the determination of the resisting forces and stiffness matrix of the element for given end node displacements \mathbf{u}_{IJ} for each iteration of the solution algorithm of the global equilibrium equations. If the warping displacements \mathbf{u}_{IJ}^w at the end sections of the element serve as global degrees of freedom, these values are also given at the start of the state determination process. If the structural model uses beam elements with and without warping displacements, then the warping displacements are treated as local degrees of freedom and their value at the previous load step is stored with the element history variables. Either way, the derivative of the warping displacements and, consequently, the normal stresses, are discontinuous at the element ends.

In the following step by step presentation of the state determination process the cases of warping displacements as global or local degrees of freedom are presented separately.

The locations of the integration scheme in the x -direction are identified with $l = 1 \dots n_{ip}$, where n_{ip} is the selected number of integration points. The warping displacements are included in n_l of these sections with $n_l \leq n_{ip}$. The number of warping displacement parameters in each section is n_w . Furthermore, the numerical evaluation of the integrals over the section area A uses the midpoint integration rule with n_f integration points or fibers.

1. Case: the warping displacements are local degrees of freedom.

In this case the end node displacement values \mathbf{u}_{IJ} are given at the start of the state determination process, which then consists of the following steps:

1. Recover the section deformations \mathbf{e}_l for sections $l = 1 \dots n_{ip}$, and the warping displacements \mathbf{u}_i^w for sections $i = 1 \dots n_l$ from the memory storage of the element.

- Use the element compatibility equation in the form

$$d\mathbf{v} = \mathbf{a}_g \mathbf{u}_{IJ} - \sum_{l=1}^{n_{ip}} w_l \mathbf{b}_l^T \mathbf{e}_l$$

where $d\mathbf{v}$ are the element deformation increments.

- Use the discrete form of equation (2.59) to determine the total strain $\boldsymbol{\epsilon}_{n,l}$ at material point n of section l for $n = 1 \dots n_f$ and $l = 1 \dots n_{ip}$.

$$\boldsymbol{\epsilon}_{n,l} = \mathbf{a}_s(y_n, z_n) \mathbf{e}_l + \sum_{i=1}^{n_l} \left[\frac{\partial \chi_{i,l}}{\partial x} \mathbf{a}_x^w(y_n, z_n) + \chi_{i,l} \mathbf{a}_{yz}^w(y_n, z_n) \right] \mathbf{u}_i^w$$

- Use the material constitutive law to determine $\boldsymbol{\sigma}_{n,l}$ and $\mathbf{k}_{mn,l}$.
- Use the equations (2.61) in the numerical evaluation form of equation (2.68) to determine the section stiffness matrices. Use equations (2.70), (2.74), (2.75) and (2.79) to determine $\mathbf{K}_{sw,l}$, \mathbf{K}_{ww} and \mathbf{B}_{wq} .
- Use equations (2.81) and (5.65) to determine the element stiffness matrix without rigid body modes \mathbf{k} and the basic force increments $d\mathbf{q} = \mathbf{k} d\mathbf{v}$. Update the basic element forces $\mathbf{q} = \mathbf{q} + d\mathbf{q}$.
- Determine \mathbf{p}_i^w with equation (2.54d) and use equation (2.76) to solve for the warping displacement increments $d\mathbf{U}^w$.
- Use equation (2.73) in the form

$$d\mathbf{e}_l = [\mathbf{k}_{ss,l}]^{-1} \left[(\mathbf{b}_l \mathbf{q} + \mathbf{s}^u - \mathbf{s}_l) - \sum_{n=1}^{nl} [\mathbf{k}_{sw}]_{ln} d\mathbf{u}_n^w \right]$$

with

$$\mathbf{s}_l = \sum_{n=1}^{n_f} w_n \mathbf{a}_{s,n}^T \boldsymbol{\sigma}_{n,l}$$

to determine the section deformation increments $d\mathbf{e}_l$.

- Update the section deformations $\mathbf{e}_l = \mathbf{e}_l + d\mathbf{e}_l$ and the warping displacements $\mathbf{U}^w = \mathbf{U}^w + d\mathbf{U}^w$ and return to step 2 until convergence.

2. Case: the end warping displacements \mathbf{u}_{IJ}^w are global degrees of freedom.

In this case the warping displacements \mathbf{u}_{IJ}^w at the end sections of the beam element are global degrees of freedom, whereas the warping displacements \mathbf{U}^w at the interior sections of the beam element are local degrees of freedom. The end node displacement values \mathbf{u}_{IJ} and \mathbf{u}_{IJ}^w are given at the start of the state determination process, which then consists of the following steps:

1. Recover the section deformations \mathbf{e}_l for sections $l = 1 \dots n_{ip}$, and the warping displacements \mathbf{u}_i^w for sections $i = 2 \dots n_l - 1$ from the memory storage of the element.
2. Use the element compatibility equation in the form

$$d\mathbf{v} = \mathbf{a}_g \mathbf{u}_{IJ} - \sum_{l=1}^{n_{ip}} w_l \mathbf{b}_l^T \mathbf{e}_l$$

where $d\mathbf{v}$ are the element deformation increments.

3. Use the discrete form of equation (2.59) to determine the total strain $\boldsymbol{\epsilon}_{n,l}$ at material point n of section l for $n = 1 \dots n_f$ and $l = 1 \dots n_{ip}$

$$\boldsymbol{\epsilon}_{n,l} = \mathbf{a}_s(y_n, z_n) \mathbf{e}_l + \sum_{i=1}^{n_l} \left[\frac{\partial \chi_{i,l}}{\partial x} \mathbf{a}_x^w(y_n, z_n) + \chi_{i,l} \mathbf{a}_{yz}^w(y_n, z_n) \right] \mathbf{u}_i^w$$

noting that all warping displacements are used in the calculation of the total strain.

4. Use the material constitutive law to determine $\boldsymbol{\sigma}_{n,l}$ and $\mathbf{k}_{mn,l}$.
5. Use the equations (2.61) in the numerical evaluation form of equation (2.68) to determine the section stiffness matrices. Use equations (2.70), (2.74), (2.75) and (2.79) to determine $\mathbf{K}_{sw,l}$, \mathbf{K}_{ww} and \mathbf{B}_{wq} , without including the contribution of the end sections.
6. Use equations (2.81) and (5.65) to determine the element stiffness matrix without rigid body modes \mathbf{k} and the basic force increments $d\mathbf{q} = \mathbf{k} d\mathbf{v}$, noting again the absence of the warping displacement contribution of the end sections. Update the basic element forces $\mathbf{q} = \mathbf{q} + d\mathbf{q}$.
7. Determine \mathbf{p}_i^w with equation (2.54d) and use equation (2.76) to solve for the warping displacement increments $d\mathbf{U}^w$.
8. Use equation (2.73) in the form

$$d\mathbf{e}_l = [\mathbf{k}_{ss,l}]^{-1} \left[(\mathbf{b}_l \mathbf{q} + \mathbf{s}^u - \mathbf{s}_l) - \sum_{n=2}^{nl-1} [\mathbf{k}_{sw}]_{ln} d\mathbf{u}_n^w \right]$$

with

$$\mathbf{s}_l = \sum_{n=1}^{n_f} w_n \mathbf{a}_{s,n}^T \boldsymbol{\sigma}_{n,l}$$

to determine the section deformation increments $d\mathbf{e}_l$.

9. Update the section deformations $\mathbf{e}_l = \mathbf{e}_l + d\mathbf{e}_l$ and the warping displacements $\mathbf{U}^w = \mathbf{U}^w + d\mathbf{U}^w$ and return to step 2 until convergence.

For both cases the element state determination converges when the work increment $d\mathcal{W}$

$$d\mathcal{W} = \sum_{l=1}^{n_{ip}} (w_l d\mathbf{e}_l^T d\mathbf{s}_l) + (d\mathbf{U}^w)^T d\mathbf{P}^w \quad (2.98)$$

in absolute or relative form becomes smaller than a specified tolerance.

Upon completion of the element state determination process the basic element stiffness matrix \mathbf{k} for the first case is available and can be transformed to global coordinates according to equation (2.85). Similarly, the basic element forces \mathbf{q} are available and can be transformed to global coordinates with equation (2.86).

For the second case the basic element forces \mathbf{q} are also available and can be transformed to global coordinates with equation (2.86). The warping forces $\mathbf{p}_{I,J}^w$ corresponding to the warping displacements $\mathbf{u}_{I,J}^w$ at the end sections can be determined with equation (2.54d). Because the final element stiffness matrix without rigid body modes \mathbf{k} includes the contribution of the end warping displacements, it differs from the stiffness matrix in step 6 of the state determination process. It is determined by inverting the flexibility matrix \mathbf{f} in equation (A.9) of Appendix A. The stiffness matrix \mathbf{k}_{IJ} of the element with rigid body modes is established by transforming the basic stiffness \mathbf{k} to global coordinates with an equation similar to (2.85), noting that the warping displacements do not require transformation.

2.6.3 Implementation of inelastic material model

The material response in equation (2.35) assumes the existence of a strain energy function W , as is the case for a hyperelastic material model. More generally, however, the stress $\boldsymbol{\sigma}$ may be defined in the form of (2.36). In plasticity theory the material stress $\boldsymbol{\sigma}$ can be expressed as a function of total strain $\boldsymbol{\epsilon}$ and additional internal variables $\boldsymbol{\xi}$

$$\boldsymbol{\sigma} = \hat{\boldsymbol{\sigma}}(\boldsymbol{\epsilon}, \boldsymbol{\xi}) \quad (2.99)$$

The following sections illustrate the incorporation of a general inelastic J2 plasticity model into the state determination algorithm of the proposed beam element. The objective of this brief discussion is to demonstrate the generality of the approach, permitting any suitable constitutive model to be incorporated in the beam formulation. The following 3d inelastic material model is used in the simulation of steel structures in the following chapters.

Multi-axial steel material model

The steel material model is based on J2 plasticity. The equations relative to the yield function, plastic flow rule and hardening rules are briefly summarized here, with details available in [85]. The parameters of the model are the yield stress σ_y , the isotropic hardening modulus H_i , and the kinematic hardening modulus H_k .

The symbol $\boldsymbol{\sigma}_t$ refers to the total stress with six components and the symbol $\bar{\boldsymbol{\sigma}}_t$ denotes the deviatoric part of the stress tensor. The yield function is expressed in terms of the deviatoric stress $\bar{\boldsymbol{\sigma}}_t$, the back stress $\boldsymbol{\sigma}_b$ and the linear hardening coefficient α :

$$f(\bar{\boldsymbol{\sigma}}_t, \boldsymbol{\sigma}_b, \alpha) = \|\bar{\boldsymbol{\sigma}}_t - \boldsymbol{\sigma}_b\| - \sqrt{\frac{2}{3}}(\sigma_y + H_i\alpha) \quad (2.100)$$

The plastic flow rule is

$$\dot{\boldsymbol{\epsilon}}_p = \beta \text{sign}(\boldsymbol{\sigma}_t - \boldsymbol{\sigma}_b) \quad (2.101)$$

and the hardening rules are

$$\dot{\alpha} = \sqrt{\frac{2}{3}}\beta \quad (2.102a)$$

$$\dot{\boldsymbol{\sigma}}_b = \frac{2}{3}H_k\dot{\boldsymbol{\epsilon}}_p \quad (2.102b)$$

The Kuhn-Tucker conditions and the consistency condition are expressed in the form

$$\beta \geq 0 \quad (2.103a)$$

$$f \leq 0 \quad (2.103b)$$

$$\beta \cdot f = 0 \quad (2.103c)$$

$$\beta \cdot \dot{f} = 0 \quad (2.103d)$$

A return map algorithm for the material state-determination under the above governing equations is well established [85].

Implementation of 3d material model in beam element formulation

The 3d constitutive material model expresses the six components of the stress tensor in terms of the total strains and additional internal variables. The incorporation of the 3d material model in the section state-determination process of a beam model requires the condensation of the stress components that are zero [46], [68], [82]. The condensation process of the material stiffness matrix is briefly summarized below for the sake of completeness. The Voigt notation is used to transform the stress and strain tensors into vectors with six components. With this convention the linearized stress-strain relation becomes

$$d\boldsymbol{\sigma} = \mathbf{k}_m d\boldsymbol{\epsilon} \quad (2.104)$$

with the material stiffness \mathbf{k}_m a matrix of size 6×6 . Any suitable stiffness matrix will do, but the availability of a tangent stiffness matrix improves computational performance and convergence characteristics significantly. $d\boldsymbol{\epsilon}$ and $d\boldsymbol{\sigma}$ denotes the strain and stress increment, respectively.

Denoting with r the index of the stress components to be retained, and with c the index of stress components to be condensed out, partitions the linearized stress-strain relation in the form

$$\begin{pmatrix} \delta\boldsymbol{\sigma}_r \\ \delta\boldsymbol{\sigma}_c \end{pmatrix} = \begin{bmatrix} \mathbf{C}_{rr} & \mathbf{C}_{rc} \\ \mathbf{C}_{cr} & \mathbf{C}_{cc} \end{bmatrix} \begin{pmatrix} \delta\boldsymbol{\epsilon}_r \\ \delta\boldsymbol{\epsilon}_c \end{pmatrix} \quad (2.105)$$

For the stress determination at a material point of the beam cross-section transverse equilibrium requires that $\boldsymbol{\sigma}_c = \mathbf{0}$. The value of $\boldsymbol{\epsilon}_c$ is updated during an iterative process until the equation $\boldsymbol{\sigma}_c = \mathbf{0}$ is satisfied. The update requires the following operations

$$\begin{aligned} d\boldsymbol{\epsilon}_{c_i} &= -\mathbf{C}_{cc}^{-1} \boldsymbol{\sigma}_{c_i} \\ \boldsymbol{\epsilon}_{c_{i+1}} &= \boldsymbol{\epsilon}_{c_i} + d\boldsymbol{\epsilon}_{c_i} \end{aligned}$$

where i is the iteration counter and $\boldsymbol{\sigma}_{c_i}$ corresponds to the value of the function $\hat{\boldsymbol{\sigma}}$ in equation (2.99) under $\boldsymbol{\epsilon}_i$. The condensed material stiffness matrix is then given by

$$\mathbf{k}_m = \mathbf{C}_{rr} - \mathbf{C}_{rc} \mathbf{C}_{cc}^{-1} \mathbf{C}_{cr} \quad (2.106)$$

For the problems of interest in this study, the stresses σ_{yy} and σ_{zz} are, in general, set to zero and condensed out of the linearized material relation. Furthermore, for sections with thin flanges and for 2d problems, the transverse stresses (σ_{xy} or σ_{xz}) can be neglected and condensed out as well.

Chapter 3

Evaluation for linear material response

This chapter presents the validation of the proposed 3d frame element under linear elastic material response by comparing its results for a few simple structural models with those of reference fiber beam elements and shell finite elements.

After summarizing the key features of the fiber beam and shell finite element models used in the validation studies, the following examples address three aspects of the element response: the shear strain and stress profile of a beam section under shear, the shear-lag effect, and the torsional response.

3.1 Reference models

The section presents a brief overview of reference fiber beam and shell finite element models used for comparison with the results of the proposed model.

3.1.1 Shear beam model

The first type of model used in the validation studies is the 2d fiber beam element for axial force, shear and flexure by Saritas [82], which was extended to 3d with the inclusion of torsion by Navarro Gregori [37].

The basic assumption of these elements concerns the strain distribution at a beam section. For the 3d case it takes the form

$$\boldsymbol{\epsilon} = \begin{bmatrix} 1 & -y & 0 & 0 & z & 0 \\ 0 & 0 & k_y \beta(y, z) & -z & 0 & 0 \\ 0 & 0 & 0 & y & 0 & k_z \alpha(y, z) \end{bmatrix} \mathbf{e} = \mathbf{a}_s \mathbf{e} \quad (3.1)$$

where \mathbf{e} is the generalized section deformation vector defined in equation (2.14) and \mathbf{a}_s is the kinematic matrix of the cross section.

The functions $\beta(y, z)$ and $\alpha(y, z)$ describe the shear strain distribution over the cross-section for the shear deformation γ_y and γ_z , respectively. The coefficients k_y and k_z are

shear correction factors to ensure longitudinal equilibrium, as described in [82] and [37]. The section forces \mathbf{s} result from the integration of the stresses $\boldsymbol{\sigma}$ over the area A of the cross-section

$$\mathbf{s} = \int_A \mathbf{a}_s^T \boldsymbol{\sigma} dA \quad (3.2)$$

The postulated shear strain profiles over the cross section depend on its geometry and may be available in closed form under linear elastic material response for sections free to warp. The models of Saritas and Navarro Gregori use the shear strain distributions of the linear elastic solution also for the inelastic element response.

The compatibility matrix \mathbf{a}_s in equation (3.1) does not couple the effects of the shear deformations in the y and z -direction, so that a shear deformation γ_y gives rise only to a shear stress σ_{xy} . The response of a wide flange beam under a shear deformation γ_y is, however, characterized by shear stresses σ_{xy} in the web, and shear stresses σ_{xz} in the flanges. The fact that the latter cannot be captured by the assumed section compatibility matrix \mathbf{a}_s in equation (3.1) is a shortcoming of these models for 3d beam analysis.

For the validation studies the mixed formulation of Taylor et al. [92] was used with the section kinematics of equation (3.1) to extend the 2d element of Saritas [82] to 3d. In the following validation studies this element is referred to as *shear beam element*.

3.1.2 Beam model with single warping mode

To improve the modeling of the torsional response for the shear beam model of the preceding section a section warping mode is inserted in the element kinematics. This approach derives from St. Venant's torsion theory, as described by Timoshenko [96], and was used in some recent 3d beam elements, such as the model by Nukala and White [66].

With an additional torsion degree of freedom ζ at each element end node for the warping amplitude, the section deformation vector becomes

$$\mathbf{e} = [\epsilon \quad \kappa_z \quad \gamma_y \quad \kappa_x \quad \kappa_y \quad \gamma_z \quad \zeta']^T \quad (3.3)$$

and the strain distribution at a beam section is given by

$$\boldsymbol{\epsilon} = \begin{bmatrix} 1 & -y & 0 & 0 & z & 0 & \omega(y, z) \\ 0 & 0 & k_y \beta(y, z) & -z + \frac{\partial \omega}{\partial y} & 0 & 0 & 0 \\ 0 & 0 & 0 & y + \frac{\partial \omega}{\partial z} & 0 & k_z \alpha(y, z) & 0 \end{bmatrix} \mathbf{e} = \mathbf{a}_s \mathbf{e} \quad (3.4)$$

where $\omega(y, z)$ describes the warping profile. Closed form expressions for the warping profile under linear elastic material response are available for particular section geometries, such as a wide flange section [96]. When warping is constrained at the element boundaries, the warping degree of freedom ζ is set equal to zero.

The corresponding section resultants are given by

$$\mathbf{s} = \int_A \mathbf{a}_s^T \boldsymbol{\sigma} dA \quad (3.5)$$

The section force in \mathbf{s} that corresponds to the warping deformation of the cross section is the bi-moment.

This beam model is an extension of St. Venant's torsion theory with the inclusion of shear deformations under the same assumptions as the shear beam model. It can be thought of as a special case of the general 3d beam element of chapter 2 with a single warping degree of freedom $n_w = 1$, noting that the function ω for the warping profile corresponds to the interpolation function ψ . With one degree of freedom for warping at each end node, the element can only accommodate a linear distribution of warping along the axis, or the exponential functions of the exact linear solution for a prismatic beam. In the following validation studies this element is referred to as *SW beam element*.

3.1.3 Shell model

Beam models are based on the assumption that the element has one privileged direction along the element axis, so that the section kinematics can be postulated independently of the response along the element axis. With this assumption the section response is established first by integration over the cross section and is then used to derive the element response by integration over the element axis. While the general 3d beam element of chapter 2 and the SW beam element account for the out-of-plane deformations of a section, they neglect the in-plane deformations ϵ_{yy} and ϵ_{zz} . To validate this assumption and its relevance for the local stress response of 3d beams, plane stress shell finite elements are used for modeling the web and flanges of the thin-walled section, as shown in figure (3.1) for a wide flange beam. The shell element used for the purpose is the Mixed Interpolation of Tensorial Component

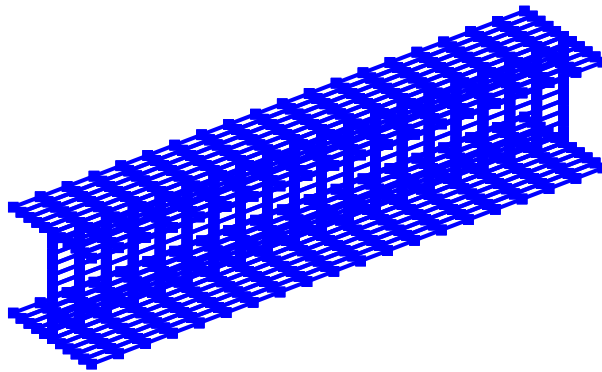


Figure 3.1: Shell model for wide flange beam

MITC element proposed by Bathe [4], which does not suffer from shear locking. This element was implemented for linear elastic and inelastic material response in FEDEASLab [28]. Its results were checked against the four node shell element in the program FEAP [91] with excellent agreement.

3.2 Examples

The selected examples compare the response of the simply supported and the cantilever beam in figure (3.2) with different cross sections shown in figure (3.3) under concentrated and uniform loading. The examples are divided into three parts in accordance with the response quantity of interest: the first part addresses the shear strain and stress profile for cases without warping constraint, the second part addresses the effect of warping constraint on shear-lag, and finally the last part investigates the torsional response.

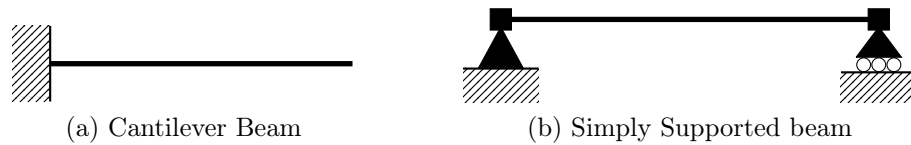


Figure 3.2: Beam geometry for examples

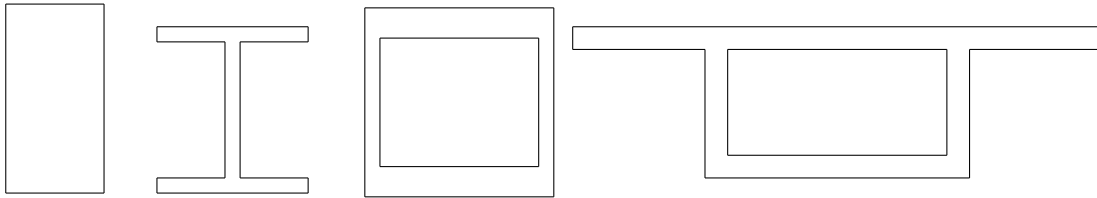


Figure 3.3: Cross-sections for examples

3.2.1 Shear stress profile

For the study of the shear stress profile the cantilever beam in figure (3.4) is selected. The cantilever beam is subjected to a concentrated transverse load P at the free end, while the fixed end is free to warp. The length of the beam is $L = 5$ units and the tip transverse load is $P = 1$ unit. The studies are conducted for a rectangular and a wide flange section.

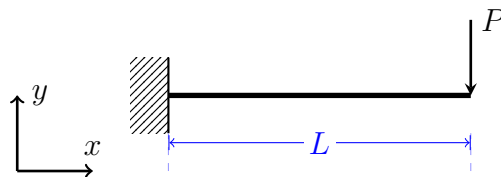


Figure 3.4: Cantilever beam with loading

The Euler-Bernoulli beam theory (EB) and the Timoshenko beam theory (T) give the

following expressions for the exact value of the tip displacement [19].

$$U_{EB} = -\frac{PL^3}{3EI_z} \quad , \quad U_T = -\frac{PL^3}{3EI_z} - \frac{PL}{GAk_y} \quad (3.6)$$

where E is the Young modulus, A the cross sectional area, I_z the moment of inertia about the z -axis, and k_y the shear correction factor in y .

Rectangular section

The geometry of the rectangular cross-section and the mechanical properties of the material are shown in figure (3.5). The general 3d beam element model of chapter 2 with cubic La-

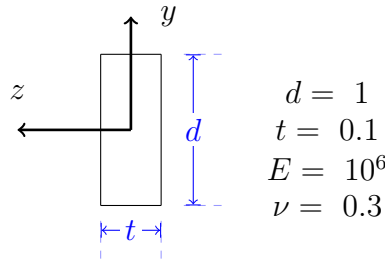


Figure 3.5: Geometry and mechanical properties for rectangular section

grange polynomials for the warping profile function $\psi(y)$ requires $n_w = 4$ warping degrees of freedom, as shown in figure (3.6a). The shear correction factor for the Timoshenko beam

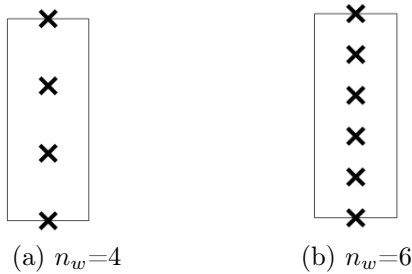


Figure 3.6: Number and location of warping degrees of freedom for rectangular section

model is $k_y = 5/6$. No correction factor is necessary for the general 3d beam element of chapter 2. The tip transverse displacement for the different models in table (3.1) shows that the proposed 3d beam model gives the exact tip displacement of the Timoshenko beam theory. The cubic warping displacement results in the exact parabolic shear stress distribution of the Timoshenko beam theory, as shown in figures (3.7a-3.7b). The same results for tip displacement and shear stress distribution can be obtained with the shear beam model of Saritas [82], since it postulates the exact parabolic shear strain distribution.

	Enh. Element	U_T	Shell Model	U_{EB}
Tip Displ (10^{-3})	-5.156	-5.156	-5.136	-5.000

Table 3.1: Tip displacement of cantilever beam with rectangular section

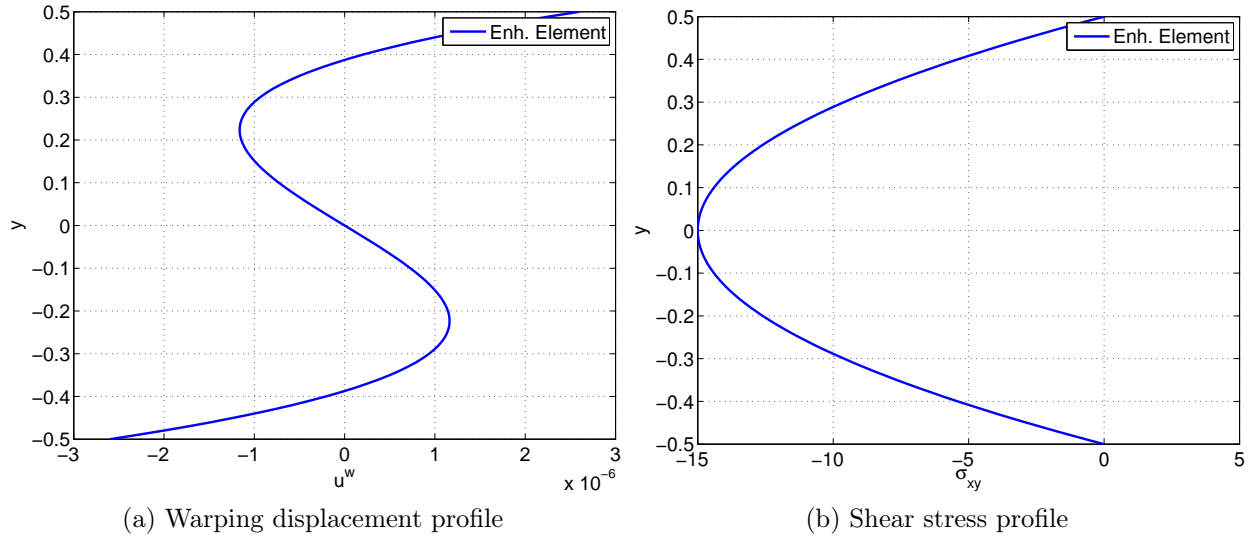


Figure 3.7: Warping displacement and shear stress distribution for rectangular section

Wide flange section

The geometry of the wide flange cross-section and the mechanical properties of the material are shown in figure (3.8). The 3d beam element uses Lagrange polynomials $\psi(y, z)$ for the

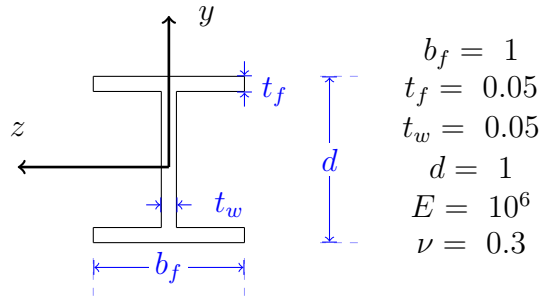


Figure 3.8: Geometry and mechanical properties for wide flange section

warping profile with four degrees of freedom in the web n_{w_w} and five degrees of freedom n_{w_f} in each flange. This results in a total number of twelve warping degrees of freedom n_w for the section, as shown in figure (3.9a). The tip displacement values of the analytical and the numerical solution are listed in table (3.2). The correction factor used for Timoshenko's

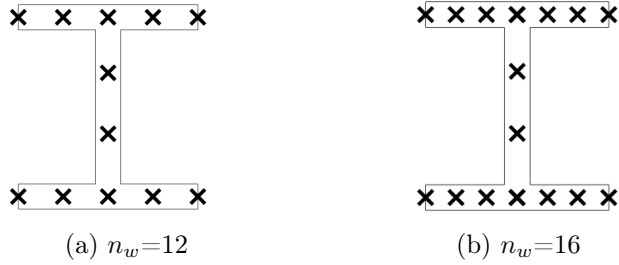


Figure 3.9: Number and location of warping degrees of freedom for wide flange section

beam theory is $k_y = 0.2956$ [19]. The agreement between the proposed beam element, the shell model and the Timoshenko beam theory is excellent, noting the approximate nature of the shear correction factor for the latter.

	Enh. Element	U_T	Shell Model	U_{EB}
Tip Displ (10^{-3})	-1.957	-1.930	-1.924	-1.626

Table 3.2: Tip displacement of cantilever beam with wide flange section

The satisfaction of longitudinal and transverse equilibrium along with the compatibility relations of the beam element give the warping profile in figure (3.10). To facilitate the

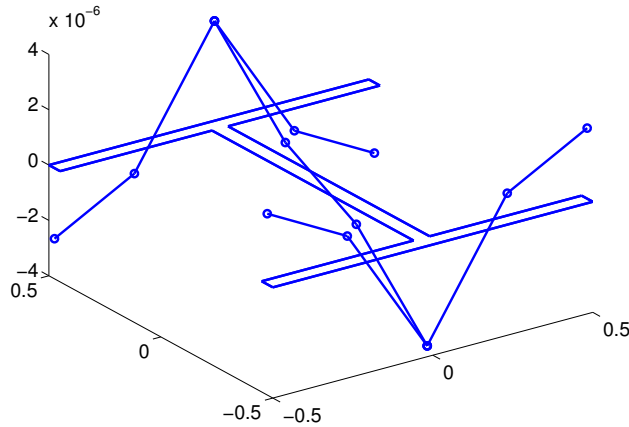


Figure 3.10: Warping profile of wide flange section with $n_w = 12$ degrees of freedom

assessment of the warping profile, the out-of-plane displacements are displayed separately for web and flanges in figure (3.11). The differentiation of the warping displacements gives the shear strain profile, which can then be used with the linear elastic constitutive relation to give the shear stress profile depicted separately for the web and flanges in figure (3.12). The proposed model correctly predicts a parabolic shear stress distribution in the web and

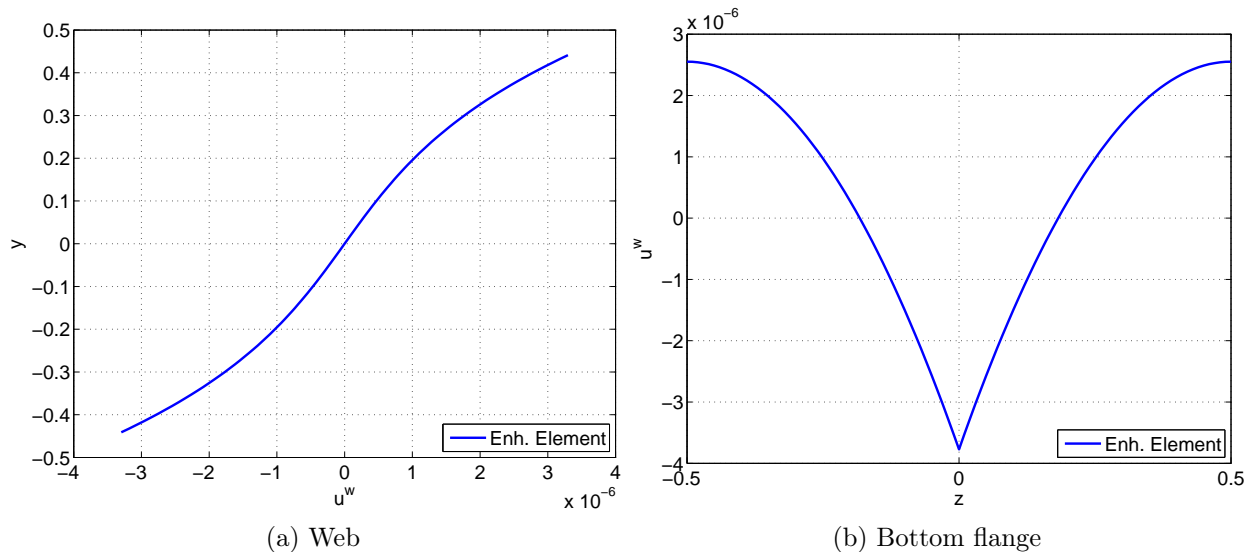


Figure 3.11: Warping displacement distribution for wide flange section

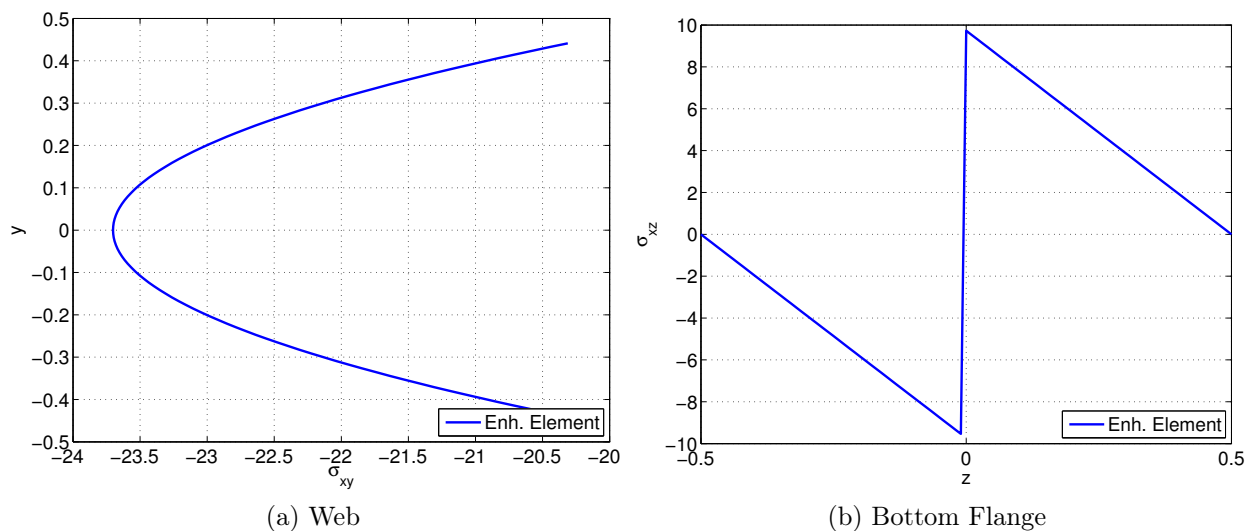


Figure 3.12: Shear stress distribution for wide flange section

a linear distribution in the flange. The advantage of this approach over shear beam models with fixed shear strain distribution [82], [68] is that the distribution adjusts to the gradual yielding of the cross section under inelastic material response, as will be illustrated in the next chapter. The two preceding examples demonstrate the ability of the proposed beam element to describe the local shear response for any cross section geometry reproducing exactly the non-uniform shear strain and stress distributions for sections with unconstrained

warping.

3.2.2 Shear-lag effect

The term *shear-lag* describes the non-uniform axial stress distribution across the flange of thin-walled profiles under flexure and shear and is pronounced in bridge box girders with wide flanges and thin-walled tubular sections of any type. The shear-lag effect is strongly dependent on the boundary conditions of the problem.

This section investigates the ability of the proposed model to represent the shear-lag effect for sections of different geometry by comparing its results with available analytical solutions and with the results of shear beam and shell finite element models. Furthermore, available experimental measurements from the response of a box girder bridge specimen are also used for the purpose.

The cross sections used for the study on the effect of warping constraint on the axial stress distribution are a wide flange section, a box section, and a rectangular section. The effect of the choice of interpolation functions for the warping profile $\psi(y, z)$ and the warping displacement distribution $\chi(x)$ along the element axis is also discussed.

To quantify the shear-lag effect in the flanges of thin-walled sections the shear-lag coefficient λ is introduced as the ratio of the axial stress $\sigma_{xx}(z)$ under bending about the z -axis by a model that accounts for section warping to the axial stress σ_{xx}^{sh} by a model that assumes that plane sections remain plane

$$\lambda(z) = \frac{\sigma_{xx}(z)}{\sigma_{xx}^{sh}} \quad (3.7)$$

In equation (3.7) it is assumed that the stress of both cases is evaluated at the same distance y from the section centroid. The shear-lag coefficient λ is typically evaluated at the intersection of the flange with the web, where it assumes its largest value $\lambda_{max} > 1$, and at the flange tip where it assumes its smallest value $\lambda_{min} < 1$. A shear-lag coefficient value greater than one corresponds to a *positive* shear-lag effect, and a value smaller than one to a *negative* effect.

Rectangular section

The cantilever beam in figure (3.4) is subjected to a concentrated force at the tip, but the out-of-plane warping is now restrained at the fixed end. The length of the beam is again $L = 5$ units and the tip transverse load is $P = 1$ unit as before. The beam has the same rectangular cross section in figure (3.5) as the earlier example.

Because the effect of the warping constraint affects only a small portion of the cantilever beam near the support, the cantilever is subdivided into two elements: the proposed 3d beam element with warping displacement degrees of freedom extends over the length of $0.15L$ from the fixed support, and the shear beam element of Saritas is used for the remaining portion.

The warping profile $\psi(y, z)$ is represented by Lagrange polynomials with $n_w = 6$ warping degrees of freedom, as shown in figure (3.6b). The warping displacement distribution $\chi(x)$ over the element length is represented with quadratic spline functions over 5 segments.

The tip displacement under the concentrated force is $-5.155 \cdot 10^{-3}$ and is practically the same as the value in table (3.1) for the earlier example leading to the conclusion that the warping constraint has insignificant influence on the global behavior of the element.

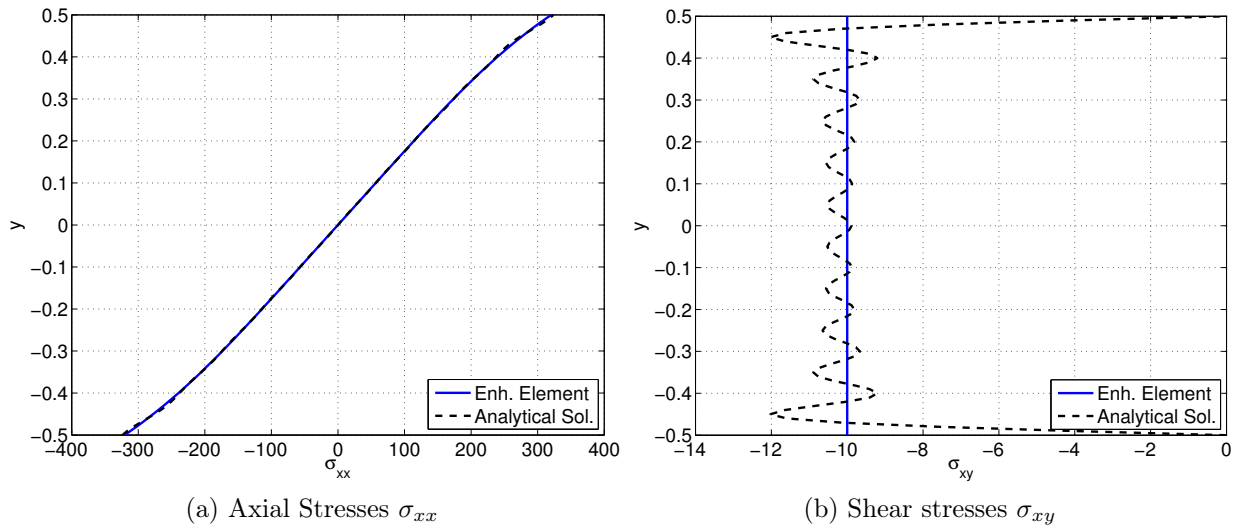


Figure 3.13: Normal and shear stress profile for rectangular section at support of cantilever

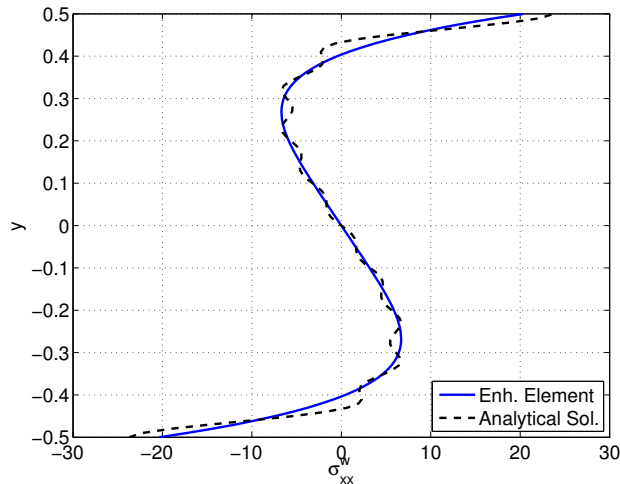


Figure 3.14: Normal stress σ_{xx}^w due to warping at support of cantilever beam

Figure (3.13) shows the axial stress and shear stress profile of the section at the support

where warping is constrained. The axial stress profile σ_{xx} is non-linear, whereas the shear stress σ_{xy} is constant over the section depth. The results are compared with the infinite Fourier series solution of the governing differential equations by Hildebrand [41] showing excellent agreement, except for the small oscillations of the analytical solution that arise from the incomplete summation of the terms of the infinite Fourier series.

The additional axial stresses σ_{xx}^w due to the axial strains ϵ_{xx}^w caused by warping displacements are determined by

$$\sigma_{xx}^w = E\epsilon_{xx}^w = E\frac{\partial u^w}{\partial x} \quad (3.8)$$

These show excellent agreement with the analytical solution by Hildebrand [41] in figure (3.14).

Wide flange section

The wide flange section for the cantilever beam of figure (3.4) is the same as for the earlier example. Its geometry and material properties are shown in figure (3.8). The cantilever beam of length $L = 5$ units is subjected again to a concentrated force P of 1 unit at the tip, with the out-of-plane warping restrained at the fixed end.

The effect of the warping constraint affects now a larger portion of the cantilever beam on account of the thin-walled section. The cantilever is, consequently, subdivided into two elements: the proposed 3d beam element with warping displacement degrees of freedom extends over a length of $0.40L$ from the fixed support, and the shear beam element of Saritas is used for the remaining portion. In the interest of accuracy the 3d beam element is subdivided into $n_{sg} = 10$ segments with quadratic spline interpolation for the warping distribution $\chi(x)$ along the element axis. The warping profile $\psi(y, z)$ is represented with four warping degrees of freedom n_{w_w} in the web and either five or seven warping degrees of freedom n_{w_f} in the flange, as shown in figure (3.9).

To assess their accuracy the results of the proposed 3d beam element are compared with the results of a 3d finite element model with a mesh of 30 by 150 plane stress shell elements for the web and each flange. This model was analyzed with program FEAP [91].

The axial stress concentrations due to the warping constraint at the support of the cantilever are depicted in figure (3.15) with the axial stress profile over the depth of the web for the proposed 3d beam element and for the shell model deviating slightly from the linear profile of the shear beam model in figure (3.15a). There is excellent agreement between the axial stress of the proposed 3d beam and that of the shell model for the distribution across the width of the lower flange in figure (3.15b), which shows that the minimum axial stress at the tip of the flange is about 80 % of the maximum axial stress value at the intersection between flange and web.

Figure (3.16) shows the variation of the shear-lag coefficient λ along the cantilever axis x . The maximum shear-lag coefficient λ_{max} corresponds to the intersection of the flange with the web, and the minimum shear-lag coefficient λ_{min} to the tip of the flange. The local

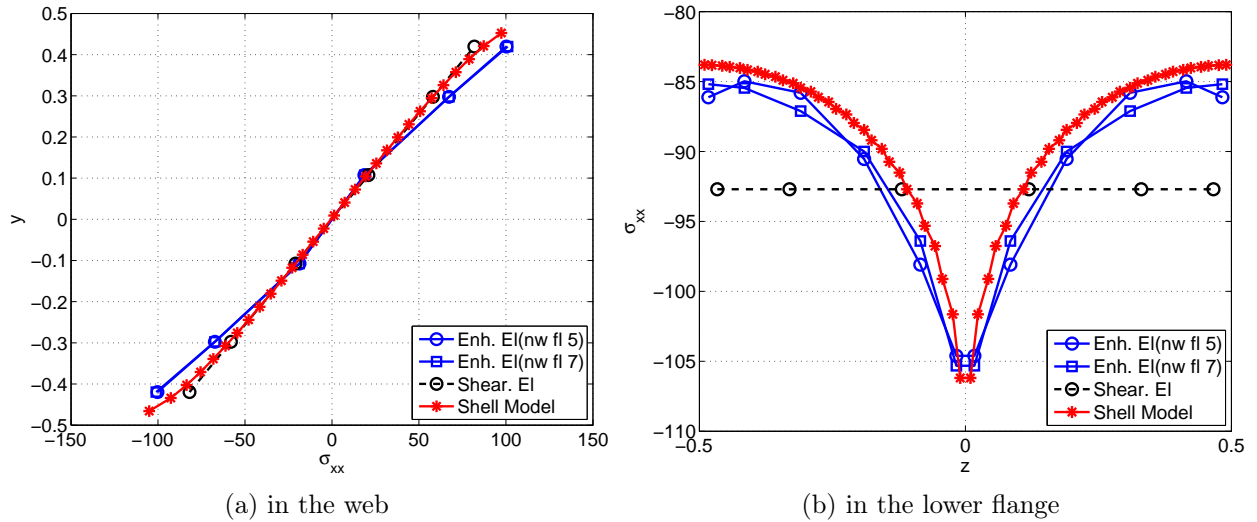


Figure 3.15: Axial stress profile at support of cantilever beam with wide flange section

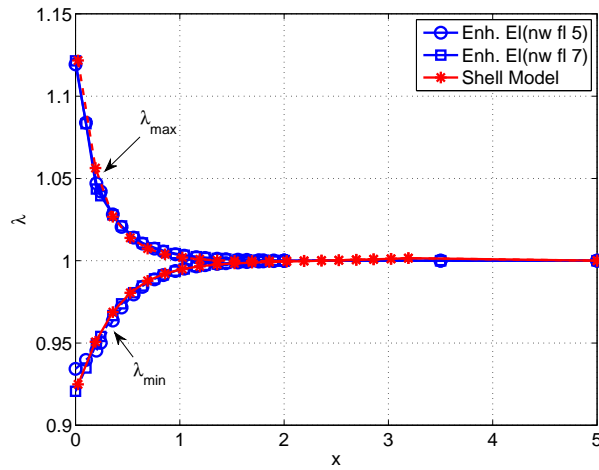


Figure 3.16: Shear-lag coefficient along x -axis of cantilever beam with wide flange section

aspect of the warping constraint is evident in the figure, which shows that the axial stress distribution across the flange width becomes practically uniform at a distance of $0.3L$ from the fixed support with restrained warping displacements.

The results in figures (3.15- 3.16) show that the finer representation of the warping profile with $n_w = 16$ warping degrees of freedom does not increase appreciably the accuracy of the axial stress distribution across the section and along the element axis relative to the case with $n_w = 12$ warping degrees of freedom to justify the higher computational cost. These

results lead to the conclusion that the parabolic warping displacement representation with three warping degrees of freedom for each half flange for a total of $n_{wf} = 5$ parameters for each flange is sufficient and will be used in the studies of the next chapter. More important for the accuracy of the results is the representation of the warping distribution $\chi(x)$ along the element axis, as will be discussed further in the following example.

Simply supported box girder

The simply supported box girder in figure (3.17) with a span of $L = 800$ mm and with the section geometry and material properties in figure (3.18) was selected because of the availability of experimental measurements on a Perspex glass specimen by Luo et al. [58]. These tests were conducted for a concentrated force $P = 0.2722$ kN at midspan and for a uniformly distributed load $q = 6$ kN/m. Furthermore, the box girder was the subject of extensive analytical studies by several authors with models ranging from beam [48], [100], to finite strip [59], to shell finite elements [53], to analytical methods [78]. This wealth of available information provides an excellent opportunity for the validation of the proposed 3d beam element.

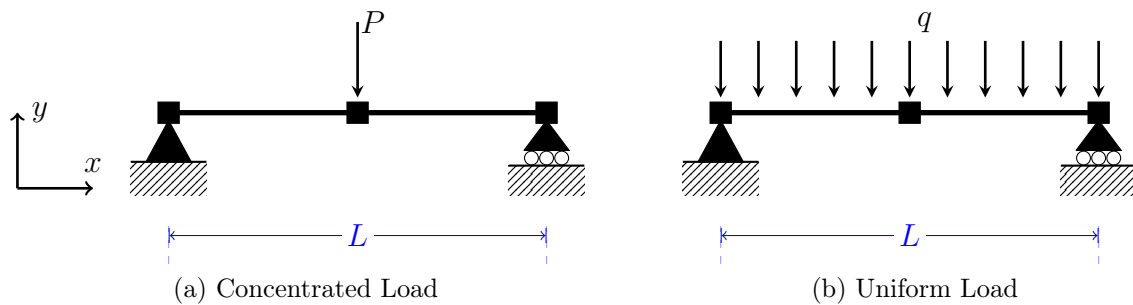


Figure 3.17: Simply supported box girder of span L under concentrated and uniform load

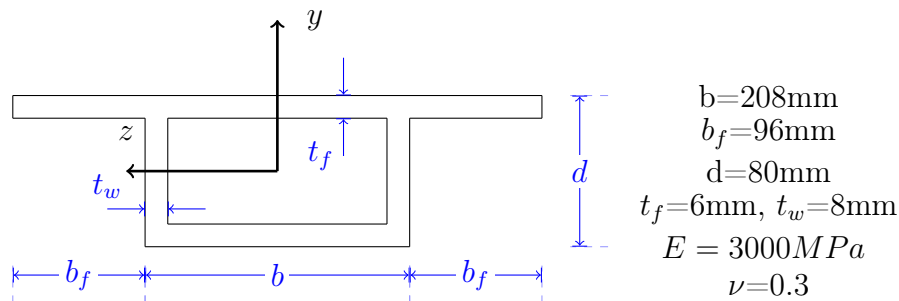


Figure 3.18: Geometry and material properties of box girder section

Figure (3.17) shows that a single 3d beam element is used for each half of the structure on account of the symmetry in geometry and loading. The warping profile at a section is

represented by Lagrange polynomials with $n_w = 16$ warping degrees of freedom located as shown in figure (2.1g). For the warping distribution $\chi(x)$ along the element axis the use of Lagrange polynomials and quadratic spline functions is studied.

The mid-span deflection of the simply supported box under the two load cases is reported in Table (3.3). The mid-span deflection of the girder under the concentrated load P with the Euler-Bernoulli (EB) and Timoshenko (T) beam theory is

$$U_{EB} = \frac{PL^3}{48EI} \quad , \quad U_T = \frac{PL^3}{48EI} + \frac{PL}{4GAk_y} \quad (3.9)$$

The same displacement under the uniform load q becomes for the two theories

$$U_{EB} = \frac{5qL^4}{384EI} \quad , \quad U_T = \frac{5qL^4}{384EI} + \frac{qL^2}{8GAk_y} \quad (3.10)$$

The mid-span deflection value of the Timoshenko beam theory in Table (3.3) is based on an estimate of the shear correction factor k_y equal to 0.1437. This factor was established with the assumption of a shear stress profile for the box girder section without warping constraint. The value also appears reasonable when compared with the shear correction factors for an I- and T-section. The deflection value of the proposed 3d beam element compares very favorably with the value of the Timoshenko beam theory suggesting that the inclusion of the shear-lag effect does not have an appreciable effect on the midspan displacement. The beam model of Zhou [100] uses two shear-lag degrees of freedom at each end node and postulates a cubic warping displacement profile in the flanges of the section, but does not include the effect of shear deformations. It is used here as representative of several models that have been proposed for the shear-lag effect representation, because the studies in [100] show relatively good agreement among the models and between model results and experimental measurements of the axial stress distribution for the Perspex glass specimen. The results of Zhou's model in Table (3.3) imply that the shear-lag effect increases the midspan deflection by about 10%, a fact that is not borne out by the proposed element. Instead, the shear deformations of the thin-walled cross section increase the midspan deflection of the Euler-Bernoulli beam theory by about 30%, despite a span to depth ratio L/d of 10, as confirmed by the Timoshenko beam theory.

Midspan deflection (mm)	proposed element	Zhou model	U_T (est)	U_{EB}
Concentrated load	-0.264	-0.210	-0.266	-0.192
Uniform load	-2.783	-2.350	-2.767	-2.116

Table 3.3: Midspan deflection of box girder under concentrated and uniform load

Figures (3.19a) and (3.19b) show the distribution of the shear-lag coefficient λ from the left support to the girder midspan. The maximum shear-lag coefficient λ_{max} arises at the

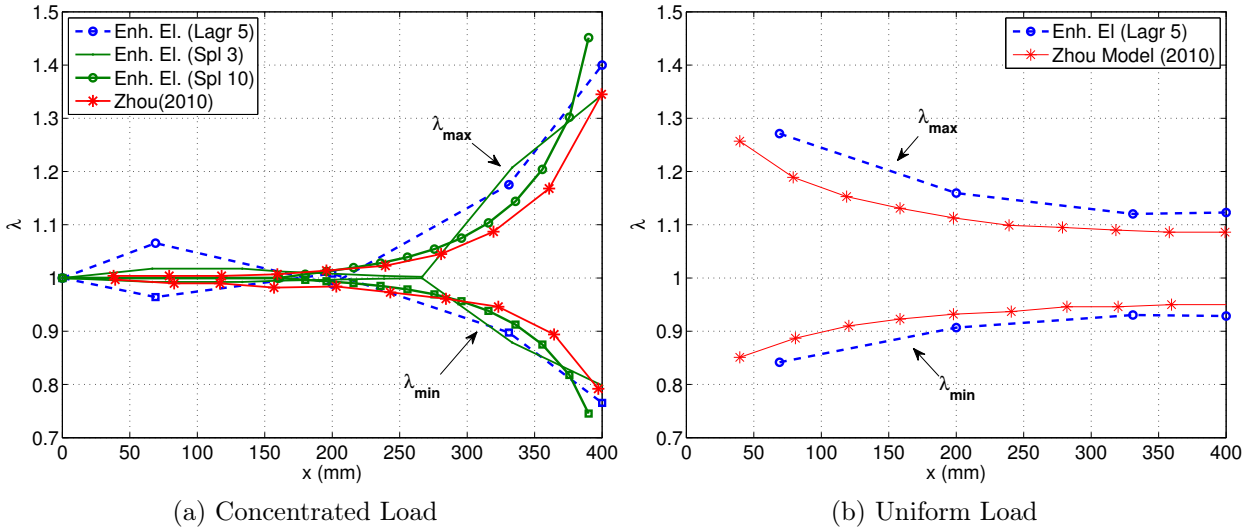


Figure 3.19: Shear-lag coefficient of box girder under concentrated and uniform load

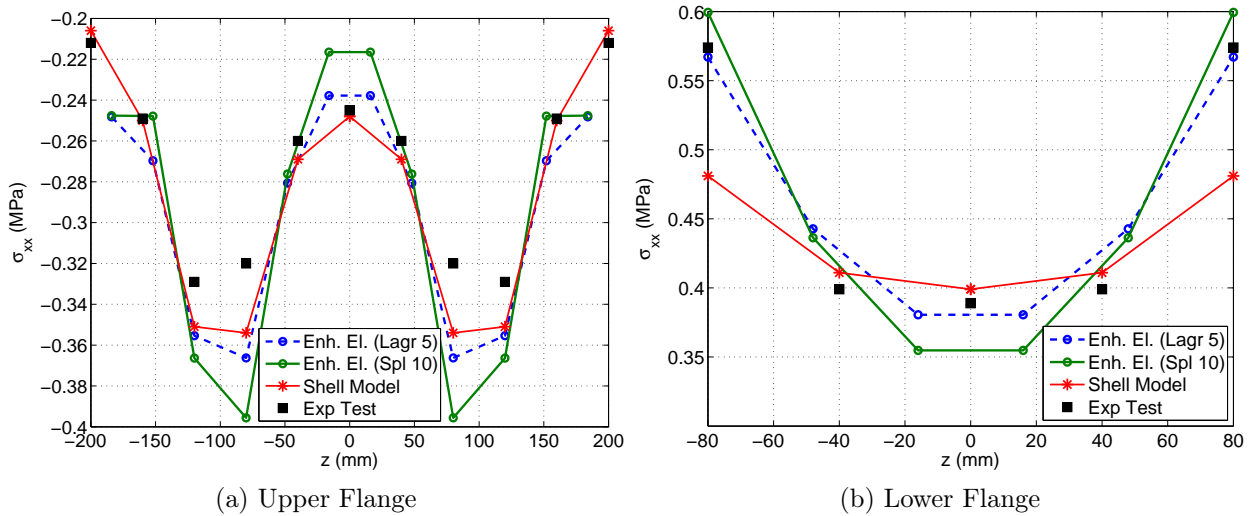


Figure 3.20: Axial stress profile at midspan section of box girder under concentrated load

intersection of the upper flange and web, while the minimum shear-lag coefficient λ_{min} occurs in the middle of the upper flange.

Figure (3.19a) shows that under a concentrated force P at girder midspan both shear-lag coefficients λ_{max} and λ_{min} assume their largest and smallest value, respectively, under the point of load application. The same figure shows that both shear-lag coefficients reduce quickly away from the girder midspan and become practically equal to one at the quarter span

point. Between the support and the quarter span point the shear-lag effect can, therefore, be neglected, and the section at the support can be assumed free to warp. For this reason the condition $d\chi/dx = 0$ is imposed at the support for the parameter determination of the quadratic spline interpolation functions for the warping distribution along the element axis, as discussed in section (2.5.2). Figure (3.19a) shows the shear-lag coefficient distribution for a model with a fourth order Lagrange polynomial with five interpolation points for the warping distribution along the element axis, and for models with quadratic spline functions over $n_{sg} = 3$ and $n_{sg} = 10$ segments. The results are also compared with those of Zhou's model. The model with Lagrange polynomials for the warping distribution exhibits some oscillation of the shear-lag coefficients near the support. By contrast, the quadratic spline functions represent better the smooth decay of the shear-lag effect away from the point of load application. There is little difference in the results of the models with $n_{sg} = 3$ and $n_{sg} = 10$ segments except in the vicinity of the point of load application, where the larger number of segments overestimates the shear-lag effect. Clearly, the large number of spline segments and the associated small integration weight for the section with constrained warping at girder midspan give rise to an overestimation of the axial stress concentration at midspan. Spline segments of variable length may be a better solution. In any case, all three choices for the warping distribution along the element axis give results that agree reasonably well with Zhou's model, which matches the analytical solution with regard to the warping displacement distribution along the girder axis. The results lead to the conclusion that the choice of Lagrange polynomials strikes a good balance between accuracy and computational efficiency, so that it will be used in the inelastic response studies of the next chapter. This conclusion is confirmed by the shear-lag coefficient distribution under uniform loading in figure (3.19b).

Figure (3.20) shows the axial stresses in the upper and lower flanges of the box girder section for the proposed model with Lagrange polynomials and with quadratic spline functions over ten segments. The results are compared with the shell finite element model from the study by Zhou [100] and with the experimental measurements from the study by Luo et al. [58]. The results of the proposed model with Lagrange polynomials show very good agreement with the experimental results and with the results of the shell finite element model.

Three-span continuous box girder

The study of the shear-lag effect in the context of a larger and more representative structural model is based on the three-span box girder bridge in figure (3.21). In this case the results of the proposed 3d beam element are compared with the recommendations of the *Eurocode*. Figure (3.21) shows the geometry of the three-span girder with $L = 80$ m, while figure (3.22) shows the geometry of the cross section. The geometry of the girder and the section dimensions derive from earlier studies on the shear-lag effect in [56] and [99]. The linear elastic material of the girder has Young modulus $E = 32.5$ GPa and Poisson ratio $\nu = 0.16$.

The response of the girder is analyzed for a uniform load $q = 1.2 \text{ kN/m}$.

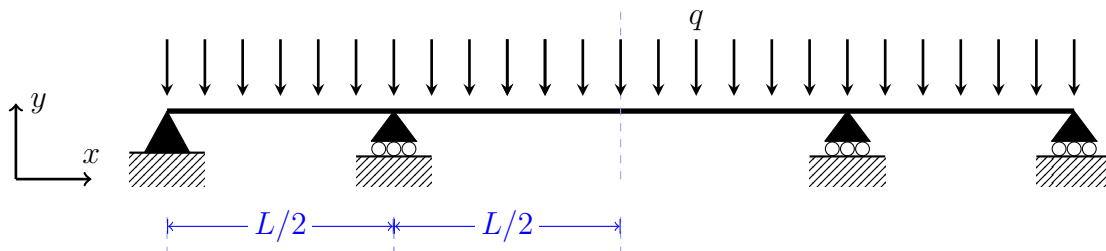


Figure 3.21: Three span continuous box girder bridge

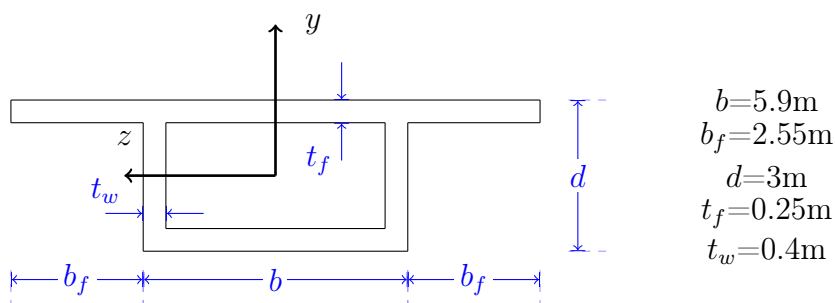
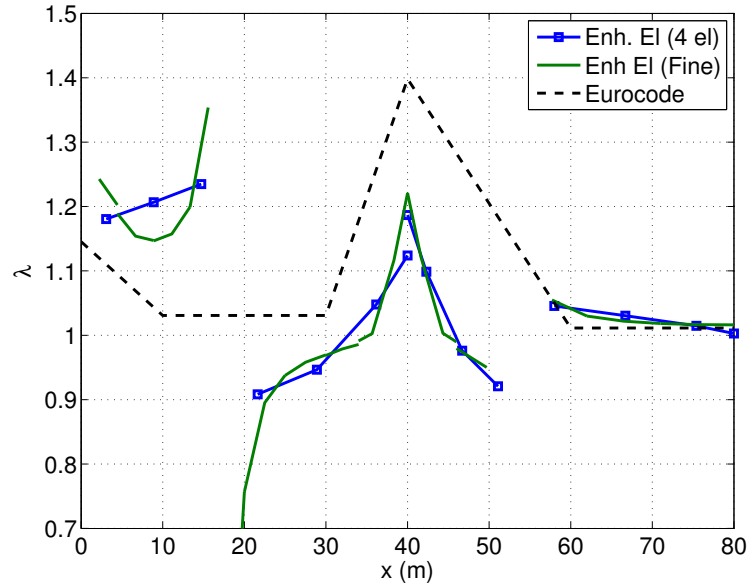


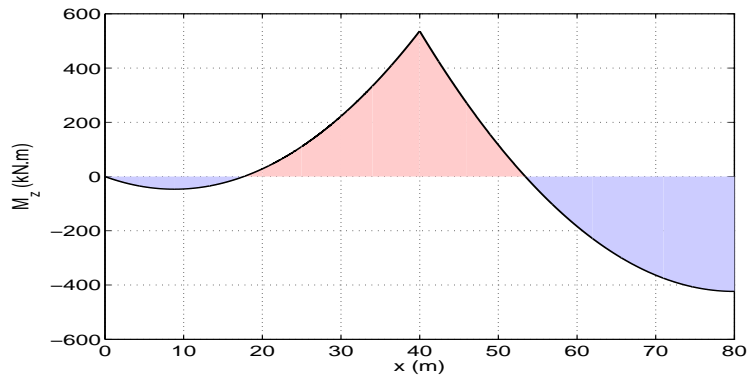
Figure 3.22: Box girder section geometry

The structural model represents only half the structure with a coarse mesh of 4 elements and a finer mesh of 14 elements. The proposed 3d beam element uses $n_w = 16$ warping degrees of freedom for the warping profile of the cross-section according to scheme (g) of table (2.1), and third and fourth order Lagrange polynomials for the warping distribution χ along the girder axis. The warping degrees of freedom at the element nodes are used as global degrees of freedom of the model in order to enforce continuity of the warping displacements between elements. The axial warping stresses are, however, discontinuous, since these are dependent on the derivative of the warping distribution with respect to x .

Figure (3.23) shows the distribution of the maximum shear-lag coefficient λ over half of the three span continuous girder. The maximum shear-lag coefficient arises at the intersection of the upper flange and web. The results of the proposed 3d beam element are compared with the recommendations of Eurocode 3 prEN 1993-1-5 [30]. The shear-lag coefficient for these recommendations is established by taking the ratio of the axial stress for the section with an effective flange width βb_f specified in Eurocode 3 to the axial stress of the full section without shear-lag. The results of the proposed 3d beam element show a similar trend with the Eurocode specifications. For the interpretation of the results in figure (3.23) it is important to note that the axial stress for the proposed element is discontinuous between elements. Moreover, the axial stress of the model that assumes that plane sections remain plane is zero at the points of zero bending moment, so that the shear-lag coefficient in equation (3.7) tends



(a) Maximum shear-lag coefficient distribution along x



(b) Moment M_z distribution

Figure 3.23: Shear-lag coefficient and moment distribution over half of continuous girder

to infinity at these locations. For this reason the moment distribution is depicted directly below the shear-lag coefficient distribution in figure (3.23). Clearly, the most significant shear-lag effect takes place over the middle support, where the bending moment value is large. By contrast, the effect over the outer span is much less significant on account of the small bending moment values.

3.2.3 Torsional response

For the study of torsional response with and without warping constraints the cantilever beam in figure (3.24) with a span of $L = 5$ units is used. A torque T of 1 unit is applied at the free

end of the beam. The cases of free and constrained warping at the fixed end of the cantilever are studied. The response of the cantilever under the concentrated torque T is studied for

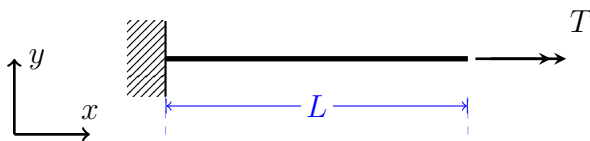


Figure 3.24: Cantilever beam of span $L = 5$ with concentrated torque T

three sections: a wide flange section, a thin-walled box section, and a rectangular section. These are representative of the three section categories of interest: open thin-walled section, closed thin-walled section, and solid cross section, respectively. Details of the section geometry are given in figure (3.25). The cantilever beam model consists of one 3d beam element with

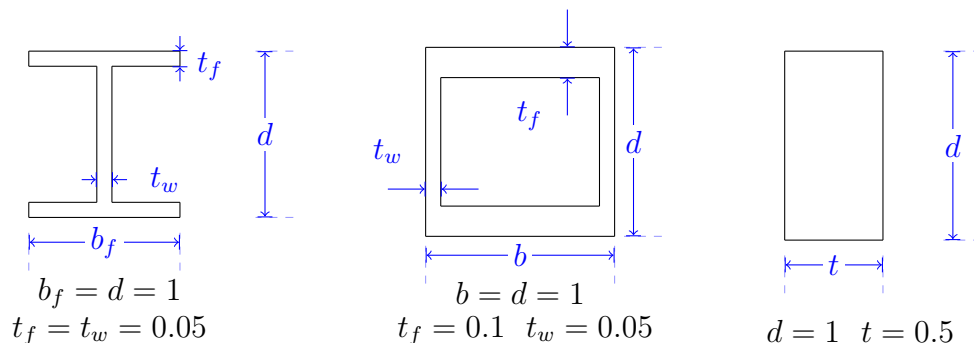


Figure 3.25: Cross section geometries

Lagrange interpolation polynomials for the warping distribution $\chi(x)$ with five interpolation points. For the description of the warping profile of the thin-walled sections two arrangements of the warping degrees of freedom are considered. For the warping profile S1 the degrees of freedom are arranged along the centerline of the flanges and web, as shown in figure (2.1) under case (c) and case (e). The total number of warping degrees of freedom n_w is twelve for both sections. For the warping profile S2, two degrees of freedom are arranged across the thickness of the flanges and the web in order to better represent their warping about the centerline. These arrangements are shown in figure (2.1) under case (d) for the wide flange I-section, and case (f) for the box section with the total number of warping degrees of freedom n_w being 28 for the I-section and 32 for the box section. The warping profile of the rectangular section is represented with a grid of four degrees of freedom over the depth by four degrees of freedom across the width for a total number n_w of 16 parameters. The results of the proposed 3d beam element are compared with the results of the shear beam model in section 3.1.1, with the results of the beam model with a single warping mode in section 3.1.2 using the warping profile of the analytical solution, and with the results of the shell finite

element model described in section 3.1.3. These analyses are conducted with FEDEASLab toolbox under Matlab®-based.

The end twist angle θ of the cantilever beam for these models is reported in table (3.4). The table also contains the value of the end twist angle for the case of St. Venant torsion with free warping according to

$$\theta = \frac{TL}{GJ} \quad (3.11)$$

where J is the polar moment of inertia, and for the case of torsion with constrained warping according to

$$\theta_w = \frac{TL}{GJ} - \frac{T}{GJ} \sqrt{\frac{EI_w}{GJ}} \tanh \left(\sqrt{\frac{GJ}{EI_w}} L \right) \quad (3.12)$$

where I_w is the warping constant of the cross section. The results in table (3.4) lead to the

Case	theory	S1	S2	SW Beam	Shear Beam	Shell Model
I section						
uniform warping	0.1076	0.4590	0.1146	0.1148	0.0006	-
constrained warping	0.0178	0.0218	0.0186	0.0182	-	0.018
Box (10^{-4})						
uniform warping	2.1933	2.4034	2.2840	-	2.1973	-
constrained warping	2.1933	2.3787	2.2423	-	-	2.4020
Rect (10^{-4})						
uniform warping	4.548	4.697	-	-	2.535	-
constrained warping	4.548	4.554	-	-	-	-

Table 3.4: End twist angle θ for cantilever beam under end torque T

following observations:

1. There are no values for the shear beam model for constrained warping, because this model does not include warping displacements.
2. There are no values for the beam with a single warping mode for sections with complex warping profiles, such as the tubular box and the solid rectangle. Such profiles need to be established first from the linear elastic solution of the problem.
3. There are no values for the shell model for cases with free warping, because of the difficulty to apply a concentrated torque to a shell model without restraining the warping displacements.

4. The theoretical solution for the tubular box and the solid rectangular section gives practically the same result for free and constrained warping, because the warping constant I_w for these sections is very close to zero.
5. The results of the shear beam model agree very well with the theoretical values only for the case of the thin-walled box section, where the warping effect is negligible. For the open thin-walled section, which is very sensitive to warping, the shear beam element overestimates the stiffness significantly. The result of the shear beam model is also inaccurate for the solid rectangular section, for which warping is also important.
6. The shell model, the proposed beam element with S1 and S2 discretization of warping and the SW beam give end twist angle values that are higher than the theoretical solution, because of the more accurate representation of the added beam flexibility due to warping.
7. The ability of the shell model to describe accurately the torsional response of thin-walled beams with warping is limited, because of its inability to capture the warping about the flange and web centerline, and the difficulty of representing accurately the transition zone between flange and web. This is evident in the results for the tubular box section.
8. The proposed beam element with S2 discretization of warping gives end twist angle values that are consistently smaller than the S1 discretization, because of the added stiffness from the warping about the flange centerline that the S2 discretization captures in contrast to the S1 discretization which does not.
9. The beam with a single warping mode gives relatively accurate results for the thin-walled open section, because the assumed warping profile is the same as the warping profile of the theoretical solution.
10. The proposed element with warping profile S1 gives results of sufficient accuracy for many practical problems except for the case of the I-section with uniform warping for which the value of the end angle of twist is significantly overestimated. It is possible that the process of improving the condition number of the stiffness matrices in section 2.5.1 was not effective in this simulation.
11. The proposed element with warping profile S2 agrees very well with the theoretical results for the thin-walled sections.
12. The proposed element agrees very well with the theoretical results for the rectangular section. The torsion constant J for the theoretical solution of St. Venant torsion without warping constraint is not based on thin-walled theory, but is derived with the help of Fourier series according to [84]. The discretization with 16 warping degrees of

freedom seems to be sufficient for the case with constrained warping, but slightly less so for the case with free warping, where more warping parameters may be required.

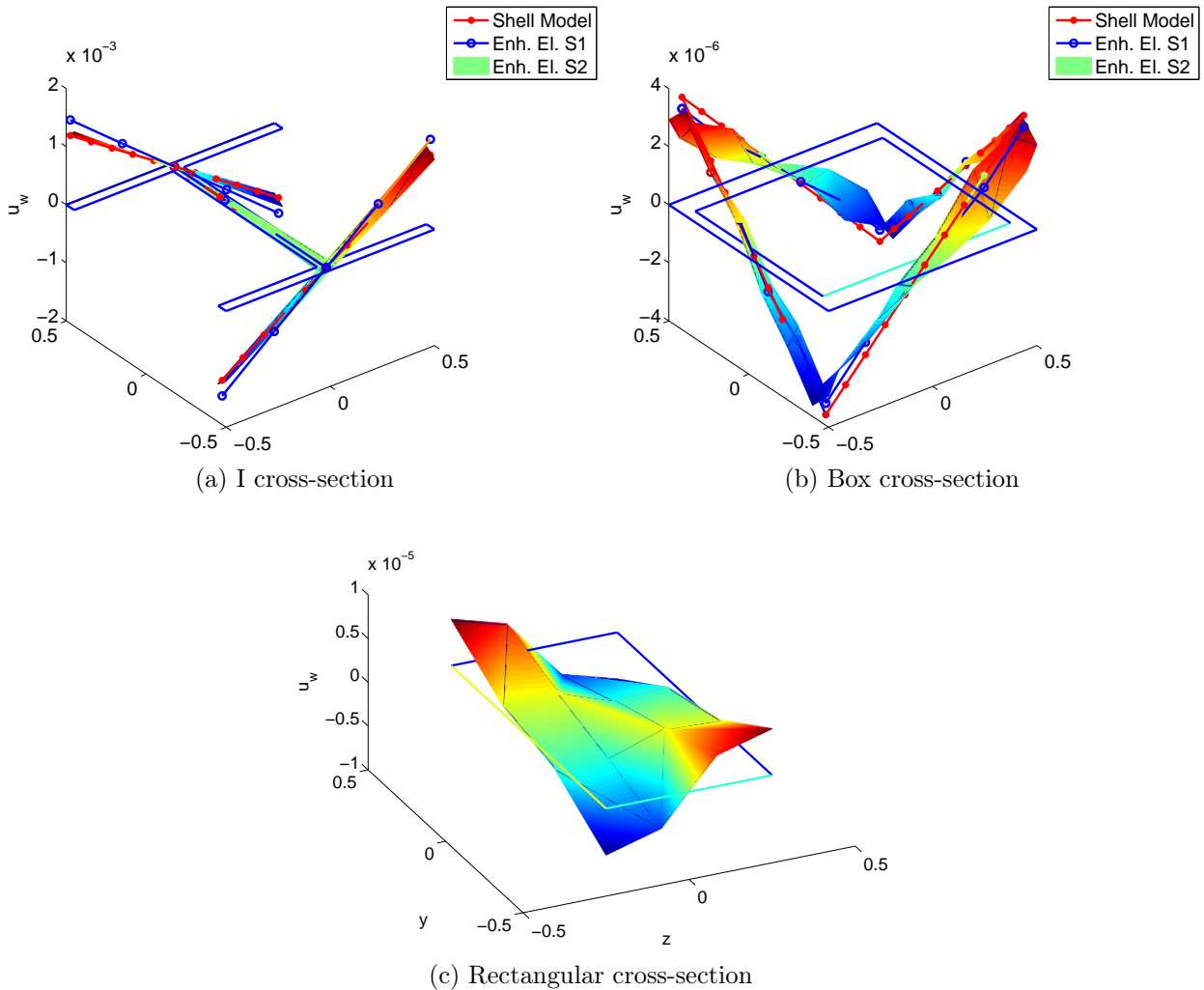


Figure 3.26: Warping profile at free end of cantilever beam

The warping profiles of the thin-walled wide-flange and tubular box section at the free end of the cantilever beam are shown in figure (3.26). The figures show the results of the shell finite element model and of the profiles S1 and S2 for the proposed 3d beam element. The warping profiles of the shell finite element model and of case S1 refer to the centerline of the section profile, whereas case S2 is able to represent the warping of the section across the thickness of the flanges and the web. The agreement of the warping displacements between the shell model and the proposed 3d beam model is very good for either S1 or S2 warping

profile. Figure (3.26c) shows the warping profile of the rectangular cross-section with the proposed 3d beam element with 16 warping degrees of freedom per section.

Figures (3.27)-(3.28) compare the results of the different models for the thin-walled wide flange section in more detail. Figure (3.27) shows the distribution of the twist angle over the cantilever beam axis for the case that warping is constrained at the fixed end.

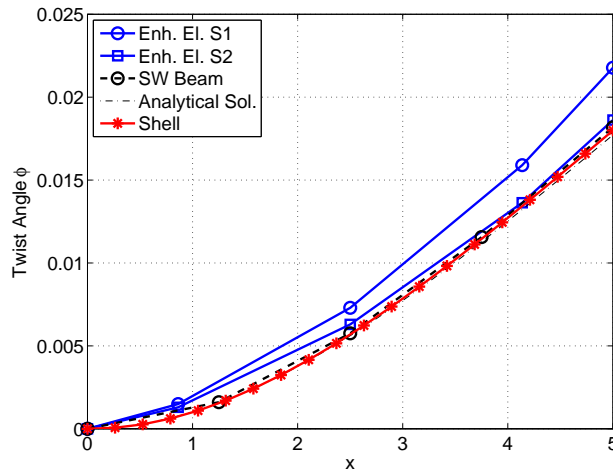


Figure 3.27: Twist angle distribution for cantilever with I-section under warping constraint

The beam model with a single warping mode and the proposed beam element with warping profile S2 match the analytical solution and the results of the shell finite element model very well. The use of Lagrange polynomials with 5 interpolation points for the warping displacement distribution is sufficient for this problem.

It is worth noting that the twist angle value is available only at the integration points of the proposed element, with no information about its distribution along the element. The markers for the SW beam model correspond to the twist angle values at the end nodes of the four elements used for the cantilever, without invoking the available displacement interpolation function for a more accurate representation of the twist angle distribution over each element.

Figure (3.28) shows the local response of the cantilever beam in terms of the axial and shear stress profile in the lower flange. Figure (3.28a) shows the axial stress profile in the lower flange at the fixed end of the cantilever under constrained warping. The axial stress distribution is practically linear over the flange. The agreement between the proposed beam element with warping profile S2 and the shell model is excellent. The same is true for the beam model with a single warping mode, because it uses the analytical solution for the warping displacement profile. The axial stresses are zero at the free end of the cantilever.

Figures (3.28b) and (3.29) show the shear stress profile at the fixed end and at the free end of the cantilever, respectively, for the case that warping is constrained at the fixed end. The values correspond to the average transverse stress σ_{xz} over the flange thickness. The beam

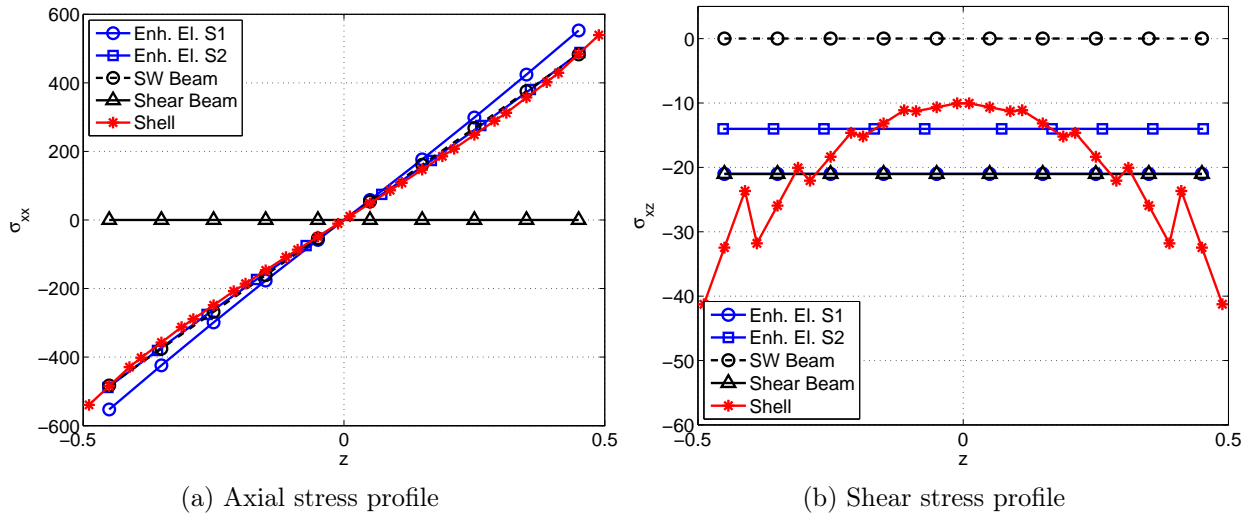


Figure 3.28: Stress profile in lower flange of fixed cantilever end under warping constraint

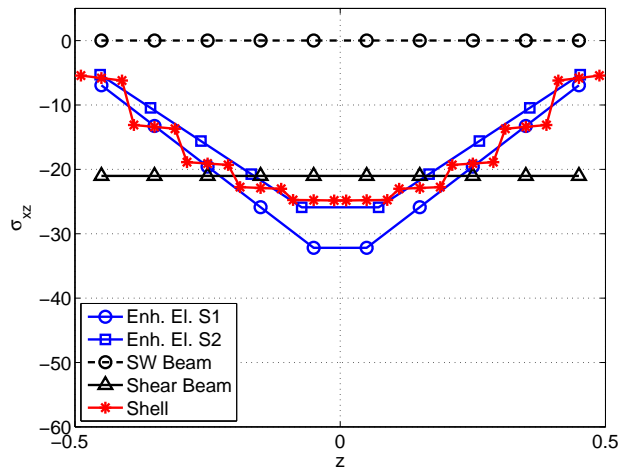


Figure 3.29: Shear stress profile in lower flange of free cantilever end

model with a single warping mode results in zero average stress, because of the underlying assumption for the warping profile. The shear beam model gives the same constant shear stress distribution at both sections on account of the constant shear force. The proposed 3d beam element gives a constant shear distribution at the fixed end under constrained warping, and a piece-wise linear distribution at the free end, which agrees very well with the results of the shell model. The constant shear stress at the fixed end is related to the following kinematic assumption of the proposed element: the shear stress at the fixed end section

$x = 0$ is

$$\begin{aligned}\epsilon_{xy} &= \gamma_y + \frac{\partial \mathbf{u}^w}{\partial y} \\ &= \gamma_y + \frac{\partial \psi}{\partial y} \sum_i \chi_i(x=0) \mathbf{u}_i^w\end{aligned}$$

With the definition for the warping distribution functions that $\chi_i(x=0) = \delta_{i0}$, where δ is the Dirac delta-function, and with the boundary condition that $\mathbf{u}_0^w = \mathbf{0}$ at the fixed end, the above equation leads to $\epsilon_{xy} = \gamma_y$.

Chapter 4

Evaluation for inelastic material response

This chapter discusses the validation of the proposed 3d beam element under inelastic material response. To this end the results of the model are compared with experimental measurements of the response of steel shear links under monotonic and cyclic loading and with the results of solid and shell finite element models. The shear links have wide flange I-section and tubular box section. The warping constraint of the thin-walled sections gives rise to an interaction between high shear and torsion, which is investigated in detail in one example.

4.1 Shear link with tubular box section

The first correlation study refers to the tubular shear link of Berman and Bruneau [13] that forms part of a one story eccentrically braced frame specimen. Details of the test setup, of the instrumentation and of the available experimental measurements can be found in the report by Berman and Bruneau [12]. The shear link length L and specimen geometry are shown in figure (4.1). The geometry of the tubular box section of the shear link is given in figure (4.2a). The specimen was designed so that the shear link is subjected to large inelastic deformations without experiencing local buckling. To this end two stiffeners are positioned along the shear link length L of 456 mm, as shown in figure (4.3a). The shear link was subjected to cycles of gradually increasing inelastic deformation by controlling the horizontal translation of the one story specimen.

Because the shear deformation γ of the link is available from the measurement of the relative transverse displacement U of the link ends during the experiment, the simulation model represents only the link, as shown in figure (4.2b). The boundary conditions of the 3d simulation model in figure (4.2b) are such as to allow for the axial deformation of the shear link, while ensuring that it deforms in the $x - y$ plane in the figure. Furthermore, all rotations and the warping displacements are restrained at both ends. The assumption of constrained warping is justified by the presence of stiffeners in figure (4.3a).

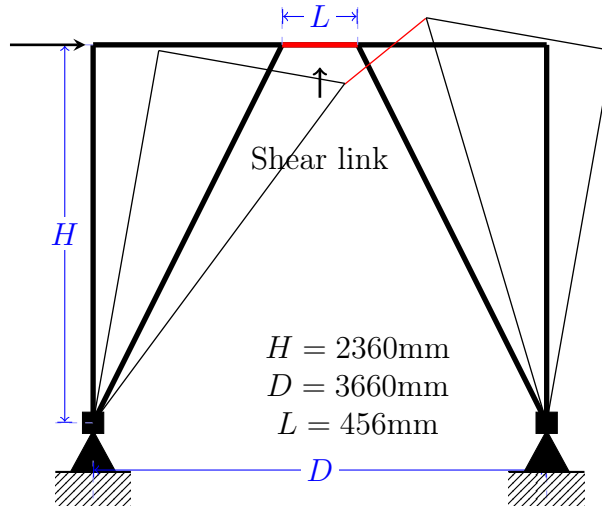


Figure 4.1: Eccentrically braced frame specimen by Berman and Bruneau [12]

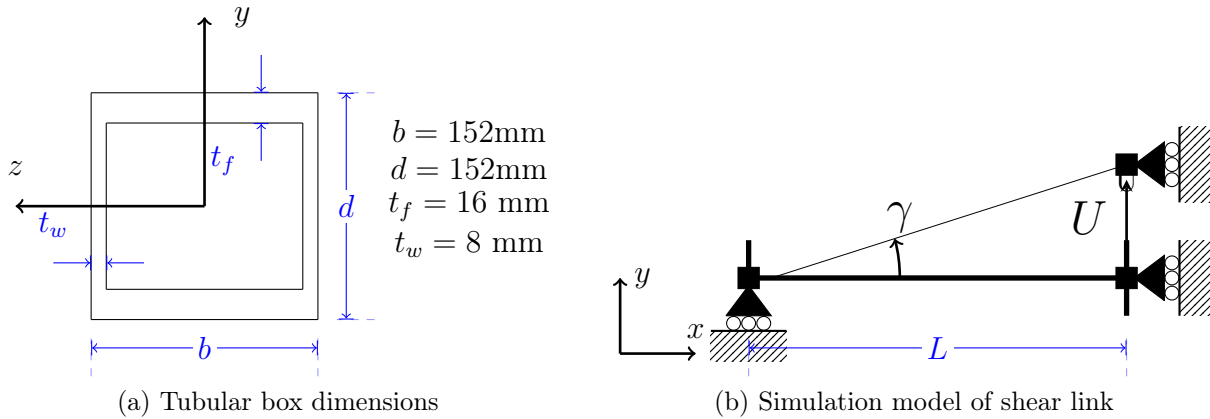
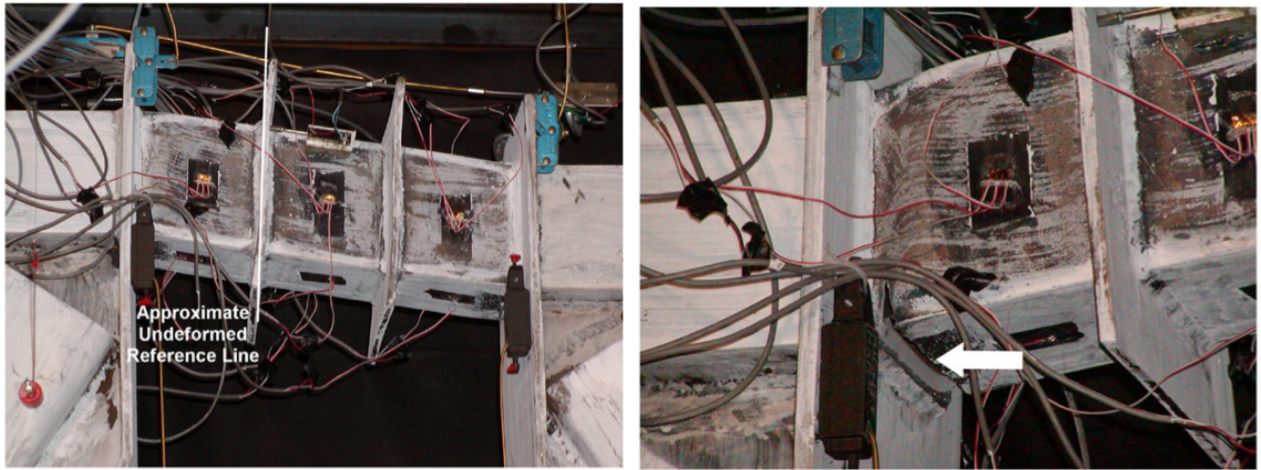


Figure 4.2: Shear link section dimensions and simulation model

The material properties of the structural steel specimen were established by coupon tests, as reported in [13]. The steel yield strength in the web and flange are 448 MPa and 393 MPa, respectively. The elastic modulus E is equal to 200 GPa. These properties are used in the steel material model for the simulations, which is based on classical J2 plasticity. The model assumes an isotropic hardening modulus of $0.001 E$ and a kinematic hardening modulus of $0.01 E$, because these values result in good agreement with the observed cyclic behavior of the steel coupons.

The correlation studies with the experimental results are based on three element types: (a) beam models for the shear link, (b) shell finite elements for the web and flange of the shear link, and (c) solid finite elements for the web and flange of the shear link. Some features of these models are briefly discussed in the following along with the specification of



(a) Deformed shear-link

(b) Crack in shear-link

Figure 4.3: Shear link with tubular box section at failure from [13]

key model parameters.

The first type of model uses a single beam element for the entire link. Two beam models are compared with the experimental measurements: the *shear beam* element by Saritas extended to 3d, as described in section 3.1, and the proposed 3d beam element with warping degrees of freedom described in chapter 2. The element response is based on numerical integration with 5 Gauss-Lobatto integration points over the shear link. The section response is based on numerical integration with the midpoint rule using 12 integration points for each web, and four integration points across the flange thickness and 6 integration points across the flange width for a total of 24 integration points for each flange. The warping profile of the proposed 3d beam element is represented with $n_w = 12$ warping degrees of freedom in the arrangement of case (e) in figure (2.1).

The second type of model makes use of plane stress shell finite elements for each web and flange of the shear link. The 4-node shell finite element is based on the formulation with Mixed Interpolation of Tensorial Components (MITC) by Bathe and Dvorkin [4] and was implemented in FEDEASLab [28]. A finite element mesh of 8x20 shell finite elements was used for each web and flange of the tubular box section of the shear link. The aspect ratio of the shell elements ranged from 1.4 to 2.9.

The third type of model makes use of solid finite elements for each web and flange of the shear link. The eight-node solid finite element with mixed formulation of program FEAP [91] was used for the purpose. To reduce the size of the model only half of the shear link was represented under consideration of symmetry. The finite element mesh consisted of 20 elements across the width of the flange and web and 30 elements across the length of the specimen. 2 solid elements were used across the thickness of the flange, and only 1 element

across the thickness of the web. The largest aspect ratio of the 8-node solid elements was 1.3.

The number of elements and degrees of freedom for the modeling alternatives of the shear link is summarized in table (4.1). The beam formulations make use of six section deformation variables. These internal variables play an important role in the iterative element state determination and are, therefore, listed as free local degrees of freedom in table (4.1). Both beam elements monitor the section deformations at each integration point resulting in thirty internal variables. In addition, the proposed 3d beam element includes twelve warping degrees of freedom at each internal section of the element, so that the total number of local variables in this case is sixty-six. The warping displacements are constrained to zero at the end sections of the element to simulate the boundary conditions of the shear link.

	Shear beam	Proposed beam	Shell FE model	Solid FE model for half link
No of elements	1	1	640	3840
Global dofs	12	12	672	43524
Local dofs	30	66	-	-

Table 4.1: Number of elements and degrees of freedom for different models of shear link

An important aspect of the shear link model concerns the modeling of the intersection of the web with the flange. In the beam models the intersection is treated as part of the web when assigning material properties and making assumptions about shear strain or stress distribution. In the shell model of the shear link the intersection of the flange and web is represented by a single line of nodes along the shear link axis. The horizontal shell elements are assigned the material properties of the flange, and the vertical shell elements are assigned the material properties of the web. In the solid finite element model, the intersection of the web and flange is assigned the properties of the web material. It turns out that the modeling of the web-flange intersection has very little influence on the response of the shell and solid finite element models. By contrast, the assumptions of material properties and shear strain or stress distribution are of some significance for the response of beam elements.

None of the models represents the intermediate stiffeners along the shear link. These ensure that the cross section retains its shape without deforming in its plane, an important kinematic assumption for the beam models. Furthermore, the stiffeners delay the occurrence of local buckling, which is not accounted for in any model.

The models were subjected to the displacement history of the specimen with the same time step increment. Figure (4.4) shows the hysteretic relation between shear force and resulting shear link deformation γ for the first three loading cycles. The analytical results refer to the shear beam model, the proposed beam model and the shell finite element model.

The latter failed to converge under the selected time step increment after two and a half cycles. The agreement of the analytical results of the proposed beam element and of the shell finite element model with the experimental measurements is very good. The results of the shear beam element slightly overestimate the shear link strength. These results are corroborated in figure (4.5), which shows the force-deformation relation of the shear link before the first deformation reversal. The response of the proposed beam element agrees very well with the response of the shell finite element model. The solid finite element model displays a slightly higher stiffness than these two models before the formation of the yield mechanism, but agrees very well with the yield strength and post-yield response of these two models. Finally, the shear beam model agrees well with the solid finite element model before the formation of the yield mechanism, but overestimates the shear link strength relative to the other three models by 8-10%. The strength overestimation is due to the assumption that the shear stress profile of the web extends over the entire depth of the tubular box-section.

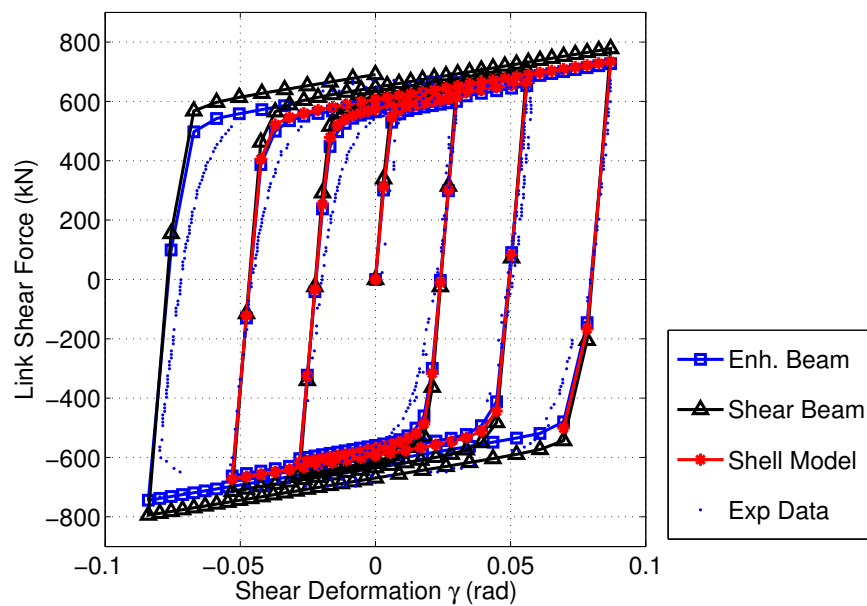


Figure 4.4: Shear force vs. deformation γ of shear link with tubular box section

In order to study the response sensitivity of the shear link to the assumption of the end warping constraint the analysis with the proposed beam element was repeated for the case that the end sections are free to warp. For this case the yield strength of the model was 3% smaller than for the case with restrained warping.

For the study of the stress profiles at different sections of the shear link, four load points of the shear link response in figure (4.4) are selected. The load points (LP) are labeled A, B, C and D. The shear deformation at each load point is the same between the models, but the corresponding shear force varies from model to model, as shown in table (4.2). The load

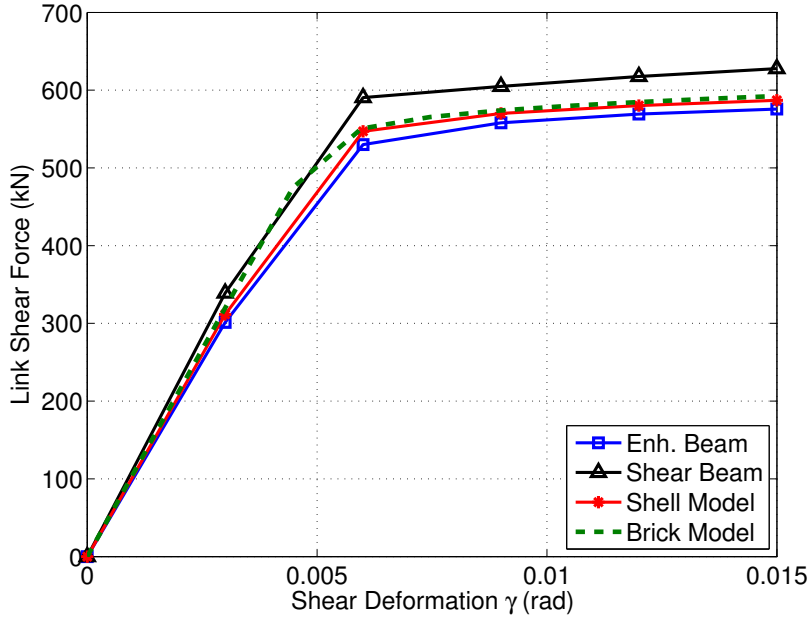


Figure 4.5: Shear force vs. deformation γ of shear link before first reversal

points correspond to different stages of the shear link response: load point A corresponds to the initial elastic response, load point B corresponds to the first inelastic excursion past the yield strength, point C corresponds to the inelastic excursion after the first load reversal, and point D corresponds to the elastic unloading after the third inelastic excursion (third half cycle).

LP	γ (10^{-2})	Beam	Shear beam	Shell FE model	Solid FE model
A	0.30	301	338	311	317
B	0.90	558	605	570	574
C	-1.12	-577	-632	-590	-
D	4.48	-412	-482	-444	-

Table 4.2: Shear force of models at specific load points (LP) of shear link response

The stress profiles are studied at the end section of the shear link at $x = 0$, which is fixed against rotation in the plane of the model with warping displacements restrained. The stress profiles are also studied at the midspan section of the link at $x = L/2$. At this section the normal stresses σ_{xx} are zero by symmetry considerations.

Figures 4.6 through 4.9 show the shear stress profile σ_{xy} in the web and the shear stress profile σ_{xz} in the lower flange first for the midspan section in (a) and (b), and then for the

fixed end section in (c) and (d). Finally, the figures show the axial stress profile in the web and lower flange in (e) and (f). The stress values are determined at the section integration points and are averaged over the thickness of the web or flange. Figures 4.6 and 4.7 for load points A and B, respectively, also include the stress profiles for the solid finite element model, which are not available for load points C and D in figures 4.8 and 4.9, respectively. For the comparison of the stress profiles it is important to note that the shear force of the shear beam model is consistently 6-7% higher than the corresponding value for the shell finite element model, and that the shear force of the proposed 3d beam element is consistently 2-3% lower than that of the shell model except for load point D where it is 8% lower. It is also important to note the difference between 3d beam model and shell model in the modeling of the zone between flange and web, evident in the marker location for the shear and axial stress profiles in figures 4.6-4.9 (b) and (f). The outermost marker of the profiles for the 3d beam model at $z = \pm 56.6$ corresponds to the outermost of six integration points across the clear flange width of $152 - 2 \times 8 = 136$. The outermost marker of the profiles for the shell FE model corresponds to the outermost of 24 integration points across the flange width of $152 - 8 = 144$ to the centerline of the web.

The stress profiles in Figures 4.6 through 4.9 permit the following observations:

1. The shear stress and axial stress profiles for load point A in the linear elastic range are shown in figure (4.6). The shear stress profile at midspan is parabolic over the web and linear over the flange width in figures (4.6a-4.6b). The assumed shear stress profile of the shear beam model over the web agrees well with that of the shell model in (4.6a). The shear beam model, however, does not account for the shear stress profile over the flange width and the stress σ_{xz} is zero in figure (4.6b). This is the limitation of beam elements with a fixed shear stress profile not accounting for the shear flow between flange and web. The response of the proposed beam element follows the trend of the shell model: the parabolic distribution in the web is slightly different from the shell model distribution in figure (4.6a) due to the transition of the shear stresses across the web-flange intersection. Noting that the web thickness is half the thickness of the flange, the nodal force equilibrium in the shell FE model results in a discontinuous shear stress at the transition from the web to the flange. In the proposed beam element the change of thickness in the transition from the web to the flange is accounted for in the evaluation of the section response and the shear stress remains continuous at the transition from the web to the flange.

At the fixed end of the shear link the shear beam element gives the same shear stress profile in the web and flange as for the midspan section in figures (4.6c) and (4.6d), since the shear force is constant. By contrast, the proposed 3d beam element gives a constant shear stress profile in the web in excellent agreement with the shell finite element model in figure (4.6c), noting the slightly higher shear force value for the latter in table (4.2). This profile also agrees well with the solid finite element model except in the vicinity of the flange, where the solid model shows a sudden reduction in the

shear stress due to the shear flow transition that is not present in the proposed model and in the shell finite element model. The shear stresses in the lower flange are zero in figure (4.6d) for the proposed 3d beam element in good agreement with the results of the solid FE model, whereas the shell model shows a small shear stress near the tip of the flange.

The axial stress profile at the fixed end of the shear link is shown in figures (4.6e) and (4.6f). The stress profile of the shear beam follows the assumption of plane sections and is linear in the web and constant across the width of the flange. The proposed 3d beam element accounts for the nonlinear stress profile over the depth of the web and across the flange width due to the warping constraint. The axial stress profile of the proposed beam element agrees very well with the profiles of the shell and solid FE models with the maximum and minimum stress values in excellent agreement. The highest axial stress arises at the intersection of web and flange in figure (4.6f). This value is on the order of 40% larger than the axial stress of the shear beam element at the same location.

2. The shear stress and axial stress profiles for load point B in the inelastic range are shown in figure (4.7). At the midspan section the web reaches the yield strength of $\sigma_y/\sqrt{3} = 260$ MPa over its entire depth in figure (4.7a). The web shear stress profile of the proposed 3d beam element agrees well with the shell model and the assumed shear stress profile of the shear beam. The shear stress profile in the flange is linear in figure (4.7b) for the proposed 3d beam element and the shell model with good agreement of extreme values between them.

At the fixed end section, the web shear stress profile in figure (4.7c) differs from that at the midspan section, because of the presence of axial stresses. The profiles of the proposed 3d beam element and the shell model show very good agreement. By contrast, the fixed shear stress profile of the shear beam model disagrees with the other models in the zone of the web near the flange, where the axial stress is significant. The shear stresses in the lower flange are zero in figure (4.7d) for the proposed 3d beam element in good agreement with the results of the solid FE model, whereas the shell model shows a small shear stress near the tip of the flange.

The axial stress profile in the web and lower flange is shown in figures (4.7e) and (4.7f), respectively. The profile of the proposed 3d beam element captures very well the highly nonlinear distribution over the depth of the web matching almost perfectly the profile of the shell and solid FE model in figure (4.7e). By contrast, the shear beam element produces a linear axial stress profile, because of its assumption that sections remain plane after deformation. The axial stress profile of the proposed 3d beam element over the flange captures relatively well the shear lag effect under inelastic response and agrees reasonably well with the shape of the distribution of the shell and solid FE model, but does not match as well the minimum value at mid-distance between

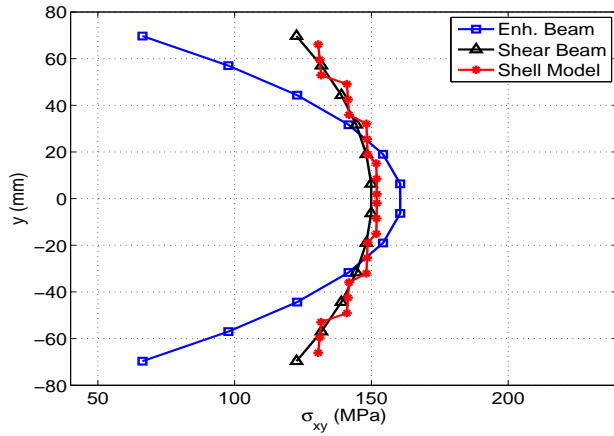
the webs ($z = 0$) in figure (4.7f). The axial stress of the shear beam model at the intersection of the web and flange is not the same in figures (4.7e) and (4.7f), because the presence of high shear stresses in the web limits the axial stress value at yield. By contrast, the shear stress is zero in the flange and the axial stress is much higher as a result. The other three models show a smooth transition of the axial stress value from the flange to the web in figures (4.7e) and (4.7f).

3. The shear stress and axial stress profiles for load point C in the inelastic range after the first load reversal are shown in figure (4.8). The shear stress profiles at the midspan section in figures (4.8a) and (4.8b) look similar to those for load point B except for the sign of the stresses. The same is true for the shear stress profiles at the fixed end section in figures (4.8c) and (4.8d).

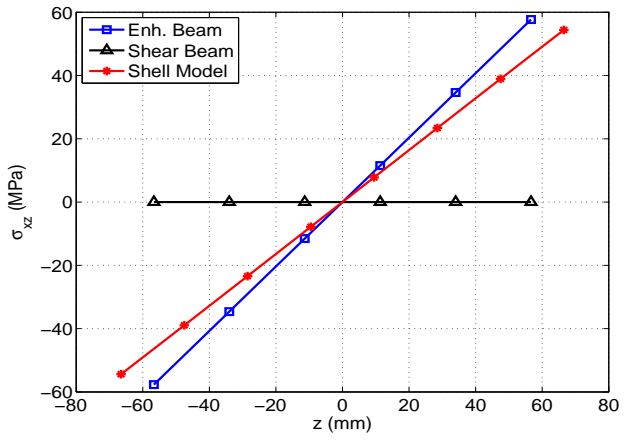
The axial stress profiles at the fixed end section are shown in figures (4.8e) and (4.8f). The axial stress profile of the shell model in figure (4.8e) shows that the stress is zero over most of the depth, but rises rapidly near the flange. The Lagrange polynomials for the stress profile of the proposed 3d beam element are unable to follow the abrupt change of the profile and produce an oscillatory distribution, while matching the extreme values of the shell model very well. As is the case in load points A and B, the linear axial stress distribution of the shear beam model in the web is not affected by the presence of high shear stresses. The axial stress profile of the shell model in the flange is shown in figure (4.8f). It shows a marked shear lag effect, which the proposed 3d beam element is not able to capture in this case.

4. The shear stress and axial stress profiles for load point D in the elastic unloading branch after the third inelastic excursion are shown in figure (4.9). The observations about the different models are similar to those made for the other load points. The agreement of the axial stress profiles for the proposed 3d beam element and the shell model is very satisfactory in figures (4.9e) and (4.9f). The highly nonlinear axial stress distribution and the pronounced shear lag effect is captured very well by these models. Excellent agreement between these models can also be observed for the web shear stress profile in figure (4.9c), particularly when accounting for the difference in total shear in table (4.2).

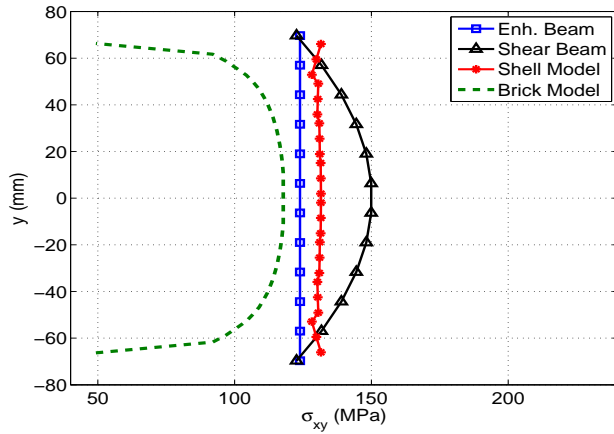
In conclusion, the study of the local response of the shear link with tubular box section under cyclic deformation reversals demonstrates the ability of the proposed 3d beam element to match well the shear and axial stress profiles of the shell model in the web and flange of the cross-section, with a computational cost that is at least an order of magnitude lower. The proposed 3d beam element provides much more accurate information about the local stress response than the shear beam model with fixed shear stress profile.



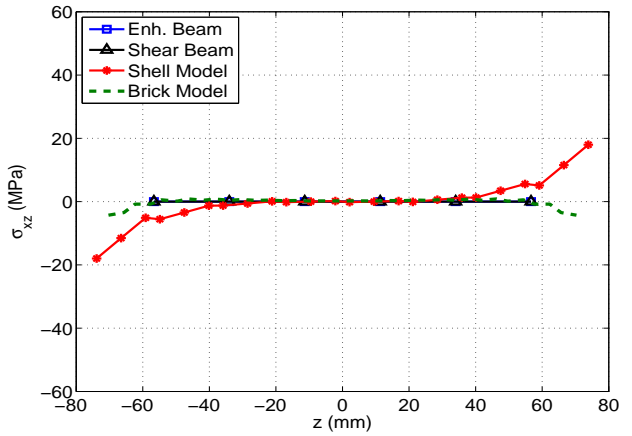
(a) Shear stress in web at midspan



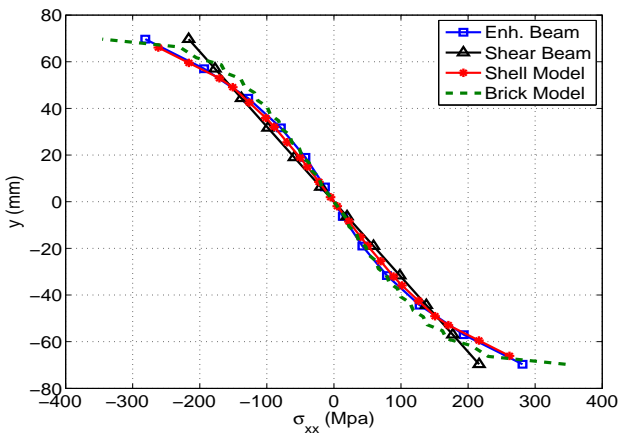
(b) Shear stress in lower flange at midspan



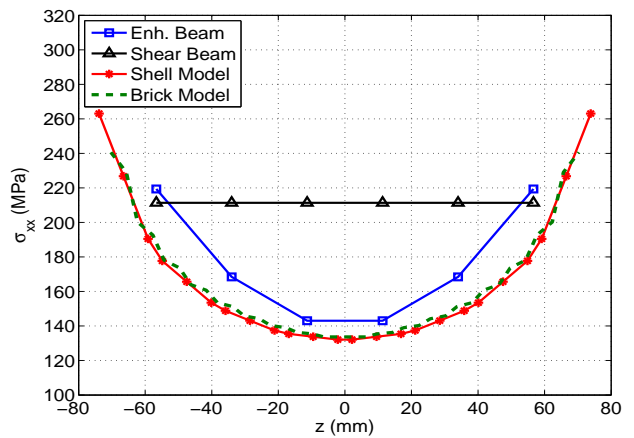
(c) Shear stress in web of fixed end



(d) Shear stress in lower flange of fixed end

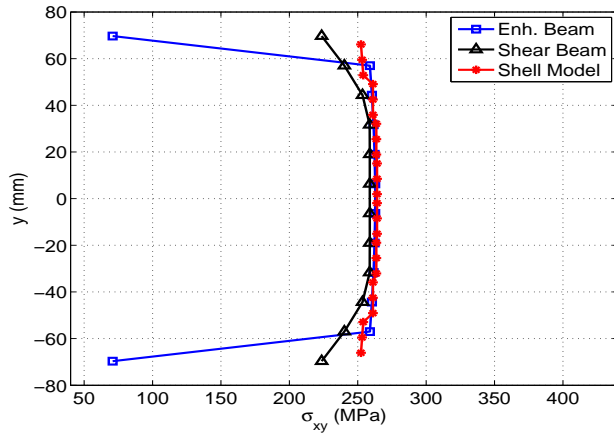


(e) Axial stress in web of fixed end

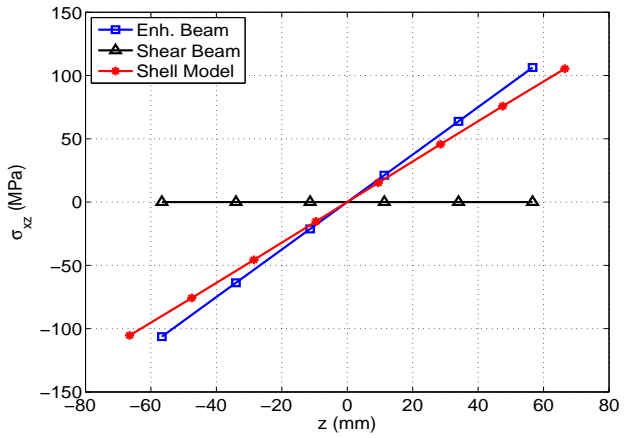


(f) Axial stress in lower flange of fixed end

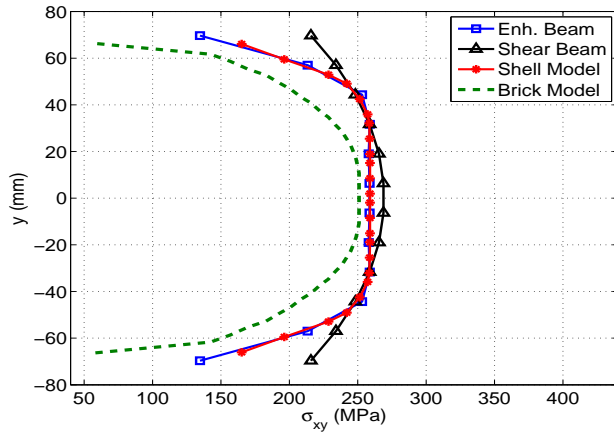
Figure 4.6: Stress profiles of shear link with tubular box section at LP A



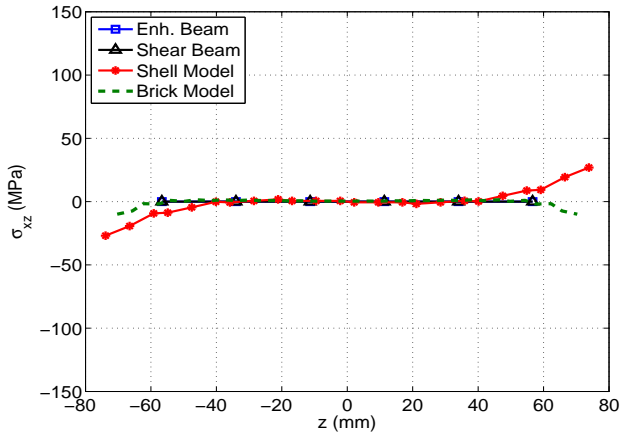
(a) Shear stress in web at midspan



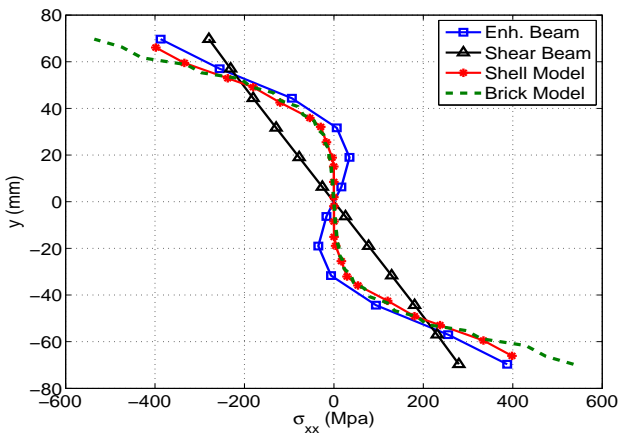
(b) Shear stress in lower flange at midspan



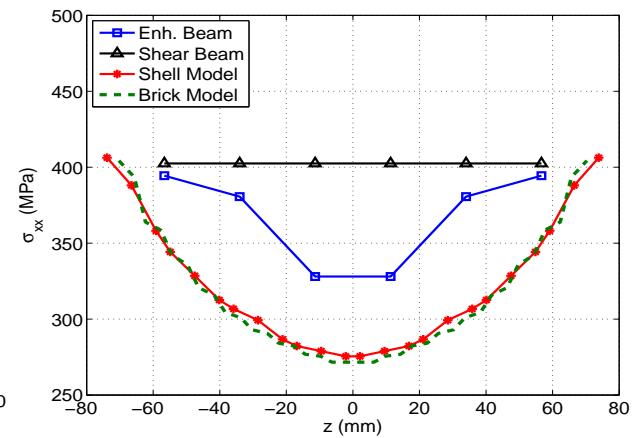
(c) Shear stress in web of fixed end



(d) Shear stress in lower flange of fixed end

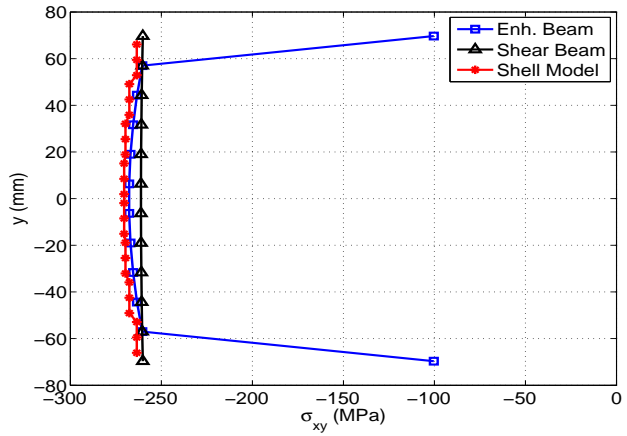


(e) Axial stress in web of fixed end

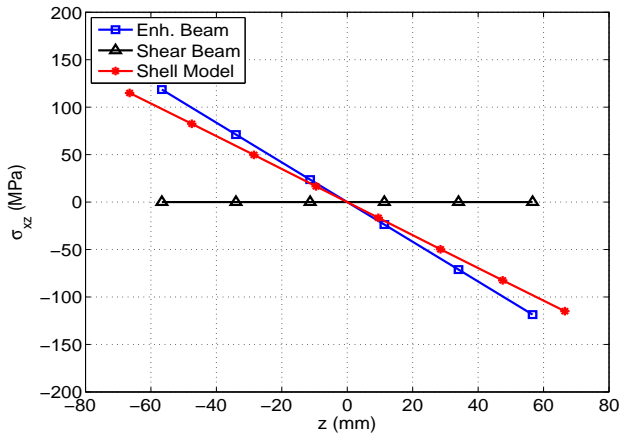


(f) Axial stress in lower flange of fixed end

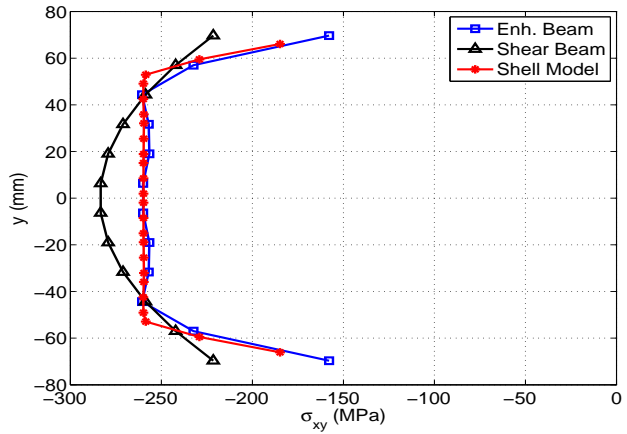
Figure 4.7: Stress profiles of shear link with tubular box section at LP B



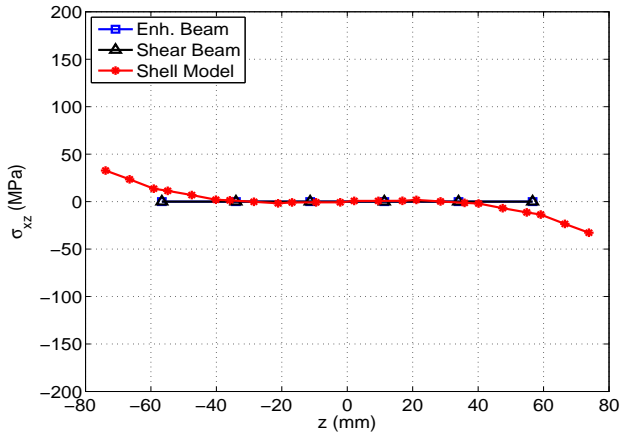
(a) Shear stress in web at midspan



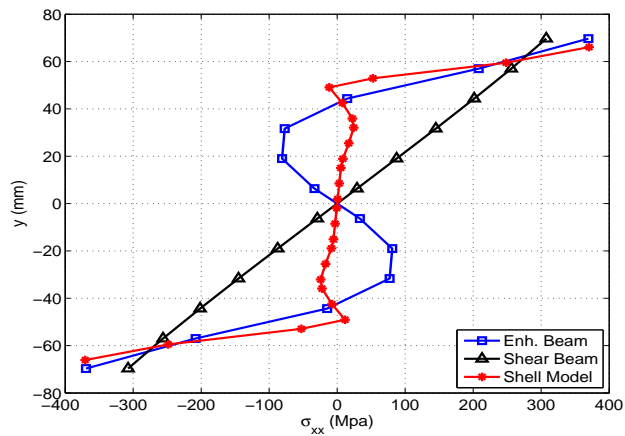
(b) Shear stress in lower flange at midspan



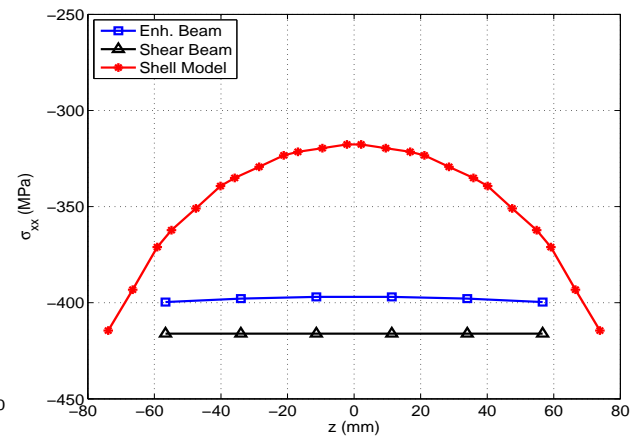
(c) Shear stress in web of fixed end



(d) Shear stress in lower flange of fixed end

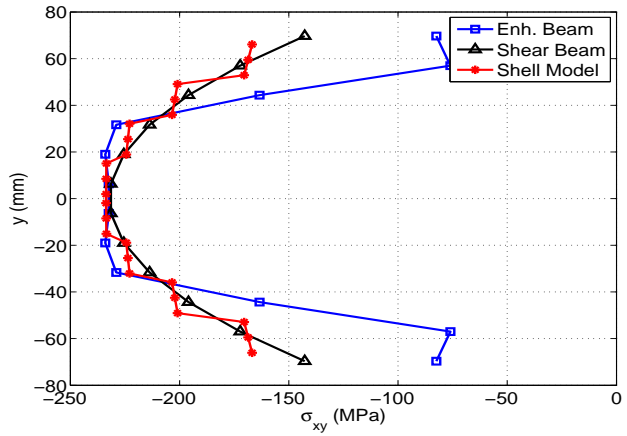


(e) Axial stress in web of fixed end

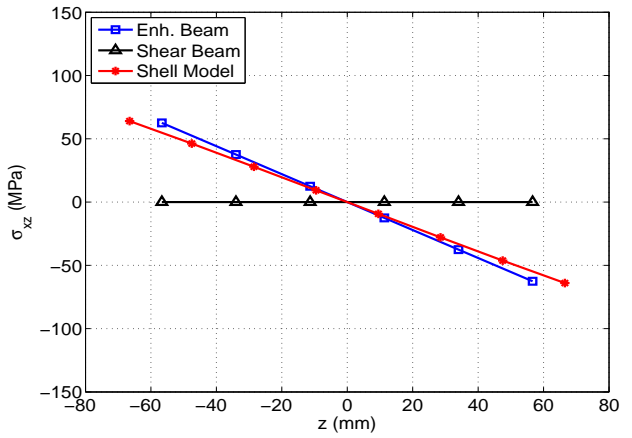


(f) Axial stress in lower flange of fixed end

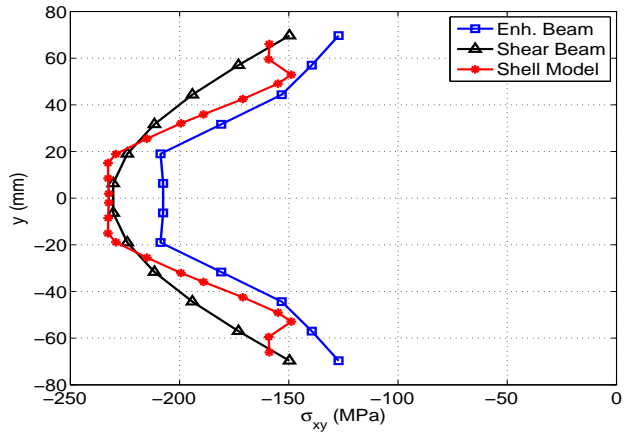
Figure 4.8: Stress profiles of shear link with tubular box section at LP C



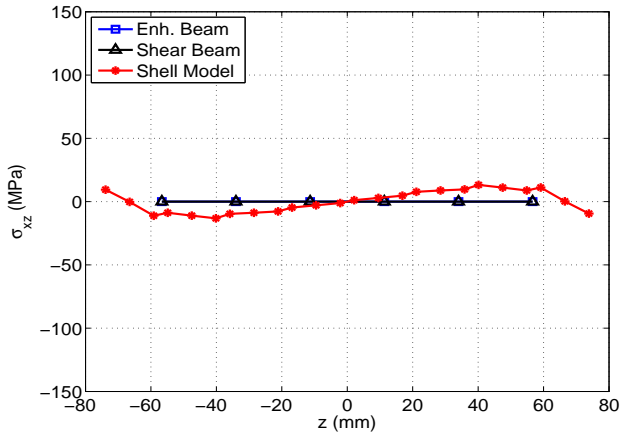
(a) Shear stress in web at midspan



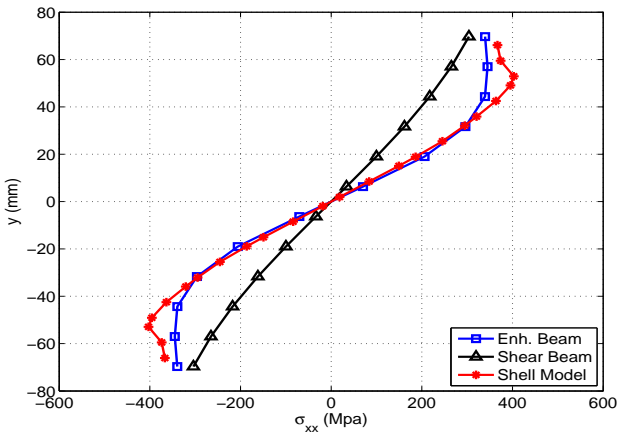
(b) Shear stress in lower flange at midspan



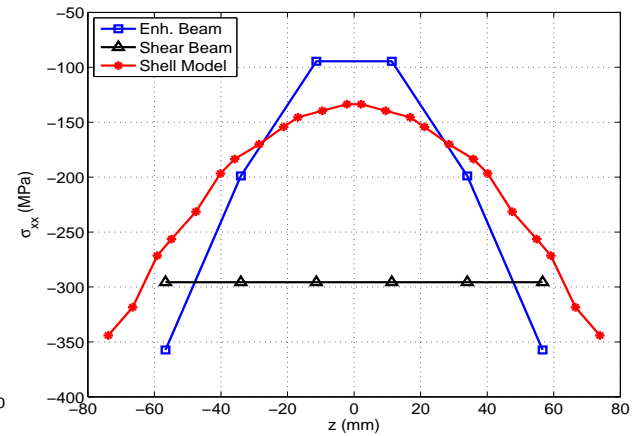
(c) Shear stress in web of fixed end



(d) Shear stress in lower flange of fixed end



(e) Axial stress in web of fixed end



(f) Axial stress in lower flange of fixed end

Figure 4.9: Stress profiles of shear link with tubular box section at LP D

A limitation of the proposed 3d beam element lies in the representation of the shear lag effect under large inelastic deformation. The axial stress profile is qualitatively correct in figure (4.7f) but the axial stress variation is underestimated by about 35%. The discrepancy of the axial stress profile in the lower flange between proposed 3d beam element and shell model is very pronounced in figure (4.8f). It is encouraging that the discrepancy reduces upon repetition of the inelastic deformation in figure (4.9f) with good agreement between the proposed element and the shell model. The cause of the discrepancy of the axial stress profile in the flanges at particular load points is not well understood and requires further study. In general, the good agreement in the stress profiles between the proposed element on the one hand and the shell and solid FE model on the other confirms the validity of the assumptions of the proposed element regarding section kinematics and plane stress conditions in the web and flanges.

The experimental study reports that failure of the shear link was observed at the end of the fifth cycle by bottom flange fracture, as can be seen in figure (4.3b). The authors of the study attribute the fracture to the plastic strain accumulation and the constraints from the presence of stiffeners as well as the altering of material behavior by welding. Consequently, the accurate representation of the local strain and stress concentration by the proposed beam element is an encouraging sign that it will be able to predict the ultimate deformation and the failure mode after appropriate enhancement of the material model to account for low cycle fatigue and for material changes due to welding.

4.2 Shear link with I-section

The second correlation study concerns a shear link with I cross-section. The shear link was used in the experimental studies for eccentrically braced frames by Hjelmstad and Popov [42] and was tested under large, inelastic shear deformation reversals. Following the correlation with the available experimental measurements, the shear link is the subject of an analytical correlation study under shear and torsion with inelastic material response.

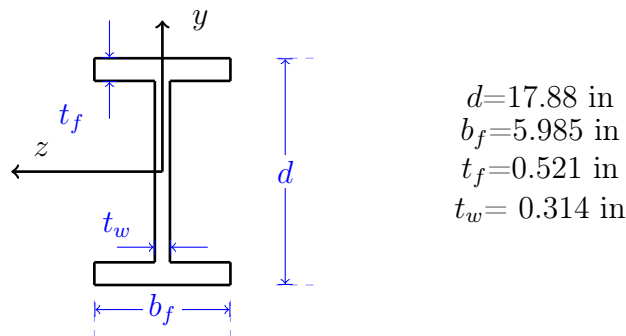


Figure 4.10: Geometry of I-section for shear link of Hjelmstad and Popov [42]

The experimental specimen consists of the shear link only with one end fixed and the other free to displace transversely to the axis, so as to impose the shear deformation, similar to figure (4.3a). The length of the specimen is $L = 28$ in. The geometry of the cross section with its dimensions is given in figure (4.10). The simulation model for the shear link is identical with the model for the link with tubular box section in figure (4.2b). The rotations in the plane of the model are constrained at both ends. The twist about the specimen axis is constrained at one end and is free at the other. Warping is constrained at both ends in accordance with the statement of the experimental study in [42] that warping of the specimen was completely restrained at the ends with the flanges welded to thick plates. The authors of the experimental study state that the warping restraint was not expected to affect the global response of the shear link.

The structural steel material is described with the J2 plasticity model with generalized plasticity by Auricchio and Taylor [2] allowing for the smooth transition between the elastic and the plastic range. The Young modulus E of the material in the web and flange was set equal to 28300 ksi and 28000 ksi, respectively. The yield strength of the material in the web was set equal to 39.5 ksi and the ultimate strength to 60.1 ksi. The corresponding values for the material in the flanges were 35 ksi for the yield strength and 58.5 ksi for the ultimate strength. The isotropic and kinematic hardening moduli are $H_i = 0.0002E$ and $H_k = 0.004E$, respectively. Values for the other parameters of the generalized J2 plasticity model are given by Saritas in [82], who conducted a correlation study of his shear beam model with the experimental results.

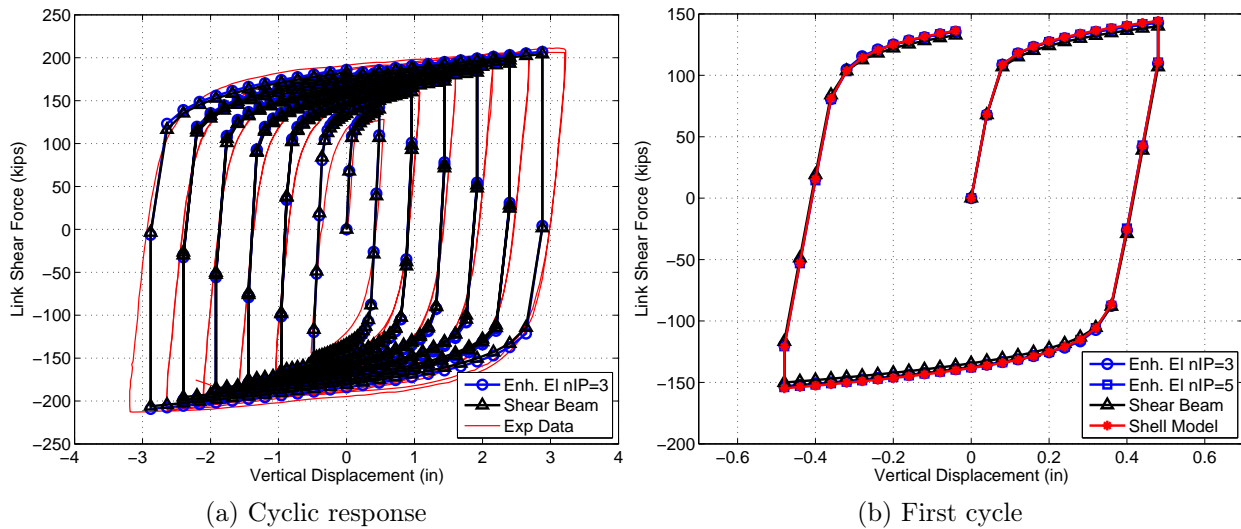
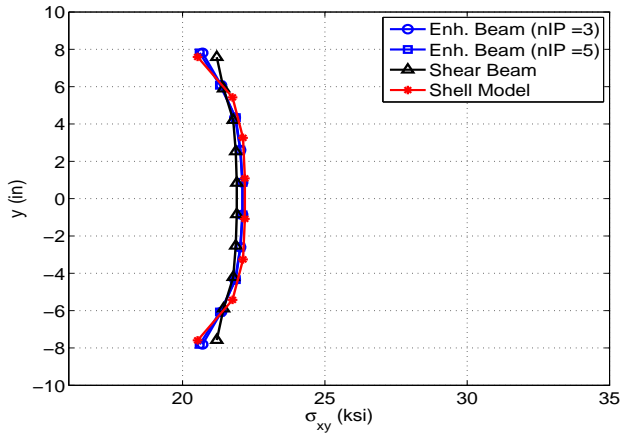
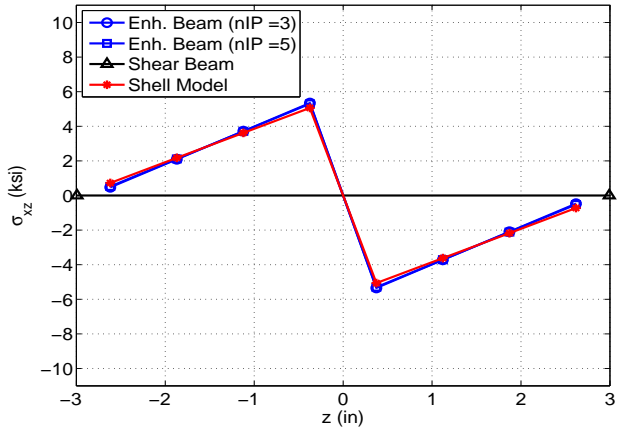


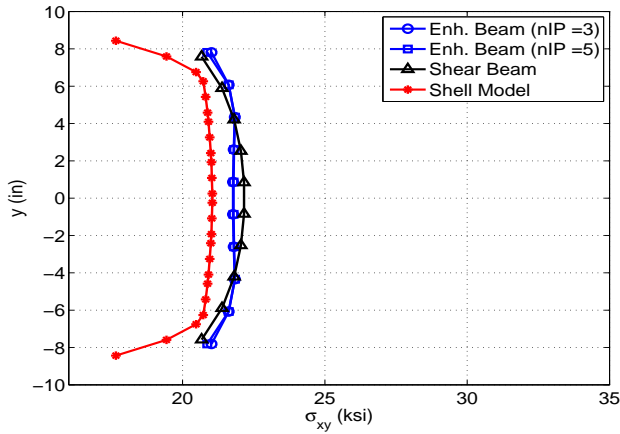
Figure 4.11: Shear force-displacement of shear-link with I-section



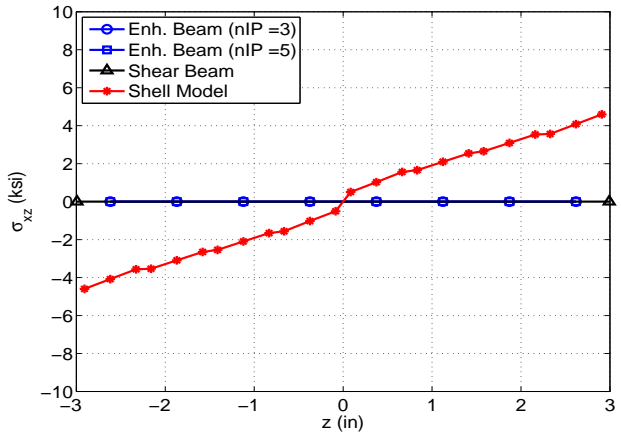
(a) Shear stress in web at midspan



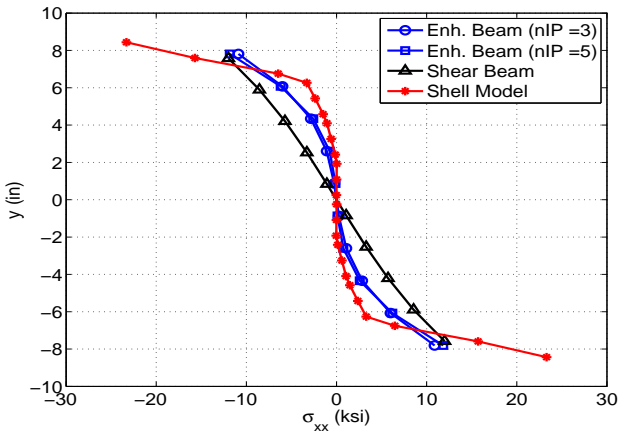
(b) Shear stress in lower flange at midspan



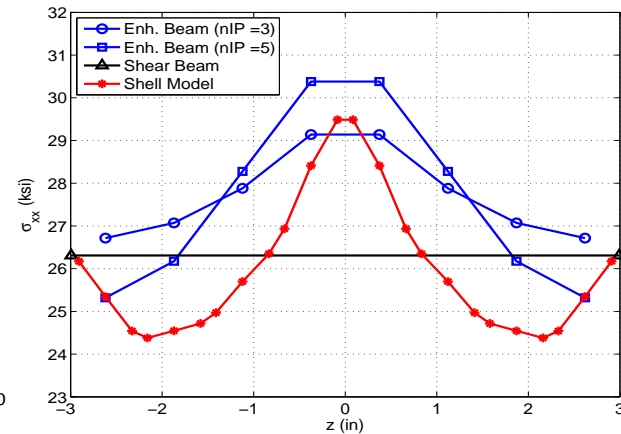
(c) Shear stress in web of fixed end



(d) Shear stress in lower flange of fixed end



(e) Axial stress in web of fixed end



(f) Axial stress in lower flange of fixed end

Figure 4.12: Stress profiles of shear link with I-section under displacement of 0.12 in

The loading regimen of the simulation model under shear matches the loading history of the specimen, which consisted of several cycles of ever increasing shear deformation. The experimental results are compared with three analytical models: the 2d shear beam element by Saritas [82], the proposed 3d beam element, and a shell FE model.

The simulation model consisted of a single shear beam element for the shear link with 5 Gauss-Lobatto integration points along the axis and a fiber section model with 10 layers for the web and 3 layers for the flange. The simulation model of the proposed 3d beam also used a single element for the shear link with 3 or 5 Gauss-Lobatto integration points along the axis, resulting in second or fourth degree polynomials for the warping distribution functions χ along the shear link axis, respectively. The fiber model of the cross section used 10 integration points over the height of the web, 3 over the flange thickness and 4 across the flange width for a total of 12 points in the flange and 34 integration points for the section. The number of warping degrees of freedom for the I-section is $n_w = 12$ in the arrangement of figure (2.1c). Finally, the shell model used the MITC shell element [4] in FEDEASLab [28] with a mesh of 8x20 plane stress MITC shell elements for the web and each flange.

Figure (4.11a) compares the complete shear force-displacement history of the specimen with the results of the shear beam model and those of the proposed 3d beam element. Figure (4.11b) shows the shear-force displacement response for the first cycle. These figures lead to the conclusion that the global response of the shear beam model and the proposed 3d beam element is practically the same. Excellent agreement of these two models with the results of the shell FE model is observed in figure (4.11b). A separate analysis of the proposed 3d beam element without any warping constraint at the end sections of the shear link specimen showed negligible difference with the results of the model with warping constraints, confirming the assumptions of the experimental study.

Figure (4.12) shows the axial stress and shear stress profiles at different sections of the shear link under a transverse displacement of $U = 0.12$ in. According to the response in figure (4.11b), this transverse displacement corresponds to the early stage of inelastic deformation of the shear link, slightly past the yield strength. The corresponding shear force for the proposed 3d beam element model is 118 kips, which is the same as the shear force of the shell FE model. The corresponding shear force of the shear beam model is 115 kips. The sections selected for the axial and shear stress profiles are: the end section fixed again rotation and with constrained warping, the midspan section with rotation and warping free on account of symmetry, and an intermediate section at $0.175L$ from the end.

The web shear stress profile at these sections in figures (4.12a), (4.12c) and (4.13a) is relatively consistent for the three models, with a slight discrepancy of the profile of the shell FE model at the fixed end section. The agreement is due to the fact that shear yielding is still local and has not spread over a large portion of the web. In this case the assumed parabolic shear stress profile of the shear beam model agrees well with the shear stress profile that satisfies longitudinal force equilibrium in the proposed 3d beam element and in the shell finite element model.

As for the preceding example, the shear stress profile in the lower flange is zero for the

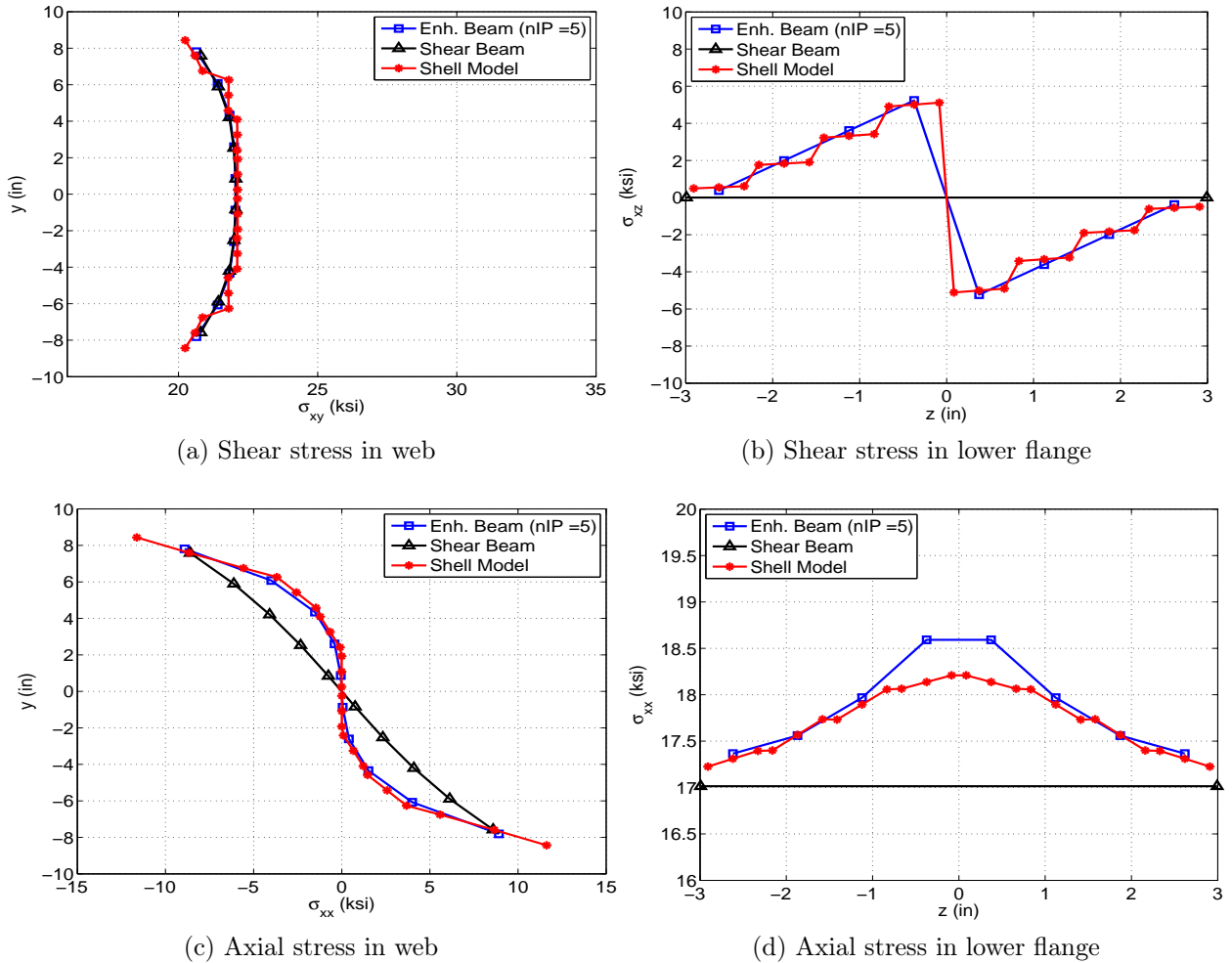


Figure 4.13: Stress profiles of shear link section at 0.175L under displacement of 0.12 in

shear beam element in figures (4.13b), (4.12d) and (4.12b), while the profile agrees very well among the other two models at the sections without warping constraint. At the fixed end section with warping constraint the proposed 3d beam model gives zero shear stress, consistent with its assumptions, while the shell FE model shows an almost linear shear stress profile in figure (4.12d).

The axial stress profile in the web and lower flange at the fixed end section and at the intermediate section are shown in figures (4.12e-f) and (4.13c-d), respectively. Without warping constraint the axial stresses at the midspan section are zero and are, therefore, not shown. Similarly to the preceding example, the warping constraint at the end section gives rise to a nonlinear axial stress profile in the web and flange, which also affects the section at 0.175L. The proposed 3d beam element captures well this behavior in excellent agreement

with the results of the shell FE model at the intermediate section, and good agreement with the latter results at the fixed end section. The proposed 3d beam element captures well the shear lag effect at both sections. The axial stress profile in the lower flange of the fixed end section in figure (4.12f) shows that better results are obtained when the number of interpolation points for the warping displacement distribution along the shear link axis increases from 3 to 5. The figures confirm again the inability of the shear beam model to represent the shear lag effect because of its assumption that plane sections remain plane after deformation.

In conclusion, the local response of the shear link specimen is represented much better by the proposed 3d beam element than by the shear beam model, even though this fact has little effect on the global shear force-deformation response of the shear link. The axial and shear stress profiles of the proposed 3d beam model agree very well with the results of the shell FE model, which is at least one order of magnitude more computationally expensive.

The shear link is now subjected to a monotonic shear force with an eccentricity of $e_z = 2$ in relative to the y -axis of the cross section in figure (4.3a), so as to test the ability of the proposed 3d beam element to represent the coupled response under shear and torsion for inelastic material behavior. The point of application of the eccentric shear force falls within the flange. The material properties are the same as for the preceding study of the shear link under shear. The study compares the results of four models: a shear beam model, a shear beam model with a single warping mode (SW beam), the proposed 3d beam element, and a shell FE element model. The warping mode of the shear beam model is based on the warping displacement profile of the linear elastic solution.

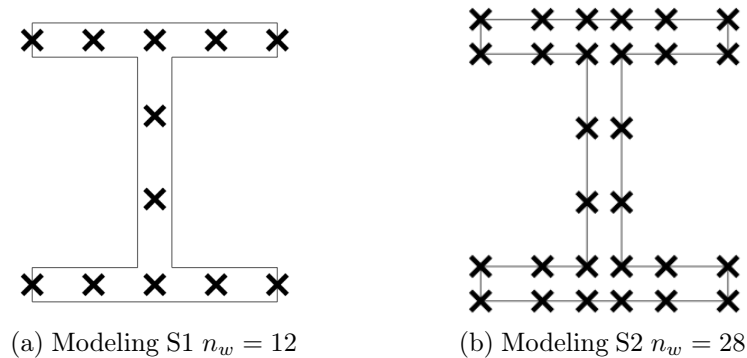


Figure 4.14: Schemes for interpolation grid of warping profile for I-section

In the interest of using a finer mesh along the shear link axis for better representation of the warping effects that are expected to spread farther into the beam from the ends, while at the same time saving time for the calculations, only half of the shear link is represented in the analytical model. A single shear beam element is used for the shear link, since further refinement does not bring any benefit. Four SW beam elements are used in the model for better representation of the nonlinear twist angle distribution along the shear link axis.

By contrast, the model with the proposed 3d beam uses a single element, since this can accommodate the nonlinear warping distribution with higher order interpolation functions for $\chi(x)$. Two schemes for the warping degrees of freedom are explored with this model, as shown in figure (4.14). The schemes are the same as those in figure (2.1), but are redrawn in figure (4.14) convenience's sake. In the first scheme S1, the warping dofs are placed along the centerline of web and flanges resulting in $n_w = 12$ warping degrees of freedom for each section in figure (4.14a). In the second scheme S2, two warping degrees of freedom are placed across the thickness of the web and flanges to capture the warping of each component about its long long axis resulting in $n_w = 28$ warping degrees of freedom for each section, as shown in figure (4.14b). Five Gauss-Lobatto integration points are used over each element axis. Finally, the shell model uses the MITC shell element [4] in FEDEASLab [28] with a mesh of 10x38 plane stress MITC elements for the web and each flange.

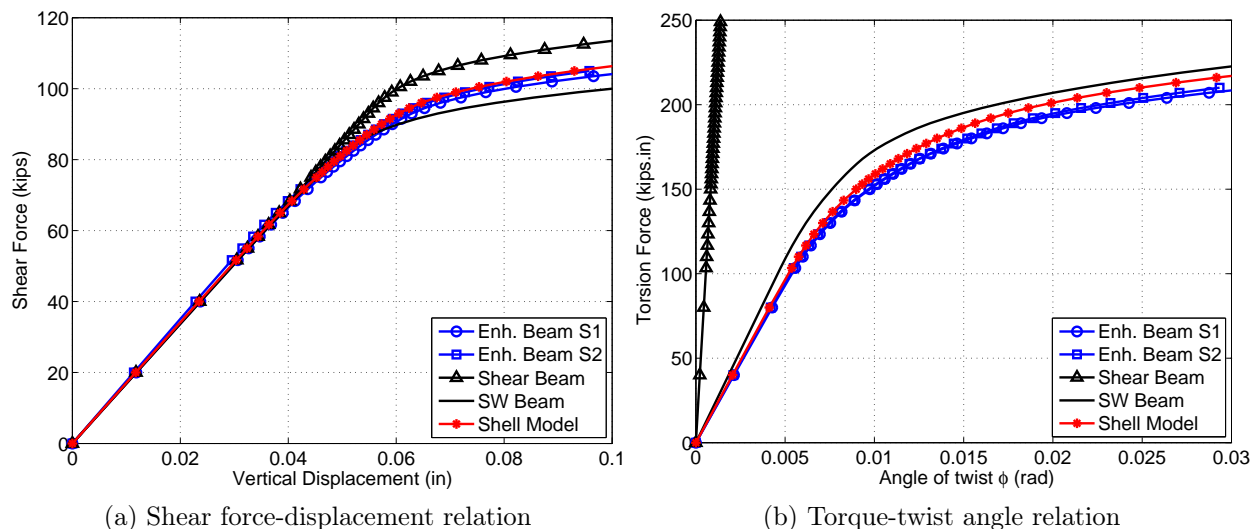


Figure 4.15: Response of shear link with I-section under eccentric shear force

Figures (4.15a) and (4.15b) show the shear force-displacement relation and the torque-twist angle relation of the shear link, respectively. The initial stiffness of the shear force-displacement relation in figure (4.15a) is the same for all models. The inelastic portion of the shear force-displacement relation shows that the shear beam overestimates the strength of the shear link, since it is not able to represent the influence of torsion on the inelastic shear response with the assumption that torsion is uncoupled from shear and remains linear elastic, as can be seen in figure (4.15b). Consequently, the shear force-displacement relation of the shear beam model is the same as for the preceding study of the shear link without torsion. On the other hand, the SW beam model slightly underestimates the strength of the shear link. The response of the proposed 3d beam element with both schemes S1 and S2 agrees very well with the response of the shell FE model. Similar excellent agreement

between the results of the proposed 3d beam element with either scheme S1 or scheme S2 and those of the shell FE model can be observed in the inelastic torque-twist angle relation in figure (4.15b). In this case the SW beam model slightly overestimates the torsional strength of the shear link.

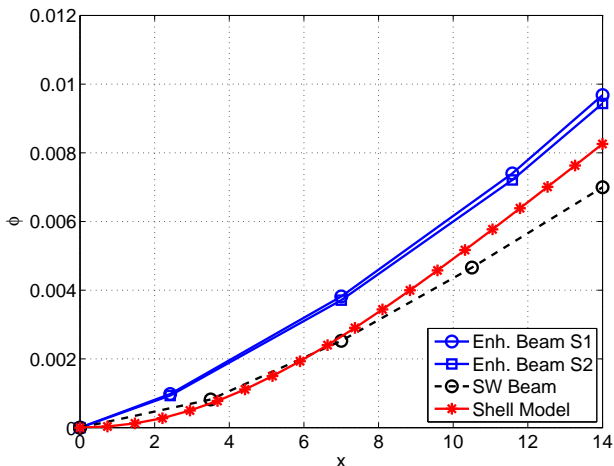


Figure 4.16: Twist angle distribution for half of shear link with I-section

The warping constraint at the ends of the link plays a very important role in its response. The simulation with free warping at the end sections gives a 100-fold reduction of the torsional stiffness of the shear link and a 3-fold reduction of shear strength to approximately 30 kips, as compared with the shear strength of approximately 90 kips in figure (4.15a).

The axial and shear stress profiles of the shear link at different sections are studied for the load point corresponding to a shear force of 96 kips with the corresponding torque equal to 192 kips-in. The transverse displacement and the angle of twist of the shear link under this loading are reported in table (4.3) for the different models.

	Beam S1	Beam S2	SW beam	Shear beam	Shell model
Trans. displacement (in)	0.0682	0.0657	0.0784	0.0567	0.0647
Twist angle (rad)	0.0194	0.0189	0.0140	0.0010	0.0165

Table 4.3: Transverse displacement and twist angle under eccentric shear force of 96 kips

Figure (4.16) shows the twist angle variation over half of the shear link. The proposed 3d beam element overestimates the value of the shell FE model at midspan by approximately 15% irrespective of the number of warping degrees of freedom. The SW model underestimates the twist angle value of the shell FE model at midspan also by approximately 15%. It is

clear from the figure that the warping constraint at the fixed end leads to the derivative of the twist angle having zero value at $x = 0$ for the shell model. The SW beam model represents well this effect, because its formulation includes the derivative of the twist angle and can impose boundary conditions for it. By contrast, the proposed 3d beam element does not include the twist angle derivative in the formulation and this fact affects the twist angle distribution and its value at midspan. It is important to recall, however, that the SW model uses 4 elements along the axis of the shear link, while the proposed 3d beam model uses only one. The twist angle distribution in the middle quarter span segment of the shear link becomes almost linear. In this region the proposed 3d beam element agrees much better with the twist rate of the shell FE model than the SW beam.

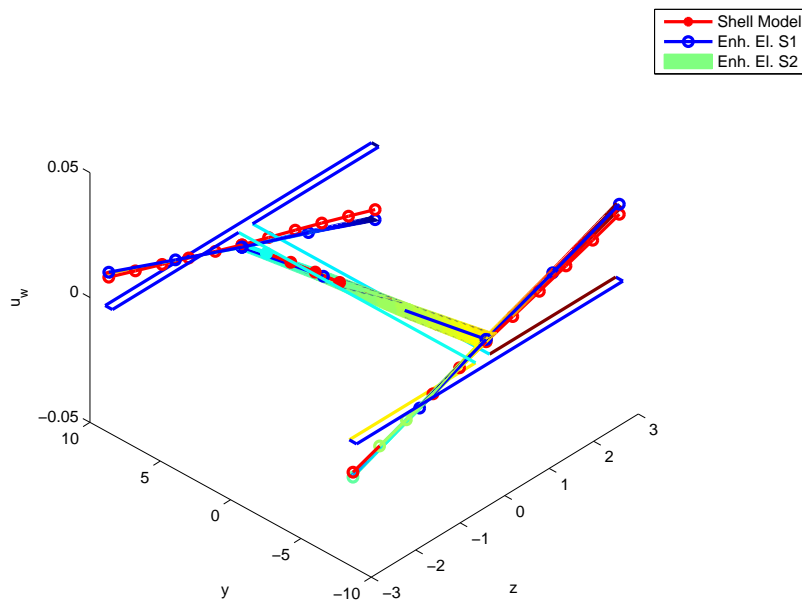


Figure 4.17: Warping displacement profile at midspan section of shear link with I-section

Figure (4.17) shows the warping displacement profile at the midspan section of the shear link. The profiles of the proposed 3d beam element and of the shell FE model agree very well. The profile for warping degree of freedom arrangement S2 in figure (4.14b), which accounts for warping about the centerline of the web and flanges does not affect the profile appreciably. The warping displacements of the three models are practically linear in the flange implying that the shear-lag effect is negligible for the I-section, because most of the warping is caused by torsion.

The axial and shear stress profiles of the I-section at the fixed end and at the quarter span section are shown in figures (4.18) and (4.19), respectively. Figures (4.18a) and (4.19a) show the shear stress profile in the web of the shear link at the fixed end and at the quarter span section, respectively. The profiles of all models with the exception of the proposed

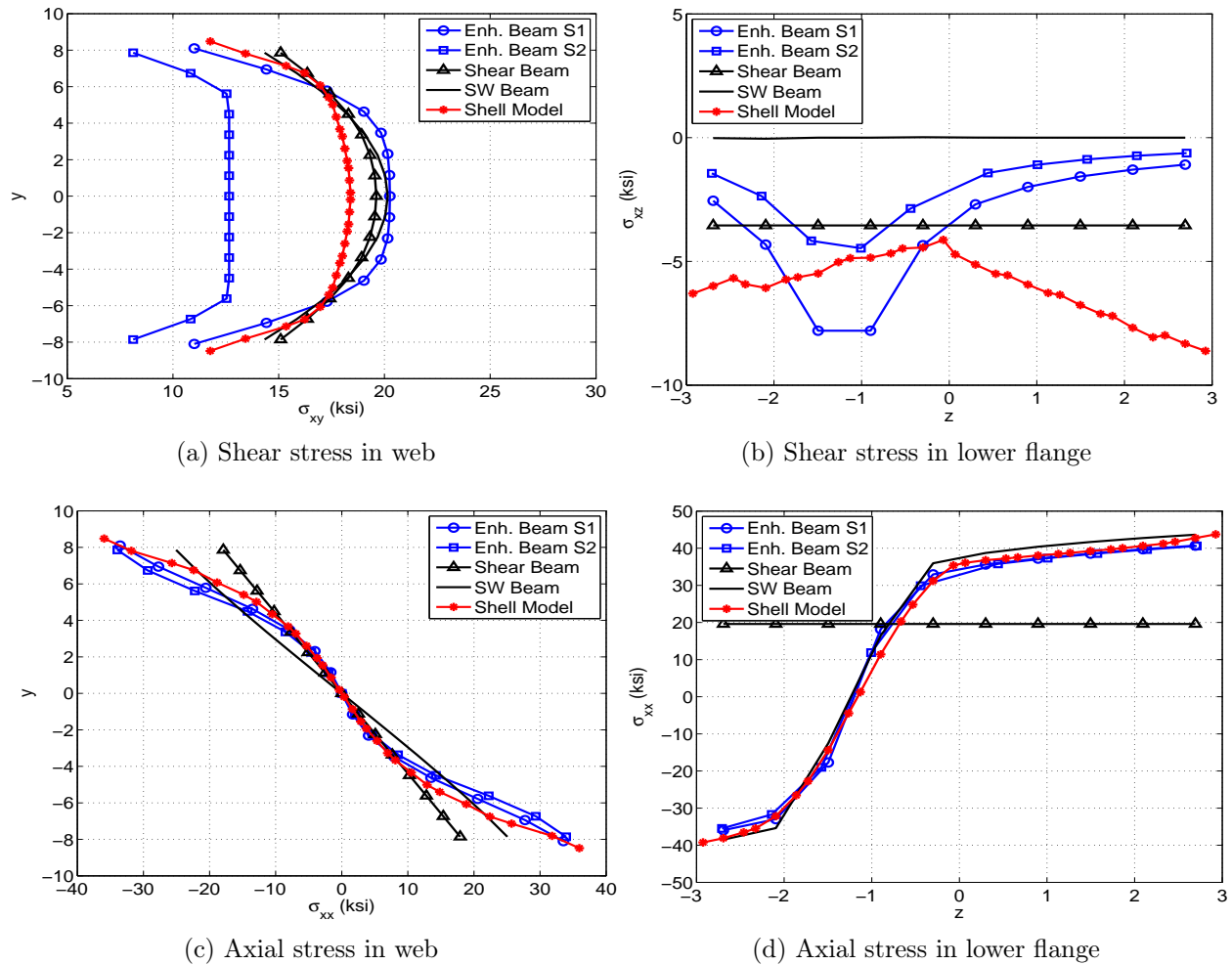


Figure 4.18: Stress profiles at fixed end of shear link under eccentric shear of 96 kips

beam with the S2 arrangement of the warping degrees of freedom agree well at the fixed end. The latter shows significantly smaller shear stress values because of the contribution of the shear stress σ_{xy} in the flange. With two warping degrees of freedom across the flange thickness the proposed formulation is the only model that can capture accurately the shear stress contribution of the flange. This can have significant influence on the response of a section with thick flanges. The shear stress profile in the lower flange of the shear link for the proposed 3d beam element agrees very well with the profile of the shell FE model at the quarter span section, but much less so at the fixed end. The latter observation justifies further study for the proposed model. The shear stress σ_{xz} is zero at both sections for the SW beam model and is constant for the shear beam model in stark contrast to the stress profiles of the shell FE model.

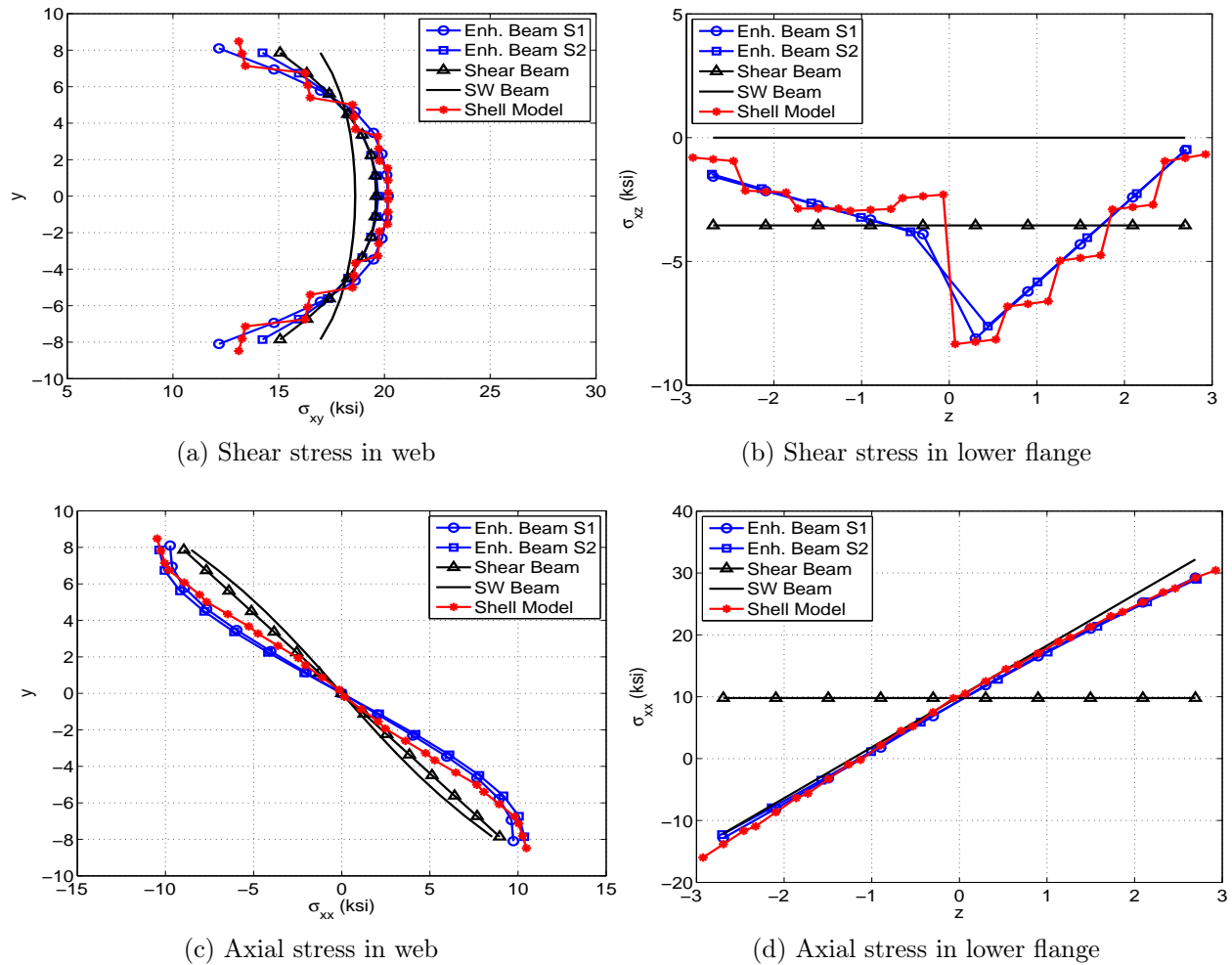


Figure 4.19: Stress profiles at quarter span of shear link under eccentric shear of 96 kips

Figures (4.18c) and (4.19c) show the axial stress profile of the shear link at the fixed end section and at the quarter span section. The higher stress value at the intersection of web and lower flange is captured very well by the proposed 3d beam in excellent agreement with the shell finite element model. The same is true for the stress profile of the web and flange. By contrast, the linear stress profile of the web for the shear beam and the SW beam underestimates the extreme values by 50% and 30%, respectively. Moreover, the shear beam fails to capture the nonlinear axial stress profile in the lower flange, which is represented very well by the proposed 3d beam element and by the SW shear beam in excellent agreement with the profile of the shell FE model. The nonlinear distribution of the axial stress in the lower flange is due to extensive yielding in tension and limited yielding in compression across the width of the flange at the fixed end, as shown in figure (4.18c). By contrast, figure (4.19c)

shows that the axial stress in the lower flange of the midspan section is linear, because of the linear warping displacement of the shear link caused by torsion.

The preceding analyses of a shear link under shear and torsion show that the proposed 3d beam element produces a global and local response that is in much better agreement with the results of a refined shell FE model than either a shear beam element with uncoupled linear elastic torsional response or a shear beam element with a single warping mode with a profile based on the linear elastic solution. Because the flanges of the selected section are relatively thin, the simpler arrangement S1 of warping degrees of freedom along the centerline of the web and flanges gives results of very good accuracy, so that the additional computational cost of the S2 arrangement is not justified for this type of section.

Chapter 5

Corotational formulation

The corotational formulation of nonlinear kinematics for 3d beams under large displacements posits that the response of the 3d beam element can be decomposed into the response relative to a rigid reference frame that follows the element as it deforms, and the rigid body motion of the reference frame. This approach permits the uncoupling of the element formulation relative to the rigid reference frame from the description of the rigid body motion of the reference frame under large displacements. The formulation of the proposed 3d beam element in chapter 2 covers the first aspect of this general approach. This chapter deals with the second. The following discussion is founded on the work of Nour-Omid and Rankin [65] and Battini and Pacoste [8], but offers new insights into the relation of the corotational approach with the nonlinear geometry of the continuum rod and identifies a limitation of the corotational approach in connection with large torsional deformations.

The following presentation starts from the kinematics of the continuous rod. After stating the assumptions for the local kinematic variables and discussing the transformation of these variables from the global to the local frame, it relates these to the kinematic variables of the corotational formulation with special attention to the presence of large axial, shear and torsional deformations. This approach reveals a limitation of the corotational formulation in correctly representing the interaction between axial force and torque. The chapter concludes with several examples.

5.1 Kinematics of continuous rod

The starting point for the following discussion is the model of the continuous Cosserat rod, as described by Reissner [79] and Simo and Vu-Quoc [87]. In this model the beam is represented by its axis, as the line connecting the section centroids, and the geometric and material properties of the cross-sections along this axis. For the following discussion the beam is assumed to be straight in the reference configuration. Additional assumptions will be introduced in the course of the derivations.

The line of centroids is described by a material arc-length parameter denoted with s . Initially, the kinematic variables are defined relative to the global orthonormal reference frame $\mathbf{E} = \{\mathbf{E}_1, \mathbf{E}_2, \mathbf{E}_3\}$. A moving frame $\mathbf{T} = \{\mathbf{t}_1, \mathbf{t}_2, \mathbf{t}_3\}$ is attached to each cross section with its origin at the section centroid. The axis \mathbf{t}_1 is normal to the plane of the section, and the axes \mathbf{t}_2 and \mathbf{t}_3 are orthogonal but arbitrarily oriented. The position of a material point of the cross-section is uniquely defined by parameters s, X_2, X_3 , where X_2, X_3 are the coordinates relative to axes \mathbf{t}_2 and \mathbf{t}_3 , respectively. With the superscript 0 denoting the initial position of the corresponding function or variable the initial position \mathbf{x}_m^0 of a material point m and the final position \mathbf{x}_m can be described by

$$\mathbf{x}_m^0 = \boldsymbol{\phi}_m^0(s, X_2, X_3) = \boldsymbol{\phi}_c^0(s) + X_2 \mathbf{t}_2^0(s) + X_3 \mathbf{t}_3^0(s) \quad (5.1a)$$

$$\mathbf{x}_m = \boldsymbol{\phi}_m(s, X_2, X_3) = \boldsymbol{\phi}_c(s) + X_2 \mathbf{t}_2(s) + X_3 \mathbf{t}_3(s) + \zeta(s) \omega(X_2, X_3) \mathbf{t}_1(s) \quad (5.1b)$$

where $\boldsymbol{\phi}_c^0(s)$ and $\boldsymbol{\phi}_c(s)$ are the initial and current position vectors of the section centroid, respectively. The function $\omega(X_2, X_3)$ represents the warping profile of the cross-section while $\zeta(s)$ represents the warping amplitude, which is equal to the twist rate of the beam according to the Saint-Venant torsion theory.

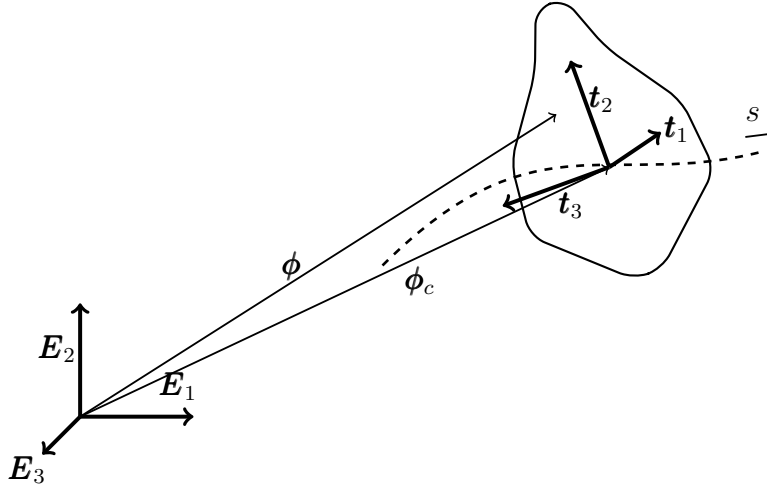


Figure 5.1: Kinematics of material point of beam element

The initial and current position of the material point m are related by the displacement vector \mathbf{d}_m in the global reference frame.

$$\mathbf{d}_m = \mathbf{x}_m - \mathbf{x}_m^0 \quad (5.2)$$

Without loss of generality the following discussion assumes that a single warping mode represents the warping profile of the section. The extension to the more general description of warping in the proposed model is straightforward.

Following Simo and Vu-Quoc [87] the motion of the Cosserat rod is described by the translations of the centroid and the rotation of the cross-section. The deformation gradient \mathbb{F} at a point m of the cross-section is

$$\mathbb{F} = \mathbf{T} \{ \mathbf{I}_3 + \zeta \mathbf{E}_1 \otimes \nabla \omega + [\mathbf{\Gamma} + \mathbf{K} \times \mathbf{T}^T (\boldsymbol{\phi}_m - \boldsymbol{\phi}_c) + (\zeta \omega)' \mathbf{E}_1] \otimes \mathbf{E}_1 \} \mathbf{T}^{0T} \quad (5.3)$$

where \otimes denotes the tensorial product, and $(\cdot)'$ refers to the derivative with respect to the arc-length s . The deformation of the cross-section consists of the material axial strain vector $\mathbf{\Gamma}$ and the material shear strain vector \mathbf{K} , which are defined according to

$$\mathbf{\Gamma} = \mathbf{T}^T (\boldsymbol{\phi}'_c - \mathbf{t}_1) \quad (5.4a)$$

$$\mathbf{K} = \text{axial}(\mathbf{T}^T \mathbf{T}') \quad (5.4b)$$

where the axial vector of the matrix $\mathbf{T}^T \mathbf{T}'$ is defined in [87].

5.2 Finite rotation parametrization

An important aspect of nonlinear rod kinematics is the treatment of finite rotations in three dimensions. The three alternatives for the finite rotation parametrization are briefly described below. A more complete review of the parametrization choices is given by Ibrahimbegovic [43].

The rotation \mathbf{R} is an orthogonal tensor belonging to the SO(3) rotation group. The corresponding 3x3 rotation matrix \mathbf{R} operates on a vector or triad according to

$$\mathbf{T} = \mathbf{R} \mathbf{T}^0 \quad (5.5)$$

where \mathbf{T}^0 is the initial orthogonal triad that is transformed to the current orthogonal triad \mathbf{T} by the spatial rotation \mathbf{R} . The orthogonal property of matrix \mathbf{R} implies that it can be represented by three independent parameters. One alternative for these parameters is the *rotation vector* $\boldsymbol{\vartheta}$. With it the rotation matrix \mathbf{R} can be expressed by means of the exponential function

$$\mathbf{R} = \exp [Sp(\boldsymbol{\vartheta})] = \mathbf{I}_3 + \frac{\sin(\vartheta)}{\vartheta} Sp(\boldsymbol{\vartheta}) + \frac{1 - \cos(\vartheta)}{\vartheta^2} Sp(\boldsymbol{\vartheta})^2 \quad (5.6)$$

where \mathbf{I}_3 is the 3x3 identity matrix and ϑ is the magnitude of the rotation vector so that it can be written as $\boldsymbol{\vartheta} = \vartheta \mathbf{t}$ with \mathbf{t} a unit vector. $Sp(\boldsymbol{\vartheta})$ represents the spin of the rotation vector $\boldsymbol{\vartheta}$ defined as

$$Sp(\boldsymbol{\vartheta}) = \boldsymbol{\vartheta} \times = \begin{bmatrix} 0 & -\vartheta_3 & \vartheta_2 \\ \vartheta_3 & 0 & -\vartheta_1 \\ -\vartheta_2 & \vartheta_1 & 0 \end{bmatrix} \quad (5.7)$$

The vector $\boldsymbol{\vartheta}$ is called the axial vector of the spin matrix $Sp(\boldsymbol{\vartheta})$ with the definition

$$\boldsymbol{\vartheta} = axial[Sp(\boldsymbol{\vartheta})]$$

For small rotations, the expression for the rotation matrix \mathbf{R} in equation (5.6) reduces to

$$\mathbf{R} = \mathbf{I}_3 + Sp(\boldsymbol{\vartheta}) \quad (5.8)$$

where the components of the rotation vector $\boldsymbol{\vartheta}$ are the rotations with respect to the axes \mathbf{t}_1 , \mathbf{t}_2 , and \mathbf{t}_3 . This simplification will be used later for the rotations relative to the element frame.

The parametrization of the rotation matrix \mathbf{R} according to equation (5.6) is computationally onerous, because it requires the evaluation of trigonometric functions. Moreover, equation (5.6) cannot be easily used to determine the rotation vector $\boldsymbol{\vartheta}$ that corresponds to a rotation matrix \mathbf{R} . A more suitable representation involves the use of quaternions, which are defined according to

$$quat = \begin{pmatrix} \sin(\vartheta/2) \mathbf{t} \\ \cos(\vartheta/2) \end{pmatrix} = \begin{pmatrix} \boldsymbol{\vartheta}_q \\ \vartheta_{q0} \end{pmatrix} \quad (5.9)$$

The rotation matrix can then be expressed in terms of quaternions with

$$\mathbf{R}(\boldsymbol{\vartheta}_q) = (\vartheta_{q0}^2 - \boldsymbol{\vartheta}_q^T \boldsymbol{\vartheta}_q) \mathbf{I}_3 + 2 \boldsymbol{\vartheta}_q \boldsymbol{\vartheta}_q^T + 2 \vartheta_{q0} Sp(\boldsymbol{\vartheta}_q) = \mathbf{I}_3 + 2 \vartheta_{q0} Sp(\boldsymbol{\vartheta}_q) + 2 Sp(\boldsymbol{\vartheta}_q)^2 \quad (5.10)$$

Operations on quaternion vectors are governed by special algebra rules with compact notation and ease of implementation. One drawback of the quaternion representation is the need for an additional parameter for the unique definition of the rotation. This drawback can be overcome with the procedure by Battini [5] which restricts the quaternion parametrization to rotations in the range $[-\pi, \pi]$. In this case the fourth component of the quaternion is not independent but can be uniquely determined from

$$\vartheta_{q0} = \sqrt{1 - \boldsymbol{\vartheta}_q^T \boldsymbol{\vartheta}_q}$$

In conclusion, the rotation of a triad can be expressed either with a rotation matrix \mathbf{R} , or with the corresponding rotation vector $\boldsymbol{\vartheta}$, or with the corresponding quaternion vector $\boldsymbol{\vartheta}_q$. The implementation challenge of large rotations in computer analysis lies in the conversion from one parametrization alternative to another, as will be discussed later.

Next, the variation of the rotation matrix is derived, because it is required for the consistent linearization of the governing nonlinear equations. To this end it is important to note that the rotations belong to the $SO(3)$ group. Thus, whereas the displacements are additive, the update of the rotation matrix \mathbf{R} under an infinitesimal rotation is

$$\mathbf{R}_\epsilon = \mathbf{R}(\epsilon \delta \boldsymbol{\theta}) \mathbf{R} \quad (5.11)$$

where \mathbf{R}_ϵ is the updated rotation matrix, and $\delta\boldsymbol{\theta}$ is known as the spatial angular variation representing the infinitesimal rotation that is superimposed on the rotation matrix \mathbf{R} for the update. With this definition the variation of the rotation matrix becomes

$$\delta\mathbf{R} = \left. \frac{d\mathbf{R}_\epsilon}{d\epsilon} \right|_{\epsilon=0} = \lim_{\epsilon \rightarrow 0} \frac{\mathbf{R}(\epsilon\delta\boldsymbol{\theta})\mathbf{R} - \mathbf{R}}{\epsilon} = \lim_{\epsilon \rightarrow 0} \frac{\exp[\epsilon Sp(\delta\boldsymbol{\theta})]\mathbf{R} - \mathbf{R}}{\epsilon} = Sp(\delta\boldsymbol{\theta})\mathbf{R} \quad (5.12)$$

Equation (5.12) can also be derived without resort to the definition of rotation update in equation (5.11) by making use of the orthogonality of the rotation matrix \mathbf{R} . The variation of $\mathbf{R}\mathbf{R}^T$ according to

$$\mathbf{R}\mathbf{R}^T = \mathbf{I}_3 \quad \Rightarrow \quad \delta(\mathbf{R}\mathbf{R}^T) = 0 \quad \Rightarrow \quad \delta(\mathbf{R})\mathbf{R}^T = -\mathbf{R}\delta(\mathbf{R}^T)$$

leads to the conclusion that the product $\delta(\mathbf{R})\mathbf{R}^T$ is a skew-symmetric matrix. Consequently, there exists a unique vector $\delta\boldsymbol{\theta}$ such that $\delta(\mathbf{R})\mathbf{R}^T = Sp(\delta\boldsymbol{\theta})$, so that

$$\delta\mathbf{R} = Sp(\delta\boldsymbol{\theta})\mathbf{R} \quad (5.13)$$

after post-multiplying both sides with \mathbf{R} . According to equation (5.12) or equation (5.13) the variation of the rotation matrix $\delta\mathbf{R}$ is proportional to the spatial angular variation $\delta\boldsymbol{\theta}$. This vector, therefore, plays an important role in incremental analysis for updating the rotation matrix \mathbf{R}^i to the rotation matrix \mathbf{R}^{i+1} according to

$$\mathbf{R}^{i+1} = \mathbf{R}(\delta\boldsymbol{\theta})\mathbf{R}^i \quad (5.14)$$

where $\boldsymbol{\vartheta}^i$ and $\boldsymbol{\vartheta}^{i+1}$ denote the rotation vectors associated with the rotation matrices \mathbf{R}^i and \mathbf{R}^{i+1} , respectively

$$\mathbf{R}^i = \mathbf{R}(\boldsymbol{\vartheta}^i) \quad \mathbf{R}^{i+1} = \mathbf{R}(\boldsymbol{\vartheta}^{i+1})$$

Because of the multiplicative update for rotations, the addition of the vector $\delta\boldsymbol{\theta}$ to $\boldsymbol{\vartheta}^i$ does not give $\boldsymbol{\vartheta}^{i+1}$, i.e. $\boldsymbol{\vartheta}^{i+1} \neq \boldsymbol{\vartheta}^i + \delta\boldsymbol{\theta}$. To solve this problem for the implementation of rotation updates in incremental analysis, Battini and Pacoste [8] proposed the conversion of the spatial angular variation $\delta\boldsymbol{\theta}$ to a vector $\delta\boldsymbol{\vartheta}$, such that the vector $\boldsymbol{\vartheta}^i + \delta\boldsymbol{\vartheta}$ corresponds to the updated rotation matrix \mathbf{R}^{i+1} . Unfortunately, the relation between $\delta\boldsymbol{\theta}$ and $\delta\boldsymbol{\vartheta}$ is quite complex

$$\delta\boldsymbol{\theta} = h_\theta(\boldsymbol{\vartheta})\delta\boldsymbol{\vartheta} \quad (5.15)$$

where

$$h_\theta(\boldsymbol{\vartheta}) = \frac{\sin(\vartheta)}{\vartheta}\mathbf{I}_3 + \left(1 - \frac{\sin(\vartheta)}{\vartheta}\right) \mathbf{t}\mathbf{t}^T + \frac{1}{2} \left(\frac{\sin(\vartheta/2)}{\vartheta/2}\right)^2 Sp(\boldsymbol{\vartheta}) \quad (5.16)$$

The inverse relation

$$\delta\boldsymbol{\vartheta} = h_\theta^{-1}(\boldsymbol{\vartheta})\delta\boldsymbol{\theta}$$

is available in the form

$$h_\vartheta^{-1}(\boldsymbol{\vartheta}) = \mathbf{I}_3 - \frac{1}{2}Sp(\boldsymbol{\vartheta}) + \frac{\sin(\vartheta/2) - \frac{\vartheta}{2}\cos(\vartheta/2)}{\vartheta^2 \sin(\vartheta/2)} Sp(\boldsymbol{\vartheta})^2 \quad (5.17)$$

The rotation update \mathbf{R}^{i+1} is then

$$\mathbf{R}^{i+1} = \mathbf{R}(\boldsymbol{\vartheta}^{i+1}) = \mathbf{R}(\boldsymbol{\vartheta}^i + \delta\boldsymbol{\vartheta}) \quad \text{with} \quad \delta\boldsymbol{\vartheta} = h_\vartheta^{-1}(\boldsymbol{\vartheta}^i) \delta\boldsymbol{\theta} \quad (5.18)$$

Seeking a simpler way for the rotation update Battini [5] proposed in a later study the use of quaternions for the parametrization of finite rotations. According to equation (5.10) the rotation matrices \mathbf{R}^{i+1} and \mathbf{R}^i can be expressed in terms of the corresponding quaternions $\boldsymbol{\vartheta}_q$

$$\mathbf{R}^i = \mathbf{R}(\boldsymbol{\vartheta}_q^i) \quad \mathbf{R}^{i+1} = \mathbf{R}(\boldsymbol{\vartheta}_q^{i+1}) \quad (5.19)$$

The relation between spatial angular variation $\delta\boldsymbol{\theta}$ and quaternion variation $\delta\boldsymbol{\vartheta}_q$ has the simple form

$$\delta\boldsymbol{\theta} = \frac{\mathbf{R}(\boldsymbol{\vartheta}_q) + \mathbf{I}_3}{\vartheta_{q0}} \delta\boldsymbol{\vartheta}_q = h_q(\boldsymbol{\vartheta}_q) \delta\boldsymbol{\vartheta}_q \quad (5.20)$$

The rotation update \mathbf{R}^{i+1} is then

$$\mathbf{R}^{i+1} = \mathbf{R}(\boldsymbol{\vartheta}_q^{i+1}) = \mathbf{R}(\boldsymbol{\vartheta}_q^i + \delta\boldsymbol{\vartheta}_q) \quad \text{with} \quad \delta\boldsymbol{\vartheta}_q = h_q^{-1}(\boldsymbol{\vartheta}_q^i) \delta\boldsymbol{\theta} \quad (5.21)$$

where

$$h_q^{-1}(\boldsymbol{\vartheta}_q) = \vartheta_{q0} [\mathbf{R}(\boldsymbol{\vartheta}_q) + \mathbf{I}_3]^{-1}$$

In the subsequent derivation of nonlinear element kinematics the rotation variation is represented by the spatial angular variation $\delta\boldsymbol{\theta}$. Depending on the implementation choice for incremental analysis the spatial angular variation $\delta\boldsymbol{\theta}$ is converted either to the quaternion variation $\delta\boldsymbol{\vartheta}_q$, or to the rotation vector variation $\delta\boldsymbol{\vartheta}$. The corresponding transformations of the element end forces and stiffness matrices are discussed in section 5.3.5.

5.3 Corotational framework

The corotational formulation of the nonlinear geometry of 3d beams postulates that the large displacement kinematics can be decomposed into the kinematics relative to a rigid reference frame that follows the element as it deforms, and the rigid body motion of the reference frame. The presentation starts with the definition of the element frame and of the kinematic variables for the problem relative to it. It is typically assumed that strains are small relative to the element frame, so as to keep the element kinematics linear. The effect of large displacements is then accounted for only in the description of the rigid body motion of the element frame. The following derivation of the corotational formulation highlights the underlying assumptions of the approach, while also pointing out clearly some of its limitations.

5.3.1 Definition of element frame

The beam element of section 5.1 is delimited by end nodes I and J with the triads \mathbf{T}_I and \mathbf{T}_J attached to the end sections at the centroid, as defined in section 5.1. The centroid displacement vector \mathbf{a} in the global reference system is composed of the translation vector \mathbf{d} and the rotation vector $\boldsymbol{\vartheta}$, so that $\mathbf{a} = [\mathbf{d} \ \boldsymbol{\vartheta}]$. Associated with the rotation vector $\boldsymbol{\vartheta}$ is the rotation matrix \mathbf{R} . The centroid translations at end nodes I and J are denoted with \mathbf{d}_I and \mathbf{d}_J , respectively, as shown in figure (5.2). The element frame \mathbf{T}_r consists of three orthonormal

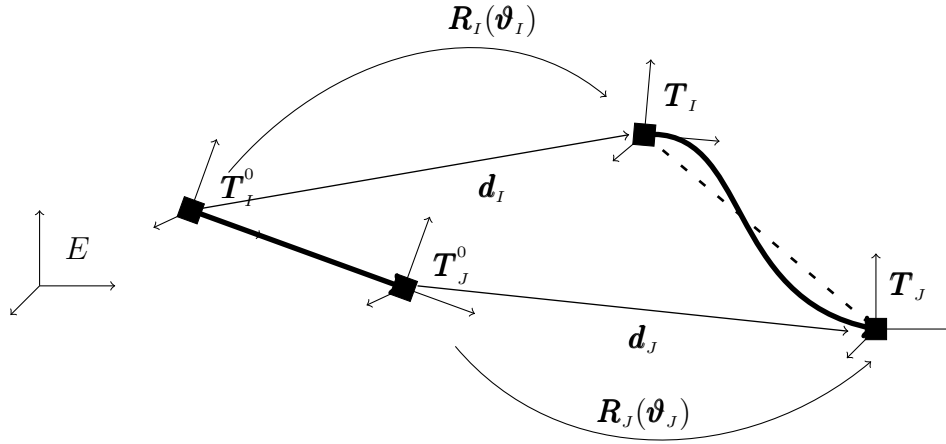


Figure 5.2: Original and deformed configuration of 3d beam element with node triads

vectors. One choice for the element frame can be the triad \mathbf{T}_I associated with node I . Because it is preferable to define the element frame independently of node numbering, it is advisable to use the element chord, i.e. the line connecting the end nodes as the first axis, as shown in figure (5.3)

$$\mathbf{t}_{r1} = \frac{\mathbf{x}_J - \mathbf{x}_I}{\|\mathbf{x}_J - \mathbf{x}_I\|} \quad (5.22)$$

where \mathbf{x}_I and \mathbf{x}_J denote the position of end node I and J, respectively. Following the suggestion of Crisfield [20], Rankin and Nour-Omid [65] and Pacoste [8], the trial choice for the second frame axis is taken as the average of the second triad vector \mathbf{t}_2 at nodes I and J

$$\mathbf{t}_{r2}^{tr} = \frac{1}{2} (\mathbf{t}_{I2} + \mathbf{t}_{J2}) \quad (5.23)$$

The third triad axis is obtained by

$$\mathbf{t}_{r3} = \frac{\mathbf{t}_{r1} \times \mathbf{t}_{r2}^{try}}{\|\mathbf{t}_{r1} \times \mathbf{t}_{r2}^{tr}\|} \quad (5.24)$$

Finally, the second triad axis becomes

$$\mathbf{t}_{r2} = \mathbf{t}_{r3} \times \mathbf{t}_{r1} \quad (5.25)$$

The choice of frame origin is irrelevant to the derivation of the 3d beam element. A convenient choice is to select the origin of the element frame at node I . Denoting the initial frame with \mathbf{T}_r^0 it holds that $\mathbf{T}_r^0 = \mathbf{T}_I^0 = \mathbf{T}_J^0$ for a straight beam in the undeformed configuration.

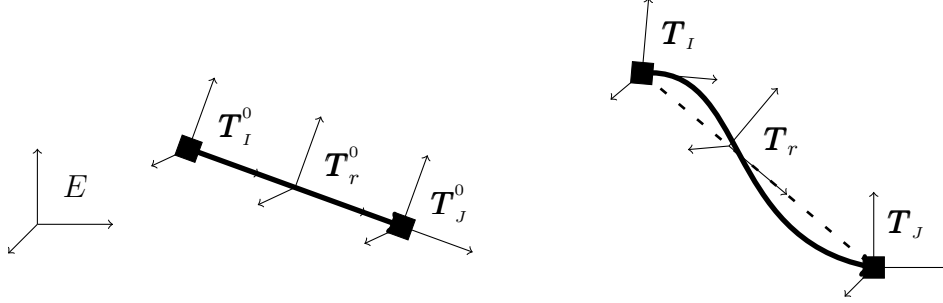


Figure 5.3: Definition of element frame with arbitrary origin

5.3.2 Element kinematics

In the global reference frame the displacements of a beam section consist of the translations \mathbf{d} of the centroid and the rotations $\boldsymbol{\vartheta}$ about the axes of a triad through the centroid. The translations \mathbf{d} are defined with

$$\mathbf{d} = \mathbf{x} - \mathbf{x}^0 \quad (5.26)$$

where \mathbf{x}^0 and \mathbf{x} denote the initial and current position of the section centroid, respectively. The rotations $\boldsymbol{\vartheta}$ are associated with a rotation matrix \mathbf{R} that transforms the initial triad through the section centroid \mathbf{T}^0 to the current triad \mathbf{T}

$$\mathbf{T} = \mathbf{R}\mathbf{T}^0 \quad (5.27)$$

The corotational formulation defines the element kinematics relative to the element frame. To this end it is necessary to transform the translations \mathbf{d} and the rotations $\boldsymbol{\vartheta}$ from the global reference system to the element frame. Denoting all variables relative to the element frame with a bar and using the initial and current position of the element frame triad it is possible to express the initial position $\bar{\mathbf{x}}^0$ and the current position $\bar{\mathbf{x}}$ of the centroid relative to the element frame according to

$$\bar{\mathbf{x}}^0 = \mathbf{T}_r^{0T} (\mathbf{x}^0 - \mathbf{x}_I^0) \quad (5.28a)$$

$$\bar{\mathbf{x}} = \mathbf{T}_r^T (\mathbf{x} - \mathbf{x}_I) \quad (5.28b)$$

The translations $\bar{\mathbf{d}}$ relative to the element frame become

$$\bar{\mathbf{d}} = \bar{\mathbf{x}} - \bar{\mathbf{x}}^0 = \mathbf{T}_r^T (\mathbf{x} - \mathbf{x}_I) - \mathbf{T}_r^{0T} (\mathbf{x}^0 - \mathbf{x}_I^0) \quad (5.29)$$

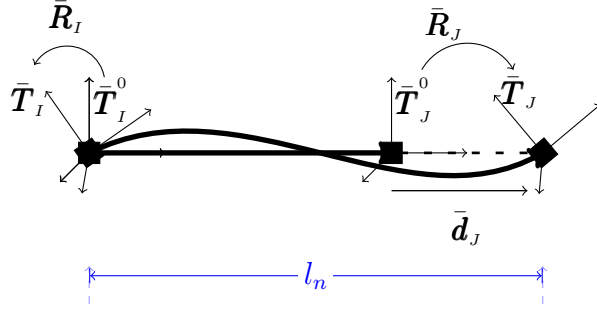


Figure 5.4: Kinematics in element frame

It is also straightforward to express the rotation matrix $\bar{\mathbf{R}}$ relative to the element frame with

$$\bar{\mathbf{R}} = \mathbf{T}_r^T \mathbf{R} \mathbf{T}_r^0 \quad (5.30)$$

The rotation vector associated with rotation matrix $\bar{\mathbf{R}}$ is denoted with $\bar{\boldsymbol{\vartheta}}$.

Incremental analysis requires the variation of the translations $\bar{\mathbf{d}}$ and the rotations $\bar{\boldsymbol{\vartheta}}$. In the following these variations are established first relative to a fixed element frame, and this information is subsequently used to set up the variations relative to a moving element frame. For a fixed element frame \mathbf{T}_r the variation of the translations $\bar{\mathbf{d}}$ in equation (5.29) is rather straightforward. It gives

$$\delta \bar{\mathbf{d}} = \mathbf{T}_r^T \delta \mathbf{d} \quad (5.31)$$

where the term $\delta \mathbf{x}_i$ is omitted following Nour-Omid and Rankin [65], because it is assumed that the element response is invariant under rigid body translations.

For determining the variation of the rotations $\bar{\boldsymbol{\vartheta}}$ relative to a fixed element frame equation (5.30) gives the variation of the rotation matrix

$$\delta \bar{\mathbf{R}} = \mathbf{T}_r^T (\delta \mathbf{R}) \mathbf{T}_r^0$$

From this equation it is possible to determine the spatial angular variation relative to a fixed element frame $\delta \bar{\boldsymbol{\theta}}$ by making use of equation (5.12)

$$\begin{aligned} Sp(\delta \bar{\boldsymbol{\theta}}) \bar{\mathbf{R}} &= \mathbf{T}_r^T Sp(\delta \boldsymbol{\theta}) \mathbf{R} \mathbf{T}_r^0 \\ \Rightarrow Sp(\delta \bar{\boldsymbol{\theta}}) \mathbf{T}_r^T \mathbf{R} \mathbf{T}_r^0 &= \mathbf{T}_r^T Sp(\delta \boldsymbol{\theta}) \mathbf{R} \mathbf{T}_r^0 \\ \Rightarrow Sp(\delta \bar{\boldsymbol{\theta}}) &= \mathbf{T}_r^T Sp(\delta \boldsymbol{\theta}) \mathbf{T}_r \end{aligned} \quad (5.32)$$

and then proceeding as follows

$$\begin{aligned} \forall \mathbf{x}, \quad \delta \bar{\boldsymbol{\theta}} \times \mathbf{x} &= Sp(\delta \bar{\boldsymbol{\theta}}) \mathbf{x} = \mathbf{T}_r^T Sp(\delta \boldsymbol{\theta}) \mathbf{T}_r \mathbf{x} \\ &= \mathbf{T}_r^T [\delta \boldsymbol{\theta} \times (\mathbf{T}_r \mathbf{x})] \\ &= (\mathbf{T}_r^T \delta \boldsymbol{\theta}) \times \mathbf{x} \end{aligned}$$

which leads to the following relation for the transformation of the spatial angular variation from the global to the element frame

$$\delta\bar{\boldsymbol{\theta}} = \mathbf{T}_r^T \delta\boldsymbol{\theta} \quad (5.33)$$

With the translation variation and the spatial angular variation relative to the global and the local reference frame collected in vectors $\delta\mathbf{u}$ and $\delta\bar{\mathbf{u}}$, respectively, equations (5.31) and (5.33) can be written in compact form as

$$\delta\bar{\mathbf{u}} = \begin{pmatrix} \delta\bar{\mathbf{d}} \\ \delta\bar{\boldsymbol{\theta}} \end{pmatrix} = \begin{bmatrix} \mathbf{T}_r^T & 0 \\ 0 & \mathbf{T}_r^T \end{bmatrix} \begin{pmatrix} \delta\mathbf{d} \\ \delta\boldsymbol{\theta} \end{pmatrix} = \begin{bmatrix} \mathbf{T}_r^T & 0 \\ 0 & \mathbf{T}_r^T \end{bmatrix} \delta\mathbf{u} \quad (5.34)$$

After establishing the translation variation and the spatial angular variation relative to a fixed element frame, the next step involves establishing these variations relative to a moving element frame \mathbf{T}_r . To this end, the notion of the corotating objective rate is introduced, which denotes the variation of a variable for an observer moving with the element frame. If \mathbf{v} is a vector in the global frame and $\bar{\mathbf{v}} = \mathbf{T}_r^T \mathbf{v}$ the same vector in the element frame, its variation relative to the element frame takes into account the change of frame orientation. Viewing the frame triad \mathbf{T}_r as a rotation matrix and making use of equation (5.12) for establishing the spatial angular variation $\delta\boldsymbol{\theta}_r$ of the frame triad \mathbf{T}_r in the global frame gives the following result for the corotating objective rate $\delta_r \bar{\mathbf{v}}$ of vector $\bar{\mathbf{v}}$

$$\begin{aligned} \delta_r \bar{\mathbf{v}} &= \mathbf{T}_r^T \delta\mathbf{v} + \delta\mathbf{T}_r^T \mathbf{v} \\ &= \mathbf{T}_r^T \delta\mathbf{v} + [Sp(\delta\boldsymbol{\theta}_r)\mathbf{T}_r]^T \mathbf{v} \\ &= \mathbf{T}_r^T \delta\mathbf{v} + [\mathbf{T}_r Sp(\delta\bar{\boldsymbol{\theta}}_r)]^T \mathbf{v} \\ &= \mathbf{T}_r^T \delta\mathbf{v} - Sp(\delta\bar{\boldsymbol{\theta}}_r) \bar{\mathbf{v}} \\ &= \delta\bar{\mathbf{v}} - Sp(\delta\bar{\boldsymbol{\theta}}_r) \bar{\mathbf{v}} \end{aligned}$$

where $\delta\bar{\boldsymbol{\theta}}_r$ denotes the spatial angular variation of the frame triad \mathbf{T}_r in the local frame, and equation (5.33) was used for the relation between $\delta\boldsymbol{\theta}_r$ and $\delta\bar{\boldsymbol{\theta}}_r$. In conclusion, the corotating objective rate $\delta_r \bar{\mathbf{v}}$ of a vector $\bar{\mathbf{v}}$ in the element frame is

$$\delta_r \bar{\mathbf{v}} = \delta\bar{\mathbf{v}} - Sp(\delta\bar{\boldsymbol{\theta}}_r) \bar{\mathbf{v}} = \delta\bar{\mathbf{v}} - \delta\bar{\boldsymbol{\theta}}_r \times \bar{\mathbf{v}} \quad (5.35)$$

with $\delta_r(\cdot)$ denoting the variation relative to a moving frame and $\delta(\cdot)$ the variation relative to a fixed frame. Rankin and Nour-Omid [76] and Nour-Omid and Rankin [65] in their seminal study define two variational symbols for differentiating the variation relative to a fixed element frame from the variation relative to a moving frame. Here a single symbol δ is used for the variation with the addition of a subscript r to denote the variation relative to a moving element frame.

Applying equation (5.35) to the translation variation $\delta\bar{\mathbf{d}}$ in equation (5.31) gives

$$\delta_r \bar{\mathbf{d}} = \delta\bar{\mathbf{d}} + \bar{\mathbf{d}} \times \delta\bar{\boldsymbol{\theta}}_r = \delta\bar{\mathbf{d}} + \bar{\mathbf{x}} \times \delta\bar{\boldsymbol{\theta}}_r \quad (5.36)$$

after setting $\bar{\mathbf{d}} = \bar{\mathbf{x}}$ by omitting $\delta \mathbf{x}_I$ following Nour-Omid and Rankin [65]. Haugen [40] and Felippa and Haugen [26] include $\delta \mathbf{x}_I$ in their work, which adds another projection matrix to the final equation (5.45).

Applying equation (5.35) to the spatial angular variation $\delta \bar{\boldsymbol{\theta}}$ in equation (5.33) gives

$$\delta_r \bar{\boldsymbol{\theta}} = \delta \bar{\boldsymbol{\theta}} - Sp(\delta \bar{\boldsymbol{\theta}}_r) \delta \bar{\boldsymbol{\theta}} = \delta \bar{\boldsymbol{\theta}} - \delta \bar{\boldsymbol{\theta}}_r \quad (5.37)$$

With the definition of the displacement vector variation $\delta \bar{\mathbf{u}}$ the above two equations can be combined into a single expression of the following form

$$\begin{aligned} \delta_r \bar{\mathbf{u}} &= \begin{pmatrix} \delta_r \bar{\mathbf{d}} \\ \delta_r \bar{\boldsymbol{\theta}} \end{pmatrix} = \begin{pmatrix} \delta \bar{\mathbf{d}} \\ \delta \bar{\boldsymbol{\theta}} \end{pmatrix} - \begin{bmatrix} -Sp(\bar{\mathbf{x}}) \\ \mathbf{I}_3 \end{bmatrix} \delta \bar{\boldsymbol{\theta}}_r \\ &= \delta \bar{\mathbf{u}} - \begin{bmatrix} -Sp(\bar{\mathbf{x}}) \\ \mathbf{I}_3 \end{bmatrix} \delta \bar{\boldsymbol{\theta}}_r \end{aligned} \quad (5.38)$$

The element frame for the 3d beam is defined by the displacement vectors at end nodes I and J. Consequently, the spatial angular rotation $\delta \bar{\boldsymbol{\theta}}_r$ of the element frame during deformation is associated with the displacement variations at end nodes I and J denoted with $\delta \bar{\mathbf{u}}_I$ and $\delta \bar{\mathbf{u}}_J$, respectively. It is expressed as follows

$$\delta \bar{\boldsymbol{\theta}}_r = \begin{bmatrix} \frac{\partial \bar{\boldsymbol{\theta}}_r}{\partial \bar{\mathbf{u}}_I} & \frac{\partial \bar{\boldsymbol{\theta}}_r}{\partial \bar{\mathbf{u}}_J} \end{bmatrix} \begin{pmatrix} \delta \bar{\mathbf{u}}_I \\ \delta \bar{\mathbf{u}}_J \end{pmatrix} = \mathbf{G} \begin{pmatrix} \delta \bar{\mathbf{u}}_I \\ \delta \bar{\mathbf{u}}_J \end{pmatrix} \quad (5.39)$$

where the rotation gradient matrix \mathbf{G} describes the change of the element frame in the local reference. Substituting equation (5.39) in equation (5.38) gives the following result for the displacement variation of a point of the 3d beam element

$$\delta_r \bar{\mathbf{u}} = \begin{pmatrix} \delta_r \bar{\mathbf{d}} \\ \delta_r \bar{\boldsymbol{\theta}} \end{pmatrix} = \begin{pmatrix} \delta \bar{\mathbf{d}} \\ \delta \bar{\boldsymbol{\theta}} \end{pmatrix} - \begin{bmatrix} -Sp(\bar{\mathbf{x}}) \\ \mathbf{I}_3 \end{bmatrix} \mathbf{G} \begin{pmatrix} \delta \bar{\mathbf{u}}_I \\ \delta \bar{\mathbf{u}}_J \end{pmatrix} \quad (5.40)$$

With the choice of element frame in section 5.3.1 the rotation gradient matrix \mathbf{G} is

$$\mathbf{G} = \begin{bmatrix} 0 & 0 & \eta/l_n & \eta_1/2 & -\eta_3/2 & 0 & 0 & 0 & -\eta/l_n & \eta_2/2 & -\eta_4/2 & 0 \\ 0 & 0 & 1/l_n & 0 & 0 & 0 & 0 & 0 & -1/l_n & 0 & 0 & 0 \\ 0 & -1/l_n & 0 & 0 & 0 & 0 & 0 & 1/l_n & 0 & 0 & 0 & 0 \end{bmatrix} \quad (5.41)$$

where l_n denotes the element length in the deformed configuration which is equal to the distance between end nodes I and J. The coefficients η along with details of the derivation are provided in the report by Le Corvec [49]. For practical purposes η , η_3 and η_4 are approximately equal to zero, while η_1 and η_2 are approximately equal to 1.

The application of equation (5.40) to the end displacements of a two node 3d beam element gives

$$\begin{pmatrix} \delta_r \bar{\mathbf{u}}_I \\ \delta_r \bar{\mathbf{u}}_J \end{pmatrix} = \left(\begin{bmatrix} \mathbf{I}_3 & 0 & 0 \\ 0 & \mathbf{I}_3 & 0 \\ 0 & 0 & \mathbf{I}_3 \\ 0 & 0 & 0 & \mathbf{I}_3 \end{bmatrix} - \begin{bmatrix} -Sp(\bar{\mathbf{x}}_I) \\ \mathbf{I}_3 \\ -Sp(\bar{\mathbf{x}}_J) \\ \mathbf{I}_3 \end{bmatrix} \mathbf{G} \right) \begin{pmatrix} \delta \bar{\mathbf{u}}_I \\ \delta \bar{\mathbf{u}}_J \end{pmatrix}$$

Using equation (5.34) to transform the end node displacements from the local to the global reference frame gives

$$\begin{pmatrix} \delta_r \bar{\mathbf{u}}_I \\ \delta_r \bar{\mathbf{u}}_J \end{pmatrix} = \left(\begin{bmatrix} \mathbf{I}_3 & 0 & 0 & \\ 0 & \mathbf{I}_3 & 0 & 0 \\ 0 & 0 & \mathbf{I}_3 & 0 \\ 0 & 0 & 0 & \mathbf{I}_3 \end{bmatrix} - \begin{bmatrix} -Sp(\bar{\mathbf{x}}_I) \\ \mathbf{I}_3 \\ -Sp(\bar{\mathbf{x}}_J) \\ \mathbf{I}_3 \end{bmatrix} \mathbf{G} \right) \begin{bmatrix} \mathbf{T}_r^T & 0 & 0 \\ 0 & \mathbf{T}_r^T & 0 & 0 \\ 0 & 0 & \mathbf{T}_r^T & 0 \\ 0 & 0 & 0 & \mathbf{T}_r^T \end{bmatrix} \begin{pmatrix} \delta \mathbf{u}_I \\ \delta \mathbf{u}_J \end{pmatrix} \quad (5.42)$$

With the definition

$$\mathbf{L} = \begin{bmatrix} -Sp(\bar{\mathbf{x}}_I) \\ \mathbf{I}_3 \\ -Sp(\bar{\mathbf{x}}_J) \\ \mathbf{I}_3 \end{bmatrix} \quad (5.43)$$

equation (5.42) can be written in compact form as

$$\delta_r \bar{\mathbf{u}} = \mathbf{a}_p \mathbf{a}_r \delta \mathbf{u} \quad (5.44)$$

where

$$\mathbf{a}_p = \mathbf{I}_{12} - \mathbf{L}\mathbf{G} \quad (5.45)$$

$$\mathbf{a}_r = \text{diag}(\mathbf{T}_r^T, \mathbf{T}_r^T, \mathbf{T}_r^T, \mathbf{T}_r^T) \quad (5.46)$$

with \mathbf{I}_{12} the identity matrix of dimension 12. In abuse of notation the vectors $\bar{\mathbf{u}}$ and \mathbf{u} from now on denote the displacements at *both ends* of the 3d beam element in the local and global reference frame, respectively.

The matrix \mathbf{a}_p is a projection matrix, because it satisfies $\mathbf{a}_p \mathbf{a}_p = \mathbf{a}_p$, which can be proven by considering that $\mathbf{G}\mathbf{L} = \mathbf{I}_3$. Matrix \mathbf{a}_p was called self-equilibrating by Haugen [40], because the multiplication by \mathbf{a}_p^T projects the element forces $\bar{\mathbf{p}}$, which are work conjugate to the end displacements $\bar{\mathbf{u}}$ in the local reference frame, onto a subspace of self-equilibrating forces. The matrix \mathbf{a}_r is the standard rotation matrix for the transformation of the element vectors from the global to the local reference system.

The principle of virtual displacements gives the relation between the forces \mathbf{p} in the global reference frame and the forces $\bar{\mathbf{p}}$ in the local frame

$$\delta \mathbf{u}^T \mathbf{p} = \delta \bar{\mathbf{u}}^T \bar{\mathbf{p}} \quad \Rightarrow \quad \mathbf{p} = \mathbf{a}_r^T \mathbf{a}_p^T \bar{\mathbf{p}} \quad (5.47)$$

With equation (5.47) the element response formulated in terms of the end forces $\bar{\mathbf{p}}$ as functions of the end displacements $\bar{\mathbf{u}}$ in the local reference frame can be transformed to the global reference frame.

5.3.3 Definition of strain in element frame

With the transformation relations of the preceding section it is now possible to express the strain tensor in the element frame. To this end equation (5.35) is used to express the deformation gradient $\bar{\mathbb{F}}$ in the element frame in terms of the deformation gradient \mathbb{F} in the global reference frame

$$\bar{\mathbb{F}} = \frac{\partial_r \bar{\mathbf{x}}}{\partial \bar{\mathbf{x}}^0} = \frac{\partial \bar{\mathbf{x}}}{\partial \bar{\mathbf{x}}^0} - \frac{\partial \bar{\boldsymbol{\theta}}_r}{\partial \bar{\mathbf{x}}^0} \times \bar{\mathbf{x}} = \frac{\partial \bar{\mathbf{x}}}{\partial \mathbf{x}} \frac{\partial \mathbf{x}}{\partial \mathbf{x}^0} \frac{\partial \mathbf{x}^0}{\partial \bar{\mathbf{x}}^0} - 0 = \mathbf{T}_r^T \mathbb{F} \mathbf{T}_r^0 \quad (5.48)$$

With equation (5.3) the deformation gradient $\bar{\mathbb{F}}$ in the element frame becomes

$$\bar{\mathbb{F}} = \bar{\mathbf{R}} \left[\mathbf{I}_3 + \zeta \mathbf{E}_1 \otimes \nabla \omega + \left\{ \bar{\boldsymbol{\Gamma}} + \bar{\mathbf{K}} \times \bar{\mathbf{T}}^T (\bar{\boldsymbol{\phi}}_m - \bar{\boldsymbol{\phi}}_c) + (\zeta \omega)' \mathbf{E}_1 \right\} \otimes \mathbf{E}_1 \right] \quad (5.49)$$

where the function $\bar{\boldsymbol{\phi}}_m$ gives the position of a material point m in the element frame and the triad $\bar{\mathbf{T}}$ is attached to the cross section and corresponds to the rotation $\bar{\mathbf{R}}$ of the cross section of an initially straight beam in the element frame. The following identities hold

$$\mathbf{T}^T (\boldsymbol{\phi}_m - \boldsymbol{\phi}_c) = \bar{\mathbf{T}}^T (\bar{\boldsymbol{\phi}}_m - \bar{\boldsymbol{\phi}}_c) \quad (5.50)$$

The section strain measures $\boldsymbol{\Gamma}$ and \mathbf{K} in equation (5.4) do not change from the global to the local reference frame because of the following relations

$$\boldsymbol{\Gamma} = \mathbf{T}^T (\boldsymbol{\phi}'_c - \mathbf{t}_1) = \bar{\mathbf{T}}^T (\bar{\boldsymbol{\phi}}'_c - \bar{\mathbf{t}}_1) = \bar{\boldsymbol{\Gamma}} \quad (5.51a)$$

$$Sp(\mathbf{K}) = \mathbf{T}^T \mathbf{T}' = \bar{\mathbf{R}}^T \bar{\mathbf{R}}' = Sp(\bar{\mathbf{K}}) \quad (5.51b)$$

a fact known as strain invariance under superimposed rigid body motion.

With the deformation gradient $\bar{\mathbb{F}}$ the Green-Lagrange strain in the element frame $\bar{\mathbb{E}}$ can be expressed in terms of the Green-Lagrange strain in the global frame \mathbb{E} according to

$$\bar{\mathbb{E}} = \frac{1}{2} (\bar{\mathbb{F}}^T \bar{\mathbb{F}} - \mathbf{I}) = \mathbf{T}_r^{0T} \mathbb{E} \mathbf{T}_r^0 \quad (5.52)$$

After the definition of the consistent Green-Lagrange strain in the element frame the following discussion deals with the conditions that permit the approximation of the actual rod kinematics by small strains in the element frame of the corotational formulation.

To this end the measure of strain *smallness* ϵ_0 is introduced due to Naghdi and Vongsarnpigoon [64].

$$\epsilon_0 = \sup_{\mathbf{x}^0 \in el} \|\mathbb{E}(\mathbf{x}^0)\| \quad (5.53)$$

This definition of smallness is valid in the global as well as in the element frame, because the Green-Lagrange tensor in the two frames in equation (5.52) differs only by a constant rotation, which does not affect the tensor norm.

A necessary condition for the approximation of the actual rod kinematics by small strains is the Euler-Bernoulli assumption of beam theory that plane sections remain plane after deformation and normal to the axis of the rod. Consequently, the shear strains are neglected in the following discussion and the components of the section strain measures in equation (5.51) are

$$\bar{\mathbf{T}} = [\bar{\epsilon} \quad 0 \quad 0]^T \quad (5.54a)$$

$$\bar{\mathbf{K}} = [\bar{\kappa}_1 \quad \bar{\kappa}_2 \quad \bar{\kappa}_3]^T \quad (5.54b)$$

With the Euler-Bernoulli assumption the Green-Lagrange strain in the element frame can be simplified, if it is further assumed that $\bar{\epsilon}$, $\bar{\kappa}_2$, $\bar{\kappa}_3$, $(\zeta\omega)'$ are of higher order than the curvature $\bar{\kappa}_1$, so that only the latter appears in a quadratic term. Under these assumptions the non-zero components of the Green-Lagrange tensor are

$$\bar{\mathbb{E}}_{11} = \bar{\epsilon} - X_2\bar{\kappa}_3 + X_3\bar{\kappa}_2 + (\omega\zeta)' + \frac{1}{2}(X_2^2 + X_3^2)\bar{\kappa}_1^2 \quad (5.55a)$$

$$2\bar{\mathbb{E}}_{12} = -X_3\bar{\kappa}_1 + \zeta \frac{\partial \omega}{\partial X_2} \quad (5.55b)$$

$$2\bar{\mathbb{E}}_{13} = X_2\bar{\kappa}_1 + \zeta \frac{\partial \omega}{\partial X_3} \quad (5.55c)$$

in agreement with the definition by Nukala and White [66]. The only quadratic term in the approximation of the Green-Lagrange strains in the element frame appears in equation (5.55a) in the form of the Wagner term due to torsion. The other contributions to the strain $\bar{\mathbb{E}}_{11}$ are the axial strain at the origin of the section coordinates, and the normal strain due to bending and warping.

After the approximation of the Green-Lagrange strains in the element frame in the context of the strain smallness measure ϵ_0 , the next task involves the linearization of the strain measures $\bar{\mathbf{T}}$ and $\bar{\mathbf{K}}$ in equation (5.51) in terms of ϵ_0 and the element length l .

In the corotational formulation, the element frame accounts for the rigid body rotations and translations. Consequently, it is assumed that the translations and rotations relative to the element frame become *small* as the element mesh is refined and the element length gets smaller. As a result, linear strain kinematics suffice in the element frame, with the expectation that the nonlinear kinematic terms will be accounted for by the geometric transformations of the element variables due to the motion of the element frame. However, the strains in the element frame depend not only on the local displacement values, but also on the local displacement changes, such as the rate of twist, which are not affected by the reduction of the element length during mesh refinement. Consequently, the nonlinear Wagner term involving $\bar{\kappa}_1$ in equation (5.55a) will not be captured by the corotational formulation in the limit unless it is either included in the beam formulation relative to the element frame, or else is expressed in terms of the end node variables, as will be discussed in section 5.4. For this reason, the linear kinematic assumption of the 3d beam formulation relative to the

element frame holds true for problems for which the nonlinear Wagner term is not significant. An approximate solution for including the nonlinear Wagner term in the framework of the corotational formulation will be discussed in section 5.4.

The justification of the linear geometry assumption in the element frame is based on showing first that the rotations are small in the element frame. To this end, one starts from the statement that under small strains the rotation in the global reference frame at any point of the 3d beam can be related to the rotation at node I

$$\mathbf{R} = \mathbf{R}_I + O(\epsilon_0) \quad \text{or} \quad \mathbf{T} = \mathbf{T}_I + O(\epsilon_0) \quad \text{as} \quad \epsilon_0 \rightarrow 0 \quad (5.56)$$

Recalling the definition of the element frame \mathbf{T}_r from section 5.3.1 the first axis points in the direction of the element chord according to equation (5.22)

$$\mathbf{T}_r \mathbf{E}_1 = \mathbf{t}_{r1} = \frac{\mathbf{x}_J - \mathbf{x}_I}{\|\mathbf{x}_J - \mathbf{x}_I\|} \quad (5.57)$$

As the element length l gets smaller the element frame triad converges to a triad tangent to the deformed shape at node I according to

$$\lim_{l \rightarrow 0} \mathbf{t}_{r1} = \lim_{\mathbf{x}_J \rightarrow \mathbf{x}_I} \frac{\mathbf{x}_J - \mathbf{x}_I}{\|\mathbf{x}_J - \mathbf{x}_I\|} = \frac{1}{\|\partial \phi_c / \partial s\|} \frac{\partial \phi_c}{\partial s} = \mathbf{t}_{I1}$$

where the Euler-Bernoulli assumption is invoked in the last step to conclude that \mathbf{t}_{I1} coincides with the tangent to the deformed shape. The last equation leads to the conclusion that

$$\mathbf{t}_{r1} = \mathbf{t}_{I1} + O(l) \quad \text{as} \quad l \rightarrow 0 \quad (5.58)$$

For the second axis at nodes I and J equation (5.56) leads to the conclusion that

$$\mathbf{t}_{I2} = \mathbf{t}_{J2} + O(\epsilon_0) \quad \text{as} \quad \epsilon_0 \rightarrow 0 \quad (5.59)$$

With equation (5.23) this leads to the conclusion that

$$\mathbf{t}_{r2}^{try} = \frac{1}{2}(\mathbf{t}_{I2} + \mathbf{t}_{J2}) = \mathbf{t}_{I2} + O(\epsilon_0) \quad \text{as} \quad \epsilon_0 \rightarrow 0 \quad (5.60)$$

so that, finally, the element frame triad satisfies the following relation

$$\mathbf{T}_r = \mathbf{T}_I + O(\epsilon_0 l) \quad \text{as} \quad \epsilon_0, l \rightarrow 0 \quad (5.61)$$

When combined with equation (5.56) the last equation shows that the rotations are small in the element frame

$$\bar{\mathbf{R}} = \mathbf{T}_r^T \mathbf{T} = \mathbf{I}_3 + O(\epsilon_0 l) \quad \text{as} \quad \epsilon_0, l \rightarrow 0 \quad (5.62)$$

justifying the first order approximation of the rotation matrices in the element frame according to

$$\bar{\mathbf{R}} = \mathbf{I}_3 + Sp(\bar{\boldsymbol{\vartheta}}) \quad (5.63)$$

Because of the use of the Euler-Bernoulli assumption of plane sections remaining plane and normal to the element axis in the description of the first element frame axis at node I, the use of the corotational formulation for 3d beams based on the Timoshenko theory for shear requires further study.

Following the preceding derivations the first order terms of the section strain measures in equation (5.51) are

$$\bar{\Gamma} = \bar{\mathbf{R}}^T (\bar{\phi}'_c - \bar{\mathbf{t}}_1) = \bar{\mathbf{R}}^T \left(\begin{bmatrix} 1 + \bar{d}'_1 \\ \bar{d}'_2 \\ \bar{d}'_3 \end{bmatrix} - \bar{\mathbf{t}}_1 \right) \approx \begin{bmatrix} \bar{d}'_1 \\ 0 \\ 0 \end{bmatrix} \quad (5.64a)$$

$$\bar{\mathbf{K}} = axial(Sp(\bar{\mathbf{K}})) \approx axial(\bar{\mathbf{R}}') \approx \begin{bmatrix} \bar{\vartheta}'_1 \\ \bar{\vartheta}'_2 \\ \bar{\vartheta}'_3 \end{bmatrix} \quad (5.64b)$$

These section strain measures are used in the definition of the Green-Lagrange strain tensor in the element frame in equation (5.55).

5.3.4 Consistent stiffness matrix

The consistent tangent element stiffness matrix \mathbf{k} is obtained by differentiation of the element end forces in equation (5.47). Noting that the transformation matrices \mathbf{a}_p in equation (5.45) and \mathbf{a}_r in equation (5.46) depend on the element end displacements $\bar{\mathbf{u}}$ in the element frame requires use of the product rule of differentiation according to

$$\mathbf{k} = \frac{\partial \mathbf{p}}{\partial \mathbf{u}} = \mathbf{a}_r^T \mathbf{a}_p^T \frac{\partial \bar{\mathbf{p}}}{\partial \bar{\mathbf{u}}} \mathbf{a}_p \mathbf{a}_r + \left. \frac{\partial (\mathbf{a}_r^T \mathbf{a}_p^T \bar{\mathbf{p}})}{\partial \bar{\mathbf{u}}} \right|_{\bar{\mathbf{p}}} \quad (5.65)$$

with the derivative of the second term determined under constant $\bar{\mathbf{p}}$. The tangent element stiffness matrix is thus made up of two contributions: the first contribution is the material stiffness \mathbf{k}_m

$$\mathbf{k}_m = \mathbf{a}_r^T \mathbf{a}_p^T \frac{\partial \bar{\mathbf{p}}}{\partial \bar{\mathbf{u}}} \mathbf{a}_p \mathbf{a}_r$$

and the second contribution is the geometric stiffness \mathbf{k}_g

$$\mathbf{k}_g = \left. \frac{\partial (\mathbf{a}_r^T \mathbf{a}_p^T \bar{\mathbf{p}})}{\partial \bar{\mathbf{u}}} \right|_{\bar{\mathbf{p}}} \quad (5.66)$$

The derivation of the geometric stiffness matrix can be found in the original paper of Nour-Omid and Rankin [65] and was later restated by Battini and Pacoste [8]. Details of the derivation are available in the report by Le Corvec [49]. According to the latter report the geometric stiffness matrix can be written in compact form as

$$\mathbf{k}_g = -\mathbf{a}_r^T (\mathbf{G}^T \mathbf{P}_n^T \mathbf{a}_p + \mathbf{P}_{nm} \mathbf{G}) \mathbf{a}_r \quad (5.67)$$

with the first term in parentheses arising from the derivative of the projection matrix \mathbf{a}_p and the second term from the derivative of the rotation matrix \mathbf{a}_r . Denoting the *self-equilibrating* element nodal forces with $\bar{\mathbf{p}}^e = \mathbf{a}_p^T \bar{\mathbf{p}}$

$$\bar{\mathbf{p}}^e = \begin{pmatrix} \bar{\mathbf{n}}^e \\ \bar{\mathbf{m}}^e \end{pmatrix}$$

where $\bar{\mathbf{n}}^e$ denotes the end forces and $\bar{\mathbf{m}}^e$ the end moments, gives the following result for the matrices \mathbf{P}_n and \mathbf{P}_{nm} in equation (5.67)

$$\mathbf{P}_n = \begin{bmatrix} Sp(\bar{\mathbf{n}}_I^e) \\ \mathbf{0}_3 \\ Sp(\bar{\mathbf{n}}_J^e) \\ \mathbf{0}_3 \end{bmatrix} \quad \mathbf{P}_{nm} = \begin{bmatrix} Sp(\bar{\mathbf{n}}_I^e) \\ Sp(\bar{\mathbf{m}}_I^e) \\ Sp(\bar{\mathbf{n}}_J^e) \\ Sp(\bar{\mathbf{m}}_J^e) \end{bmatrix} \quad (5.68)$$

where the subscript I and J denotes the force variables at node I and node J, respectively.

5.3.5 Transformations due to rotation parametrization

The derivation of the corotational transformation relations for the element response in the preceding sections is based on the spatial angular variation $\delta\boldsymbol{\theta}$, which differs from the variation of the rotation vector $\delta\boldsymbol{\vartheta}$. As discussed in section 5.2, the lack of an additive update for the rotation vectors requires transformations from one form of rotation parametrization to another. These transformations are necessary in the element frame as well as in the global reference frame and give rise to additional contributions to the geometric stiffness in equation (5.67).

In the **element frame** the rotation is represented by matrix $\bar{\mathbf{R}}$ or by rotation vector $\bar{\boldsymbol{\vartheta}}$, which is included in the displacement vector $\bar{\mathbf{a}}$. The element end forces conjugate to this displacement vector are denoted with $\bar{\mathbf{p}}$

$$\bar{\mathbf{p}} = \begin{pmatrix} \bar{\mathbf{n}} \\ \bar{\mathbf{m}} \end{pmatrix} \quad (5.69)$$

The force vector $\bar{\mathbf{p}}(\bar{\mathbf{a}})$ represents the resisting forces of the element response. Since $\delta\bar{\boldsymbol{\theta}} \neq \delta\bar{\boldsymbol{\vartheta}}$, an additional transformation matrix is required to convert the forces $\bar{\mathbf{p}}$ to the end forces $\bar{\mathbf{p}}$ in the element frame, which are conjugate with $\bar{\mathbf{u}}$. This requirement is discussed in the original paper by Nour-Omid and Rankin [65], where the exact transformation is derived. Under the assumption of small rotations in the element frame in section 5.3.3 an approximate transformation may be used in this case following the idea of Battini [5] for shell elements. Both the exact and the approximate transformation are presented in the following.

- The relation between the spatial angular variation $\delta\bar{\boldsymbol{\theta}}$ and the variation of the rotation vector $\delta\bar{\boldsymbol{\vartheta}}$ is given by

$$\delta\bar{\boldsymbol{\vartheta}} = h_\theta^{-1}(\bar{\boldsymbol{\vartheta}})\delta\bar{\boldsymbol{\theta}}$$

with $h_\theta^{-1}(\bar{\vartheta})$ from equation (5.17). With the principle of virtual displacements the moments $\bar{\mathbf{m}}$ and $\bar{\mathbf{n}}$ are related by

$$\bar{\mathbf{m}} = h_\theta^{-T}(\bar{\vartheta})\bar{\mathbf{n}} \quad (5.70)$$

The transformation from spatial angular variation to variation of rotation vector gives rise to the following transformation matrix \mathbf{a}_θ

$$\mathbf{a}_\theta = \begin{bmatrix} \mathbf{I}_3 & 0 & 0 & 0 \\ 0 & h_\theta^{-1}(\bar{\vartheta}_I) & 0 & 0 \\ 0 & 0 & \mathbf{I}_3 & 0 \\ 0 & 0 & 0 & h_\theta^{-1}(\bar{\vartheta}_J) \end{bmatrix} \quad (5.71)$$

The force transformation in equation (5.47) can be rewritten as

$$\mathbf{p} = \mathbf{a}_r^T \mathbf{a}_p^T \mathbf{a}_\theta^T \bar{\mathbf{p}} \quad (5.72)$$

The consistent stiffness matrix for this expression of the end forces is

$$\mathbf{k} = \mathbf{a}_r^T \mathbf{a}_p^T \mathbf{a}_\theta^T \frac{\partial \bar{\mathbf{p}}}{\partial \bar{\mathbf{a}}} \mathbf{a}_\theta \mathbf{a}_p \mathbf{a}_r + \mathbf{k}_g + \mathbf{k}_{g\theta} \quad (5.73)$$

An additional geometric stiffness $\mathbf{k}_{g\theta}$ arises from the derivative of transformation matrix \mathbf{a}_θ^T according to

$$\mathbf{k}_{g\theta} = \begin{bmatrix} 0 & 0 & 0 & 0 \\ 0 & \frac{\partial [h_\theta^{-T}(\bar{\vartheta}_I)\bar{\mathbf{n}}_I]}{\partial \bar{\vartheta}} & 0 & 0 \\ 0 & 0 & 0 & 0 \\ 0 & 0 & 0 & \frac{\partial [h_\theta^{-T}(\bar{\vartheta}_J)\bar{\mathbf{n}}_J]}{\partial \bar{\vartheta}} \end{bmatrix} \bar{\mathbf{n}}_I, \bar{\mathbf{n}}_J \quad (5.74)$$

The differential in matrix $\mathbf{k}_{g\theta}$ under constant $\bar{\mathbf{n}}$ is

$$\left. \frac{\partial [h_\theta^{-T}(\bar{\vartheta})\bar{\mathbf{n}}]}{\partial \bar{\vartheta}} \right|_{\bar{\mathbf{n}}} = \left[-\frac{1}{2}Sp(\bar{\mathbf{n}}) + \eta \left(\bar{\vartheta}^T \bar{\mathbf{n}} I + \bar{\vartheta} \bar{\mathbf{n}}^T - 2\bar{\mathbf{n}} \bar{\vartheta}^T \right) + \mu Sp(\bar{\vartheta})^2 \bar{\mathbf{n}} \bar{\vartheta}^T \right] h_\theta \quad (5.75)$$

where the coefficients η and μ are

$$\eta = \frac{\sin(\frac{\bar{\vartheta}}{2}) - \frac{\bar{\vartheta}}{2} \cos(\frac{\bar{\vartheta}}{2})}{\bar{\vartheta}^2 \sin(\frac{\bar{\vartheta}}{2})} \quad \mu = \frac{\bar{\vartheta} [\bar{\vartheta} + \sin(\bar{\vartheta})] - 8 \sin(\frac{\bar{\vartheta}}{2})^2}{4\bar{\vartheta}^4 \sin(\frac{\bar{\vartheta}}{2})^2} \quad (5.76)$$

- If the rotation in the element frame can be assumed *small* according to section (5.3.3), then the preceding transformation \mathbf{a}_θ can either be approximated or neglected. According to Nour-Omid and Rankin [65] and Battini and Pacoste [8] neglecting the

transformation \mathbf{a}_θ affects the convergence of the numerical solution. Consequently, it is advisable to approximate the matrix \mathbf{a}_θ by retaining the first order terms in $\bar{\boldsymbol{\vartheta}}$. To this end the transformation h_θ^{-1} in equation (5.17) is rewritten as

$$h_\theta^{-1}(\bar{\boldsymbol{\vartheta}}) = \mathbf{I}_3 - \frac{1}{2}Sp(\bar{\boldsymbol{\vartheta}}) + O(\bar{\boldsymbol{\vartheta}}) \quad (5.77)$$

The corresponding geometric tangent stiffness $\mathbf{k}_{g\theta}$ involves the following term on the diagonal according to equation (5.74)

$$\left. \frac{\partial [h_\theta^{-T}(\bar{\boldsymbol{\vartheta}})\bar{\mathbf{m}}]}{\partial \bar{\boldsymbol{\vartheta}}} \right|_{\bar{\mathbf{m}}} = -\frac{1}{2}Sp(\bar{\mathbf{m}}) \quad (5.78)$$

The resulting expression for $\mathbf{k}_{g\theta}$ is similar to the transformation matrix used by Battini and Pacoste [8].

A study with the full and the approximate expression of h_θ^{-1} leads to the conclusion that the numerical convergence and the final results are not affected by the approximation. Consequently, the approximate solution is completely sufficient for practical applications. Only problems with very large rotations, such as the example for the hocking cable in section 5.5, justify the use of the full expression for h_θ^{-1} .

In the **global reference frame** the need for avoiding the multiplicative update of the rotation vectors at the nodes of the finite element mesh necessitates the transformation from the spatial variation vector $\delta\boldsymbol{\theta}$ to either the variation of the rotation vector $\delta\boldsymbol{\vartheta}$, or the variation of the quaternion vector $\delta\boldsymbol{\vartheta}_q$. The transformation to the variation of the rotation vector $\delta\boldsymbol{\vartheta}$ introduces another transformation matrix involving h_θ according to equation (5.15). Because the rotations are large in the global reference frame, the expression for h_θ in equation (5.16) cannot be simplified.

The alternative approach is to use the transformation to the variation of the quaternion vector following equation (5.20), as proposed by Battini [5]

$$\delta\boldsymbol{\theta} = h_q(\boldsymbol{\vartheta}_q)\delta\boldsymbol{\vartheta}_q$$

The compact expression of h_q in equation (5.20) makes this choice more attractive than the first approach from the computational standpoint. The introduction of quaternions $\boldsymbol{\vartheta}_q$ for the parametrization of rotations is associated with the definition of a new force vector \mathbf{p}_q conjugate to \mathbf{u}_q

$$\mathbf{p}_q = \begin{pmatrix} \mathbf{n} \\ \mathbf{m}_q \end{pmatrix} \quad (5.79)$$

where the moments \mathbf{m}_q are related to the moments \mathbf{m} of the end force vector \mathbf{p} by the principle of virtual displacements

$$\mathbf{m}_q = h_q(\boldsymbol{\vartheta}_q)^T \mathbf{m} \quad (5.80)$$

The transformation to the variation of the quaternion vector thus involves a transformation matrix \mathbf{a}_q of the form

$$\mathbf{a}_q = \begin{bmatrix} \mathbf{I}_3 & 0 & 0 & 0 \\ 0 & h_q(\boldsymbol{\vartheta}_q) & 0 & 0 \\ 0 & 0 & \mathbf{I}_3 & 0 \\ 0 & 0 & 0 & h_q(\boldsymbol{\vartheta}_q) \end{bmatrix} \quad (5.81)$$

With it the force transformation in equation (5.72) takes the form

$$\mathbf{p}_q = \mathbf{a}_q^T \mathbf{a}_r^T \mathbf{a}_p^T \mathbf{a}_\theta^T \bar{\mathbf{p}} \quad (5.82)$$

and the consistent stiffness matrix in equation (5.73) becomes

$$\mathbf{k} = \mathbf{a}_q^T \mathbf{a}_r^T \mathbf{a}_p^T \mathbf{a}_\theta^T \frac{\partial \bar{\mathbf{p}}}{\partial \bar{\mathbf{a}}} \mathbf{a}_\theta \mathbf{a}_p \mathbf{a}_r \mathbf{a}_q + \mathbf{a}_q^T (\mathbf{k}_g + \mathbf{k}_{g\theta}) \mathbf{a}_q + \mathbf{k}_{gq} \quad (5.83)$$

where the additional geometric stiffness \mathbf{k}_{gq} comes from the derivative of the transformation matrix \mathbf{a}_q^T

$$\mathbf{k}_{gq} = \begin{bmatrix} 0 & 0 & 0 & 0 \\ 0 & \frac{\partial [h_q(\boldsymbol{\vartheta}_{qI})^T \mathbf{m}_I]}{\partial \boldsymbol{\vartheta}_{qI}} & 0 & 0 \\ 0 & 0 & 0 & 0 \\ 0 & 0 & 0 & \frac{\partial [h_q(\boldsymbol{\vartheta}_{qJ})^T \mathbf{m}_J]}{\partial \boldsymbol{\vartheta}_{qJ}} \end{bmatrix} \mathbf{m}_I, \mathbf{m}_J \quad (5.84)$$

where

$$\left. \frac{\partial [h_q(\boldsymbol{\vartheta}_q)^T \mathbf{m}]}{\partial \boldsymbol{\vartheta}_q} \right|_{\mathbf{m}} = \frac{2\boldsymbol{\vartheta}_q^T \mathbf{m}}{\vartheta_{q0}^3} \boldsymbol{\vartheta}_q \boldsymbol{\vartheta}_q^T + \frac{2}{\vartheta_{q0}} (\boldsymbol{\vartheta}_q \mathbf{m}^T - \mathbf{m} \boldsymbol{\vartheta}_q^T + \boldsymbol{\vartheta}_q^T \mathbf{m} I) + 2Sp(\mathbf{m}) \quad (5.85)$$

This result matches the component expression provided by Battini and Pacoste [8]. Details of the proof are available in the report by Le Corvec [49].

Local variables			Global variables	
$\delta \bar{\mathbf{a}} = [\delta \bar{\mathbf{d}} \ \delta \bar{\boldsymbol{\vartheta}}]$		$\delta \bar{\mathbf{u}} = [\delta \bar{\mathbf{d}} \ \delta \bar{\boldsymbol{\theta}}]$	$\delta \mathbf{u} = [\delta \mathbf{d} \ \delta \boldsymbol{\theta}]$	$\delta \mathbf{u}_q = [\delta \mathbf{d} \ \delta \boldsymbol{\vartheta}_q]$
$\bar{\mathbf{p}}$	\longrightarrow	$\bar{\mathbf{p}}$	\mathbf{p}	\mathbf{p}_q
	\mathbf{a}_θ^T		$\mathbf{a}_r^T \mathbf{a}_p^T$	\mathbf{a}_q^T

Table 5.1: Transformation sequence for corotational formulation

The corotational formulation thus involves the following element force transformation

$$\mathbf{p}_q = \mathbf{a}_q^T \mathbf{a}_r^T \mathbf{a}_p^T \mathbf{a}_\theta^T \bar{\mathbf{p}} \quad (5.86)$$

and the corresponding tangent element stiffness matrix is

$$\mathbf{k} = \mathbf{a}_q^T \mathbf{a}_r^T \mathbf{a}_p^T \mathbf{a}_\theta^T \frac{\partial \bar{\mathcal{P}}}{\partial \bar{\mathbf{a}}} \mathbf{a}_\theta \mathbf{a}_p \mathbf{a}_r \mathbf{a}_q + \mathbf{a}_q^T (\mathbf{k}_g + \mathbf{k}_{g\theta}) \mathbf{a}_q + \mathbf{k}_{gq} \quad (5.87)$$

The transformation sequence for the corotational formulation is summarized in table 5.1.

5.3.6 On the non-symmetry of the tangent stiffness

The geometric stiffness in equation (5.67) is non-symmetric. The antisymmetric contribution to the stiffness matrix is

$$\mathbf{k}_g^{as} = \frac{1}{2} (-\mathbf{G}^T \mathbf{L}^T \mathbf{P}_m \mathbf{G} + \mathbf{P}_m \mathbf{G} - \mathbf{G}^T \mathbf{P}_m) \quad (5.88)$$

According to equation (5.68) the matrix \mathbf{P}_m is

$$\mathbf{P}_m = \mathbf{P}_{nm} - \mathbf{P}_n = [\mathbf{0}_3 \quad Sp(\bar{\mathbf{m}}_I^e) \quad \mathbf{0}_3 \quad Sp(\bar{\mathbf{m}}_J^e)]^T \quad (5.89)$$

This expression indicates that the antisymmetric contribution of the geometric stiffness matrix depends on the frame geometry \mathbf{G} and the element moments. For elements without rotation degrees of freedom, such as truss and membrane elements, the geometric stiffness is symmetric. The lack of symmetry of the geometric stiffness is attributed by Simo and Vu-Quoc [86], Nour-Omid and Rankin [65], Crisfield [21] and Battini and Pacoste [8] to the non-additive update of the spatial angular variation vector $\delta\boldsymbol{\theta}$.

At the equilibrium state the geometric stiffness becomes symmetric, if there are no applied moments at the element nodes, and if the loads and boundary conditions are conservative, as shown for the beam formulation with exact geometry by Simo and Vu-Quoc [86]. The result is assumed to also hold for the corotational formulation according to Nour-Omid and Rankin [65] and Felippa [26], but a proof was not provided. Nour-Omid and Rankin [65] demonstrate that the use of the symmetric stiffness part does not affect the convergence of the Newton-Raphson algorithm for the nonlinear governing equations of the problem.

The use of additive rotation parameters such as the rotation vector $\boldsymbol{\vartheta}$ or the quaternions $\boldsymbol{\vartheta}_q$ is supposed to give a symmetric stiffness matrix, even though no rigorous proof was provided. Instead, Battini and Pacoste [8] verified numerically this result for shell elements.

For the present formulation the antisymmetric contribution of the geometric stiffness matrix becomes negligible relative to the symmetric contribution when both matrices $\mathbf{k}_{g\theta}$ and \mathbf{k}_{gq} are included. This confirms the assumption that the lack of symmetry can be attributed to the use of the spatial angular variation $\delta\boldsymbol{\theta}$ and $\delta\bar{\boldsymbol{\theta}}$.

5.3.7 Conclusions

The corotational framework in the preceding sections is general, because it is independent of element response, so that the resulting expressions for the geometric transformations under large displacements can be also applied to multi-node elements, such as plate and shell

elements. Details of the extension to multi-node elements are not presented here, but the outcome of the implementation effort in FEDEASLab can be seen in the following examples involving shell finite elements. The element response follows the kinematic assumptions in section (5.3.3) with the requirement that local rotations are *small*, which allows simplification of the local strain tensor and of the rotation transformations in section (5.3.5). The assumption of small rotations in the local frame is not sufficient for linearizing the local strain for cases with significant contribution of the nonlinear Wagner term due to torsion, as the example of the following section 5.5.4 demonstrates.

5.4 Element with nonlinear axial-torsion interaction

The kinematic equations in the local reference system are given in equation (5.55). The local strain measures can be simplified according to equation (5.64) in the framework of the corotational formulation. In this case the expression of the Green-Lagrange strain $\bar{\mathbb{E}}$ in terms of the local displacements $\bar{\mathbf{u}}$ takes the form

$$\bar{\mathbb{E}}_{11}(\bar{\mathbf{u}}) = \bar{d}'_1 - X_2 \bar{\vartheta}'_3 + X_3 \bar{\vartheta}'_2 + \omega \bar{\vartheta}''_1 + \frac{1}{2}(X_2^2 + X_3^2) \bar{\vartheta}'_1{}^2 \quad (5.90a)$$

$$2\bar{\mathbb{E}}_{12}(\bar{\mathbf{u}}) = -X_3 \bar{\vartheta}'_1 + \omega_{,2} \bar{\vartheta}'_1 \quad (5.90b)$$

$$2\bar{\mathbb{E}}_{13}(\bar{\mathbf{u}}) = X_2 \bar{\vartheta}'_1 + \omega_{,3} \bar{\vartheta}'_1 \quad (5.90c)$$

The nonlinear term of the Green-Lagrange strain $\frac{1}{2}(X_2^2 + X_3^2) \bar{\vartheta}'_1{}^2$ that describes the interaction between axial and torsional displacement is known as the Wagner term. Most beam elements with the corotational formulation include only the linear strain terms, and thus cannot capture the axial-torsional interaction under nonlinear geometry, such as torsional buckling instabilities [96], as identified by Teh and Clarke [93] and Battini and Pacoste [8]. To address the problem the authors of these studies propose a second order element in the local frame.

Here an alternative approach is followed that is more in line with the spirit of the corotational formulation of allowing the element to follow linear kinematics in the local frame. To capture the nonlinear Wagner term in the axial Lagrange strain of equation (5.90a) a corresponding term is added to the corotational formulation of the preceding section. There are two limitations: first, the nonlinear term in equation (5.90a) involves the coordinates of the material point, and secondly, it involves the square of the twist rate $\bar{\vartheta}'_1{}^2$. To overcome the first problem, the nonlinear Wagner term is averaged over the cross-section, as suggested first by Timoshenko [96]. With the definition for r_0^2

$$r_0^2 = \frac{1}{A} \int_A (X_2^2 + X_3^2) dA = \frac{I_2 + I_3}{A} \quad (5.91)$$

where A is the cross section area, and I_2 and I_3 the moments of inertia, the nonlinear Wagner

term simplifies to

$$\frac{1}{2}(X_2^2 + X_3^2)\bar{\vartheta}'_1 \approx \frac{r_0^2}{2}\bar{\vartheta}'_1 \quad (5.92)$$

The examples in the following section assess the validity of this assumption. With the simplification of the Wagner term, the axial strain in the local frame can be expressed as

$$\bar{\mathbb{E}}_{11}(\bar{\mathbf{u}}) = (\bar{d}'_1 + \frac{r_0^2}{2}\bar{\vartheta}'_1) - X_2\bar{\vartheta}'_3 + X_3\bar{\vartheta}'_2 + \omega\bar{\vartheta}''_1 \quad (5.93)$$

In order to use linear kinematics for the element response in the local frame the axial element deformation v_1 is defined as

$$v_1 = \bar{d}_{1,J} + \frac{r_0^2}{2l}(\bar{\vartheta}_{1,IJ})^2 \quad (5.94)$$

with $\bar{\vartheta}_{1,IJ}$ the average of the two end rotations $\bar{\vartheta}_1$

$$\bar{\vartheta}_{1,IJ} = \frac{1}{2}(\bar{\vartheta}_{1,I} + \bar{\vartheta}_{1,J})$$

In equation (5.94) it is assumed that the rate of twist is uniform over the element. This is approximately true as the element length is reduced by mesh refinement.

With the definition for the axial element deformation v_1 in equation (5.94) the axial strain in the reference axis of the element of length l becomes

$$\epsilon_a = \frac{v_1}{l} = \frac{\bar{d}_{1,J}}{l} + \frac{r_0^2}{2} \left(\frac{\bar{\vartheta}_{1,IJ}}{l} \right)^2 \quad (5.95)$$

which matches the corresponding axial strain in equation (5.93) as $l \rightarrow 0$ noting that

$$\frac{\bar{d}_{1,J}}{l} \rightarrow \bar{d}'_1 \quad \text{and} \quad \frac{\bar{\vartheta}_{1,IJ}}{l} \rightarrow \vartheta'_1$$

The deformations \mathbf{v} of a 3d beam element with warping deformations are defined as

$$\mathbf{v}(\bar{\mathbf{a}}) = (v_1 \quad \bar{\vartheta}_{3,I} \quad \bar{\vartheta}_{3,J} \quad \bar{\vartheta}_{1,IJ} \quad \bar{\vartheta}_{2,I} \quad \bar{\vartheta}_{2,J} \quad \bar{\vartheta}'_{1,I} \quad \bar{\vartheta}'_{1,J})^T \quad (5.96)$$

and can be expressed in terms of the node displacements in the local frame as

$$\mathbf{v} = \mathbf{a}_v(\bar{\mathbf{a}}) \bar{\mathbf{a}} \quad (5.97)$$

with the following definition for the kinematic matrix \mathbf{a}_v

$$\mathbf{a}_v = \begin{bmatrix} -1 & 0 & 0 & -\frac{r_0^2}{l}\bar{\vartheta}_{1,IJ} & 0 & 0 & 0 & 1 & 0 & 0 & \frac{r_0^2}{l}\bar{\vartheta}_{1,IJ} & 0 & 0 & 0 \\ 0 & 0 & 0 & 0 & 0 & 1 & 0 & 0 & 0 & 0 & 0 & 0 & 0 & 0 \\ 0 & 0 & 0 & 0 & 0 & 0 & 0 & 0 & 0 & 0 & 0 & 0 & 1 & 0 \\ 0 & 0 & 0 & -1 & 0 & 0 & 0 & 0 & 0 & 0 & 1 & 0 & 0 & 0 \\ 0 & 0 & 0 & 0 & 1 & 0 & 0 & 0 & 0 & 0 & 0 & 0 & 0 & 0 \\ 0 & 0 & 0 & 0 & 0 & 0 & 0 & 0 & 0 & 0 & 0 & 1 & 0 & 0 \\ 0 & 0 & 0 & 0 & 0 & 0 & 0 & 0 & 0 & 0 & 0 & 0 & 1 & 0 \\ 0 & 0 & 0 & 0 & 0 & 0 & 0 & 0 & 0 & 0 & 0 & 0 & 0 & 1 \end{bmatrix} \quad (5.98)$$

The basic forces \mathbf{q} conjugate to deformations \mathbf{v} satisfy the following relation by the principle of virtual displacements

$$\bar{\mathbf{p}} = \mathbf{a}_v^T \mathbf{q} \quad (5.99)$$

These forces are the axial force N , the bending moments M_{3I} and M_{3J} about axis \mathbf{E}_3 at node I and J, respectively, the bending moments M_{2I} and M_{2J} about axis \mathbf{E}_2 at node I and J, respectively, the torque T and the bi-moments M_{wI} and M_{wJ} at nodes I and J, respectively. The consistent tangent stiffness matrix from the local equilibrium equation (5.86) gives rise to the stiffness matrix (5.87).

The transformation matrix \mathbf{a}_v can be added to the corotational formulation of equation (5.86) for the transformation of the basic forces \mathbf{q} , however this transformation is no longer strictly geometric, because it includes section property information. The coupling between axial force and torque gives rise to the following stiffness expression

$$\frac{\partial \bar{\mathbf{p}}}{\partial \bar{\mathbf{a}}} = \mathbf{a}_v^T \frac{\partial \mathbf{q}}{\partial \mathbf{v}} \mathbf{a}_v + \mathbf{k}_{gv} \quad (5.100)$$

to be substituted in equation (5.87) with the geometric stiffness contribution \mathbf{k}_{gv} given by

$$\mathbf{k}_{gv} = \frac{r_0^2 N}{l} \begin{bmatrix} 0 & 0 & 0 & 0 & 0 & 0 & 0 & 0 & 0 & 0 & 0 & 0 & 0 & 0 \\ 0 & 0 & 0 & 0 & 0 & 0 & 0 & 0 & 0 & 0 & 0 & 0 & 0 & 0 \\ 0 & 0 & 0 & 0 & 0 & 0 & 0 & 0 & 0 & 0 & 0 & 0 & 0 & 0 \\ 0 & 0 & 0 & 1 & 0 & 0 & 0 & 0 & 0 & 0 & -1 & 0 & 0 & 0 \\ 0 & 0 & 0 & 0 & 0 & 0 & 0 & 0 & 0 & 0 & 0 & 0 & 0 & 0 \\ 0 & 0 & 0 & 0 & 0 & 0 & 0 & 0 & 0 & 0 & 0 & 0 & 0 & 0 \\ 0 & 0 & 0 & 0 & 0 & 0 & 0 & 0 & 0 & 0 & 0 & 0 & 0 & 0 \\ 0 & 0 & 0 & 0 & 0 & 0 & 0 & 0 & 0 & 0 & 0 & 0 & 0 & 0 \\ 0 & 0 & 0 & 0 & 0 & 0 & 0 & 0 & 0 & 0 & 0 & 0 & 0 & 0 \\ 0 & 0 & 0 & 0 & 0 & 0 & 0 & 0 & 0 & 0 & 0 & 0 & 0 & 0 \\ 0 & 0 & 0 & -1 & 0 & 0 & 0 & 0 & 0 & 0 & 1 & 0 & 0 & 0 \\ 0 & 0 & 0 & 0 & 0 & 0 & 0 & 0 & 0 & 0 & 0 & 0 & 0 & 0 \\ 0 & 0 & 0 & 0 & 0 & 0 & 0 & 0 & 0 & 0 & 0 & 0 & 0 & 0 \\ 0 & 0 & 0 & 0 & 0 & 0 & 0 & 0 & 0 & 0 & 0 & 0 & 0 & 0 \end{bmatrix} \quad (5.101)$$

With this approach the element response in the local frame determines the basic forces \mathbf{q} and the corresponding tangent stiffness $\frac{\partial \mathbf{q}}{\partial \mathbf{v}}$ for given deformations \mathbf{v} under the assumption of small deformations. Nonlinear kinematic effects due to large displacements are included in the transformation of the nodal variables according to the corotational formulation theory with the addition of the transformation matrix \mathbf{a}_v for the Wagner effect.

5.5 Examples

The following examples illustrate some aspects of the nonlinear geometry behavior of 3d beam elements under large displacements. The mesh discretization of the structural model

ensures that the assumption of small deformations and rotations in the element frame is appropriate. The first two examples deal with the case of lateral buckling, which involves coupling of flexural and torsional response. The third example addresses the simulation of the axial-torsional buckling of a beam with the modification of the corotational formulation to account for the nonlinear Wagner term. The last two examples present the simulation of nonlinear material response under large displacements.

5.5.1 L-shape cantilever beam

This example studies the lateral buckling behavior of the L-shape cantilever beam with the dimensions and properties in figure (5.5). This model was the subject of past studies of the corotational formulation by Crisfield [20] and Battini [8] using beam elements, by Nour-Omid and Rankin [65] using quadrilateral plane stress shell elements, and Pacoste [67] using triangular plane stress shell elements. The present study compares the lateral buckling behavior of the cantilever beam with the proposed 3d beam element and with the quadrilateral 4-node shell element with mixed interpolation of tensorial components (MITC) by Bathe and Dvorkin [4].

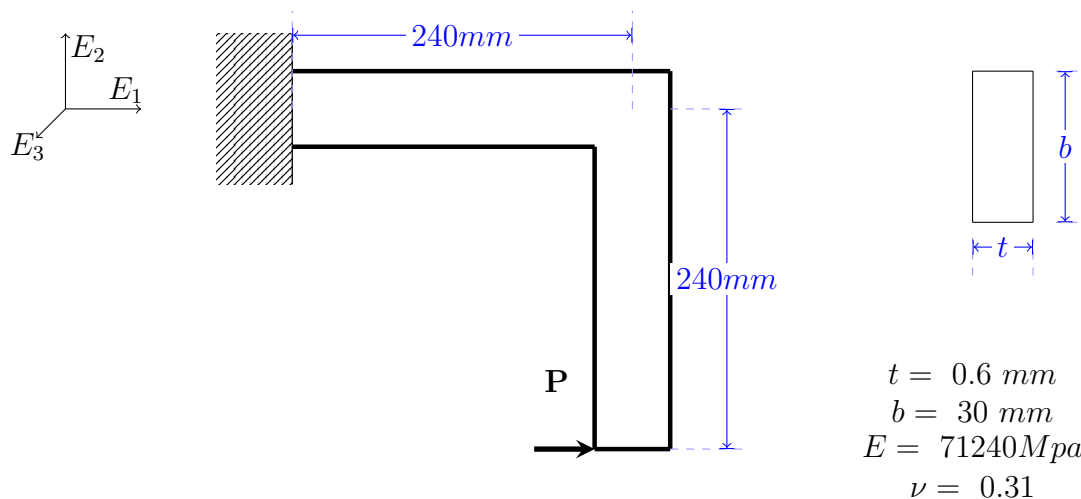


Figure 5.5: Geometry and properties of L-shape cantilever beam

Each leg of the L-shape cantilever in figure (5.5) is modeled with five beam elements, or with a mesh of 16x2 quadrilateral shell elements with 16 elements along the axis and 2 elements across the width. The warping constraint is not accounted for in the beam element, but the section stiffness J includes the effect of warping. The corotational formulation in the form of equation (5.86) is used with the beam and shell elements to include the effect of large displacements. The nonlinear Wagner term is not included in the formulation, because it is not significant for this problem.

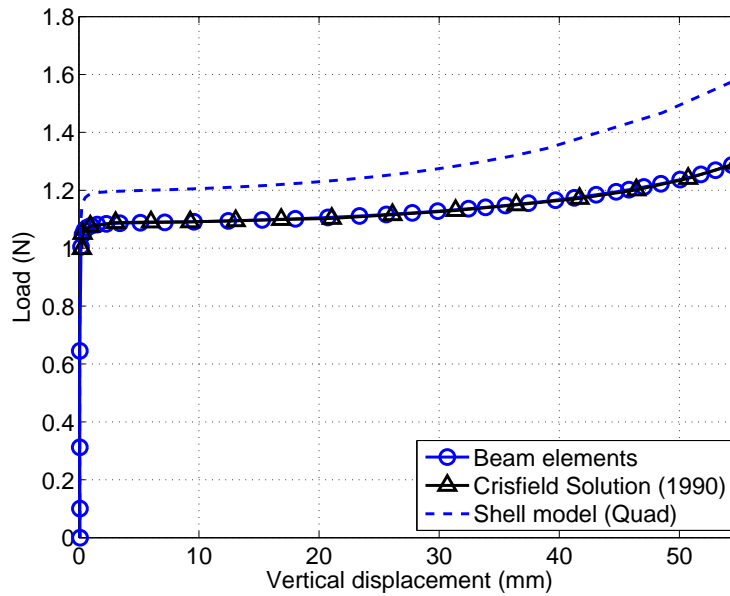


Figure 5.6: Load-displacement relation for L-shape cantilever beam

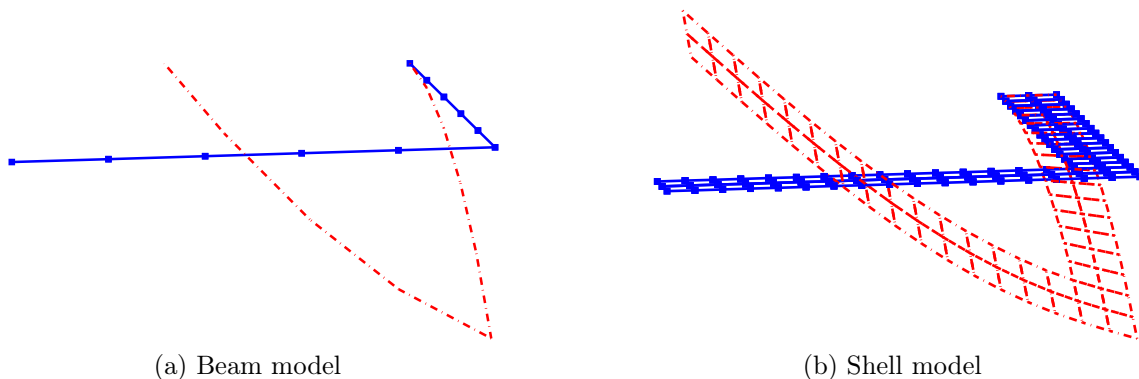


Figure 5.7: Deformed shapes of L-shape cantilever beam with five-fold magnification

The structure is subjected to a horizontal force P at the tip of the cantilever, as shown in figure (5.5). Under this force the two legs of the cantilever experience bending about the E_3 axis in figure (5.5). When the load reaches a critical value an unstable torsional mode arises. To induce this lateral buckling mode a perturbation load of $2 \cdot 10^{-4}$ N is applied at the tip of the cantilever in the E_3 direction.

Figure (5.6) shows the relation between applied load and translation in the E_3 direction of the L-shape cantilever beam. The response with the proposed beam element is compared with the response of the MITC shell element and with the solution of Crisfield [20] with beam elements. The two beam element responses are practically the same. The load-displacement

relation of the shell element model deviates slightly from that of the beam element model because of the effect of the panel zone at the intersection of the two legs of the cantilever, as discussed by Battini [8].

5.5.2 Hockling of a cable

The example of the hockling of a cable, first proposed by Nour-Omid and Rankin [65], is selected to demonstrate the ability of the corotational formulation to simulate the nonlinear torsional response due to bending instability. The word 'cable' is used in lieu of the more precise expression 'flexible rod' in the following discussion.

Figure (5.8) shows the geometry and properties of the cable, which is subjected to a concentrated torque at the tip.

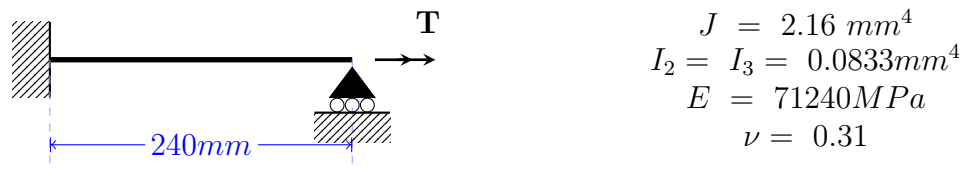


Figure 5.8: Geometry and properties of propped cantilever with torque at the tip

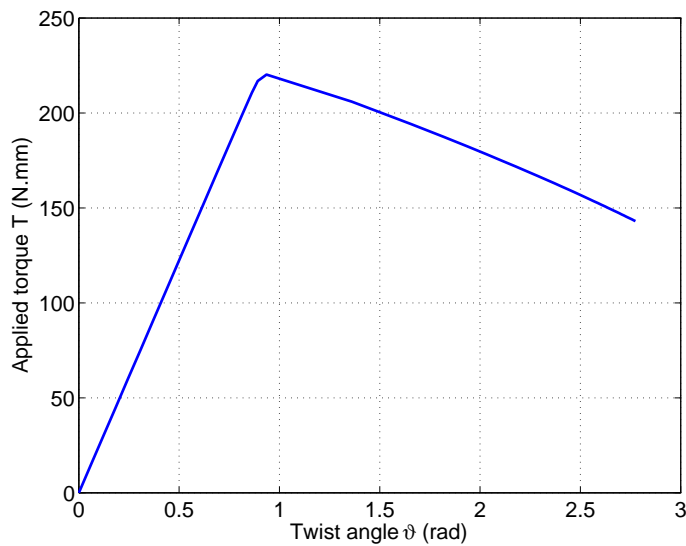


Figure 5.9: Torque versus twist angle at the tip of the hockling cable

The cable is modeled with 20 linear elastic beam elements. The nonlinear kinematics under large displacements are described with the corotational formulation, but large rotations are also accounted for in the local frame according to equations (5.71) and (5.75). The section warping and the nonlinear Wagner term are ignored in the beam model.

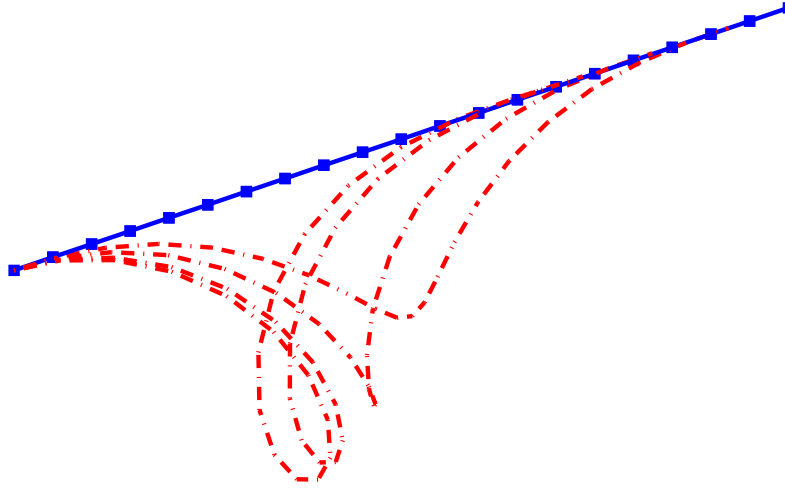


Figure 5.10: Deformed shape history of twisting cable with magnification factor of 1

The simulation under large displacements uses the quaternion parametrization for the rotations. During the incremental analysis under the applied end torque \mathbf{m}_q , the quaternions $\boldsymbol{\vartheta}_q$ are transformed to rotations $\boldsymbol{\vartheta}$, and the torque to the conjugate moment \mathbf{m} according to equations (5.9) and (5.80). With displacement control the analysis proceeds until the end twist angle $\boldsymbol{\vartheta}$ reaches the value of 2.8 rad. Figure (5.9) shows the relation between applied torque and resulting twist angle at the tip of the cable. The cable response is in complete agreement with the results by Nour-Omid and Rankin [65]. At first, the cable exhibits a linear torque-twist relation in figure (5.9). Due to its low flexural stiffness the cable buckles laterally after reaching the critical load. To induce this response bifurcation the cable model is assigned a small eccentricity. In the post-buckling branch the twisting cable experiences bending, as is clear from figure (5.10), which shows the deformed shape history of the twisting cable. The final shape of the cable is a perfect circle, but the present analysis was not pursued until this point.

5.5.3 Axial-torsional buckling

The example of the axial-torsional buckling of a beam with cruciform section is selected for testing the approach proposed in section 5.3 to approximately include the nonlinear Wagner effect in the corotational formulation, while allowing the element formulation in the local frame to retain the convenience and ease of linear kinematics.

Figure (5.11) shows the geometry of the propped cantilever model with the dimensions and material properties of the cross section. An axial force P is applied at the propped end of the cantilever with warping deformations constrained at both ends.

Timoshenko [96] gives the following formulas for the theoretical buckling load of the

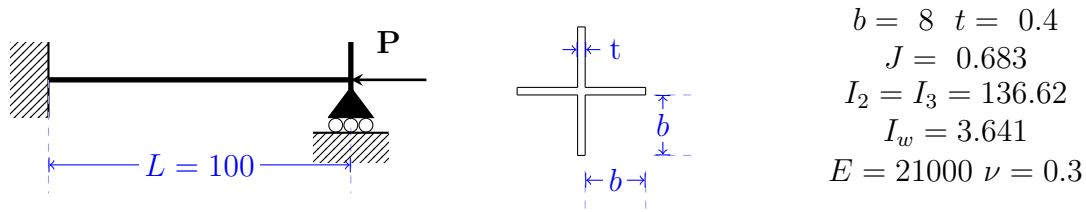


Figure 5.11: Axial buckling

propped cantilever with and without warping

$$P_c = \frac{A}{I_2 + I_3} GJ = 258 \quad P_{cw} = \frac{A}{I_2 + I_3} \left(GJ + 4 \frac{\pi^2}{L^2} EI_w \right) = 273 \quad (5.102)$$

where P_c is the buckling load with free warping, and P_{cw} the buckling load with constrained warping. The buckling load of the model is determined by determining the value of the axial load P that renders the global stiffness matrix singular using the bisection strategy. Two beam elements with the proposed corotational formulation suffice to give the theoretical buckling load of 258 units with free warping, whereas *ten* elements are required to give the theoretical buckling load of 273 units for the case with constrained warping. For reference purposes the Euler-buckling load of a simply supported beam with the same length is 2832 units.

5.5.4 Inelastic torsion of girder

This example discusses the inelastic torsion of a girder under particular consideration of the effect of the nonlinear Wagner term on the response. Of special interest is the effectiveness of the proposed corotational formulation to represent this effect.

The geometry and section dimensions of the girder in figure (5.12) are based on the study by Pi and Trahair on inelastic torsion of I-girders [71]. The girder is subjected to a torque at midspan, with the twist constrained at both ends but with the sections free to warp. The nonlinear steel material is modeled with a J2-plasticity model having Young modulus of $E = 200$ GPa, yield strength $f_y = 250$ MPa, and kinematic hardening modulus $H_k = 0.03E$. The girder response under the torque at midspan is studied for two cases of axial restraint: in case A the axial displacement is restrained at both beam ends, whereas case B refers to a beam without any axial restraints at the ends.

The girder is represented with ten 3d beam elements with linear kinematics in the local frame and the inclusion of warping displacements with a single warping mode, as described in section 3.1.2. Three Gauss-Lobatto integration points are used in each element. The fiber discretization of the cross section involves a grid of 10x3 for the web and flanges, with 10 fibers across the depth or width and 3 fibers across the thickness. The model accounts for large displacements with the modified corotational formulation in section 5.4. The results

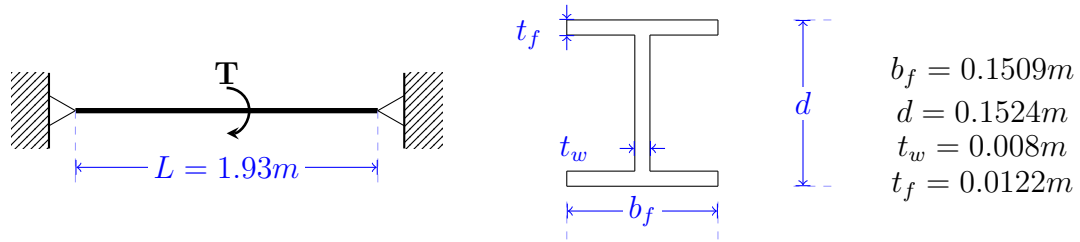


Figure 5.12: Geometry and section dimensions of I-Beam with torque at midspan

are compared with the model by Pi and Trahair [71], which includes the exact nonlinear Wagner term in a total Lagrangian element formulation.

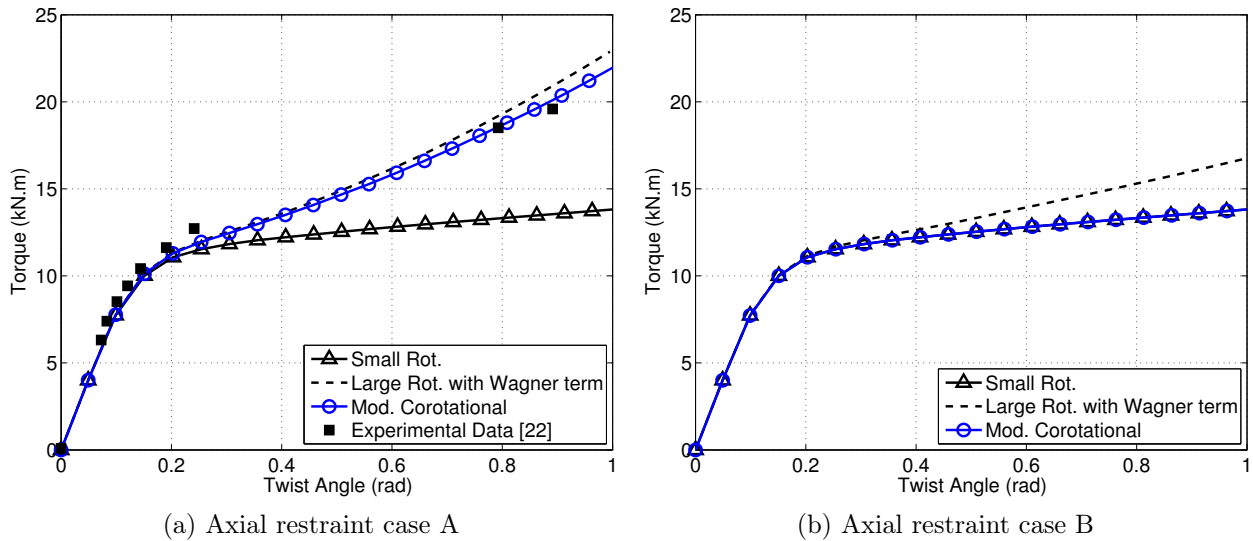


Figure 5.13: Relation of applied torque with midspan twist angle for different models

Figures (5.13a) and (5.13b) show the relation between applied torque and resulting twist angle at midspan for axial restraint cases A and B.

For case A with restrained axial displacements, an axial force arises under the applied torque in the models with nonlinear geometry. This force leads to a strong interaction between axial and torsional effects through the nonlinear Wagner term, as is evident in figure (5.13a) from the difference in the post-yield response of the models that account for large displacements and the nonlinear Wagner term from the response of the model that assumes small rotations. The Wagner term leads to the increase in torsional strength under increasing rotation in figure (5.13a). The proposed corotational formulation agrees very well with the model of Pi and Trahair [71] and with the available experimental results [22].

If the axial displacements are not restrained at the girder ends in case B, there is no axial

force in the girder. In this case the proposed corotational formulation is unable to represent the nonlinear Wagner term and the response under large rotations is indistinguishable from the response under small rotations in figure (5.13b). The figure also shows that the strength increase due to the nonlinear Wagner term is much less significant in this case and of little practical interest, amounting to a 20% increase under a very large twist angle.

5.5.5 Six-story steel frame

The last example deals with the lateral response of a six-story irregular steel frame under large displacements. The geometry of the frame with the member sizes from the study by Liew et al. [55] is shown in figure (5.14). It is assumed that the structural members consist of A36 steel. No steel hardening was assumed in the analysis.

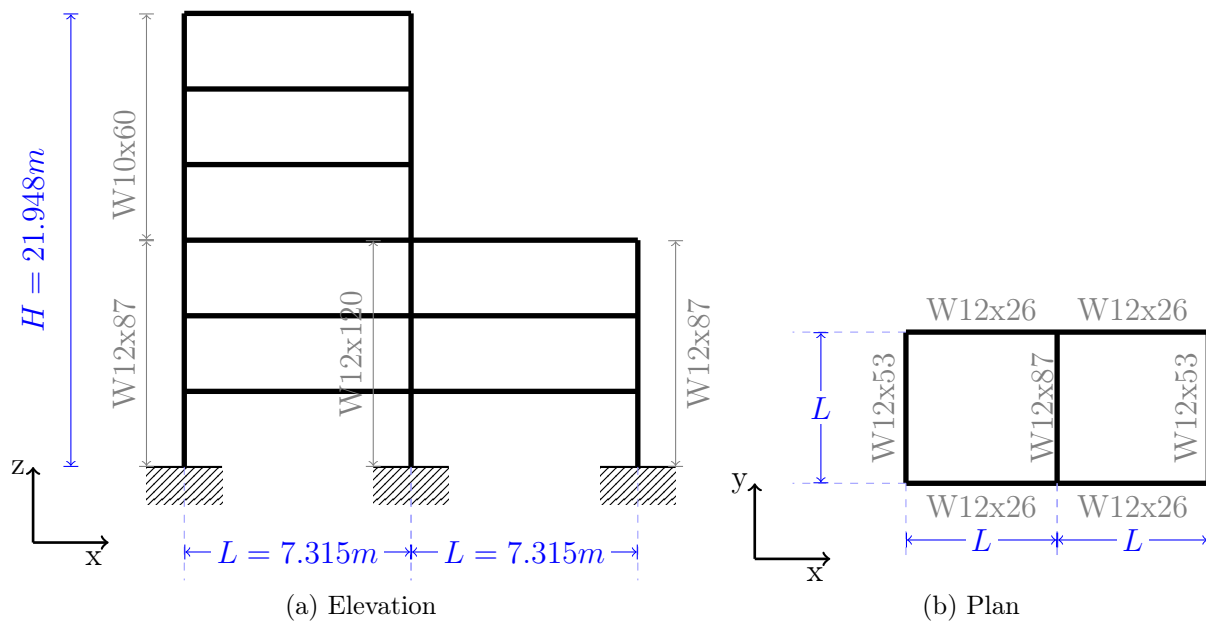


Figure 5.14: Geometry and member sizes of six-story steel frame

The frame is subjected to proportional gravity and lateral wind loads. The gravity loads correspond to a uniform load of 9.6kN/m^2 on each floor slab, and are applied as equivalent concentrated nodal forces. The wind load is assumed to be uniformly distributed over the height of the building resulting in a horizontal nodal force of 53.376 kN . Each frame member is represented with one 3d beam element with linear kinematics in the local frame. The warping displacements are included with the single parameter profile, as described in section 3.1.2. Three Gauss-Lobatto integration points are used in each element. The fiber discretization of the cross section involves a grid of 10×3 for the web and flanges, with 10 fibers across the depth or width and 3 fibers across the thickness. The six-story frame is

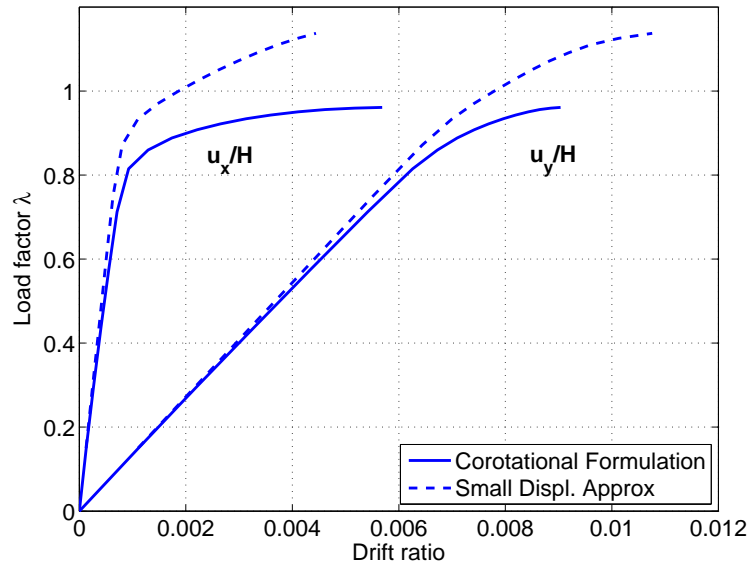


Figure 5.15: Roof drift in x and y -direction under gravity and wind loading

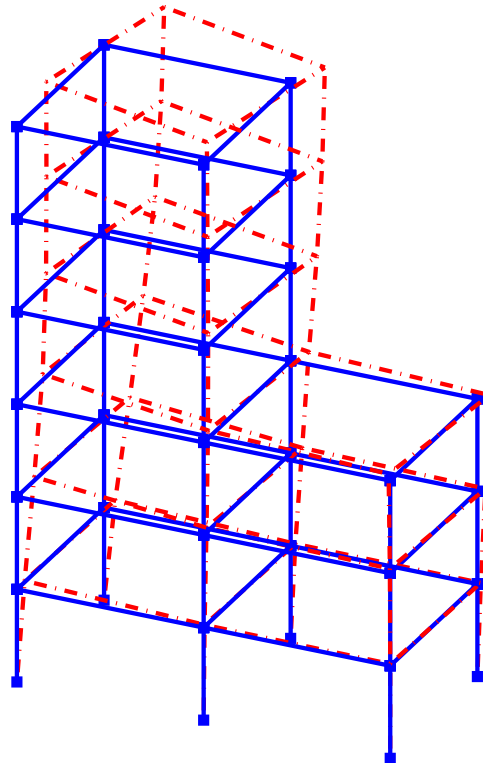


Figure 5.16: Deformed shape of six-story frame with tenfold magnification

analyzed under the assumption of small displacements, and under consideration of large displacements with the modified corotational formulation in sections 5.3 and 5.4.

Figure (5.15) shows the roof drift in the x and y directions of the frame. The consideration of nonlinear geometry reduces the lateral load capacity of the frame by approximately 20%. Moreover, the effect of nonlinear geometry on the lateral stiffness of the six-story steel frame becomes evident as the lateral loads approach the lateral capacity.

Figure (5.16) shows the deformed shape of the frame at a load factor of $\lambda = 0.934$. Due to its irregular geometry, the frame twists under the application of wind loading, but the nonlinear geometry effect is predominantly due to the axial-bending interaction rather than axial-torsion interaction. To confirm this, an additional analysis was conducted with uncoupled torsional response for the beam elements without inclusion of the Wagner effect. The load-displacement response of this analysis was practically identical to the response in figure (5.15).

Chapter 6

Summary and conclusions

6.1 Summary

The scope of this thesis is the development and validation of a 3d frame element that describes the interaction of axial, flexural, shear and torsional effects for inelastic material response under general loading conditions. The element is capable of describing the effect of warping constraints on the normal stress of 3d beams as well as the shear-lag effect of wide flanges in thin walled open and box cross sections. The element is formulated in a reference system without rigid body modes and nonlinear geometry effects under large displacements are included with the corotational formulation.

The 3d beam element is derived from the consistent variation of a mixed Hu-Washizu potential with the stress, the section deformations, and the warping displacements as independent fields of the formulation. The inclusion of the warping displacements permits the higher order description of normal and shear strains for the coupled response under shear and torsion. The warping displacements are described as the product of interpolation functions for the warping displacement distribution along the element axis and of independent interpolation functions for the warping profile at each monitored section.

The proposed 3d frame element is validated by studying the linear response of 3d structural models under shear and torsion and comparing its results with finite element models utilizing shell and brick elements. The correlation studies demonstrate the ability of the 3d beam element to capture accurately the normal and shear stress distribution of the models, including the local response of beams with warping constraints. The studies also show the ability of the model to describe the shear lag effect of a three span box girder bridge model.

The proposed 3d frame element is also validated for inelastic material response by comparing its results with experimental measurements of the local and global inelastic response of shear links in two eccentrically braced frame specimens under monotonic and cyclic load conditions.

The response of 3d beams under large displacements is investigated in the framework

of the corotational formulation. After the review of the most pertinent studies the general framework for the formulation is presented and used to study the large displacement response of several characteristic examples from the literature. The validity and accuracy of the method are evaluated and its range of validity is carefully assessed with particular attention to problems involving torsional deformation.

6.2 Conclusions

The proposed 3d beam element is variationally consistent with a mixed formulation based on a Hu-Washizu potential that includes warping displacements with independent interpolation functions for the warping profile over the cross section and the warping displacement distribution over the element axis.

The conclusions of the present study are:

- The variationally consistent formulation of the 3d beam leads to a set of governing equations for the state determination of a numerically robust and computationally efficient element for the inelastic analysis of structural elements under the combination of axial force, biaxial bending moment, biaxial shear force, and torque. A salient feature of the formulation is the coupling of the section responses by the interpolation of the basic element forces and the warping displacements along the element axis.
- The derivation of the section response is based on consistent section kinematics and the numerical integration of the multi-axial material response by the midpoint rule (fiber model). The formulation supports any type of multi-axial, inelastic material model.
- The interpolation of the section warping profile with Lagrange polynomials is versatile and gives good results for wide-flange, tubular box, and solid rectangular sections. The parametrization of the warping profile with n_w warping degrees of freedom in different arrangements provides modeling flexibility in terms of the desired accuracy of local response and proves advantageous over existing models with specified warping profiles that only adjust the warping amplitude.
- The number of warping degrees of freedom n_w for nonlinear material response can remain the same as for linear elastic response. Suggestions for the selection of the number and arrangement of the warping degrees of freedom are presented in Chapter 3.
- For the non-uniform warping distribution along the beam element axis the use of Lagrange polynomials and quadratic splines is studied. Lagrange polynomials give good results under elastic and inelastic material response with three or five control

points along the element axis. They suffer, however, from errors in the higher order derivatives when more than five interpolation points are used along the axis leading to inaccurate determination of local strains and stresses. The interpolation of the warping distribution with quadratic spline functions is more accurate but also more costly than the interpolation with Lagrange polynomials. Quadratic spline functions should be used when the accurate modeling of local inelastic material response is of interest. In such case two integration points per segment are necessary with one additional integration point at each element end.

- The mixed formulation of the 3d beam element is free of shear-locking problems and is able to represent accurately the effect of shear on the response of structural elements with a single element per member.
- The proposed element represents accurately the shear stress profile over any type of cross section without the need for a shear correction factor. The number of warping displacement parameters can be used to adjust the profile to any desired level of accuracy.
- The proposed element represents accurately the effect of warping on the global response of structural elements with the accurate determination of the torsional stiffness under free and constrained warping.
- The proposed element can represent accurately the axial stress profile due to shear-lag at the point of load application. Some difficulties arise with the representation of the axial stress profile due to shear lag in the flange of thin-walled sections under inelastic material response with low post-yield stiffness.
- The proposed element can represent accurately the shear and axial stress distribution under combined shear force and torque with a small number of warping degrees of freedom per section. Its general assumptions make it suitable for an extensive range of applications, in contrast to existing special purpose elements.
- The proposed element is capable of describing the effect of warping at the boundary sections of 3d beams with warping constraints as well as along the element. This effect manifests itself in the axial stress profile of thin-walled sections. The correlation studies show that the axial stress profile of the proposed element under warping constraints matches the profile of much more expensive shell and brick finite element models. The element is, therefore, suitable not only for the analysis of large structural models, but also for the evaluation of the local stress fields at the boundaries.
- With the implementation strategy of the warping displacement degrees of freedom as local variables the proposed element can be combined with standard 3d elements for the representation of critical regions of the structural model with significant reduction

of computational effort. Alternatively, the warping displacement degrees of freedom can be treated as global variables so that the effect of warping constraints and the interaction of shear forces with the torque can be studied over larger portions of the structural model.

- The proposed compact formulation of the corotational formulation for 3d beam elements permits the efficient representation of the nonlinear kinematics under large displacements, while the element formulation in the local frame is limited to linear kinematics. In the spirit of this approach it is possible to represent the nonlinear Wagner effect in the interaction of axial force with torque with very few exceptions. The compact formulation can be extended to triangular and quadrilateral shell elements. The most serious limitation of the formulation at present is its inability to accommodate 3d beam element formulations with shear deformations.

6.3 Recommendations for further research

It is possible to extend the range of applications for the proposed 3d beam element with the inclusion of additional constitutive models. In particular, the inclusion of a 3d concrete material law and the modeling of transverse and longitudinal reinforcement will allow the simulation of the response of reinforced concrete structures, such as the service core of high-rise buildings with tubular cross-section and box girder bridges.

Furthermore, certain aspects of the proposed model require additional study. These are:

- The optimum choice of the number of warping degrees of freedom for certain type of problems and for different combinations of 3d shear forces with torque.
- The study of warping constraints for structural elements that meet at an angle.
- The inclusion of shear deformable elements in the proposed corotational formulation.
- The inclusion of the nonlinear Wagner effect in the proposed corotational formulation in a consistent and rational way that covers all cases of axial force-torque interaction.

Bibliography

- [1] M. Abramowitz and I.A Stegun. *Handbook of Mathematical Functions (with Formulas, Graphs, and Mathematical Tables)*. Dover, 1972.
- [2] F. Auricchio and R.L. Taylor. Two material models for cyclic plasticity: nonlinear kinematic hardening and generalized plasticity. *International journal of plasticity*, 11(1):65–98, 1995.
- [3] J.M. Bairan. *A non-linear totally-coupled model for RC sections under 3D bending, shear, torsion and axial loading*. PhD thesis, Technical University of Catalonia, Barcelona, 2005.
- [4] K.-J. Bathe and E.N. Dvorkin. Four-node plate bending element based on mindlin/reissner plate theory and a mixed interpolation. *International Journal for Numerical Methods in Engineering*, 21(2):367–383, 1985.
- [5] J-M. Battini. A modified corotational framework for triangular shell elements. *Computer Methods in Applied Mechanics and Engineering*, 196:1905–1914, March 2007.
- [6] J-M. Battini. Large rotations and nodal moments in corotational elements. *CMES - Computer Modeling in Engineering and Sciences*, 33:1–15, 2008.
- [7] J-M. Battini. A non-linear corotational 4-node plane element. *Mechanics Research Communications*, 35(6):408–413, September 2008.
- [8] J-M. Battini and C. Pacoste. Co-rotational beam elements with warping effects in instability problems. *Computer Methods in Applied Mechanics and Engineering*, 191:1755–1789, February 2002.
- [9] J-M. Battini and C. Pacoste. On the choice of the linear element for corotational triangular shells. *Computer Methods in Applied Mechanics and Engineering*, 195:6362–6377, September 2006.
- [10] S.U. Benscoter. Theory of torsion bending for multicell beams. *American Society of Mechanical Engineers – Transactions – Journal of Applied Mechanics*, 21(1):25–34, 1954.

- [11] E.C. Bentz. *Sectional analysis of reinforced concrete members*. PhD thesis, University of Toronto, Toronto, Canada, 2000.
- [12] J.W. Berman and M. Bruneau. Approaches for the seismic retrofit of braced steel bridges piers and proof-of-concept testing of an eccentrically braced frame with tubular link. Technical Report 05-0004, MCEER, 2005.
- [13] J.W. Berman and M. Bruneau. Experimental and analytical investigation of tubular links for eccentrically braced frames. *Engineering Structures*, 29(8):1929–1938, 2007.
- [14] P. Ceresa, L. Petrini, and R. Pinho. Flexure-shear fiber beam-column elements for modeling frame structures under seismic loading - state of the art. *Journal of Earthquake Engineering*, 11:46–88, 2007.
- [15] P. Ceresa, L. Petrini, R. Pinho, and R. Sousa. A fibre flexure-shear model for seismic analysis of RC-framed structures. *Earthquake Engineering and Structural Dynamics*, 38(5):565–586, 2009.
- [16] S. T. Chang. Shear lag effect in simply supported prestressed concrete box girder. *Journal of Bridge Engineering*, 9(2):178–184, 2004.
- [17] S. T. Chang and D. Yun. Shear lag effect in box girder with varying depth. *Journal of structural engineering New York, N.Y.*, 114(10):2280–2292, 1988.
- [18] R.W. Clough, K.L. Benuska, and E.L. Wilson. Inelastic earthquake response of tall buildings. In *Proceedings of the 3rd World Conference on Earthquake Engineering, Jan 22-Feb 1 1965*, volume 2 of *New Zealand. World Conference on Earthquake Engineering*, pages –68–89, 1965.
- [19] G.R. Cowper. Shear coefficient in timoshenko’s beam theory. *American Society of Mechanical Engineers – Transactions – Journal of Applied Mechanics*, 33(2):335–340, 1966.
- [20] M.A. Crisfield. A consistent co-rotational formulation for non-linear, three-dimensional, beam-elements. *Computer Methods in Applied Mechanics and Engineering*, 81:131–150, August 1990.
- [21] M.A. Crisfield. *Non-linear Finite Element Analysis of Solids and Structures*, volume 1-2. John Wiley & Sons, 1991.
- [22] C.R. Farwell, Jr., and T.V. Galambos. Nonuniform torsion of steel beams in inelastic range. *J.Struct. Engrg. ASCE*, 95:2813–2829, 1969.

- [23] R. El Fatmi. Non-uniform warping including the effects of torsion and shear forces. part i: A general beam theory. *International Journal of Solids and Structures*, 44(18-19):5912–5929, 2007.
- [24] R. El Fatmi. Non-uniform warping including the effects of torsion and shear forces. part II: analytical and numerical applications. *International Journal of Solids and Structures*, 44(18-19):5930–5952, 2007.
- [25] R. El Fatmi and N. Ghazouani. Higher order composite beam theory built on Saint-Venant’s solution. Part-I: theoretical developments. *Composite Structures*, 93(2):557–566, 2011.
- [26] C.A. Felippa and B. Haugen. A unified formulation of small-strain corotational finite elements: I. theory. *Computer Methods in Applied Mechanics and Engineering*, 194:2285–2335, June 2005.
- [27] K. Ferradi. Etude du gauchissement et modelisation en element fini. Report, Setec TPI, France, 2010.
- [28] F.C. Filippou and M. Constantinides. Fedeaslab getting started guide and simulation examples. Technical Report 22, NEESgrid, www.nees-grid.org, 2004.
- [29] F.C. Filippou and G.L. Fenves. Methods of analysis for earthquake-resistant structures. In *Earthquake engineering: From engineering seismology to performance-based engineering*, chapter 6. Y. Bozorgnia and V.V. Bertero CRC Press LLC, 2004.
- [30] European Committee for Standardisation. Eurocode 3 prEN 1993-1-5 : 2003.
- [31] G. Garcea, A. Madeo, G. Zagari, and R. Casciaro. Asymptotic post-buckling fem analysis using corotational formulation. *International Journal of Solids and Structures*, 46:377–397, 2009.
- [32] J.M. Bairan Garcia and A.R. Mari Bernat. Shear-bending-torsion interaction in structural concrete members: A nonlinear coupled sectional approach. *Archives of Computational Methods in Engineering*, 14(3):249–278, 2007.
- [33] N. Ghazouani and R. El Fatmi. Higher order composite beam theory built on Saint-Venant’s solution. Part-II: built-in effects influence on the behavior of end-loaded cantilever beams. *Composite Structures*, 93(2):567–581, 2011.
- [34] Y.M. Ghugal and R.P. Shimpi. A review of refined shear deformation theories for isotropic and anisotropic laminated beams. *Journal of Reinforced Plastics and Composites*, 20(3):255–272, 2001.

- [35] M.F. Giberson. *The response of nonlinear multi-story structures subjected to earthquake excitation*. PhD thesis, California Institute of Technology, United States – California, 1967.
- [36] A. Gjelsvik. *The theory of thin walled bars*. Wiley, New York, 1985.
- [37] J. N. Gregori, P. M. Sosa, M.A. Prada, and F.C. Filippou. A 3D numerical model for reinforced and prestressed concrete elements subjected to combined axial, bending, shear and torsion loading. *Engineering Structures*, 29(12):3404–3419, 2007.
- [38] J. Navarro Gregori. *Modelización de elementos lineales de hormigón armado incluyendo el efecto del esfuerzo cortante*. PhD thesis, Universidad Politécnica de Valencia, 2009.
- [39] F. Gruttmann, R. Sauer, and W. Wagner. Theory and numerics of three-dimensional beams with elastoplastic material behaviour. *International Journal for Numerical Methods in Engineering*, 48:1675–1702, 2000.
- [40] B. Haugen. *Buckling and stability problems for thin shell structures using high-performance finite elements*. PhD thesis, University of Colorado, Boulder, 1994.
- [41] F.B. Hildebrand. On stress distribution in cantilever beams. *Journal of Mathematics and Physics*, 22(4):188–203, 1943.
- [42] K. D. Hjelmstad and E. P. Popov. Cyclic behavior and design of link beams. *Journal of Structural Engineering*, 109(10):2387–2403, 1983.
- [43] A. Ibrahimbegovic. On the choice of finite rotation parameters. *Computer Methods in Applied Mechanics and Engineering*, 149(1-4):49–71, 1997.
- [44] G.-W. Jang and Yoon Young Kim. Fully coupled 10-Degree-of-Freedom beam theory for piecewise straight Thin-Walled beams with general quadrilateral cross sections. *Journal of Structural Engineering*, 136(12):1596, 2010.
- [45] J. Jin and S. El-Tawil. Inelastic cyclic model for steel braces. *Journal of Engineering Mechanics*, 129(5):548–557, 2003.
- [46] S. Klinkel and S. Govindjee. Using finite strain 3D-material models in beam and shell elements. *Engineering Computations*, 19(3):254–271, 2002.
- [47] S. Klinkel and S. Govindjee. Anisotropic bending-torsion coupling for warping in a non-linear beam. *Computational Mechanics*, 31(1-2 SPEC.):78–87, 2003.
- [48] K.K. Koo and Y.K. Cheung. Mixed variational formulation for thin-walled beams with shear lag. *Journal of Engineering Mechanics*, 115(10):2271–2286, 1989.

- [49] V. Le Corvec. Corotational formulation for 3d frame, membrane and shell elements. Ce 299 report, University of California, Berkeley, 2009.
- [50] C-L. Lee. *Hu-Washizu three-dimensional frame formulations including bond-slip and singular section response*. PhD thesis, University of California, Berkeley, United States – California, 2008. Ph.D.
- [51] C.-L. Lee and F.C. Filippou. Frame elements with mixed formulation for singular section response. *International Journal for Numerical Methods in Engineering*, 78(11):1320–1344, 2009.
- [52] C. Lee Sung, C. H. Yoo, and D.Y. Yoon. Analysis of shear lag anomaly in box girders. *Journal of Structural Engineering*, 128(11):1379–1386, 2002.
- [53] C. Lertsima, T. Chaisomphob, and E. Yamaguchi. Stress concentration due to shear lag in simply supported box girders. *Engineering Structures*, 26(8):1093–1101, 2004.
- [54] R. Levy and W.R. Spillers. *Analysis of geometrically nonlinear structures*. Chapman & Hall, New York, 1994.
- [55] J.Y.Richard Liew, H. Chen, N.E. Shanmugam, and W.F. Chen. Improved nonlinear plastic hinge analysis of space frame structures. *Engineering Structures*, 22(10):1324–1338, October 2000.
- [56] Q.Z. Luo, Q.S. Li, and J. Tang. Shear lag in box girder bridges. *Journal of Bridge Engineering*, 7(5):308–312, 2002.
- [57] Q.Z. Luo, J. Tang, and Q.S. Li. Finite segment method for shear lag analysis of cable-stayed bridges. *Journal of Structural Engineering*, 128(12):1617–1622, 2002.
- [58] Q.Z. Luo, Tang J. Wu, Y.M., and Q.S. Li. Experimental studies on shear lag of box girders. *Engineering Structures*, 24(4):469–477, 2002.
- [59] Q.Z. Luo, Y.M. Wu, Q.S. Li, J. Tang, and Liu G.D. A finite segment model for shear lag analysis. *Engineering Structures*, 26(14):2113–2124, 2004.
- [60] A. Marini and E. Spacone. Analysis of reinforced concrete elements including shear effects. *ACI Structural Journal*, 103(5):645–655, 2006.
- [61] J. Mazars, P. Kotronis, F. Ragueneau, and G. Casaux. Using multifiber beams to account for shear and torsion. applications to concrete structural elements. *Computer Methods in Applied Mechanics and Engineering*, 195(52):7264–7281, 2006.
- [62] S. Mohr, J.M. Bairan, and A.R. Mari. A frame element model for the analysis of reinforced concrete structures under shear and bending. *Engineering Structures*, 32(12):3936–3954, 2010.

- [63] T. R. Mullapudi and A. Ayoub. Modeling of the seismic behavior of shear-critical reinforced concrete columns. *Engineering Structures*, 32(11):3601–3615, 2010.
- [64] P.M. Naghdi and L. Vongsarnpigoon. Small strain accompanied by moderate rotation. *Archive for Rational Mechanics and Analysis*, 80(3):263–294, 1982.
- [65] B. Nour-Omid and C.C. Rankin. Finite rotation analysis and consistent linearization using projectors. *Computer Methods in Applied Mechanics and Engineering*, 93:353–384, December 1991.
- [66] P.K.V.V. Nukala and D.W. White. A mixed finite element for three-dimensional nonlinear analysis of steel frames. *Computer Methods in Applied Mechanics and Engineering*, 193:2507–2545, June 2004.
- [67] C. Pacoste. Co-rotational flat facet triangular elements for shell instability analyses. *Computer Methods in Applied Mechanics and Engineering*, 156:75–110, April 1998.
- [68] A. Papachristidis, M. Fragiadakis, and M. Papadrakakis. A 3D fibre beam-column element with shear modelling for the inelastic analysis of steel structures. *Computational Mechanics*, 45(6):553–572, 2010.
- [69] M. Petrangeli. Fiber element for cyclic bending and shear of RC structures. II: verification. *Journal of Engineering Mechanics*, 125(9):1002–1009, 1999.
- [70] M. Petrangeli, P.E. Pinto, and V. Ciampi. Fiber element for cyclic bending and shear of RC structures. i: Theory. *Journal of Engineering Mechanics*, 125(9):994–1001, 1999.
- [71] Y.L. Pi and N.S. Trahair. Inelastic torsion of steel i-beams. *Journal of structural engineering New York, N.Y.*, 121:609–619, 1995.
- [72] G.H. Powell and P. Chen. 3d beam-column element with generalized plastic hinges. *Journal of Engineering Mechanics*, 112(7):627–641, 1986.
- [73] A. Prokic. New warping function for thin-walled beams. i: Theory. *Journal of structural engineering New York, N.Y.*, 122(12):1437–1442, 1996.
- [74] A. Prokic. New warping function for thin-walled beams. II: finite element method and applications. *Journal of structural engineering New York, N.Y.*, 122(12):1443–1451, 1996.
- [75] K.N. Rahal and M.P. Collins. Analysis of sections subjected to combined shear and torsion - a theoretical model. *ACI Structural Journal*, 92(4):459–469, 1995.
- [76] C.C. Rankin and B. Nour-Omid. The use of projectors to improve finite element performance. *Computers & Structures*, 30:257–267, 1988.

- [77] J.N. Reddy. Simple higher-order theory for laminated composite plates. In *Winter Annual Meeting of the American Society of Mechanical Engineers.*, New Orleans, LA, USA, 1984. ASME.
- [78] E. Reissner. Analysis of shear lag in box beams by principle of minimum potential energy. *Brown University Quarterly of Applied Mathematics*, 4(3):268–278, 1946.
- [79] E. Reissner. On some problems of buckling of prismatical beams under the influence of axial and transverse loads. *Zeitschrift fur Angewandte Mathematik und Physik (ZAMP)*, 34(5):649–667, 1983.
- [80] K. Saade, B. Espion, and G. Warzee. Non-uniform torsional behavior and stability of thin-walled elastic beams with arbitrary cross sections. *Thin-Walled Structures*, 42(6):857–881, 2004.
- [81] K. Saade, G. Warzee, and B. Espion. Modeling distortional shear in thin-walled elastic beams. *Thin-Walled Structures*, 44(7):808–821, 2006.
- [82] A. Saritas. *Mixed formulation frame element for shear critical steel and reinforced concrete members*. PhD thesis, University of California, Berkeley, United States – California, 2006.
- [83] H. Shakourzadeh, Y.Q. Guo, and J.L. Batoz. A torsion bending element for thin-walled beams with open and closed cross sections. *Computers & Structures*, 55(6):1045–1054, June 1995.
- [84] I.H. Shames and F.A. Cozzarelli. *Elastic and inelastic stress analysis*. Taylor and Francis, Washington, DC, 1997.
- [85] J. C. Simo and T. J. R. Hughes. *Computational inelasticity*. Springer, 1998.
- [86] J. C. Simo and L. Vu-Quoc. A three-dimensional finite-strain rod model. part ii: Computational aspects. *Computer Methods in Applied Mechanics and Engineering*, 58:79–116, October 1986.
- [87] J.C. Simo and L. Vu-Quoc. Geometrically-exact rod model incorporating shear and torsion-warping deformation. *International Journal of Solids and Structures*, 27:371–393, 1991.
- [88] Q. Song and A. C. Scordelis. Shear-lag analysis of t-, i-, and box beams. *Journal of structural engineering New York, N.Y.*, 116(5):1290–1305, 1990.
- [89] E. Spacone, F.C. Filippou, and F.F. Taucer. Fibre beam-column model for non-linear analysis of R/C frames: part i. formulation. *Earthquake Engineering and Structural Dynamics*, 25(7):711–725, 1996.

- [90] E. Spacone, F.C. Filippou, and F.F. Taucer. Fibre beam-column model for non-linear analysis of R/C frames: part II. applications. *Earthquake Engineering and Structural Dynamics*, 25(7):727–742, 1996.
- [91] R. Taylor. Feap - a finite element analysis program - user manual. User manual, UC Berkeley, www.ce.berkeley.edu/feap, 2011.
- [92] R.L. Taylor, F.C. Filippou, A. Saritas, and F. Auricchio. A mixed finite element method for beam and frame problems. *Computational Mechanics*, 31(1-2 SPEC.):192–203, 2003.
- [93] L.H. Teh and M.J. Clarke. Co-rotational and lagrangian formulations for elastic three-dimensional beam finite elements. *Journal of Constructional Steel Research*, 48(2-3):123–144, 1998.
- [94] R.T. Tenchev. Shear lag in orthotropic beam flanges and plates with stiffeners. *International Journal of Solids and Structures*, 33(9):1317–1334, 1996.
- [95] S. Timoshenko. *Theory of elasticity*. McGraw-Hill, New York, 3d ed. edition, 1969.
- [96] S. Timoshenko and J.M. Gere. *Theory of elastic stability*. McGraw-Hill, New York, 2nd ed. edition, 1961.
- [97] N.S. Trahair. Nonlinear elastic nonuniform torsion. *Journal of Structural Engineering*, 131:1135–1142, 2005.
- [98] F.J. Vecchio and M.P. Collins. Predicting the response of reinforced concrete beams subjected to shear using modified compression field theory. *ACI Structural Journal*, 85(3):258–268, 1988.
- [99] Y. Wu, S. Liu, Y. Zhu, and Y. Lai. Matrix analysis of shear lag and shear deformation in Thin-Walled box beams. *Journal of Engineering Mechanics*, 129(8):944, August 2003.
- [100] S-J. Zhou. Finite beam element considering Shear-Lag effect in box girder. *Journal of Engineering Mechanics*, 136(9):1115–1122, 2010.
- [101] O.C. Zienkiewicz and R.L. Taylor. *Finite Element Method: Volume 1, Fifth Edition*. Butterworth-Heinemann, 5 edition, September 2000.

Appendix A

Warping displacements as global degrees of freedom

When the warping displacements at the end sections of the beam element are treated as global degrees of freedom of the structure, the interior warping degrees of freedom \mathbf{U}^w are separated from the global degrees of freedom at the two end nodes \mathbf{u}_{IJ}^w . In this case, equation (2.76) is rewritten as

$$\delta \mathbf{P}^w = \mathbf{B}_{wq} \delta \mathbf{q} + \mathbf{K}_{ww} \delta \mathbf{U}^w + \mathbf{K}_{ww}^* \delta \mathbf{u}_{IJ}^w \quad (\text{A.1a})$$

$$\delta \mathbf{p}_{IJ}^w = \mathbf{B}_{wq}^{IJ} \delta \mathbf{q} + (\mathbf{K}_{ww}^*)^T \delta \mathbf{U}^w + \mathbf{K}_{ww}^{IJ} \delta \mathbf{u}_{IJ}^w \quad (\text{A.1b})$$

where \mathbf{K}_{ww} , \mathbf{K}_{ww}^* and \mathbf{K}_{ww}^{IJ} are submatrices of the stiffness matrix \mathbf{K}_{ww} which includes all warping displacement degrees of freedom.

The solution of the second equation for the warping displacements $\delta \mathbf{u}_{IJ}^w$ at the end sections of the beam element gives

$$\delta \mathbf{u}_{IJ}^w = [\mathbf{K}_{ww}^{IJ}]^{-1} [\delta \mathbf{p}_{IJ}^w - \mathbf{B}_{wq}^{IJ} \delta \mathbf{q} - (\mathbf{K}_{ww}^*)^T \delta \mathbf{U}^w] \quad (\text{A.2})$$

Substituting this result into the first equation gives the warping forces at the interior warping degrees of freedom

$$\begin{aligned} \delta \mathbf{P}^w &= (\mathbf{B}_{wq} - \mathbf{K}_{ww}^* (\mathbf{K}_{ww}^{IJ})^{-1} \mathbf{B}_{wq}^{IJ}) \delta \mathbf{q} \\ &+ \mathbf{K}_{ww}^* (\mathbf{K}_{ww}^{IJ})^{-1} \delta \mathbf{p}_{IJ}^w + (\mathbf{K}_{ww} - \mathbf{K}_{ww}^* (\mathbf{K}_{ww}^{IJ})^{-1} (\mathbf{K}_{ww}^*)^T) \delta \mathbf{U}^w \end{aligned} \quad (\text{A.3})$$

With the following definition of the force influence matrices that account for the global warping displacements \mathbf{u}_{IJ}^w

$$\begin{aligned} \tilde{\mathbf{B}}_{wq} &= \mathbf{B}_{wq} - \mathbf{K}_{ww}^* (\mathbf{K}_{ww}^{IJ})^{-1} \mathbf{B}_{wq}^{IJ} \\ &= \mathbf{B}_{wq} - \tilde{\mathbf{B}}_{ww} \mathbf{B}_{wq}^{IJ} \quad \text{with} \quad \tilde{\mathbf{B}}_{ww} = \mathbf{K}_{ww}^* (\mathbf{K}_{ww}^{IJ})^{-1} \end{aligned} \quad (\text{A.4})$$

The equation for the warping forces at the interior warping degrees of freedom becomes

$$\delta \mathbf{P}^w = \tilde{\mathbf{B}}_{wq} \delta \mathbf{q} + \tilde{\mathbf{B}}_{ww} \delta \mathbf{p}_{IJ}^w + \tilde{\mathbf{K}}_{ww} \delta \mathbf{U}^w \quad (\text{A.5})$$

where

$$\tilde{\mathbf{K}}_{ww} = \mathbf{K}_{ww} - \mathbf{K}_{ww}^* (\mathbf{K}_{ww}^{IJ})^{-1} (\mathbf{K}_{ww}^*)^T$$

Under the condition $\delta \mathbf{P}^w = \mathbf{0}$, the warping displacements at the interior degrees of freedom are

$$\delta \mathbf{U}^w = -[\tilde{\mathbf{K}}_{ww}]^{-1} \tilde{\mathbf{B}}_{wq} \delta \mathbf{q} - [\tilde{\mathbf{K}}_{ww}]^{-1} \tilde{\mathbf{B}}_{ww} \delta \mathbf{p}_{IJ}^w \quad (\text{A.6a})$$

$$\begin{aligned} \delta \mathbf{u}_{IJ}^w &= \left(-[\mathbf{K}_{ww}^{IJ}]^{-1} \mathbf{B}_{wq}^{IJ} + (\tilde{\mathbf{B}}_{ww})^T [\tilde{\mathbf{K}}_{ww}]^{-1} \tilde{\mathbf{B}}_{wq} \right) \delta \mathbf{q} \\ &+ \left([\mathbf{K}_{ww}^{IJ}]^{-1} + (\tilde{\mathbf{B}}_{ww})^T [\tilde{\mathbf{K}}_{ww}]^{-1} \tilde{\mathbf{B}}_{ww} \right) \delta \mathbf{p}_{IJ}^w \end{aligned} \quad (\text{A.6b})$$

From equation (2.73) the section deformations δe_l become

$$\delta e_l = [\mathbf{k}_{ss,l}]^{-1} (\mathbf{b}_l \delta \mathbf{q} - \mathbf{K}_{sw,l} \delta \mathbf{U}^w - \mathbf{K}_{sw,l}^{IJ} \delta \mathbf{u}_{IJ}^w) \quad (\text{A.7})$$

and substituting this into equation (2.69a) gives the element deformations $\delta \mathbf{v}$ in the form

$$\delta \mathbf{v} = \sum_{l=1}^{n_{ip}} w_l \mathbf{b}_l^T [\mathbf{k}_{ss,l}]^{-1} \mathbf{b}_l \delta \mathbf{q} - [\mathbf{B}_{wq}]^T \delta \mathbf{U}^w - [\mathbf{B}_{wq}^{IJ}]^T \delta \mathbf{u}_{IJ}^w \quad (\text{A.8})$$

with the definitions for the force influence matrix \mathbf{B}_{wq} from equation (2.75). Substituting the expressions for $\delta \mathbf{U}^w$ and $\delta \mathbf{u}_{IJ}^w$ into the last equation gives

$$\begin{aligned} \delta \mathbf{v} &= \mathbf{f}_b \delta \mathbf{q} + \left([\mathbf{B}_{wq}]^T [\tilde{\mathbf{K}}_{ww}]^{-1} \tilde{\mathbf{B}}_{wq} + [\mathbf{B}_{wq}^{IJ}]^T [\mathbf{K}_{ww}^{IJ}]^{-1} \mathbf{B}_{wq}^{IJ} - [\mathbf{B}_{wq}^{IJ}]^T (\tilde{\mathbf{B}}_{ww})^T [\tilde{\mathbf{K}}_{ww}]^{-1} \tilde{\mathbf{B}}_{wq} \right) \delta \mathbf{q} \\ &+ \left([\mathbf{B}_{wq}]^T [\tilde{\mathbf{K}}_{ww}]^{-1} \tilde{\mathbf{B}}_{ww} - [\mathbf{B}_{wq}^{IJ}]^T [\mathbf{K}_{ww}^{IJ}]^{-1} - [\mathbf{B}_{wq}^{IJ}]^T (\tilde{\mathbf{B}}_{ww})^T [\tilde{\mathbf{K}}_{ww}]^{-1} \tilde{\mathbf{B}}_{ww} \right) \delta \mathbf{p}_{IJ}^w \\ &= \left(\mathbf{f}_b + \tilde{\mathbf{B}}_{wq}^T [\tilde{\mathbf{K}}_{ww}]^{-1} \tilde{\mathbf{B}}_{wq} + [\mathbf{B}_{wq}^{IJ}]^T [\mathbf{K}_{ww}^{IJ}]^{-1} \mathbf{B}_{wq}^{IJ} \right) \delta \mathbf{q} \\ &+ \left(\tilde{\mathbf{B}}_{wq}^T [\tilde{\mathbf{K}}_{ww}]^{-1} \tilde{\mathbf{B}}_{ww} - [\mathbf{B}_{wq}^{IJ}]^T [\mathbf{K}_{ww}^{IJ}]^{-1} \right) \delta \mathbf{p}_{IJ}^w \end{aligned}$$

The last equation defines the element flexibility matrix \mathbf{f} in the form

$$\begin{pmatrix} \delta \mathbf{v} \\ \delta \mathbf{u}_{IJ}^w \end{pmatrix} = \begin{bmatrix} \mathbf{f}_b & 0 \\ 0 & 0 \end{bmatrix} + \mathbf{f}_w \begin{pmatrix} \delta \mathbf{q} \\ \delta \mathbf{p}_{IJ}^w \end{pmatrix} \quad (\text{A.9})$$

where the flexibility contribution \mathbf{f}_w due to the warping displacements is

$$\begin{aligned} \mathbf{f}_w &= \begin{bmatrix} \tilde{\mathbf{B}}_{wq}^T [\tilde{\mathbf{K}}_{ww}]^{-1} \tilde{\mathbf{B}}_{wq} + [\mathbf{B}_{wq}^{IJ}]^T [\mathbf{K}_{ww}^{IJ}]^{-1} \mathbf{B}_{wq}^{IJ} & \tilde{\mathbf{B}}_{wq}^T [\tilde{\mathbf{K}}_{ww}]^{-1} \tilde{\mathbf{B}}_{ww} - [\mathbf{B}_{wq}^{IJ}]^T [\mathbf{K}_{ww}^{IJ}]^{-1} \\ (\tilde{\mathbf{B}}_{ww})^T [\tilde{\mathbf{K}}_{ww}]^{-1} \tilde{\mathbf{B}}_{wq} - [\mathbf{K}_{ww}^{IJ}]^{-1} \mathbf{B}_{wq}^{IJ} & (\tilde{\mathbf{B}}_{ww})^T [\tilde{\mathbf{K}}_{ww}]^{-1} \tilde{\mathbf{B}}_{ww} + [\mathbf{K}_{ww}^{IJ}]^{-1} \end{bmatrix} \\ &= \begin{bmatrix} \tilde{\mathbf{B}}_{wq}^T \\ \tilde{\mathbf{B}}_{ww}^T \end{bmatrix} [\tilde{\mathbf{K}}_{ww}]^{-1} \begin{bmatrix} \tilde{\mathbf{B}}_{wq} & \tilde{\mathbf{B}}_{ww} \end{bmatrix} + \begin{bmatrix} [\mathbf{B}_{wq}^{IJ}]^T \\ -I \end{bmatrix} [\mathbf{K}_{ww}^{IJ}]^{-1} \begin{bmatrix} \mathbf{B}_{wq}^{IJ} & -I \end{bmatrix} \end{aligned} \quad (\text{A.10})$$

The stiffness matrix of the beam element without rigid body modes is the inverse of the element flexibility \mathbf{f} , and the element stiffness matrix \mathbf{k}_{IJ} is given by an equation similar to (2.85) noting that the warping degrees of freedom do not need to be transformed. The element stiffness matrix is assembled into the structure stiffness matrix with standard procedures of structural analysis.